‘Tri-3D’ electron microscopy tomography by FIB, SEM and TEM : Application to polymer nanocomposites

Yang Liu

To cite this version:

Yang Liu. ‘Tri-3D’ electron microscopy tomography by FIB, SEM and TEM : Application to polymer nanocomposites. Materials. INSA de Lyon, 2013. English. NNT : 2013ISAL0076 . tel-01077950

HAL Id: tel-01077950
https://theses.hal.science/tel-01077950

Submitted on 27 Oct 2014

N° 2013-ISAL-0076 Year 2013

Thesis

'Tri-3D' electron microscopy tomography by FIB, SEM and TEM: Application to polymer nanocomposites

Submitted to
L'Institut National des Sciences Appliquées de Lyon

To obtain
The degree of doctor

By
Yang LIU

Under the supervision of
Thierry EPICIER
Agnès BOGNER-VAN DE MOORTELE†

Defense on 25th July, 2013

Jury

OBERDISSE Julian	Director of research CNRS	L2C, University of Montpellier 2	Referee
CANTONI Marco	Doctor	CIME, EPF Lausanne	Referee
GERARD Jean-François	Professor	IMP, INSA de Lyon	Examiner
GIOT Maud	Doctor	Laboratoire central d'analyse, Michelin	Examiner
CHAZEAU Laurent	Professor	MATEIS, INSA de Lyon	Examiner
EPICIER Thierry	Director of research CNRS	MATEIS, INSA de Lyon	Supervisor
VAN DE MOORTELE Bertrand	Engineer of research CNRS	LGL, ENS de Lyon	Invited

Laboratory *Matériaux: Ingénierie et Science* (MATEIS)

INSA Direction de la Recherche - Ecoles Doctorales – Quinquennal 2011-2015

SIGLE	ECOLE DOCTORALE	NOM ET COORDONNEES DU RESPONSABLE
CHIMIE	**CHIMIE DE LYON** **http://www.edchimie-lyon.fr** Insa : R. GOURDON	M. Jean Marc LANCELIN Université de Lyon – Collège Doctoral Bât ESCPE 43 bd du 11 novembre 1918 69622 VILLEURBANNE Cedex Tél : 04.72.43 13 95 directeur@edchimie-lyon.fr
E.E.A.	**ELECTRONIQUE, ELECTROTECHNIQUE, AUTOMATIQUE** **http://edeea.ec-lyon.fr** Secrétariat : M.C. HAVGOUDOUKIAN eea@ec-lyon.fr	M. Gérard SCORLETTI Ecole Centrale de Lyon 36 avenue Guy de Collongue 69134 ECULLY Tél : 04.72.18 65 55 Fax : 04 78 43 37 17 Gerard.scorletti@ec-lyon.fr
E2M2	**EVOLUTION, ECOSYSTEME, MICROBIOLOGIE, MODELISATION** **http://e2m2.universite-lyon.fr** Insa : H. CHARLES	Mme Gudrun BORNETTE CNRS UMR 5023 LEHNA Université Claude Bernard Lyon 1 Bât Forel 43 bd du 11 novembre 1918 69622 VILLEURBANNE Cédex Tél : 06.07.53.89.13 e2m2@ univ-lyon1.fr
EDISS	**INTERDISCIPLINAIRE SCIENCES-SANTE** **http://www.ediss-lyon.fr** Sec : Samia VUILLERMOZ Insa : M. LAGARDE	M. Didier REVEL Hôpital Louis Pradel Bâtiment Central 28 Avenue Doyen Lépine 69677 BRON Tél : 04.72.68.49.09 Fax :04 72 68 49 16 Didier.revel@creatis.uni-lyon1.fr
INFOMATHS	**INFORMATIQUE ET MATHEMATIQUES** **http://infomaths.univ-lyon1.fr** Sec :Renée EL MELHEM	Mme Sylvie CALABRETTO Université Claude Bernard Lyon 1 INFOMATHS Bâtiment Braconnier 43 bd du 11 novembre 1918 69622 VILLEURBANNE Cedex Tél : 04.72. 44.82.94 Fax 04 72 43 16 87 infomaths@univ-lyon1.fr
Matériaux	**MATERIAUX DE LYON** **http://ed34.universite-lyon.fr** Secrétariat : M. LABOUNE PM : 71.70 –Fax : 87.12 Bat. Saint Exupéry Ed.materiaux@insa-lyon.fr	M. Jean-Yves BUFFIERE INSA de Lyon MATEIS Bâtiment Saint Exupéry 7 avenue Jean Capelle 69621 VILLEURBANNE Cedex Tél : 04.72.43 83 18 Fax 04 72 43 85 28 Jean-yves.buffiere@insa-lyon.fr
MEGA	**MECANIQUE, ENERGETIQUE, GENIE CIVIL, ACOUSTIQUE** **http://mega.ec-lyon.fr** Secrétariat : M. LABOUNE PM : 71.70 –Fax : 87.12 Bat. Saint Exupéry mega@insa-lyon.fr	M. Philippe BOISSE INSA de Lyon Laboratoire LAMCOS Bâtiment Jacquard 25 bis avenue Jean Capelle 69621 VILLEURBANNE Cedex Tél :04.72 .43.71.70 Fax : 04 72 43 72 37 Philippe.boisse@insa-lyon.fr
ScSo	**ScSo*** **http://recherche.univ-lyon2.fr/scso/** Sec : Viviane POLSINELLI Brigitte DUBOIS Insa : J.Y. TOUSSAINT	M. OBADIA Lionel Université Lyon 2 86 rue Pasteur 69365 LYON Cedex 07 Tél : 04.78.77.23.86 Fax : 04.37.28.04.48 Lionel.Obadia@univ-lyon2.fr

*ScSo : Histoire, Géographie, Aménagement, Urbanisme, Archéologie, Science politique, Sociologie, Anthropologie

The author and his supervisor Thierry Epicier dedicate this work to the co-supervisor, their dear colleague and friend:

Agnès Bogner-Van de Moortèle (†, 28/02/2012).

Acknowledgements

Arriving at the end of this work at MATEIS laboratory, I am so grateful to have received so many help from others who have contributed to the advance of my research. I want to leave their tracks by mentioning their names, not only in this work but also in my life.

First of all, I have special appreciation for Agnès Bogner-Van de Moortèle. She was my co-supervisor, and has left us on February 28th, 2012 after a two-year struggle against an unjust illness. Without her efforts, this work would probably not have been possible. Although we haven't worked together for a very long time, I have known her as a decent person and an honest friend who was very kind and nice to everyone all the time. She had great enthusiasm and passions for her work as a researcher and professor, and she was always dynamic, sportive and motivated about life. She was also very patient, especially while working with me. This long and hard fight against cancer didn't destroy her optimism, she picked up her work whenever she was OK in condition. I am still very moved and inspired by her spirits and positive attitude and so grateful that she has even thought about my work three days before the end of her life when she was conscious. I will be always thinking of her.

Then I want to express my gratitude to Bertrand Van de Moortèle, husband of Agnès, who is also our colleague and dear friend. I am very sorry for his loss. Since I started my PhD work, I have received a great deal of help from him for the microscopic experiments especially in FIB and also for some of my personal matters. To me, he is like a kind elder brother in my heart even if he is sometimes very strict.

I would like to thank Thierry Epicier, my supervisor, my boss and also my friend. I just want to indicate that he has put a lot of efforts on me and on my work in particular after Agnès' depart. He always has excellent ideas about the experiments and programming, and I have appreciated a lot our discussions and experiments together. I am extraordinarily glad of having worked with him and grateful for his care and concern to my personal life.

Next, I'd like to express my gratitude to the members of my thesis' jury: Julian Oberdisse (referee), Marco Cantoni (referee), Jean-François Gérard (president of jury), Maud Giot (examiner), Laurent Chazeau (examiner), Bertrand (invited) and Thierry (supervisor). It's very generous of all members to take so much interest in judging my work and to participate the jury. For Julian and Marco, I have furthermore appreciated their reports on my thesis.

As a member of two groups: SNMS and PVMH, I am happy having worked with so many gentle and intelligent people.
Particularly, in PVMH, I thank Catherine Gauthier, Jean-Marc Chenal and Laurent for their kind guidance during my thesis work and Jean-Yves Cavaillé for the constructive discussions with him and I want to thank all the group members for their years' accompany which I appreciate very much;
in SNMS, I thank Thierry Douillard, Annie Malchère, Karine Masenelli-Varlot and Gilbert Thollet for their continuous instructions and great propositions on my experiments, and Lucian Roiban and Philippe Steyer for their constructive advices about my thesis and defence preparation, and I thank all the members for their sharing in the domain of microscopy and for the time we did spend together.

I also want to thank all the members of the microscope groups (FIB, (E)SEM and TEM 2010F). They have done a marvellous job to maintain these machines. I thank Armel Deschamps, Nicolas Blanchard and France Simonet for their help and advices to me.

And I haven't forgotten the help and assistance form administrative staffs: Antonia Riccobene, Concetta Contet, Sandrine Gonnet, Erika Sattler, Emmanuel Montero, Jacqueline Fournier† and Claude Bernavon. I thank them for taking care of the paperwork for me that could be really annoying sometimes and also for our chat of diverse subjects.

I am, as well, grateful for the help from outside of MATEIS and INSA: I thank Cederic Messaoudi for his instructions on TomoJ and Sergio Marco for his help with the experiments carried out on JEOL 2200FS in Orsay; I thank Kazuhisa Sato and Toyohiko Konno for their essential contribution to the experiments in Tohoku University of Japan; I thank Mouna Tatou and Julian at L2C of Montpellier University 2 for providing me the polymer-based samples; I thank Jean-Jacques Blandin, Bruno Fayolle and Florent Dalmas for participating my thesis committee of both years and their productive suggestions on my work.

Finally, I want to thank Feng Xu, Hui Yuan, Jichao Qiao, Tao Zhang, Junlei Tang and other Chinese workmates and friends for our time shared together. And at last, I would like to express my gratitude to my wife, Xueying, she has always been supporting me by my side and I appreciate her passions about life and her courage against difficulties.

Table of contents

Résumé français

Ce travail a porté sur la caractérisation et la quantification en 3D de la répartition de charges de différents types (nanoparticules, nanotubes) dans des matrices polymères. De tels systèmes nano-composites sont élaborés aux fins d'améliorer les propriétés physiques (mécanique, électrique, etc.) du matériau polymère constituant la matrice, grâce à une addition contrôlée de charges nanométriques. La caractérisation de tels matériaux, et l'établissement de corrélations précises entre la microstructure et les propriétés d'usage requiert une approche tridimensionnelle. Ainsi, nous nous focalisons sur les techniques de tomographie en microscopie électronique.

La tomographie électronique peut être classée en deux genres : la tomographie tiltée (en MET et en MEB) et la tomographie usinage/imagerie séquentiels (en FIB/MEB) :

- La tomographie 'tiltée' est une manière de reconstruire un volume 3D à partir d'une série de projections d'un objet mince observé selon certains angles de vue (voir Figure 1). En microscopie électronique, les images de projections sont obtenues dans un domaine angulaire d'inclinaison aussi large que possible, éventuellement jusqu'à 360° avec un petit incrément. Elles sont ensuite traitées avec des algorithmes dédiés pour reconstruire des tomogrammes qui correspondent au volume original. La clé pour cette opération de reconstruction repose sur la nécessité d'une relation biunivoque entre l'intensité et la masse-épaisseur pour toute la série d'images (*critère de projection*) [Midgley2003]. Cette technique est le plus souvent mise en œuvre dans un microscope électronique en transmission (MET) pour l'étude des nanostructures. Avec la capacité de changer le mode d'imagerie : champ clair (Bright Field), énergie filtrée (EFTEM), STEM (microscope électronique à balayage par transmission) HAADF (champ sombre annulaire à grand angle), elle est largement appliquée en science des matériaux [Koster2000] [Baldock2002] [Weyland2006] [Jinnai2009]. Récemment, cette technique a été étendue à la microscopie électronique à balayage (MEB) dans une variante développée au laboratoire MATEIS [Jornsanoh2011]. Cette approche, dénommée 'tomo-STEM®', utilise un mode d'imagerie très similaire au STEM-HAADF en MET. Elle permet par essence de travailler à des tensions d'accélération des électrons plus faibles qu'en MET, et d'utiliser des angles de collecte des électrons transmis par l'échantillon plus grands, ce qui conduit à des différences parfois majeures en termes de contraste, résolution, endommagement par le faisceau et épaisseur traversée.

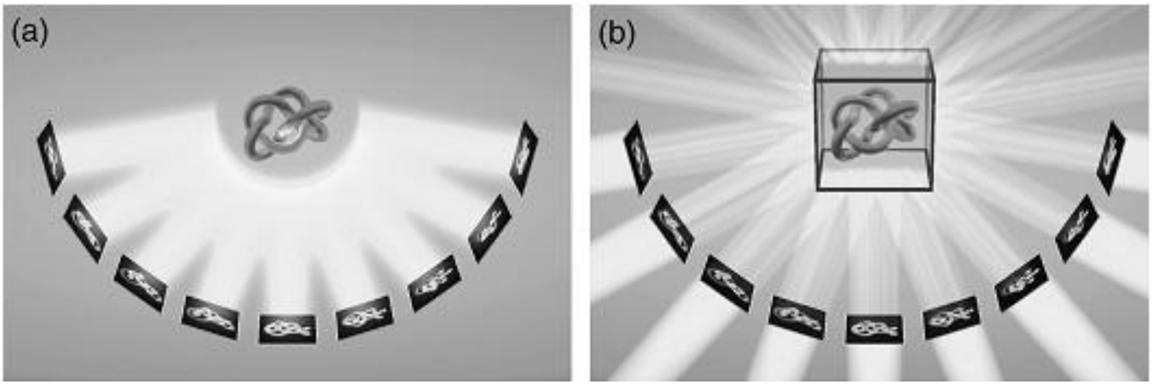

Figure 1 : L'acquisition des projections 2D et la reconstruction 3D associé à un axe d'inclinaison unique. a) Une série de projection en 2D peut être enregistrée par inclinaison soit de l'objet, soit de la source (faisceau incident) et du détecteur de façon incrémentielle ; b) une reconstruction pourrait se faire en additionnant tous les éléments 'rétroprojetés', calculés à partir de chaque image initiale. [Baumeister1999]

- La tomographie par usinage et imagerie séquentiels est une autre technique 3D, combinant résolution nanométrique et volume analysé relativement important par rapport à ce qui est permis en tomographie ‘tiltée’, réalisée dans un système FIB (faisceau d'ions focalisé)/MEB. Le microscope est équipé de deux colonnes (électronique et ionique), et développé sur la base d’un MEB conventionnel. L’échantillon n’est pas incliné, et n’a pas besoin d’être mince contrairement à la tomographie en projection. Un faisceau d’ions est utilisé pour usiner localement l’échantillon et réaliser une section dans une zone d’intérêt. Une image ‘MEB’ classique est ensuite réalisée avec le faisceau d’électrons. Cette procédure est répétée en abrasant à chaque fois une couche d’épaisseur constante (voir Figure 2). Un volume peut ainsi être visualisé à partir de la série d’images obtenue pendant la procédure séquentielle. La taille de ce volume est principalement limitée par le temps d’usinage, éventuellement par celle de l’objet.

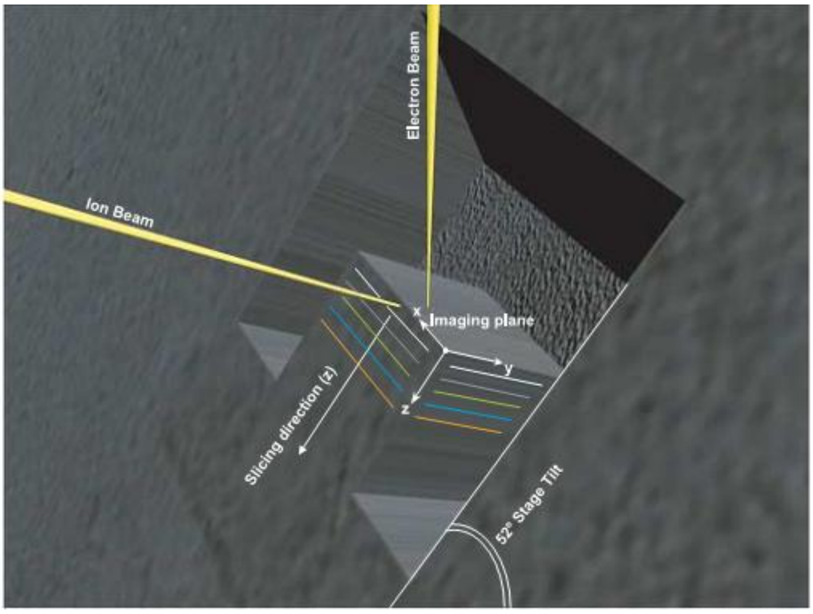

Figure 2 : Illustration d'une zone d'intérêt préparée pour la procédure usinage/imagerie séquentiels en FIB. [Holzer2004]

Dans ce travail, deux types de nanocomposite polymère ont été étudiés par une approche multiple en tomographie électronique et nous allons successivement développer les expériences réalisées et les résultats obtenus sur ces 2 systèmes.

● Le premier concerne un système développé au laboratoire MATEIS (Matériaux : Ingénierie et Science) : P(BuA-*stat*-S)/MWNTs, copolymère statistique poly (styrène-*co*-acrylate de butyl) renforcé par des nanotubes de carbone multi-parois. Deux méthodes de synthèse ont été mises en œuvre pour élaborer ce système avec un même taux de charges (de 0.2 à 3 vol. %) : évaporation (‘E’), et lyophilisation + pression (‘FP’) [Dalmas2005]. Différentes caractérisations préalables à notre étude ont montré que ces deux matériaux ne possèdent pas des propriétés physiques uniformes, et des hypothèses fortes ont été avancées pour en attribuer la raison aux interactions entres les nanotubes constituant les charges (voir Figure 3 et Figure 4) [Dalmas2007]. Notre objectif a été ici de caractériser et quantifier en 3D les nanotubes et leurs interactions, pour établir une corrélation entre la nanostructure et des propriétés de transport, i.e. la conductivité électrique qui s’avère très différente dans les 2 systèmes étudiés (Figure 3).

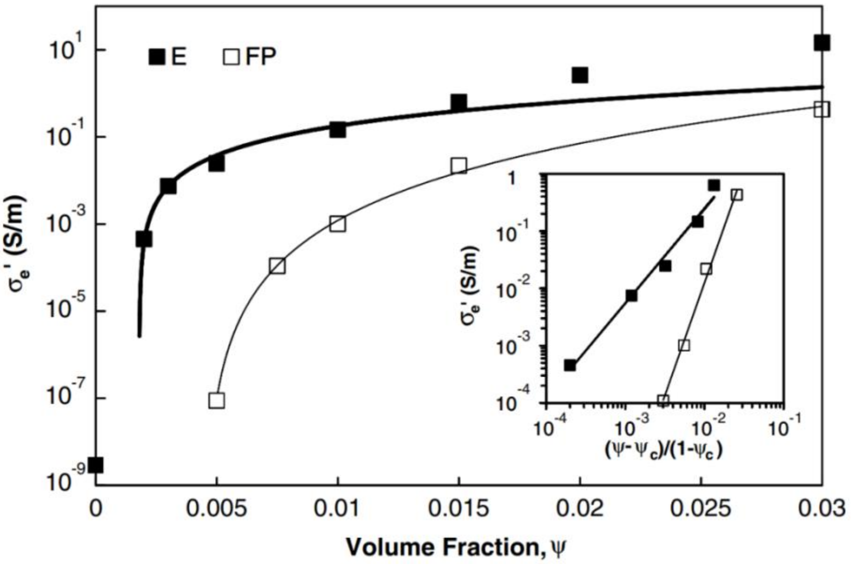

Figure 3 : Partie réelle de la conductivité électrique en courant alternatif à 1 Hz, pour le matériau évaporé ‘E’ et le matériau lyophilisé et pressé ‘FP’ avec différentes fractions de nanotubes, en comparaison avec les prédictions de la théorie de la percolation statistique (traits pleins).

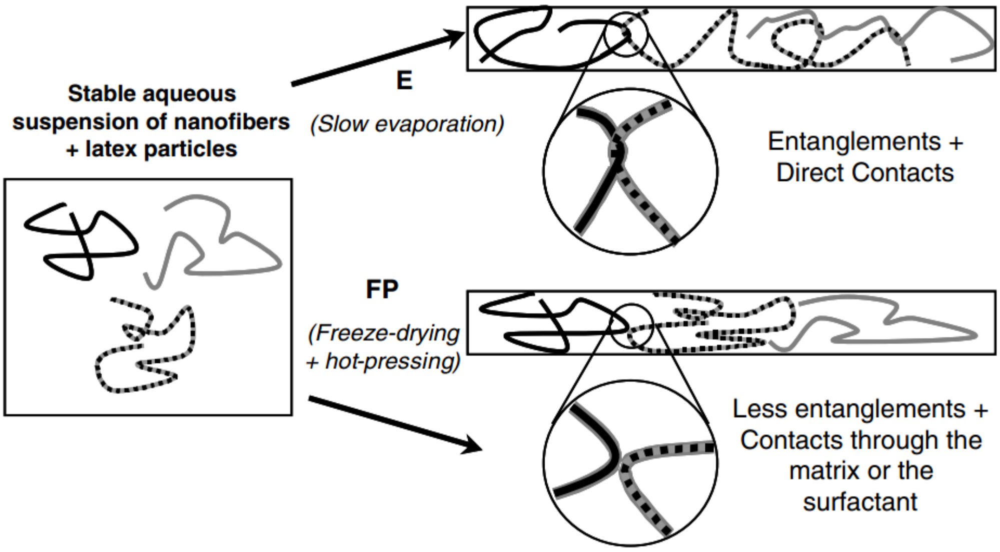

Figure 4 : Génération possible de géométries différentes des enchevêtrements et des contacts selon les conditions différentes d’élaboration.

Une analyse 3D de tels matériaux (3 vol. %) a été réalisée, et nous avons mis en œuvre de nombreuses techniques :

- ✓ En premier lieu, la nano-tomographie dans un MET (JEOL 2010F du CLYM : Centre Lyonnais de Microscopie, *www.clym.fr*) à 200 kV, en mode STEM-HAADF (cf. illustration Figure 5). Lors de cette étude, un problème important de contraction de la matrice polymère a clairement été mise en évidence (voir Figure 6). Cet effet est classique dans les polymères qui sont très sensibles à l’exposition à un faisceau d’électrons, d’autant plus que leur T_g est basse (dans le cas présent, - 7°). Deux solutions ont été envisagées : soit la correction des images, soit l’optimisation des conditions d’acquisition pour éliminer le problème. La première stratégie nous a conduits à une étude de la contraction, qui a permis de mettre en évidence un effet de saturation et une stabilisation de la matrice après un certain laps de temps d’irradiation (voir Figure 7). Une piste de traitement numérique a ainsi pu être proposée, mais qui s’avère lourde à mettre en œuvre, et surtout dangereuse du point de vue des résultats possibles :

s'agissant de caractériser les interactions entre nanotubes, toute contraction (ou déformation) de la matrice créerait immanquablement des contacts supplémentaires non représentatifs de l'état initial des matériaux, et les mesures finales seraient donc caduques. La deuxième approche proposée a été plus simplement de travailler à plus basse température (tomographie MET en utilisant un porte-objet refroidi dédié), ou de diminuer la tension d'accélération des électrons, soit à 80 kV dans un MET, soit en pratiquant la tomographie dans un microscope à balayage.

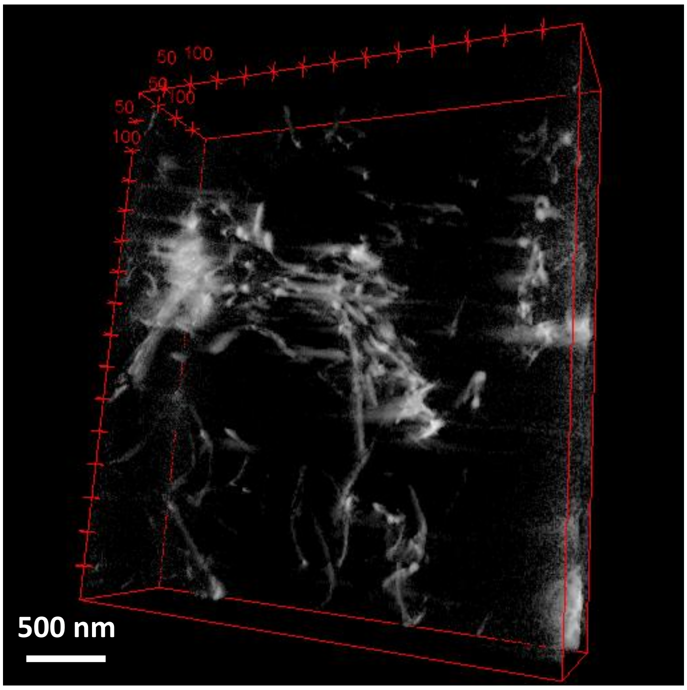

Figure 5 : Rendu de volume reconstruit à partir d'une série d'inclinaisons obtenue entre - 62° et 55° d'inclinaison avec incrément de 1,5° (MET 200 kV).

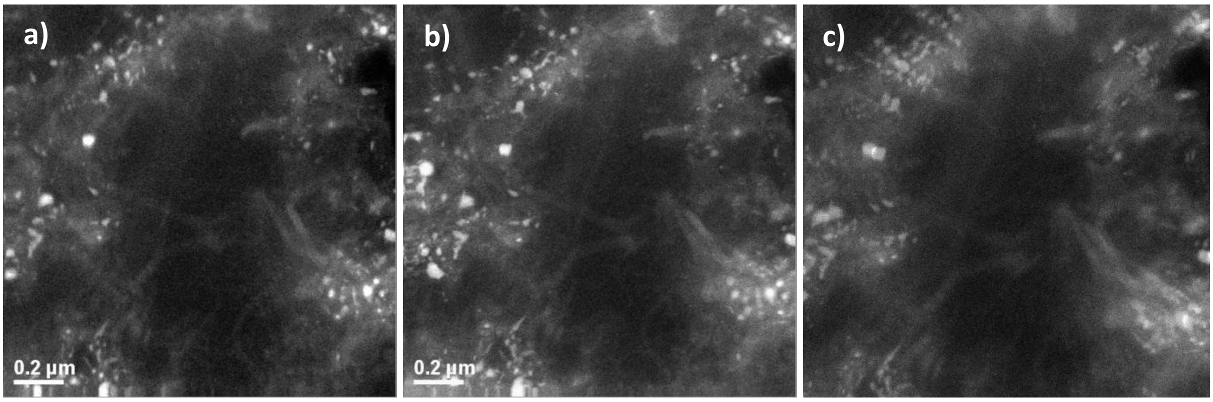

Figure 6 : a) Première et b) dernière trames d'une vidéo de 5 minutes enregistrée pour une section lyophilisée (FP) en mode STEM-HAADF à 200 kV. c) La superposition des deux images montre l'effet de contraction.

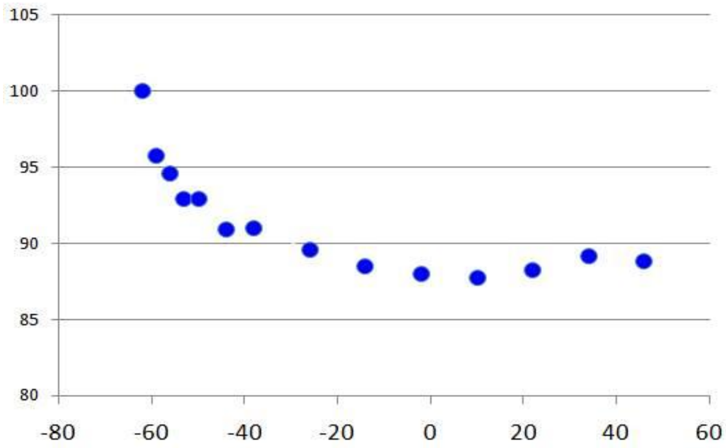

Figure 7 : Mesure en 3D sur une série de projection tomographique en STEM-HAADF à partir d'une modélisation simple d'une contraction isotrope (τ en % en fonction de l'angle d'inclinaison en °).

- ✓ La tomographie à 80 kV a été réalisée dans le cadre de collaborations au sein du laboratoire international 'Elyt lab' (*www.elyt.com*) sur un microscope 'EFTEM' FEI Titan (C_s-correcteur) installé à l'université Tohoku de Sendai, Japon (voir un résultat dans Figure 8). Ce microscope corrigé permet une bonne résolution à plus basses tensions d'accélération. Différents essais ont été réalisés, et malgré une pré-irradiation de stabilisation, une correction d'une partie des images obtenues a été nécessaire. Durant cette expérience, le mode 'filtré en énergie' est apparu capital pour conserver un contraste raisonnable entre les nanotubes et la matrice environnante (tous 2 constitués d'atomes légers avec peu de contraste en numéro atomique), notamment aux fortes inclinaisons où l'épaisseur projetée importante conduit à un rapport signal-sur-bruit très faible sur des images non filtrées en raison des évènements inélastiques. Dans ce cas, les images filtrées sur les électrons élastiques (images dites '*zero-loss*') ont permis d'optimiser le contraste et de rendre possible la reconstruction tridimensionnelle.

  Une variante de cette approche en imagerie filtrée a également été mise en œuvre à plus basse température, sur un microscope équipé en cryo-tomographie, mais à 200 kV et sans correcteur d'aberration (EFTEM JEOL 2200FS de l'Institut Curie, Orsay). Le porte-objet étant refroidi à la température de l'azote, la contraction est quasiment totalement bloquée sans aucune pré-irradiation. Cette stratégie a donné le meilleur résultat de reconstruction parmi tous les essais tentés (200 kV STEM, 80 kV EFTEM corrigé, 200 kV EFTEM à froid, voir Figure 9). Néanmoins, le principal inconvénient de la nano-tomographie en MET demeure : faible volume (faible épaisseur), donc statistiques peu favorables pour une étude quantitative des interactions entre nanotubes.

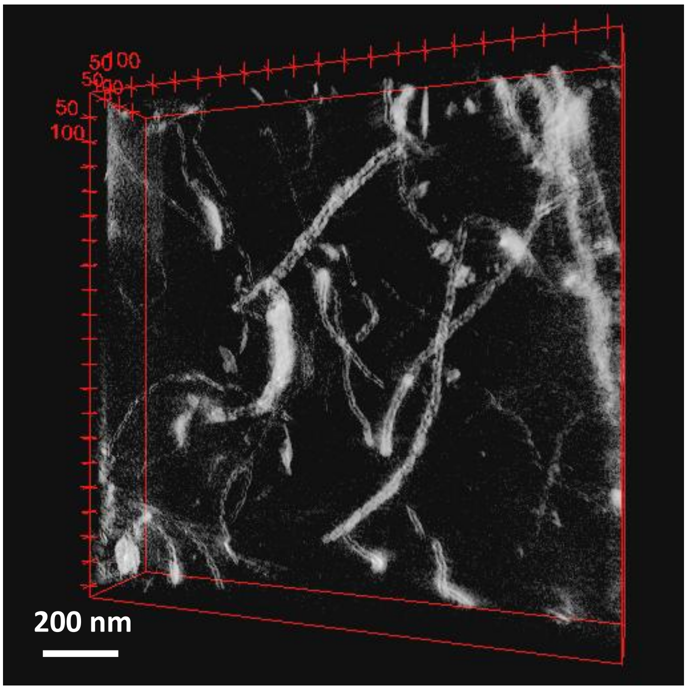

Figure 8 : Reconstruction à partir d'une série d'images EFTEM corrigées en C_s à 80 kV.

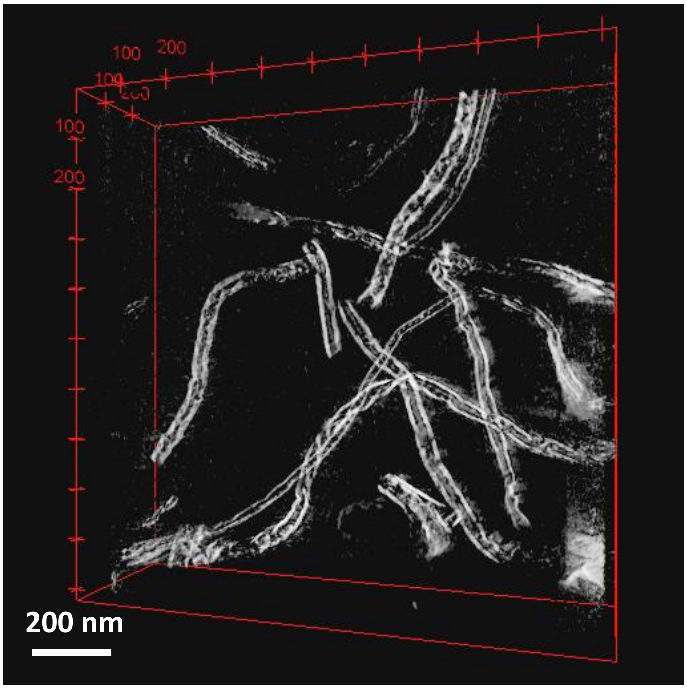

Figure 9 : Rendu de volume reconstruit à partir d'une série obtenue entre - 65,43° to 64,97° en 'schéma Saxton' avec un incrément de 2° sur un microscope EFTEM 200 kV à froid.

- ✓ La tomographie en MEB nous semblait intéressante du fait de la faible tension d'accélération (30 keV), et du champ de vue plus large tout en conservant une résolution raisonnable telle que permis par la technique de microscopie à balayage dans un microscope à émission de champ. De fait, nous n'avons pas rencontré de problème significatif de contraction, même sans pré-irradiation. Les tomogrammes en mode 'tomo-STEM®' sur un ESEM FEI XL30 nous ont donné plusieurs séries de projections, mais malheureusement la qualité des images s'est révélée insuffisante pour permettre des reconstructions raisonnables, notamment en raison de problèmes de contamination des échantillons sous le faisceau d'électrons. Dans le cadre de la collaboration avec l'Université Tohoku à Sendai, Japon, nous avons pu conduire des expériences similaires en mode transmission sur un MEB Hitachi S5500 équipé d'une émission de champ froide. Celles-ci ont produit des volumes reconstruits assez larges et de bonne qualité en termes de résolution et de contraste), malgré un champ angulaire d'inclinaison limité à ± 40°.

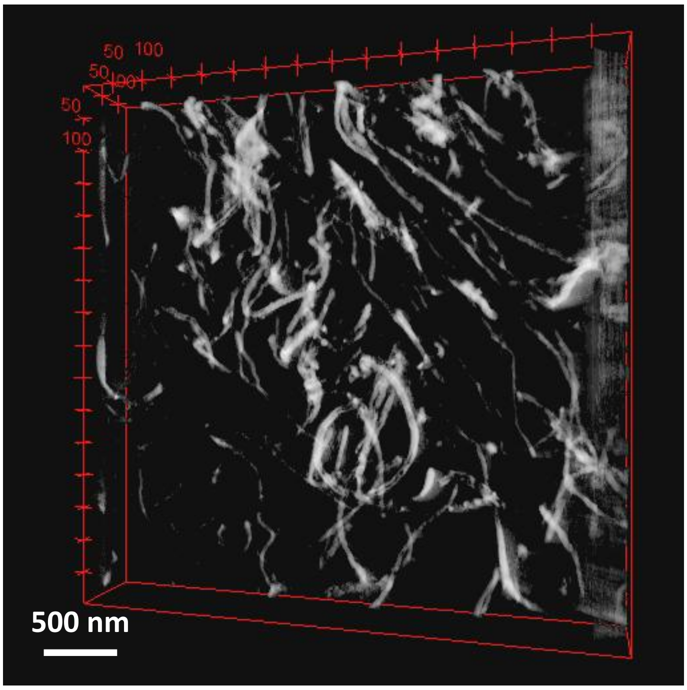

Figure 10 : Un rendu de volume reconstruit à partir d'une série obtenue en MEB 'émission de champ froide à 30 kV entre ± 40° avec un incrément de 1°.

- ✓ En dernier lieu, la tomographie en FIB/MEB a également été essayée. Malheureusement nous avons été confrontés à des problèmes de dégradation importante de l'échantillon lié à l'impact des faisceaux ionique et électronique (contraction de la matrice et effet de 'drapeau' [Orloff2003]) et au manque de contraste des nanotubes en mode MEB classique (imagerie de la surface et non du volume projeté comme en 'STEM', voir Figure 11). Des améliorations semblent possibles en travaillant à froid pour réduire la contraction, et en cherchant des pistes de marquage des nanotubes pour en améliorer le contraste.

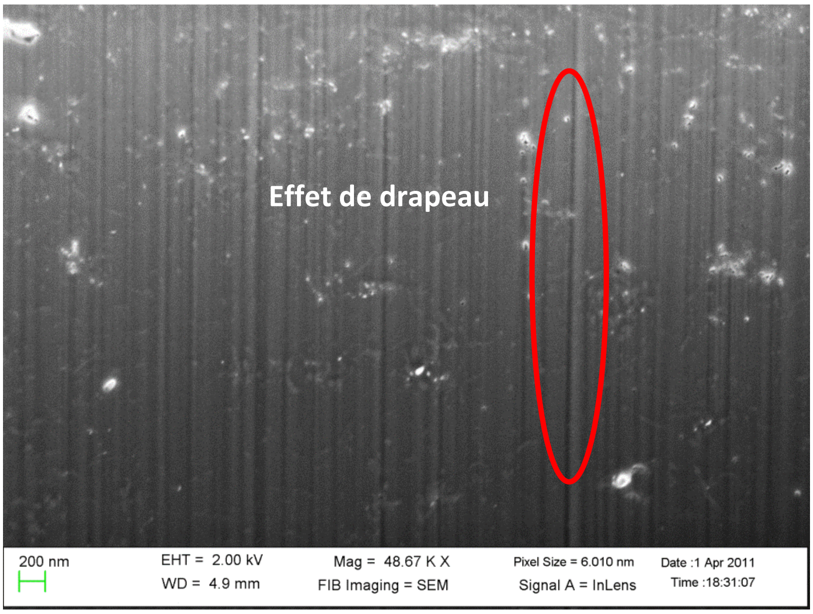

Figure 11 : Image typique en électrons secondaires d'une section usinée par FIB sur le matériau 'E'.

A partir de ces différents résultats, nous avons procédé à une quantification des contacts entre nanotubes pour expliquer le comportement électrique des 2 matériaux étudiés (cf. Figure 3). Cette quantification des contacts de nanotubes a été faite sur les tomogrammes obtenus en MEBs, car la résolution un peu moins bonne que dans les images MET a facilité le traitement numérique de 'détourage' de l'enveloppe des nanotubes. Un programme informatique dédié a été développé pour mesurer et comparer le niveau de contact dans les deux matériaux élaborés : évaporé et lyophilisé + pressé. Même si ce programme reste grandement améliorable, le résultat final montre qu'il y a une différence relative de près de 50 % entre les deux matériaux (voir Tableau 1), ce qui nous permet de conclure que plus de contacts ont été mesurés dans le matériau lyophilisé + pressé que dans le matériau évaporé. Comme les propriétés électriques varient en sens opposé, cela indique très clairement un meilleur rendement électrique de contacts dans le matériau évaporé.

	Vol. % tubes	**Rapport contacts/tubes**	Surf. % contacts
Matériau évaporé	7,29 %	**2,37 %**	0,16 %
Matériau lyophilise et pressé	4,53 %	**3,71 %**	0,19 %

Tableau 1 : Quantification des contacts entre CNTs. [Liu2012, EMC]

● Le deuxième nanocomposite étudié est P(BuA-*stat*-MMA)/SiO_2, copolymère statistique poly(butyl acrylate-*co*-méthyl méthacrylate) renforcé par des nanoparticules de silice. Ce système a été synthétisé et caractérisé préalablement au laboratoire L2C de l'université Montpellier 2 [Tatou2011]. Différents niveaux de particules ont été ajoutés dans la matrice polymère sous différentes conditions d'élaboration : pH 5 et 9 du mélange des latex de particules de copolymère et de silice. La taille moyenne des particules de silice est d'environ 16 nm de diamètre. La valeur de pH impacte l'agglomération de particules de silice, ce qui influence in fine les propriétés mécaniques de la matrice polymère. Par conséquent, ces nanocomposites polymères à base de matrice renforcée par des nanoparticules sphériques (et des agrégats) constituent un bon système, a priori simple et relativement idéal, pour une caractérisation 3D multi-échelle en utilisant différentes techniques de tomographie électronique. De plus, nous disposions de données précises quant aux fractions volumiques des particules incorporées, ce qui nous a permis d'évaluer les différentes causes d'incertitude dans les mesures 3D effectuées. Dans ce contexte, une stratégie couplant ces différentes tomographies a été mise en œuvre sur une série d'échantillons comprenant 1 ou 5 vol. % de silice avec pH 5 ou 9. Les principaux résultats sont ainsi résumés :

- ✓ La tomographie en FIB/MEB (usinage/imagerie séquentiels) a été réalisée en premier lieu dans le FIB Carl Zeiss Nvision40 du CLYM, pour son intérêt essentiel de pouvoir étudier des volumes de grandes dimensions (plusieurs dizaines de μm^3) [Holzer2006] [Kato2007]. Comme pour le système précédent, nous avons été confrontés à des problèmes de contraction de la matrice polymère sous les faisceaux ionique et électronique. Compte-tenu du bon contraste augurant de reconstructions de bonne qualité probable (voir Figure 12), nous avons persévéré en corrigeant, après mesure, la diminution de volume due à la contraction, et en proposant également une géométrie d'usinage plus favorable pour permettre au matériau polymère de mieux résister à l'effondrement induit par le faisceau ionique (voir Figure 13). Les mesures de fractions volumiques sont reportées dans le Tableau 2. Une configuration de la préparation de la zone d'intérêt était ensuite proposée pour s'affranchir ou au moins réduire cette contraction. Pour les matériaux synthétisés sous pH 5, peu importe la fraction originale, les valeurs obtenus d'un traitement effectué dans des conditions similaires aux autres échantillons (pH 9) conduisent à des valeurs largement surévaluées (5,6 % et 25 %) par rapport à celles attendues (1 % et 5 %). Une analyse plus fine et complémentaire a ainsi été effectué en tomographie MET de l'architecture des agrégats. Étant donné que le niveau de l'agglomération de particules sous conditions acides est nettement plus important que sous conditions basiques, il s'avère qu'un traitement des données FIB sous-évalue la quantité de matrice du fait des régions de polymères 'emprisonnées' dans les amas et non résolues dans la tomographie FIB/MEB.

- ✓ Avant de passer à la tomographie en MET, des essais en tomographie 'tomo-STEM®' ont été tentés, mais qui ne donnent pas une meilleure résolution, ni meilleure statistique, que la tomographie FIB/MEB.

- ✓ La tomographie STEM-HAADF en MET nous a permis de résoudre l'espace entre les particules constituant les agrégats (voir Figure 14). De telles observations et reconstructions ont conduit à des mesures de fraction volumique de particules dans les agrégats (Figure 15). En corrigeant les premières valeurs de cet effet de 'matrice cachée', nous obtenons des mesures en accord avec les résultats attendus (voir Tableau 2). Ainsi, l'intérêt du couplage multi-techniques et multi-résolution est démontré : le FIB a permis de grandes statistiques sur la dispersion et la distribution d'objets, et le MET a permis l'examen d'objets individuels à une résolution suffisamment élevée pour compléter les données partielles obtenues par FIB.

L'ensemble de ce travail a donc porté sur l'application de techniques de tomographie en Microscopie électronique, notamment FIB, à l'étude de nanocomposites polymères renforcés par des charges nanométriques.

Nous avons démontré que ces approches 3D ne permettent pas simplement de caractériser les nanostructures, mais aussi de les quantifier. Des couplages intéressants ont été mis en valeur, entre le FIB et le MET, le MET et le MEB. Concernant l'utilisation du FIB en Sciences des Matériaux, il s'agit d'une démarche encore 'jeune' qui présente un grand intérêt pour une très large variété de matériaux, comme nous avons d'ailleurs pu le démontrer lors de travaux menés en parallèle à l'étude principale faisant l'objet de ce mémoire [Fiorido2013] [Destouches2013].

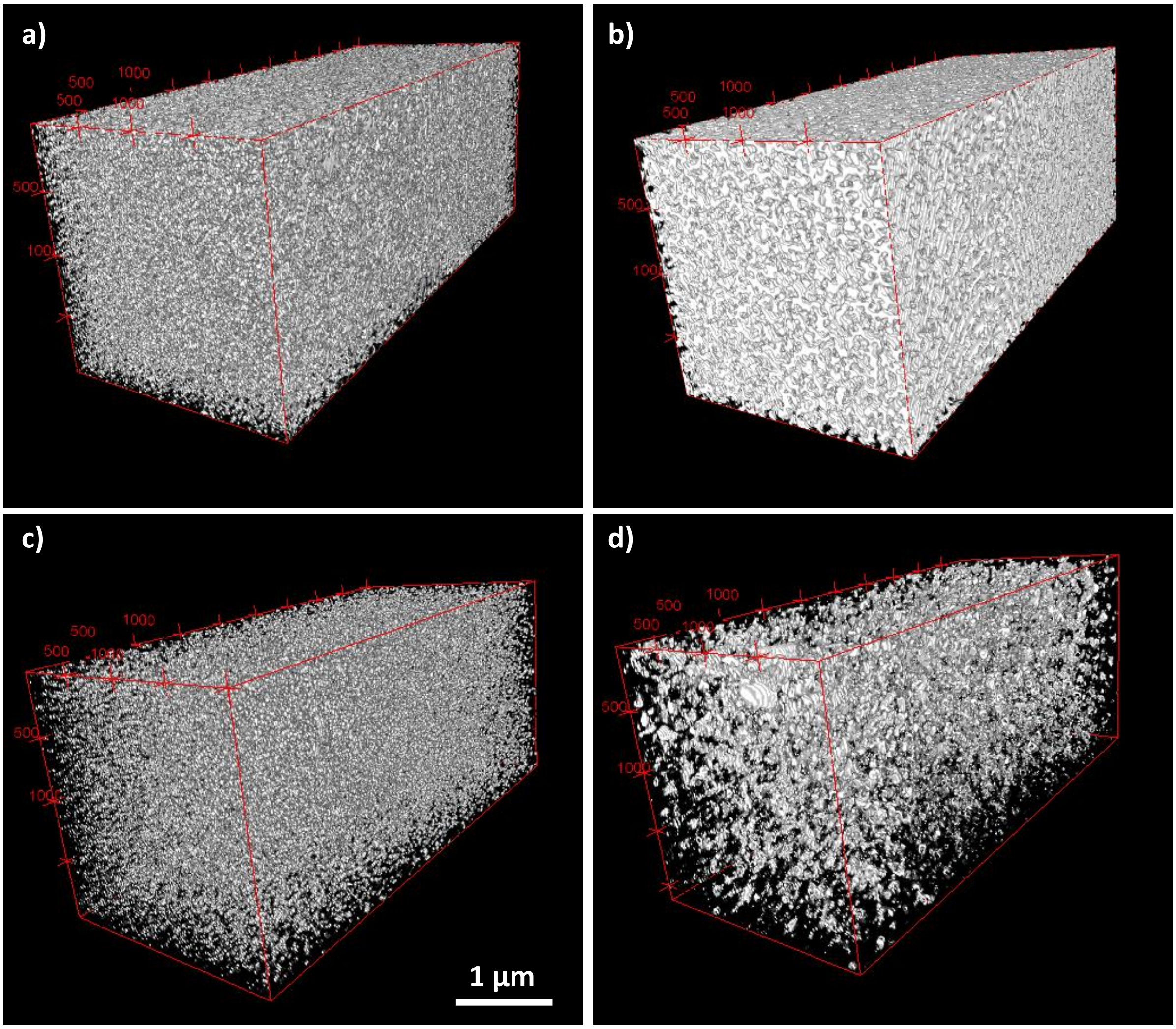

Figure 12 : Visualisations 3D (réalisée avec le plugin "3D volume viewer" de Fiji) des volumes reconstruits à partir de la première série d'expériences tomographiques FIB/MEB. Sections présentées de 500 * 500 pixels extraites de séries originales de 500 images à 2048 * 1536 avec une taille de voxel 4 * 4 * 10 nm³ ; a) M49, 5% pH 9; b) M57, 5% pH 5; c) M82, 1 % pH 9; d) M86, 1% pH 5.

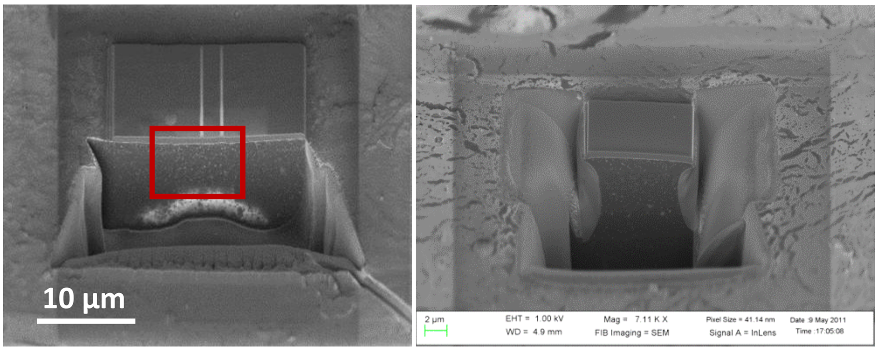

Figure 13 : À gauche : géométrie adoptée d'une nouvelle cavité pour réduire l'effet de retrait / contraction dans les polymères (nanocomposites) ; la cavité classique dite 'en U' est montrée à droite pour comparaison. La région d'intérêt utilisée pour la reconstruction tomographique est repérée par un cadre rouge.

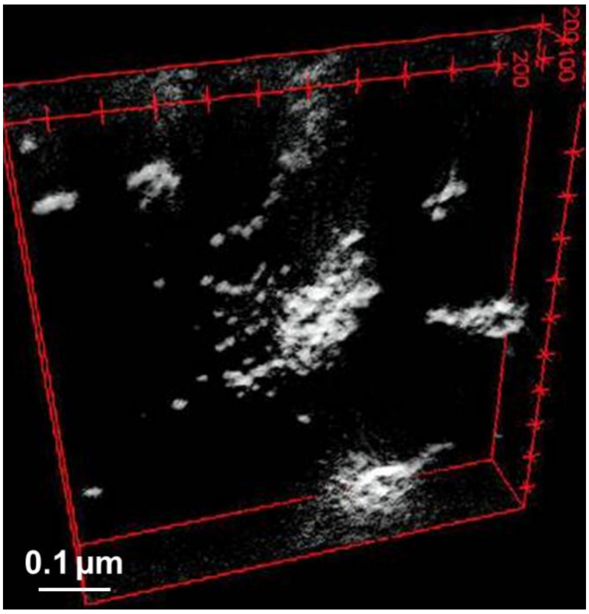

Figure 14 : Représentation 3D d'une tomographie MET reconstruite à partir d'une série obtenue sur un ensemble d'agrégats (échantillon sous PH 5) entre 30° et – 58° avec un incrément de 4°.

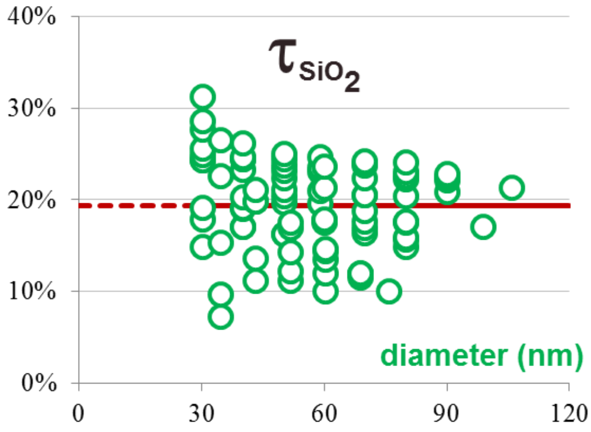

Figure 15 : Fractions volumiques mesurées des nanoparticules de silice à l'intérieur des agrégats en fonction de leur diamètre (échantillons élaborés sous pH 5).

Echantillon	Volume analysé (μm^3)	Fraction volumique de silice (%)				Conditions d'élaboration	
		Après segmentation + érosion-dilation	**Après correction de contraction**	***Après correction de la densité des agrégats***	***Valeur attendue***	pH	Présence d'agrégats ?
M82	82	1,7 %	**1,4 %**	***1,4 %***	***1 %***	9	Non
M49	61	5,0 %	**4,1 %**	***4,1 %***	***5 %***	9	Non
M86	45	8,0 %	**5,6 %**	***1,2 %***	***1 %***	5	Oui
M57	87	31,6 %	**25,0 %**	***5,20 %***	***5 %***	5	Oui

Tableau 2 : Les résultats définitifs concernant les fractions volumiques de silice dans les 4 P(BuA-*stat*-MMA)/SiO_2 nanocomposites.

Références du résumé français

[Baldock2002] Baldock C., Gilpin C.J., Koster A.J., Ziese U., Kadler K.E., Kielty C.M., and Holmes D.F. *Three-dimensional reconstructions of extracellular matrix polymers using automated electron tomography*. Journal of Structural Biology (2002), vol.138, pp: 130–136.

[Baumeister1999] Baumeister W., Grimm R., and Walz J. *Electron tomography of molecules and cells*. Trends in Cell Biology (1999), vol.9, pp: 81–85.

[Dalmas2005] Dalmas F., Chazeau L., Gauthier C., Masenelli-Varlot K., Dendievel R., Cavaillé J.Y., and Forró L. *Multiwalled carbon nanotube/polymer nanocomposites: Processing and properties*. Journal of Polymer Science Part B: Polymer Physics (2005), vol.43, pp: 1186–1197.

[Dalmas2007] Dalmas F., Cavaillé J.-Y., Gauthier C., Chazeau L., and Dendievel R. *Viscoelastic behavior and electrical properties of flexible nanofiber filled polymer nanocomposites. Influence of processing conditions*. Composites Science and Technology (2007), vol.67, pp: 829–839.

[Destouches2013] Destouches N., Crespo-Monteiro N., Vitrant G., Lefkir Y., Reynaud S., Liu Y., Epicier T., Vocanson F., Pigeon F. *When light plays with metal nanoparticles in thin films and creates spontaneously active color filters*. Soumis à Nature Communications (NCOMMS-13-03011-T).

[Fiorido2013] Fiorido T., Galineau J., Salles V., Seveyrat L., Belhora F., Cottinet P.-J., Hu L., Liu Y., Guiffard B., Brioude A., Epicier T., and Guyomar D. *Innovative organic/inorganic nanocomposites for actuators and magnetic sensors applications. Soumis à* Advanced Functional Materials.

[Holzer2004] Holzer L., Indutnyi F., Gasser P.H., Münch B., and Wegmann M. *Three-dimensional analysis of porous BaTiO3 ceramics using FIB nanotomography*. J Microsc (2004), vol.216, pp: 84–95.

[Holzer2006] Holzer L., Muench B., Wegmann M., Gasser P., and Flatt R.J. *FIB-Nanotomography of Particulate Systems—Part I: Particle Shape and Topology of Interfaces*. Journal of the American Ceramic Society (2006), vol.89, pp: 2577–2585.

[Jinnai2009] Jinnai H., and Spontak R.J. *Transmission electron microtomography in polymer research*. Polymer (2009), vol.50, pp: 1067–1087.

[Jornsanoh2011] Jornsanoh P., Thollet G., Ferreira J., Masenelli-Varlot K., Gauthier C., and Bogner A. *Electron tomography combining ESEM and STEM: A new 3D imaging technique*. Ultramicroscopy (2011), vol.111, pp: 1247–1254.

[Kato2007] Kato M., Ito T., Aoyama Y., Sawa K., Kaneko T., Kawase N., and Jinnai H. *Three-dimensional structural analysis of a block copolymer by scanning electron microscopy combined with a focused ion beam*. Journal of Polymer Science Part B: Polymer Physics (2007), vol.45, pp: 677–683.

[Koster2000] Koster A.J., Ziese U., Verkleij A.J., Janssen A.H., and de Jong K.P. *Three-Dimensional Transmission Electron Microscopy: A Novel Imaging and Characterization Technique with Nanometer Scale Resolution for Materials Science*. J. Phys. Chem. B (2000), vol.104, pp: 9368–9370.

[Liu2012, EMC] Liu Y., Bogner-Van de Moortèle A., Epicier T., Sato K. and Konno T. *TEM and SEM tomography of polymer-based nanocomposites reinforced by carbon nanotubes.* EMC 2012, Manchester (September 17-21, 2012), Vol. 2, PS 2.4, pp: 313-314.

[Midgley2003] Midgley P.A., and Weyland M. *3D electron microscopy in the physical sciences: the development of Z-contrast and EFTEM tomography*. Ultramicroscopy (2003), vol.96, pp: 413–431.

[Orloff2003] Orloff J., Swanson L.W., and Utlaut M.W. *High Resolution Focused Ion Beams: Fib and Its Applications : The Physics of Liquid Metal Ion Sources and Ion Optics and Their Application to Focused Ion Beam Technology*, Springer,(2003).

[Tatou2011] Tatou M., Genix A.-C., Imaz A., Forcada J., Banc A., Schweins R., Grillo I., and Oberdisse J. *Reinforcement and Polymer Mobility in Silica–Latex Nanocomposites with Controlled Aggregation*. Macromolecules (2011), vol.44, pp: 9029–9039.

[Weyland2006] Weyland M., Yates T.J.V., Dunin-Borkowski R.E., Laffont L., and Midgley P.A. *Nanoscale analysis of three-dimensional structures by electron tomography*. Scripta Materialia (2006), vol.55, pp: 29–33.

1 Introduction

1.1 Context of this work

1.1.1 The necessity of electron tomography

Nowadays, three-dimensional (3D) knowledge of micro- and nano-structures in material sciences becomes more and more essential to study the elaboration and assembly of materials, to gain insights in the understanding of their physical and chemical properties. 3D characterization can be performed through different tomography techniques within optical, X-ray and electron microscopes. Through this large variety of tomography approaches, the range of resolution accessible extends from the micrometre to the nanometre and even sub-nanometre levels [Koster2000] [Maire2001] [Kano2002].

Indeed 3D imaging is essential to obtain a correct knowledge of the microstructure of materials? Figure 1.1 shows that the information extracted from a two-dimensional (2D) projection may frequently not represent the nature of the target objects; 2D projections introduce errors for the localization, distance, distribution of the objects, etc. Although the real structures could be explored by changing the orientations of observation if the objects are regular and symmetric, it is still difficult to obtain complete and quantitative information for the objects with complex shapes and structures [Ward2007] [Kim2008] [Tan2011]. Having the ability to reconstruct 3D structures is thus a significant advantage in the course of a general characterization of any kind of materials.

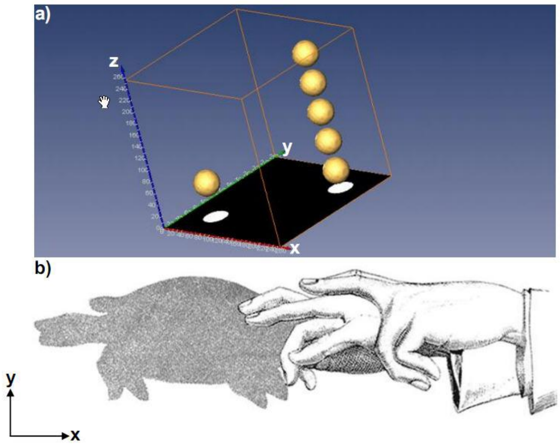

Figure 1.1: a) Projection of a volume containing spheres showing the lack of information in the 2D projection [Benlekbir2009, thesis]; b) 'shadow projection' made by hands showing the misleading interpretation of the morphology of the real object as deduced from the projection (from Henry Bursill, *http://www.gutenberg.org/ebooks/12962*))

It is not within the scoop of the present work to establish an extensive bibliographic overview of Electron tomography (ET); indeed, a search on http://www.webofknowledge.com with the keywords 'transmission electron tomography' yields to more than 1000 results a year since 2008. ET has thus already been proved to be an efficient tool to investigate the nano-structures of biological samples in life science [Fernández2002] [Leapman2004] [Yakushevska2007] [Aoyama2008] and materials science [Koster2000] [Koning2009] [Baldock2002] [Weyland2006] [Loos2009b] [Jinnai2009]. One of the most interesting features of ET is that it can bridge the gap between X-ray tomography and the atom probe tomography (APT, [Kelly2007] [Miller2005]) in terms of spatial resolution in the nanometre range.

Electron tomography is conventionally carried out in transmission electron microscopy (TEM). The 3D structural information from a volume is reconstructed from a set of 2D projections acquired by tilting the specimen with a reasonable step over a large angular range, using one or several tilting directions (see Figure 1.2). In principle a rotation amplitude of 180° is needed. But in practice, due to the experimental setups and the limitations in sample preparation, this is not easily possible and a reasonable range is ± 70°. The reconstruction of the 3D information is processed by applying dedicated algorithms.

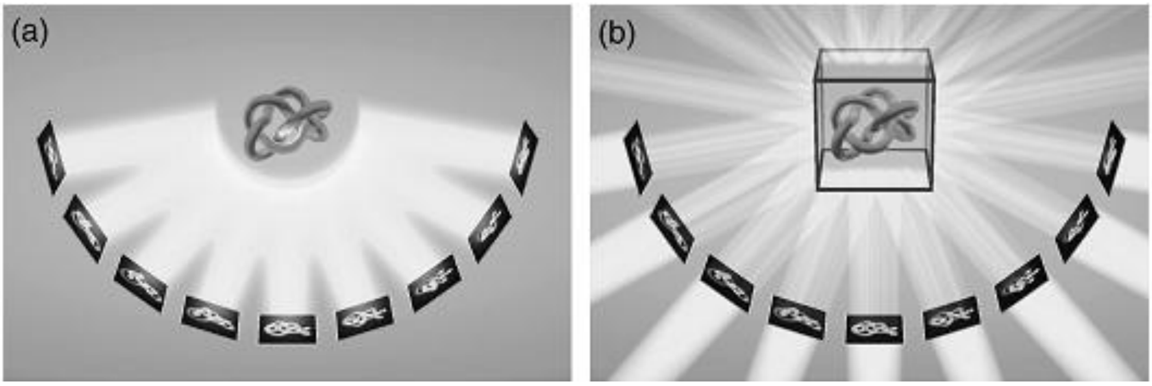

Figure 1.2: The 2D projections acquisition and associated 3D reconstruction with one single tilt axis. a) A series of 2D projection images could be recorded by either tilting the object or the incident beam source and the detector incrementally; b) a reconstruction is performed by summing all back-projection bodies calculated from every obtained projection image [Baumeister1999].

An alternative electron tomography technique is the sequential slicing approach which is also referred as 'slice-and-view' or serial-sectioning procedure (Figure 1.3). This technique is carried out on a dual-beam Focused Ion Beam (FIB) / scanning electron microscopy (SEM) [Krueger1999] [Bansal2006] [Jeanvoine2008] when a 'good' resolution is desired, or on ultramicrotomic section in optical microscopy at a micrometric scale. In FIB instruments, an ion beam is used to produce fresh cross-section from the area of interest in the specimen, and successive SEM images are recorded [Holzer2004]. This procedure is performed repeatedly in a sequential manner for a desired depth, possibly in an automatic way without operator intervention. At last, the series of slices are used to restore the volume after adequate re-alignments and possible numeric image processing.

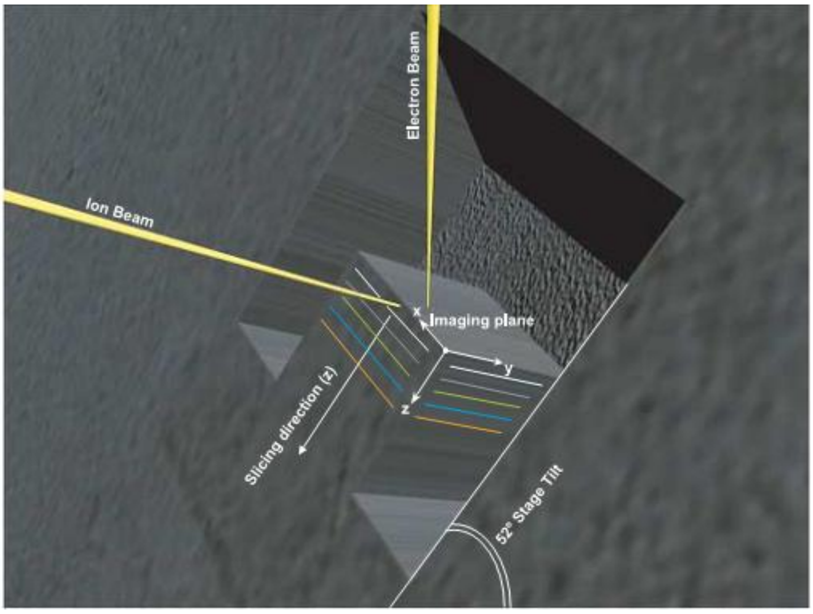

Figure 1.3: Illustration of a prepared zone of interest ready for serial-sectioning procedure in a FIB [Holzer2004].

1.1.2 Tomography at MATEIS

As devoted to the research of a variety of materials, the laboratory '*Matériaux: Ingénierie et Science*' (MATEIS) has always been applying and developing all kinds of characterization methodologies in material sciences, including 3D imaging techniques. In this context, several tomography approaches have already been developed in order to allow 3D characterizations at different scales.

1.1.2.1 Transmission Electron nano-tomography

Scanning TEM in the HAADF (high angle annular dark field) imaging mode has been applied to several materials, including nanoparticles and alloys and precipitates in a recent PhD work [Benlekbir2009, thesis] using a high resolution FEG (Field Emission Gun) transmission electron microscope JEOL 2010F (see Figure 1.4 and Figure 1.5).

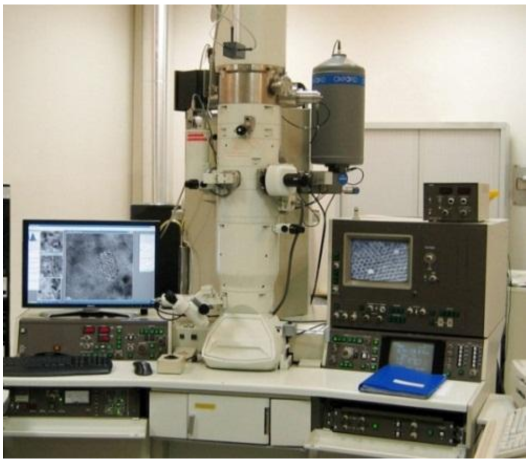

Figure 1.4: The TEM JEOL 2010F in CLYM-Lyon ('*Centre Lyonnais de Microscopie*', http://www.clym.fr/).

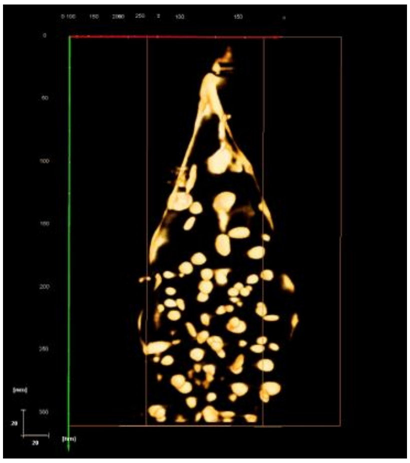

Figure 1.5: 3D Reconstruction of an AlZnMg alloy tip from a tilt series of projections obtained in the STEM-HAADF mode [Benlekbir2009, thesis].

1.1.2.2 Tomography in the SEM: Low-voltage STEM

Simultaneously, another electron tomography technique was developed in an environmental SEM (ESEM, Figure 1.6) [Jornsanoh2008, thesis]. Rather than the conventional SEM imaging which only permits to observe the surfaces of the sample, the technique that has been developed with the help of a home-made dedicated sample stage operates in the transmission mode, owing to the availability of a detector for transmitted electrons located below the sample. Since a SEM could only offer an acceleration voltage of 30kV at maximum which is much lower than in a TEM, this configuration for electron tomography can be referred as low-voltage STEM (LV-STEM) or STEM-in-SEM. According to the fact that the detection is also similar to the HAADF mode in STEM, this new technique has been named 'tomo-STEM®' [Jornsanoh2011].

Figure 1.6: ESEM FEI XL30 of CLYM.

Figure 1.7 exhibits a reconstruction based on an experiment performed in this home-developed system of tomography in ESEM. It is a tungsten tip supporting SiC nanowires with diameters from 120 to 150 nm.

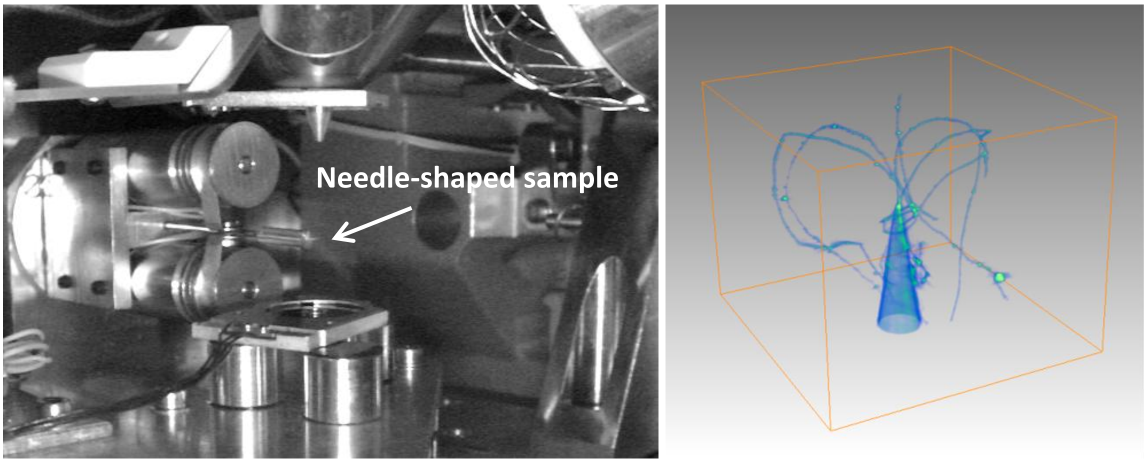

Figure 1.7: Tomo-STEM®: view of the dedicated 180° rotation home-made specimen holder (holding a needle-shaped sample - left -) and visualization of a reconstructed volume (41 × 32 × 40 mm^3) of SiC nanowires grown on a tungsten tip (right) [Jornsanoh2011].

1.1.2.3 Tomography in a FIB/SEM dual-beam system

As mentioned earlier, a sequential slicing tomography can be done in FIB/SEM, a dual-beam system. This approach now attracts more and more attention in the domain of material sciences. CLYM has acquired such a double-column microscope by the end of the year 2009 (Figure 1.8). With the sequential milling-imaging technique in FIB/SEM, it will enlarge the range of 3D characterization techniques already developed and/or available in the laboratory.

Figure 1.8: FIB/SEM NVision 40 of Carl Zeiss installed at CLYM.

1.1.2.4 X-ray tomography

As a matter of fact, tomography was first performed with X-ray, as known to all, for medical examinations. It is now used in material science for metals, ceramics and polymers, and also in life science for biological specimens [Maire2001].

Figure 1.9: The x-ray 'Phoenix *v|tome|x s*' installed in MATEIS.

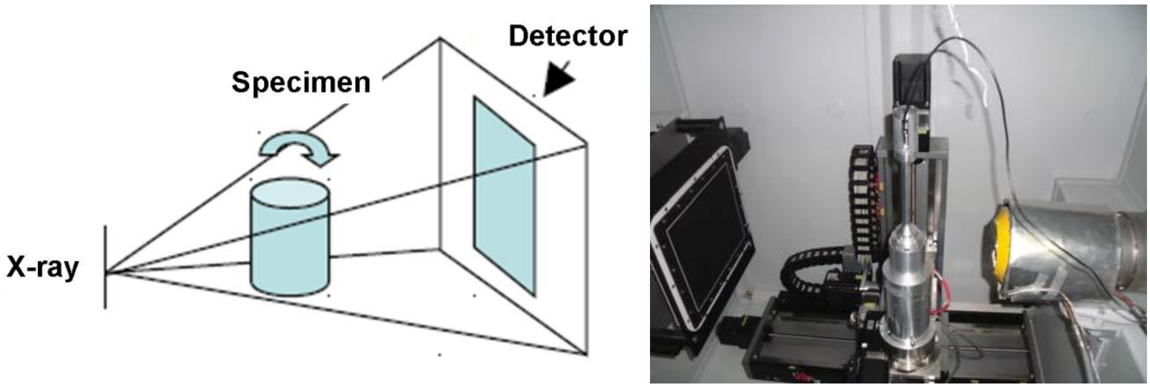

Figure 1.10: Geometry and device configuration of the cone beam X-ray tomography. [Zhang2012, thesis]

For about a decade, the laboratory MATEIS has been putting efforts in developing X-ray tomography for its applications to material science. A 'Phoenix *v|tome|x s*' tomograph is thus installed in the laboratory (Figure 1.9). This machine is a high-resolution system for 2D X-ray inspection and 3D computed tomography (Figure 1.10). It holds an inter-space of $1m^3$ and the possibility to connect with water, gases and electricity, which permits certain in-situ experiences using dedicated montages for mechanic solicitation. The acceleration voltage of the X-ray tube can be set between 40 kV and 160 kV with a best resolution estimated to 1 µm.

An example of tomogram reconstructed with this instrument is shown in Figure 1.11. It concerns a piece of foam showing the stack of metallic spheres.

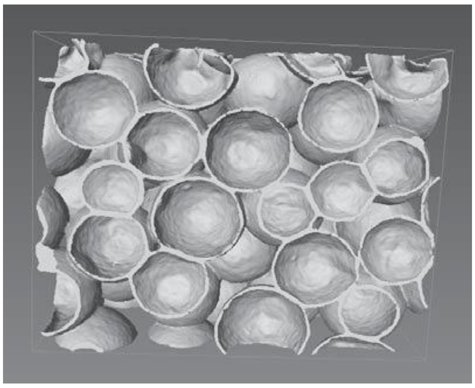

Figure 1.11: A reconstructed volume of a stacking of hollow metallic spheres stack [Zhang2012, thesis].

1.1.2.5 About the interest of tomographic studies of polymer nanocomposites

Polymer nanocomposites (PNC), the performances of which are obviously better than standard polymer materials, are of great use nowadays in the civil and industry applications. Pure polymers could be reinforced efficiently by adding just a small amount of certain fillers at the nanometre scale, and then the optimization of certain physical properties, like electrical conductivity, mechanical resistance, fire resistance, etc. can be realized. Usually it can also help reducing the production cost of the associated products with even longer life duration or better utilization experience. As a matter of fact, over 95% of the plastics used in the present day are made from PNC.

Characterizing the structures, morphology and interactions of the nano-fillers is a key requirement for optimizing the properties of PNCs. According to the geometry of such composites, the 3D organization of the fillers is of crucial importance: not only the shape, but the distribution features, in terms of homogeneity, localisation, volume fraction, are relevant parameters that can be linked to the physical properties of the materials in view of improving their performances.

A few years ago, the research group PVMH (‘*Polymères, Verres et Matériaux Hétérogènes*’) of MATEIS started such analyses with a dedicated correlation with electron microscopy observations. A first system has concerned a copolymer matrix reinforced by multi-walled carbon nanotubes (MWNTs) [Dalmas2007]. A careful study has enabled to partly explain some difference of reinforcement behaviours in two differently elaborated materials with the same amount of fillers, but clearly 3D data are still lacking for a fully comprehensive analysis. This was the starting point of this thesis, which initially aimed at checking the possibilities of FIB tomography applied to such PNC, with the intention to correlate these results with what can also been obtained via electron tomography in the TEM and in the SEM. This strategy is further developed in the next sub-section.

1.1.3 Aim of the thesis

Since various tomography techniques are developed and available at MATEIS and through the instruments available at CLYM (ESEM, TEM-FEG and the new double-column FIB/SEM), it was tempting to develop a multi-techniques 3D approach on materials usually delicate to be observed with electron microscopy techniques, in order to state upon the possibilities of each method, and the complementary information that can be gathered by an associated use, if possible, of several instruments on the same system. Indeed, fillers in the PNC systems are generally at the nanometre scale, and the use of electron microscopy techniques is required to achieve the needed resolution, from tens of nanometres to several nanometres and even one nanometre. One may recall here that X-ray tomography stays principally in the field of the micrometre [Salvo2003], although submicron, and even sub-100 nm, resolution can be achieved in Synchrotron facilities, such as the European Synchrotron Radiation Facility (ESRF) [Adrien2007] [Maire2007], [Rau2007].

Simultaneously, we were curious to compare the 3 techniques in terms of specifications and performances in a 3D perspective: resolution, contrast, difficulties and experimental limitations, methods of reconstruction and of segmentation, etc. Also we aimed at exploring possible optimizing paths of the experimental setups and conditions in order to better adjust the ET techniques on complex and damageable materials such as polymer nanocomposites. Effective strategies for applying the most adapted electron tomography technique will be proposed for the study of some polymer nanocomposites, in order to avoid or resolve the possible difficulties and to obtain reasonable and interpretable 3D results.

1.2 Introduction on different electron tomography techniques

The ET techniques to be applied in this work could be classified into two sorts: tilting (TEM and SEM) tomography and serial-milling (FIB/SEM, 'slice-and-view') tomography.

1.2.1 TEM tomography (TEMT)

In general, 'Electron tomography' usually concerns experiments carried out in a TEM microscope. Owing to the variety of signals available in a TEM for imaging with electrons (see in Figure 1.12), it is so far the most widely applied electron tomography technique in both life and material sciences with the best 3D resolution.

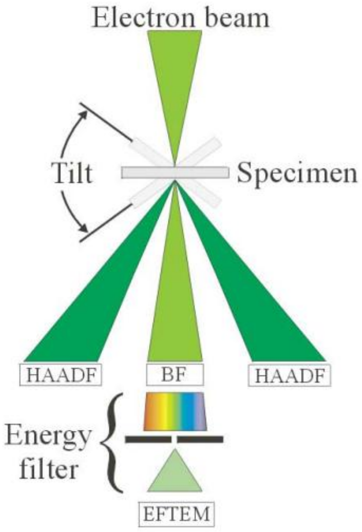

Figure 1.12: Summary of the geometries of various signals that may be used for tomographic reconstruction in TEM. A bright-field (BF) detector is used to collect electrons scattered at low angles. A high angle angular dark field (HAADF) detector has an inner radius ideally beyond Bragg scattering angles and so collects predominantly incoherently scattered electrons. An energy filter can be used to select out those electrons that have lost a defined energy, characteristic of a particular element, allowing the rapid acquisition of elemental maps [Weyland2002].

For obtaining 2D projections in a tomography experiment, the sample must be very thin because the incident electrons with a limited acceleration tension could not pass through 'thick' material. Therefore, as in conventional TEM, but maybe with more severe constraints, a dedicated sample preparation is necessary. In the case of polymer-based materials which cannot generally prepared as self-standing thin foils, the key point is to process thin sections of the sample and deposit them on a grid as for a conventional TEM (CTEM) observation. For soft materials as polymers and PNC, the slices are usually cut by cryo-ultramicrotomy, which freezes the sample at low temperatures to be more solid before slice cutting with a glass or a diamond knife. In this way, the soft materials can retain their natural structures without structural deformation. The slices are usually from tens of nanometres to 200 or 250 nanometres thick, and may appear more or less transparent to the electron beam in the microscope, depending on the operating voltage.

The thickness of the sample is a very important parameter, because the projections obtained in a tomography experiment should follow the principle of the 'projection requirement', that is the image intensity should be a monotonically varying function of the specimen thickness or the element mass [Midgley2003].

1.2.1.1 Limits and difficulties of TEMT and possible solutions

As stated in section 1.1.1 and Figure 1.2, TEM tomography needs to tilt the grid on which the sample slices are deposited over a as large as possible angular range with as small as possible tilt increments [Baumeister1999] [Midgley2003]. Theoretically, wide tilt ranges until 180° and small increments as 1° or even 0.5° will lead to more valid reconstructions close to the original volume (see an example in Figure 1.13).

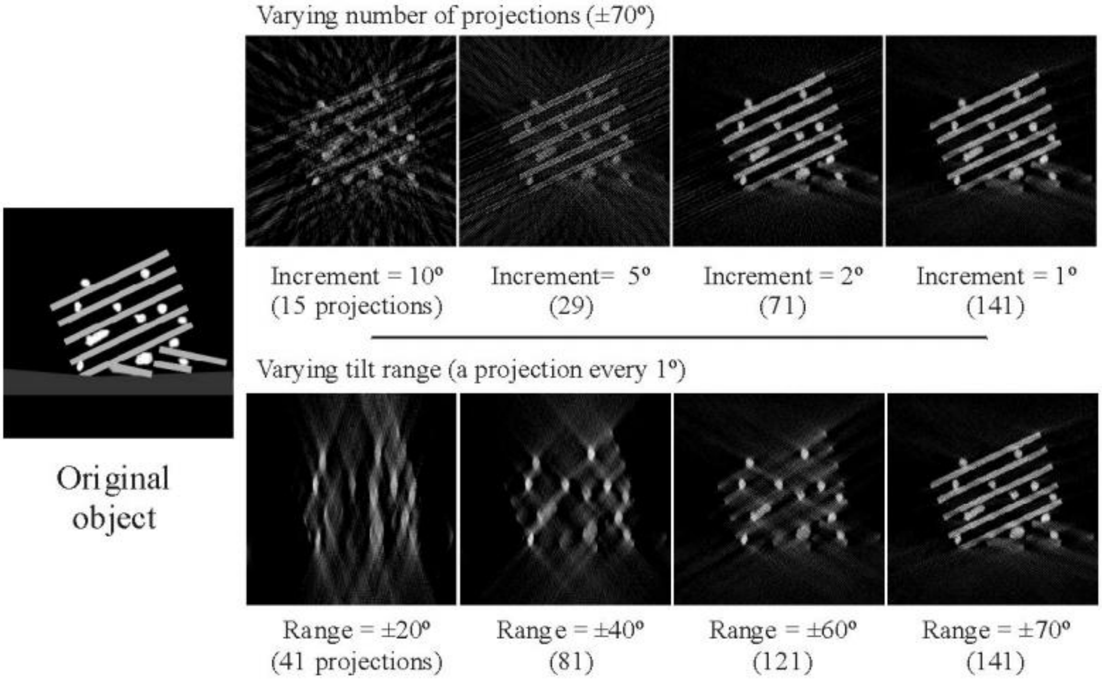

Figure 1.13: Effect of acquisition parameters on reconstruction quality. In this example a test object has been constructed, shown far left, which resembles a heterogeneous catalyst structure, with high-density particles in a lower-density ordered support, resting on a very low-density C grid. Projections have been generated from this object from a series of different sampling geometries varying the number of projections and the angular range of projection [Weyland2002].

But due to the geometries of the grid holder and the sample chamber, a 180° tilt isn't always possible. The missing tilt range produces what is called the 'Missing wedge' (see Figure 1.14 and [Penczek1995]) which causes an under-sampling of the high special frequencies information of the object and a 'blurred' reconstruction. Another reason limiting the 'ideal' tilting sequence is linked to the irradiation time which directly increases with the tilt amplitude and the smallness of increments; this can damage the specimen and simply make the reconstruction impossible. This limitation is particularly true for soft materials such as polymers and PNCs. A special attention will be brought to this problem in the following.

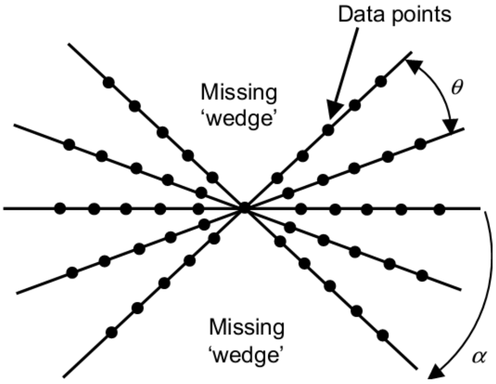

Figure 1.14: An illustration of the 'Missing wedge' effect in Fourier space caused by a restricted tilt series. θ is the angular increment between two projections and α is the maximum tilt angle [Midgley2003].

The 'Missing wedge' as well leads also to an elongation effect which impacts the resolution in the tomograms. If the tilt axis is X-axis, hence the resolution d_x equals to the original resolution in the projection images. The resolution in the other dimensions perpendicular to tilt axis can then be expressed by:

$$\boldsymbol{d_z = d_y = \frac{\pi D}{N}}$$

where D is the diameter of the object and N is the number of projections recorded with constant increment. But as the projections don't fulfil a complete 180° tilt, according to the 'Missing wedge', the resolution d_z along the optic axis is degraded by an elongation factor e_{yz}:

$$\boldsymbol{d_z = d_y e_{yz}}$$

$$\boldsymbol{e_{yz} = \sqrt{\frac{\alpha + \sin\alpha\cos\alpha}{\alpha - \sin\alpha\cos\alpha}}}$$

In this case, for a tilt range less than 180° in which α is inferior to 90°, the resolution d_z in the direction of optic axis is decreased [Midgley2003].

When the specimen is tilted at high tilt angles, the dramatic increase of thickness along the incident beam direction is another issue that induces a loss of signal-to-noise ratio (SNR) and limits the quality of the projection series which may not contribute and even degrade the reconstruction [Kaneko2005] [Kawase2007]. A 'Saxton scheme' is then proposed to optimize the condition: the increment should not be constant but defined as $\boldsymbol{\Delta\theta = \Delta\theta_0 \cos\theta}$, where the $\Delta\theta_0$ is the tilt step when the sample is positioned perpendicularly to the probe (flat position) and θ is the current tilt increment. With this scheme, the increment can be automatically altered to small step at high angles, which will preserve more information and restrict the artefacts [Aoyama2008].

Since a tilt range of 180° is commonly impossible with one single tilt axis for thin slices (i.e. thin foils cut from the bulk, or grid supported objects), double tilt axis and conical geometry can be applied to minimize the problem of missing information caused by the 'Missing wedge'. For a double tilt axis tomography, two tilt series are acquired with two perpendicular axes (Figure 1.15 B). It reduces the 'Missing wedge' to a 'Missing pyramid' which decreases distortions caused by the missing angular information and thus improve the fidelity of the reconstruction [Penczek1995]. Conical tilt geometry works as an improved version of double tilt axis; its principle is to obtain several tilt series around various tilt axes (Figure 1.15 C) [Lanzavecchia2005] [Zampighi2005]. Both geometries prove to be useful to reduce the missing regions in the tomogram; they do not require any transformation of the electron microscope but special specimen holders. Then the acquisition time is longer, which increases the total electron dose and may result in sample degradation. From this point of view, these sophisticated tilting strategies are not easily applicable to materials that are sensible to electron dose level.

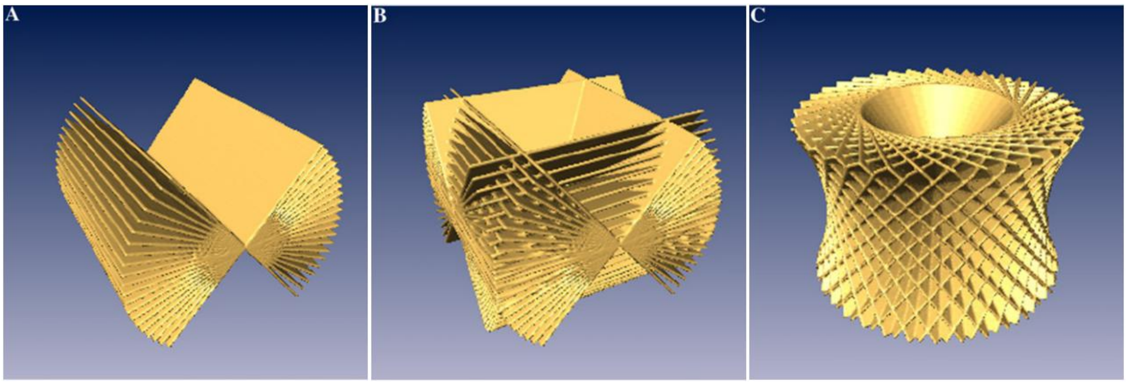

Figure 1.15: Comparison of the single-tilt, double-tilt, and conical tilt geometries used to image specimens in electron tomography. In Fourier space, each image is represented by a central plane oriented orthogonal to the viewing direction. The empty regions represent the 'missing volume' resulting from limitations in tilt. A) The stack of central planes obtained in single-tilt with the missing volume shaped as a double wedge. B) The stack of planes obtained in double-tilt geometry with the missing volume shaped as a double pyramid. C) The layout obtained in conical tilt geometry. The missing volume is shaped as a double cone, which greatly reduces the anisotropy in the resolution along the XY plane. The tilt angle was 55° in all three examples [Lanzavecchia2005].

Besides the multi-tilt axis geometry, other efforts have been made towards a 180° tilt range in a single tilt axis system in order to overcome the 'Missing wedge' issue. The specimen is then prepared with a rod shape, mainly machined by FIB, and mounted on a specific adapted holder [Arslan2008a] [Kawase2007] [Yaguchi2008] [Kato2008]. A typical illustration is given in Figure 1.16 a-c). This device has been applied to a polymer nanocomposites system, i.e. a polymer matrix filled by 5 % in volume zirconium dioxide (zirconia) particles. The size of these fillers was about 5 - 20 nm, and the final sample rod was 150 - 300 nm of diameter from the top to the bottom. Electron micrographs (Figure 1.16 d-e) have been extracted from a tilting projection series which was taken between ± 90° tilt (a range of 180°) with a 1° increment. The reconstructed 3D structure (where white areas correspond to zirconia grains) is shown in Figure 1.16 f-g).

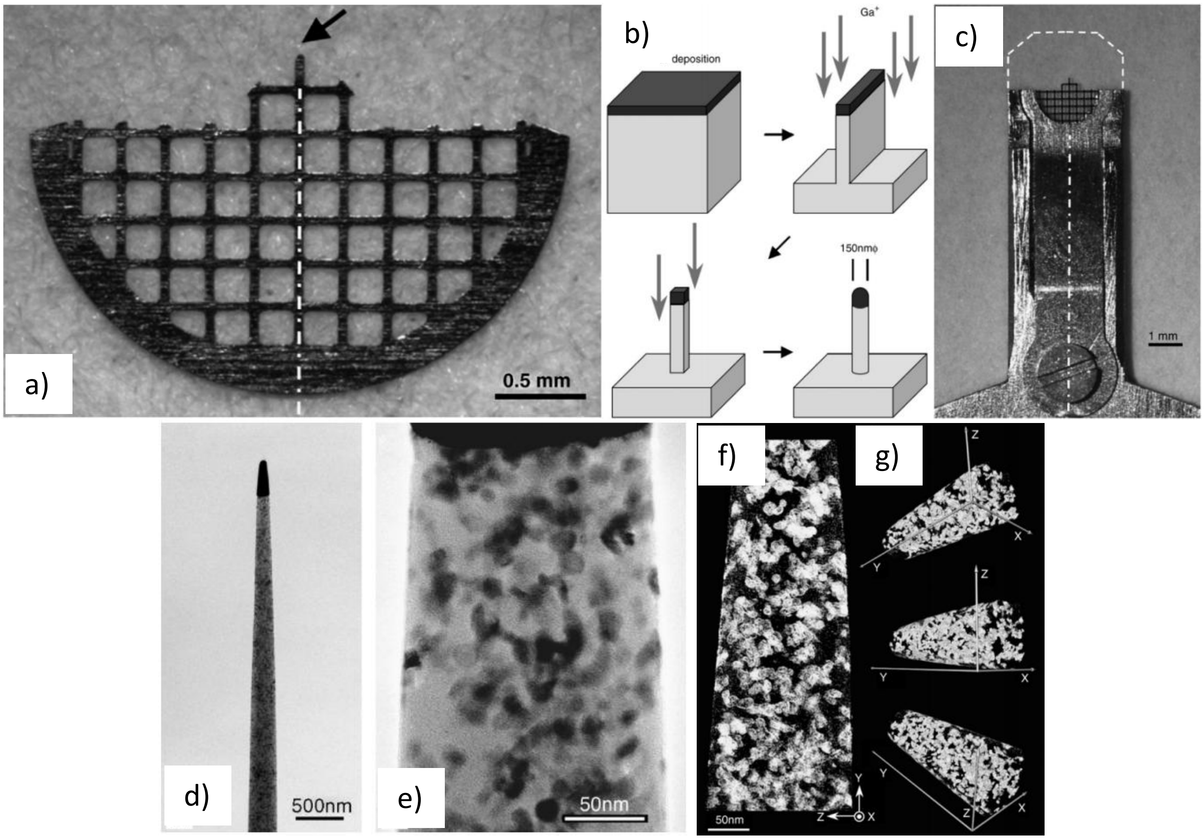

Figure 1.16: a) A modified molybdenum specimen grid, with the fixing position of the needle-shaped specimen indicated by an arrow. b) Schematic illustrations of procedures to form the rod-shaped specimen. After a tungsten deposition for the purpose of protection against the gallium ion beam, the specimen was first fabricated in a plate form, a prism form next, and finally a rod form by FIB. c) A modified JEM2200FS specimen holder allowing ± 90° tilt. The original shape is shown by the dashed line. d) An electron micrograph of a rod-shaped polymer nanocomposite containing zirconia fillers. e) Enlarged electron micrograph of the thinnest region of the rod-shaped specimen. f) Volume-rendered visualization and g) surface-rendered 3D images of the rod-shaped specimen from various viewing angles [Kawase2007].

1.2.1.2 Conventional TEM (CTEM) and energy-filtered TEM (EFTEM) tomography

Early electron tomography experiments were nearly all performed in conventional imaging, which means collection of bright-field (BF) images in a nearly parallel beam configuration [Koster2000]. The contrast in those images being essentially governed by elastic scattering (Bragg diffraction in crystals, see Figure 1.17 a)), this BF mode cannot easily be applied to crystalline materials, owing to the rapid contrast variation with orientation. However, it may be useful for amorphous materials if Fresnel diffraction is not too important [Baldock2002].

Besides conventional TEM, EFTEM is an imaging technique which produces images almost without Fresnel and diffraction contrast. The key idea is to apply an imaging filter which selects either only elastic scattering electrons which haven't lost energy (zero-loss) to improve the contrast of BF images, or inelastic scattering arising from a given energy range (i.e., ionisation edge as shown in Figure 1.17 b)) to produce elementary mapping. In both cases, the contrast exhibits roughly a monotonic mass-thickness relationship, which remains valid even for thick specimens [Angert2000] [Midgley2003] [Leapman2004].

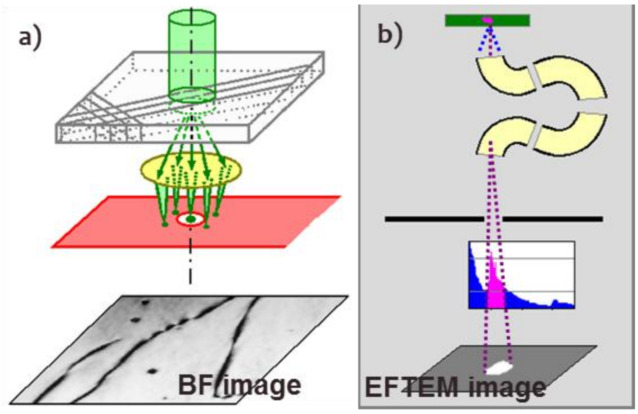

Figure 1.17: Basic illustration of a) CTEM and b) EFTEM.

1.2.1.3 Scanning transmission electron microscopy (STEM) – high angle angular dark field (HAADF) tomography

The STEM was firstly built by Baron Manfred von Ardenne in 1938 and then further developed by Albert Crewe in the 1970s. Contrary to the TEM mode where the probe is enlarged to illuminate the area of interest as a whole, it is focused and scanned ‘point-by-point’ on the surface of the object in the STEM mode. Different types of signals can be generated in STEM, such as mapping by energy dispersive X-ray (EDX) spectroscopy, electron energy loss spectroscopy (EELS) and annular dark-field imaging (ADF) [Utsunomiya2003] [Friedrich2005] [Liu2005]. These signals can be obtained simultaneously, allowing direct correlation of image and quantitative data.

Using a HAADF detector (see Figure 1.18) in STEM produces images with little or no diffraction effect (see Figure 1.19, where ‘high angle’ annular dark field and annular dark filed images are compared), the intensity of which is approximately proportional to Z^2 (so called ‘Z-contrast’, where Z is the atomic number of the specie present in the object). Indeed, coherent electron scattering occurs at low angles, and these electrons carrying the information due to diffraction are not collected by the annular detector, providing its inner radius is large enough to only collect largely scattered incoherent electrons [Utsunomiya2003] [Weyland2006]. From this we can understand why the STEM-HAADF technique is ideal for tomographic reconstruction; it generates good contrast that satisfies the projection requirement, which makes it more widely appropriated than conventional BF imaging to be applied in material science [Kübel2005] [Aoyama2008] [Ortalan2009] [Hungría2009] [Sueda2010] [Weyland2006] [Arslan2008b]. Also it can be more suitable for imaging thick sections and materials consisting of only light elements [Thomas1994] [Bals2007] [Ortalan2009] [Loos2009a] [Loos2009b] [Lu2010] [Hindson2011].

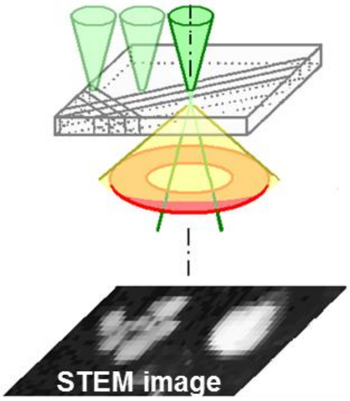

Figure 1.18: Scheme of STEM mode with a HAADF detector.

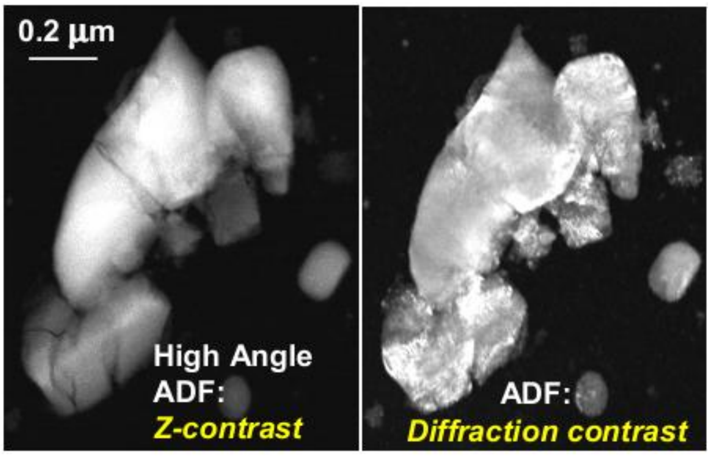

Figure 1.19: A comparison of contrast on HAADF and ADF mode.

To perform high tilting experiments in the JEOL 2010F TEM available at CLYM (see Figure 1.4) and equipped with a high resolution pole pieces enabling only tilting up to ± 20° with a standard commercial holder, dedicated sample holder tips were previously designed to offer a tilting capability of about ± 85° [Benlekbir2009, thesis].

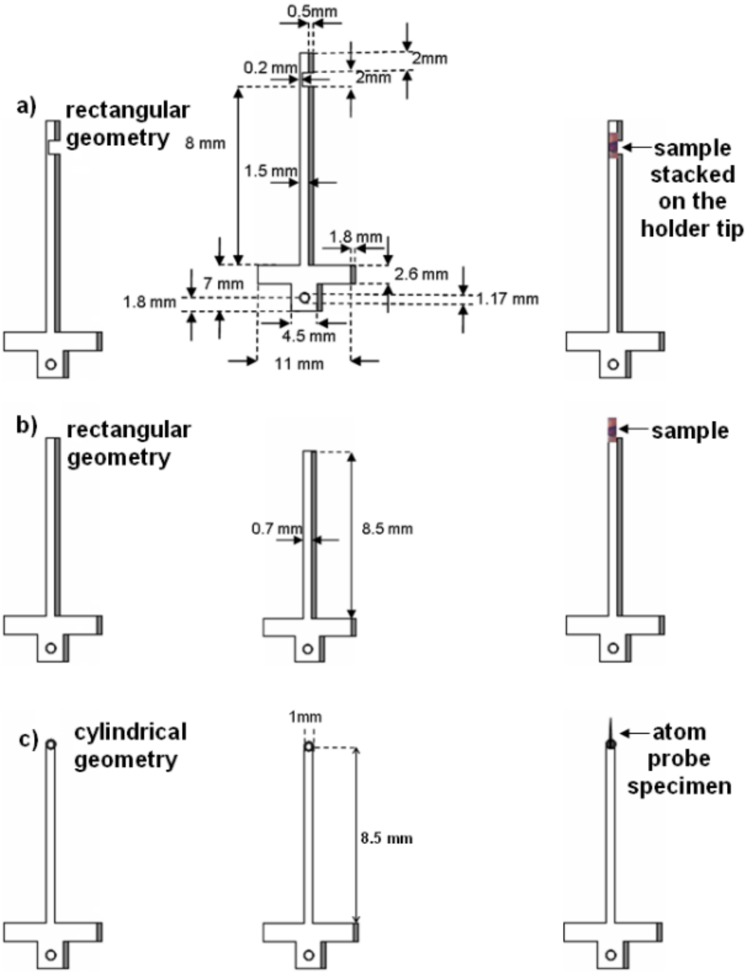

Figure 1.20: Holder tips used for tomography in MATEIS. a) Copper rectangular geometry with a notch; b) steel rectangular geometry without a notch; c) cylindrical geometry compatible with samples adapted to APT [Benlekbir2009, thesis].

Figure 1.20 exhibits different tips enabling large tilt capabilities even in a 'small gap' pole pieces. The tip with a notch (Figure 1.20 a) and Figure 1.21 a)) was used to mount TEM carbon grids. As this tip is only about 1.5 mm wide, the grid of originally 3 mm in diameter needs to be reduced in size to be adequately glued (Figure 1.21 b-c)). The grid is preferentially cut in a way that the tilt axis is parallel to the diagonal orientation of the grid grating (Figure 1.21 c- d)), in order to minimize any shadowing effect at high tilt angles. The 3D rendering of the AlZnMg needle prepared by electrolytic polishing which was presented in Figure 1.5 was related to an experiment performed with such a cylindrical geometry tip (Figure 1.20 c); Figure 1.22 illustrates how it is mounted on the TEM holder.

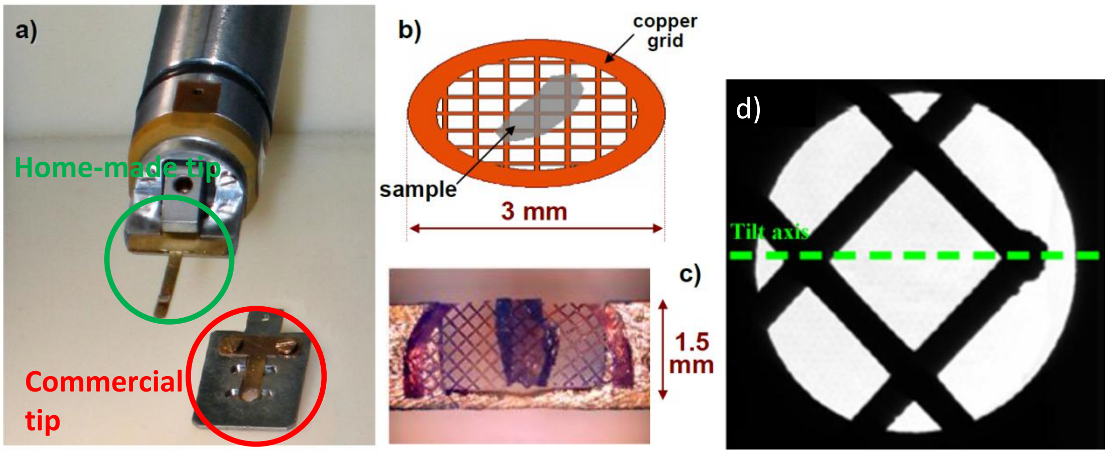

Figure 1.21: a) Simple tilt specimen holder commercially provided by JEOL for the TEM 2010F. A home-made tip compatible with a ± 85° tilting is replacing the original one, which limits the tilt capabilities to about ± 20 (25)°; b) Conventional 3 mm copper grid; c) Reduction of the grid size to be mounted on the home-made tip; d) a projection image at 0° showing the tilt axis parallel to the diagonals' direction of the grid grating [Benlekbir2009, thesis].

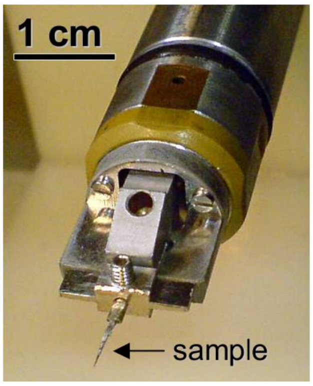

Figure 1.22: Home-made needle shape sample holder tip.

Besides the adaption of holder tips for TEM tomography, Benlekbir et al. have also developed a program to reduce the limitation produced by the weak depth of focus in STEM-HAADF mode, especially when the specimen is tilted to high angles. This focus problem is shown in Figure 1.23: if the converging incident probe is focused at the upper part of the tilted specimen (Figure 1.23 a)), it will be out of focus at its lower part (Figure 1.23 b)). A 'dynamic focus' procedure, where the beam is automatically refocused following a focus ramp when scanning the sample form 'top' to 'bottom', has allowed correct imaging as explained in Figure 1.23 c) and demonstrated in Figure 1.24. In this geometry, the line scanning direction must be parallel to the tilt axis. During the acquisition of the image, the focus is then updated automatically and progressively in synchronization with the imaging.

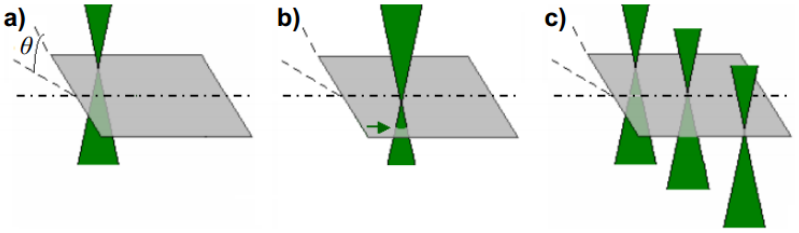

Figure 1.23: An illustration of the week depth of focus in STEM-HAADF mode when the sample is inclined by a sufficiently large angle θ. In a) the beam is focused at the top of the sample, which means that is will be out of focus at the bottom (b). c) shows an ideally adjusted dynamic focus for correct imaging [Benlekbir2009, thesis].

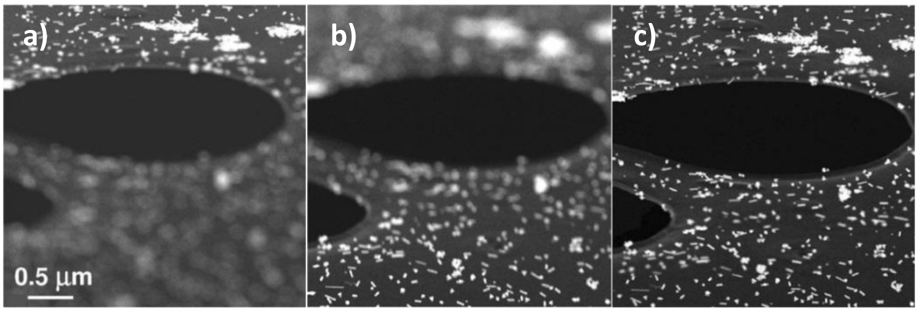

Figure 1.24: Demonstration of the functionality of 'dynamic focus' on a carbon supporting film covered with Pd nanoparticles, which was inclined at + 73° (the tilt axis is horizontal). a) - b) correct focus respectively at the top and bottom of the image; c) 'dynamic focus' correction during acquisition [Benlekbir2009].

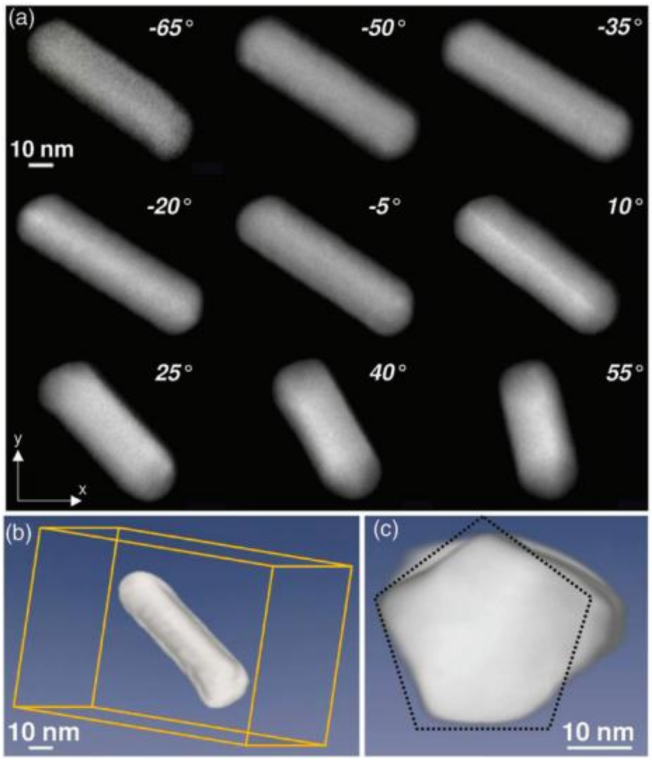

Figure 1.25: Reconstruction of a pentagonal rod; a) Selection of images recorded every15° from a HAADF tilted series acquired on a Pd nanoparticle between - 65° and 65° by step of 1° (tilt axis parallel to y-axis); b) Surface rendering of the reconstructed particle; c) Nearly edge-on projection: the dotted line shows a perfect pentagon superimposed for comparison [Benlekbir2009, thesis].

Figure 1.25 exhibits an example of tomographic series on Pd pentagonal rod obtained by STEM-HAADF imaging with the JEOL 2010F instrument available at CLYM, together with the associated reconstruction and visualization. In this particular case, the morphology of individual particles is revealed at the nanometre scale (particle sizes ranging from 10 to 50 nm), and the resolution in 3D was then estimated to be around 2 nm.

1.2.2 SEM tomography

Unlike in a TEM, the SEM is generally not considered as a possible platform for tomography experiments. At first conventional SEM imaging with secondary of backscattered electrons reveals the surface of a bulk sample, which is not adequate to reconstruct a microstructure in 3D. As far as a transmission mode might be concerned, because the energy of the electrons produced in a SEM, typically 30 keV at maximum, is much lower than in a TEM, it may be thought that the penetration power of electrons is too low. However, STEM imaging is possible, and it is referred as low-voltage STEM or STEM-in-SEM [Merli2003]. Consequently STEM tomography is also possible. This was demonstrated recently in an ESEM (FEI XL30, shown in Figure 1.6) equipped with a detector for transmitted electrons mounted below the sample [Jornsanoh2011].

1.2.2.1 Tomo-STEM®

The tomography approach on transmission mode of ESEM was named 'tomo-STEM®' [Jornsanoh2011]. The initial aim of developing such technique was to provide 3D information on large volumes with high resolution.

The tomo-STEM developments took benefits from a previous work undertaken to observed liquids in the SEM, using the transmission imaging mode (so-called 'wet-STEM' [Bogner2005]). It is a 'STEM-in-SEM' technique but applied to an environmental SEM. With the home-made device shown in Figure 1.26, a TEM grid supporting thin sample sections can be mounted and frozen by the Peltier support, and transmitted electrons are collected in projections with an ADF-type detector under the grid. This imaging mode allows the observation of wet samples or objects in a liquid phase in the transmission mode, in parallel with classical imaging with the usual SE and BSE detectors.

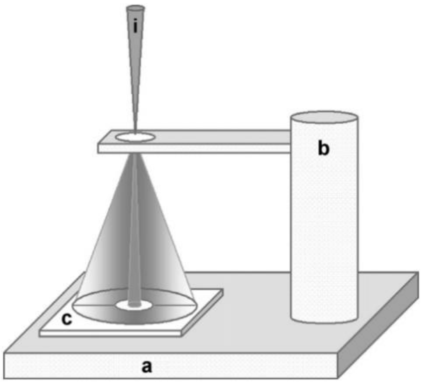

Figure 1.26: The 'wet-STEM' device available at the MATEIS laboratory: a) Peltier stage; b) SEM mount maintaining the TEM grid; c) solid-state annular detector; i) incident convergent electron beam [Bogner2007].

For tomography experiments, not only the transmission mode is needed but also the ability to tilt the sample in order to acquire projections at different angles. A dedicated device has thus been developed as shown in Figure 1.27. It consists in 3 principal parts: a rotation generator; a eucentric setter; a detection system. The rotation system permits tilting the sample around the horizontal axis up to 360° with an accuracy of 0.1°. Using a simple montage shown in Figure 1.28, a TEM grid is maintained at the tip of the eucentric setter, which allows the tilt axis to be adjusted in order to pass through the grid mean plane in order to keep the area of interest in the field of view while tilting (typical eucentric adjustment). The detection of transmitted electrons is realized as for the 'wet-STEM' imaging, an ADF detector being fixed under the sample grid. The distance between the grid and the detector may be varied, which will modify the collection angles of the transmitted signals. According to the similitude in geometry, this 'tomo-STEM®' technique can be considered as the low-voltage version of the STEM-HAADF mode in TEM. However, it is significantly more complicated in terms of nature of collected electrons, since the wavelength of the primary beam, as well as the value of collection angles are very different from the case of STEM-HAADF in the TEM: thus, all types of electrons (elastic and inelastic) can be collected contrarily to the case of STEM-HAADF [Bogner2007]. Because various types of electrons can be detected, contrasts can be exploited even for surprisingly large thicknesses (up to the micrometre range in favourable cases), and this why conventional thin foils or ultramicrotomic sections adequate for TEM observations can easily be observed in this tomo-STEM technique.

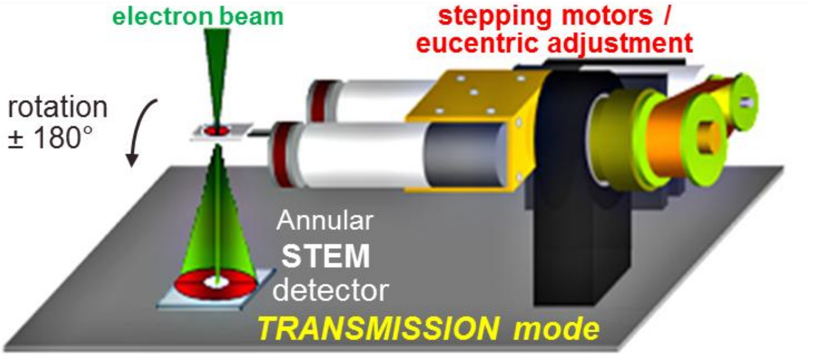

Figure 1.27: The 'tomo-STEM®' stage for electron tomography experiments [Jornsanoh2008, thesis].

Figure 1.28: Home-made TEM grid holder adapted for 'tomo-STEM®' stage [Jornsanoh2011].

Figure 1.29 shows a general view of the stage is installed in the ESEM, thanks to the large sample chamber. It must be reminded here that, as for conventional SEM imaging, the differential vacuum system will be much appreciable to reduce the charging effects when observing non-conductive materials.

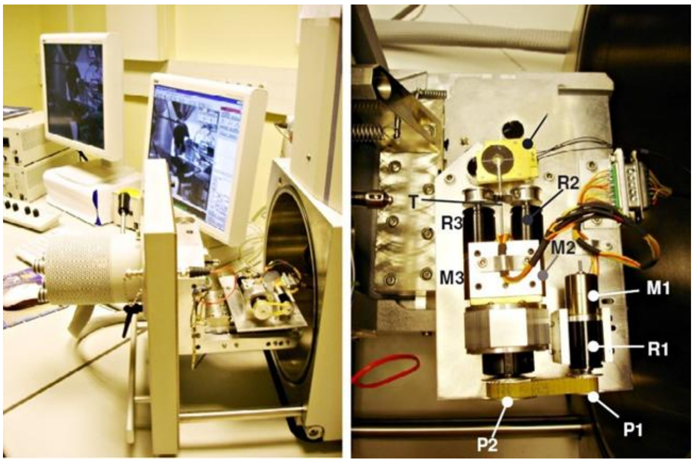

Figure 1.29: The installation of 'tomo-STEM®' stage in ESEM. [Jornsanoh2011]

By combing ESEM and STEM performances, the 3D characterization of material structures can be realized with a resolution level estimated to about 10 nm. Because of the environmental mode, it is easily suitable for studying non-conductive samples; if further offers a good contrast for low-atomic number materials, which can then be observed in relatively 'thick' states, up to several hundreds of nanometres. In the case of grid supported samples, the range of tilt angles (up to ± 90°) is only limited by the geometry of the grid.

Figure 1.30 illustrates a typical tomographic reconstruction using the 'tomo-STEM®' technique. It concerns a polymer composite constituted of a unstained PVC (poly(vinylchloride)) matrix filled by a variety of micronic and sub-micronic $CaCO_3$, TiO_2 and shock modifiers particles. The section was prepared by ultramicrotomy and is 500 nm thick. The projection series was obtained between ± 67° with an increment of 1°.

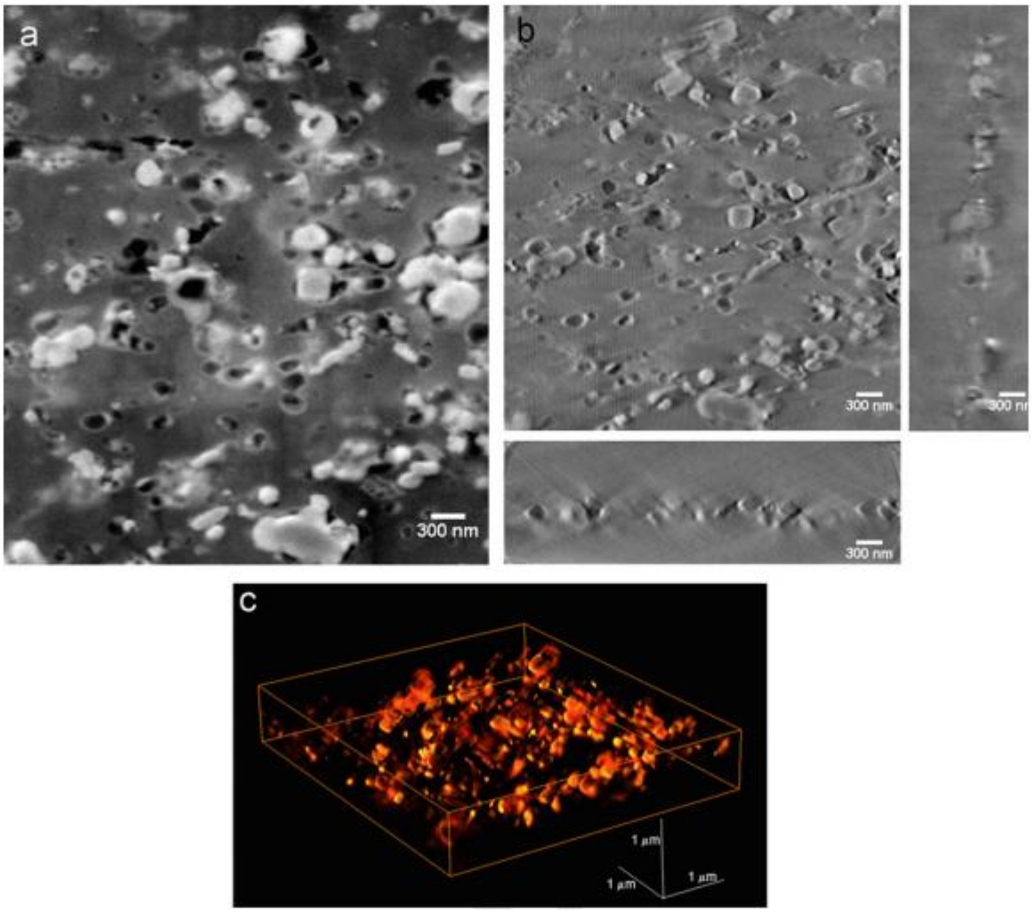

Figure 1.30: a) STEM image at 0°; b) tomogram XY, XZ and YZ slices and c) reconstructed volume (4.2 × 4.8 × 0.8 μm^3) of impact-resistant poly(vinylchloride) [Jornsanoh2011].

Figure 1.31 exhibits another 'tomo-STEM®' result on a sample of natural ribbon reinforced by stained poly(methyl methacrylate) particles (NR/PMMA). The polymer particles are stained with osmium and they appear in dark in the STEM image (their contrast was inverted in the reconstructed tomogram).

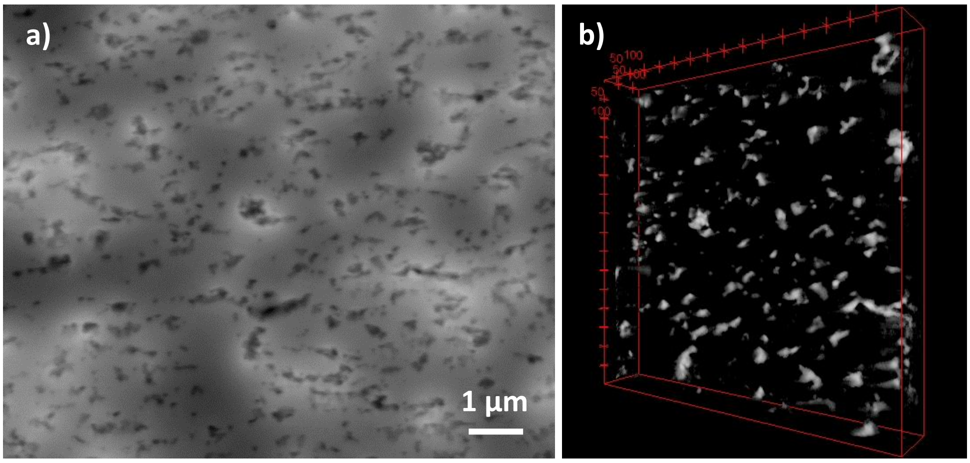

Figure 1.31: a) STEM projection at 0° and b) a reconstructed tomogram (2.4 × 2.4 × 0.4 µm^3) of NR_PMMA-stained.

1.2.2.2 STEM-in-SEM

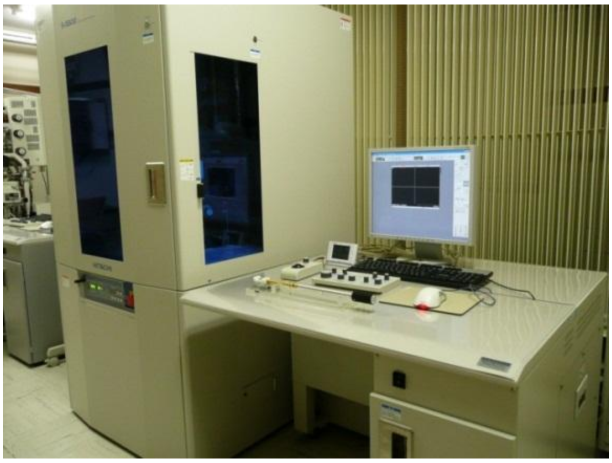

Figure 1.32: SEM Hitachi S5500 cold-FEG available at Tohoku University (Sendai, Japan).

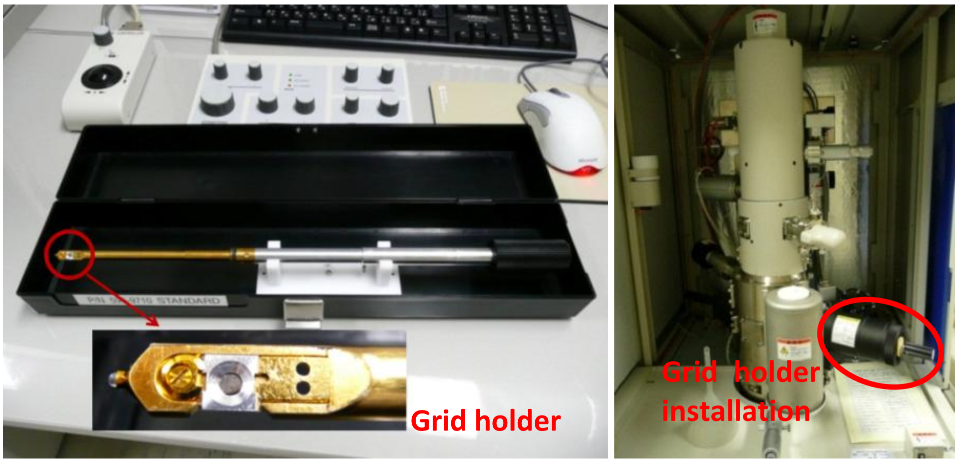

Figure 1.33: The commercial grid holder for STEM imaging and its mounting in the Hitachi SEM.

Besides the tomo-STEM® montage, we have also used a commercial instrument permitting low-voltage STEM observations in a SEM: this is a Hitachi S5500 SEM (Figure 1.32) installed at the Institute of Materials Research at Tohoku University, Sendai-Japan. It is equipped with a cold field emission gun (cold-FEG). The microscope is directly compatible with the utilization of TEM grid holders (Figure 1.33) and allows projection imaging with an annular detector. With the cold-FEG, the resolution and contrast can be improved especially for low-atomic number materials, like polymers. The major limitation of this setup is the tilt angle which is limited to be only ± 40° by the geometry and space available below the objective lens in the sample chamber. [Liu2012, EMC]

1.2.2.3 Other possible SEM tomography techniques

As previously mentioned, the conventional use of a SEM is to image the surface of the sample. This provides the opportunity to perform surface tomography. Lück et al. have realized such analyses of intermediate filament (IF) network in pancreatic cancer cells using the secondary electron signal at an accelerating voltage of 5 kV. The thickness of the networks investigated in this SEM tomography experiment was up to 550 nm. They have first tested and compared STEM imaging and SE imaging in a Hitachi S5200 SEM (see Figure 1.34). STEM images provided a rather low signal of IFs in comparison to the strong signal of non-IF cytoplasmic leftovers after extraction of the cells. Secondary electron imaging enhanced the signal of IFs.

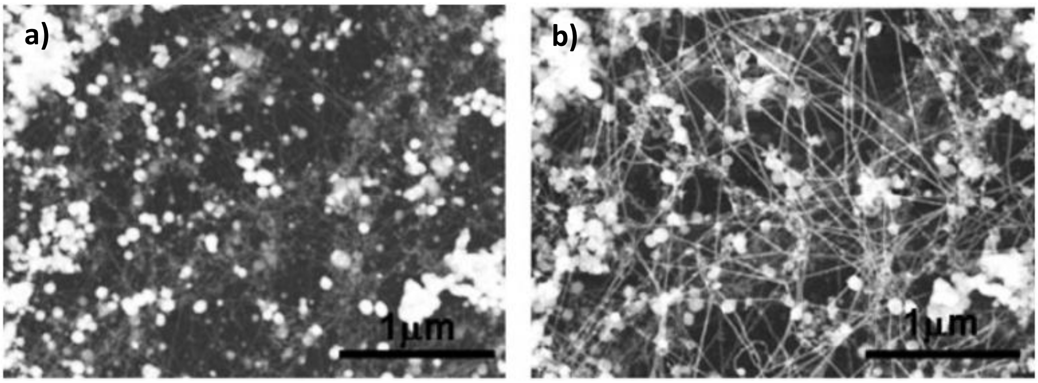

Figure 1.34: a) STEM dark field image at 30 kV; b) SEM image at 30 kV [Lück2010].

A SE tilt series was obtained with 2° increment first from + 60° to 0° and then 0° to - 60° after a rotation of the sample by 180° due to the maximum tilt of the stage is limited to 40°. And SEM tomograms (Figure 1.35) were reconstructed by weighted back-projection (WBP) algorithm (see chapter 1.2.5.1) even if the images were not projections.

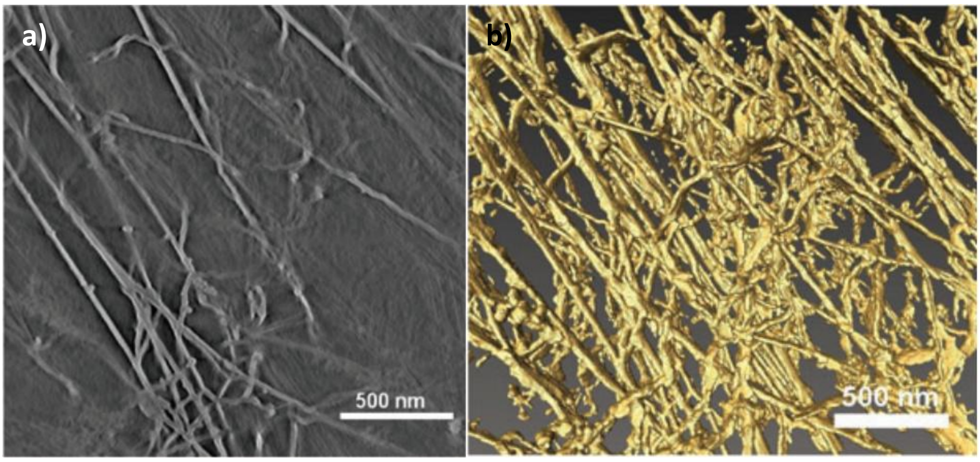

Figure 1.35: Reconstruction of SEM tilt series. a) Horizontal cut through SEM tomogram; b) Visualization of tomogram after binarisation (top view) [Lück2010].

A further simulation of WBP reconstructions from TEM signal and SEM signal (Figure 1.36) shows that the surface dependent signal (SE in SEM) reconstruction doesn't differ substantially from what can be retrieved from real projections. The main difference is that the interior of the circle is more faded in the SE reconstruction, which will be less noticeable in 3D visualization and of minor importance in situations where the external shape is the essential microstructural factor, as in the case of filaments shown in the previous figures.

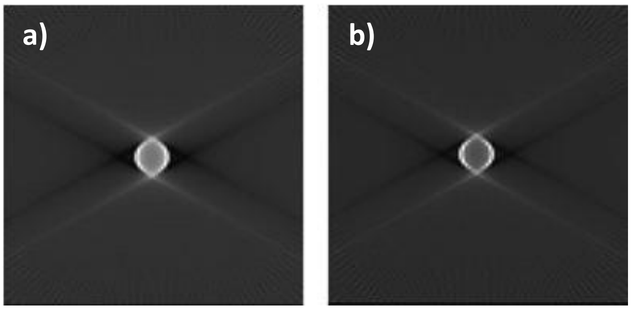

Figure 1.36: WBP reconstructions of a circle (diameter of 11 pixel lengths) from simulated projections (corresponding to TEM) and from a simulated surface dependent signal (corresponding to the secondary electron signal of SEM). The tilt range was chosen from− 60° to + 60° at an increment of 2°. a) WBP from simulated TEM signal. b) WBP from simulated secondary electron signal [Lück2010].

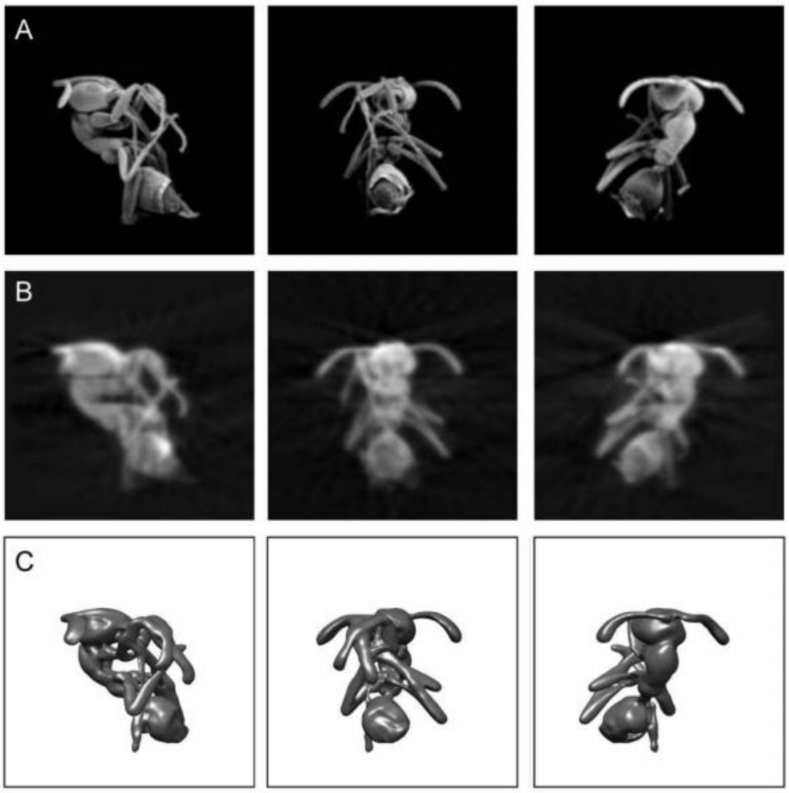

Figure 1.37: 3D reconstruction of surfaces: (A) typical aligned input images. (B) Re-projections of the three-dimensional volume at orientations corresponding to the images in (A). The re-projections closely approximate the input images, but represent projections of the entire secondary electron escape probability distribution. (C) Iso-density surface representations of the reconstructed volume. The fitted surface closely approximates the (low-resolution) geometry of the input images [Woodward2010].

A similar SEM reconstruction has been done by Woodward et al. [Woodward2010] in a LEO S440 SEM. An Argentine ant was mounted on a conventional SEM stub, then freeze-dried and finally coated with Gold-Palladium. A series of SE images were taken by from the surface of the glued ant with a 7.2° increment for a full rotation (360°), so 50 images were obtained. Then the stage was rotated in its plane, and other tilt series were also recorded to carry out a conical tomography. The post image processing was done as for TEM tomography data: the image series were aligned by the cross-correlation method and the surface rendering tomogram was reconstructed by the BP algorithm (see section 1.2.5.1).

Figure 1.37 shows some examples of the original SE images, re-projection images and tomogram slices at different tilt angles. The reconstructed object shows a reasonable rendering of its surface, the internal structure being obviously not accessible. This tomography technique might be interesting when only the surface geometry reconstruction is required; it demands multiple tilt series for a better result.

1.2.3 FIB/SEM tomography

The FIB, or Focused Ion Beam instrument was first developed for specific sample preparations or machining of devices at a micrometre or sub-micrometre scale [Talbot1996] [Giannuzzi1999] [Rubanov2004] [Gamo1996] [Li2006] [Menard2011]. This wonderful tool was gradually adapted for producing thin sections of biological samples for TEM exploitation in 2D and potentially 3D. This tradition of sample preparation in FIB has been extended to materials sciences, not only for simple planar cuts but also for more complex shapes, such as conical or cylinder forms as it is needed for optimizing tilting tomography. Since the last decade, the FIB unit was enriched in the sense that the ionic gun has been coupled with a SEM column in what is called a dual-beam or double-column system. It can also be referred as FIB/SEM (focused ion beam/scanning electron microscope) [Krueger1999] [Bansal2006] [Jeanvoine2008].

The literal understanding of ‘tomography’ would be the visualization of slices. In such a system of FIB/SEM, this classic idea of tomography can be achieved: once a region of interest has been selected in the sample, it is milled layer by layer with the ion beam, and electronic images are successively taken from each fresh milling as in a conventional SEM. At last all image slices are assembled, after some possible corrections and alignments, to represent the original volume of erased matter. The reason why this tomography technique possesses almost no volume restriction is because the length in the slicing direction is not really limited [Kato2007], except by time and real size of the object. If a large volume is needed, a long isolated zone of interest must be prepared, which will increase not only the time for the acquisition but also the time for the preparation.

1.2.3.1 Presentation of the NVision 40 of Carl Zeiss

A FIB/SEM system has been recently installed at CLYM and is functional since the first half of 2010. Figure 1.38 presents the general configuration of this machine, a NVision40 from Carl Zeiss. It essentially consists in an electron column with a field emission gun (vertical in the center), a liquid metal ion source (LMIS) within the inclined ionic column (at 54° from the SEM column axis), a gas injection system (GIS) permiting the deposition of various gasous resources for different purposes. The machine is also equipped by a EDX detector for chemical analysis, and a EBSD camera for crystallographic characterization; both analytical devices can be used in in 2D and 3D. Two nano-manipulators are available, especially to help the TEM specimen preparation, and also specific other operations(like nano-machining and handling of nano-objects). A second electron source (floodgun) can illumate the surface of the sample at grazing incidence in order to reduce the positive charging effect during the ionic milling.

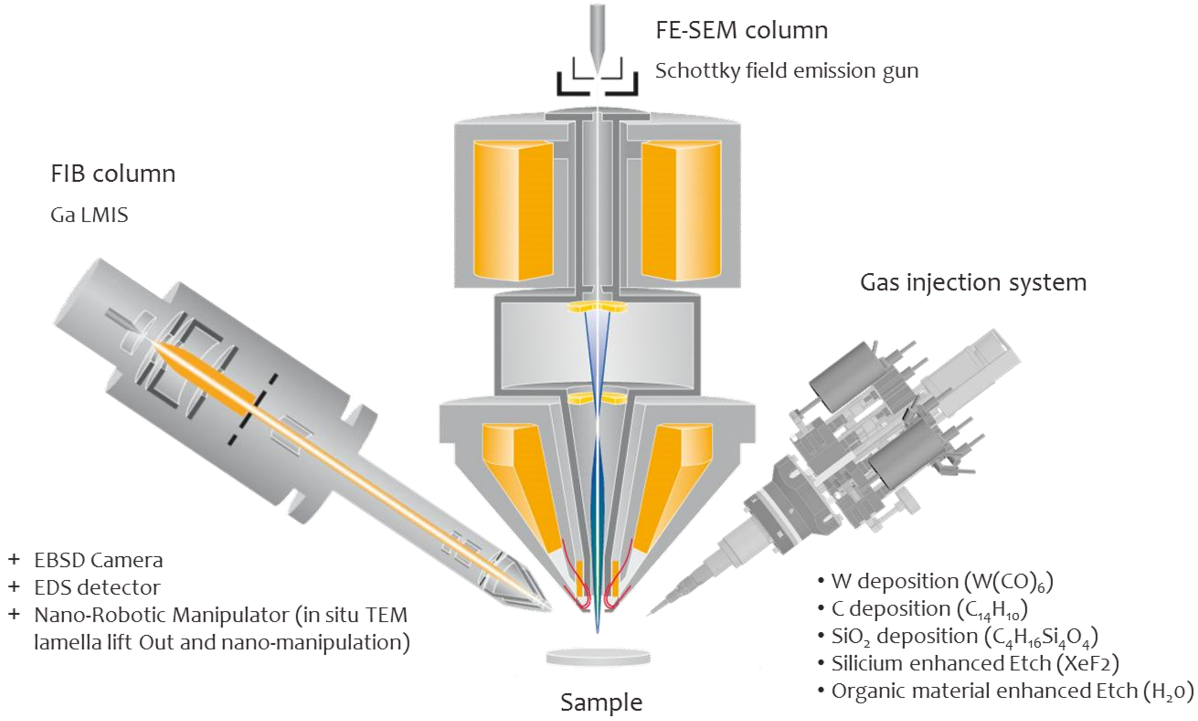

Figure 1.38: Presentation of the Carl Zeiss NVision 40 FIB/SEM.

The present work intended to use this instrument for extensive application of tomography in the nanocomposites. For this purpose, it is useful to say a few words about sample preparation. Basically the sample preparation is not very different than for SEM imaging. A small part of the material is attached onto a SEM stub by a conductive carbon scotch or silver laquer. As compared to TEM, it does not request any specific preparation like ultramicrotomy for thin section cutting.

In the case of non-conductive materials (like polymer-based nanocomposites), the surface of the sample should also be painted with silver laquer to improve the electron conduction between the surface of the material and the stub. Then a thin gold layer can also be deposited. This metalisation procedure will not just help the conduction of the charging electrons from the incident signal beam but also protect the material from being degraded during the milling. The sub-surface implantation of ions (Ga ions in the case of the NVision 40) might be an important issue for tomography experiments since it may cause microstructural artefacts, like the curtaining effect that will be illsutrated in the next chapters.

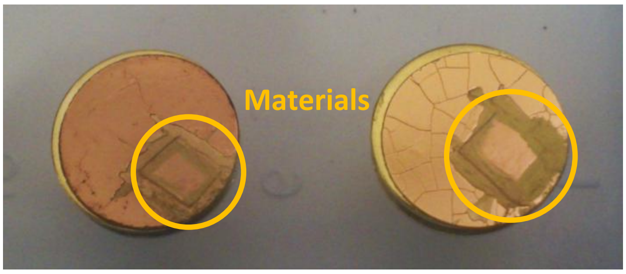

Figure 1.39: Prepared samples (corresponding to the materials shown in Figure 1.48) for FIB/SEM exploitations.

1.2.3.2 The 3D technique

For carrying out the 'classical' tomography experiment, there are some standard procedures to follow:

- Like in a conventional SEM, the electron beam of FIB/SEM system arrives at the surface of the sample perpendicularly. For a tomographic acquisition, as demonstrated in Figure 1.3 and Figure 1.40, the sample stage should firstly be inclined by 54° (this angle could be different, depending on the manufacture geometry) that is the angular difference between FIB and SEM columns. This allows the surface of the sample to be perpendicular to the direction of the incident ion beam; the ion beam will then allow to erase a thin slice of matter parallel to the front surface which is observed in SEM.

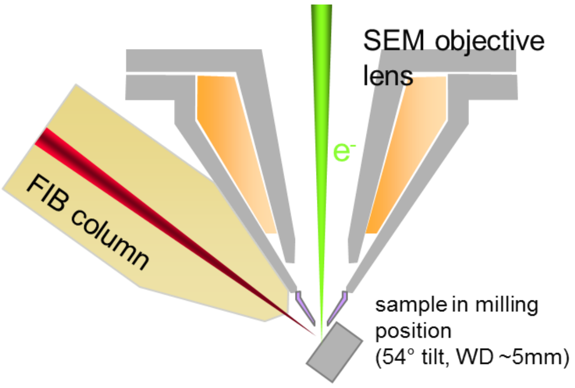

Figure 1.40: Geometry of two source columns and sample configuration for tomographic acquisition.

- Secondly, the sample stage is adjusted to the coincidence position which means that both ion and electron beams are focussed exactly at the same exact position on the region of interest. The surrounding area of the region of interest with a 'U' form is then milled by the ion beam. The size of the front section in the thickness direction, more importantly its width, is determined according to a compromise between the requested resolution (at least, numerical resolution as defined by the step size of the scan) and the size of images to be generated.
- Once the preparation of the experiment through preliminary milling around the region of interest has been performed, the generated front section is 'polished' with a lower ion current than what was used for rough milling; this will insure a smooth surface state enabling correct electron imaging.
- After having chosen various experimental conditions like the scanning speed, the imaging mode (i.e. acceleration voltage of incident beams, imaging signals and detectors), the thickness to be erased at each slice, the 3D acquisition of the 'slice-and-view' procedure begins: in a repeated manner, the ion beam erases a thin layer of the prepared surface of interest, and the SEM image is next recorded from the fresh front section. Once imaging is finished, another layer of the material is milled …. In principle, the focus of the electron beam in each image is automatically actualized by the system according to the theoretically known 'z', or working distance WD variation, related to the thickness of the slab erased during the milling process.

As illustrated in Figure 1.41, one slice which corresponds to one image could be considered to be consisted of a certain number of voxels *N*. The amount of slices *n* to be achieved depends on the choice made by the user regarding the height of volume desired. Note that in this general procedure, the voxel is not necessarily isotropic: in the (X, Y) plane, the voxel size is defined by the pixel size, itself linked to the magnification / numerical resolution of the SEM images; in the 'z' direction, the voxel size is defined by the expected constant thickness of the erased slices. Typically, the latter value is larger than the (X, Y) pixel size.

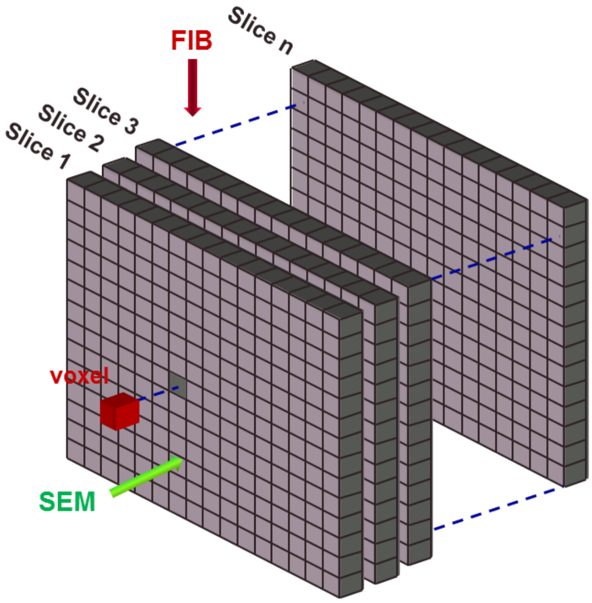

Figure 1.41: Sketch of 'slice-and-view' procedure.

Since the sample is inclined 54° and the ionic beam is perpendicular to the surface of the sample, the imaged section has an angle of 36° with the incident electron beam. Conventionally, the electrons arrive at the surface of the sample vertically. Thus the electron images have to be corrected to have the same scale along x and y: this is automatically performed by the microscope controlling software 'SmartSEM' without any action from the user.

At the end of the whole procedure, we obtain a series of several hundreds, or even thousands of images. This image stack would not need any further treatment if everything worked perfectly, but this ideal situation never (or rarely) occurred. Because of some instabilities during the long duration of the experiment (a few hours till several days - possibly -), various problems affect the experiment: drift of the sample, loss of focus, environmental issues (electromagnetic stray fields) [Holzer2006]. As a consequence the images need to be re-aligned post-mortem, or possibly partly during the acquisition itself. The 'live' re-alignment is frequently performed manually, which means that the user must assist the experiment. The post-mortem alignment is realized by some dedicated software (see section 1.2.5.2).

1.2.4 Brief comparison of electron tomography techniques

In Table 1.1, some recent results of electron tomography experiments from the literature are shown. Many efforts have been made to apply these approaches in various materials domains. As it can be seen, TEM tomography generally offers the best resolution. On another side, the 'slice-and-view' tomography in FIB stays in the SEM resolution range of about 10 nm but offers the great advantage of a quasi-unlimited volume. SEM tomography in the transmission mode can still be considered in period of development, so very few results have been reported so far.

Author	Material	Resolution (pixel or voxel size)	Analysed volume	Device and technique	Sample preparation
P. Penczek [Penczek1995]	Stained plastic section of rat liver mitochondria	3 nm (pixel)	940*940 pixels	Double-tilt CTEM	
W. Baumeister [Baumeister1999]	Macromolecules	~ 2 nm		CTEM	
A.J. Koster [Koster2000]	Catalytic materials	11 nm, 3.3 nm	1150*1150*1150 nm^3, 270*200*170 nm^3	Philips CM 200 FEG, 200 kV	Suspension drying on grid
Chyong-Ere Hsieh [Hsieh2002]		~ 8 nm		JEOL JEM-4000FX (400 keV)	Cryo-ultramicrotomy
M. Weyland [Weyland2004]	Heterogeneous catalyst active nanoparticles	~ 1 nm		STEM-HAADF	
N. Kawase [Kawase2007]	A polymer matrix with zirconia particles	5 - 10 nm		CTEM, JEOL JEM 2200FS, ± 90° tilt	Rod-shaped specimen by FIB milling, Hitachi FB2100
I. Arslan [Arslan2008b]	Porous catalyst	~ 1 nm	~ 60 nm^3	STEM-HAADF	
S. Benlekbir [Benlekbir2009]	Pd particles	2 nm		JEOL 2010F, STEM-HAADF, 200 kV	
P. Jornsanoh [Jornsanoh2011]	SiC nanowires on tungsten tip	~ 78 nm	41*32*40 μm^3	tomo-STEM® (WBP)	
	PVC/$CaCO_3$, TiO2, shock modifiers	~ 20 nm	4.2*4.8*0.8 μm^3	tomo-STEM® (ART)	Ultramicrotomy (500 nm)
L. Holzer [Holzer2006]	Portland cement (OPC)	12 - 116 nm	81 - 100000 μm^3	FIB, slice-and-view	
M. Kato [Kato2007]	Poly(styrene-*block*-isoprene) block copolymer		6*6*4 μm^3	FIB, slice-and-view, FEI Nova200 Nanolab	
		4 nm	3.8*3.9*0.24 μm^3	CTEM, JEOL JEM2200FS	Ultramicrotomy
H.Ostadi [Ostadi2010]	Gas diffusion layer	8*8*14 nm	~ 10 μm^3	FIB, slice-and-view, Skyscan2011	
S. Sinha Ray [Sinha Ray2010]	Polymer/clay composites, poly[(butylene succinate)-co-adipate]/organoclay	15*15*30 nm	24*12*10 μm^3	FIB, slice-and-view, Zeiss NVision40	
P. Schneider [Schneider2011]	Mouse femur	18.6*18.6*29.5 nm	19*14.3*11.5 μm^3	FIB, slice-and-view	Embedding in a methacrylate-based media

Table 1.1: Short indicative selection of electron tomographic results from the literature.

1.2.5 Data treatment

For all tomography techniques, the image data obtained should be properly processed for 3D visualization, quantification and any other exploitation. This processing usually consists of re-alignment of image series and volume reconstruction. A segmentation treatment is also generally needed in most cases [Frangakis2006].

Software and programs that are dedicated for these data treatments are available freely and also commercially. Due to the different natures of tomography techniques, different processing solutions are needed.

1.2.5.1 Treatments for tilting tomography

Before reconstruction, the tilt series should be re-aligned since different kinds of drifts are generally occurring during the acquisition, owing to the limited mechanical accuracy of the sample holder, deviations while tilting if the eucentricity is not perfectly adjusted, or the tilt axis not perfectly in the object mean plane.

The orientation of the tilt axis is to be identified at first. For a single-axis experiment, tracking the trajectories of some peculiar details of the sample, or markers intentionally deposited on it, allows the tilt axis to be accurately positioned. As an illustrative example, Figure 1.42 shows the superimposition of all images from a tilting series, where elongated trajectories give the direction perpendicular to the tilt axis (or the elongation in the Fourier transform gives the tilt direction).

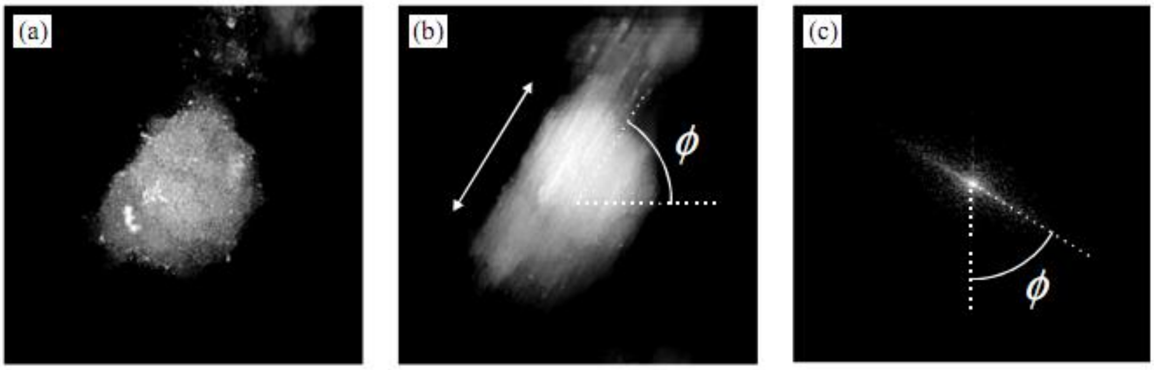

Figure 1.42: Tilt axis direction determination in a STEM-HAADF series. a) A single image at zero tilt from a catalyst structure (a carbon matrix embedded with palladium particles); b) The summation of the entire tilt series showing a distinct movement in one direction at an angle ϕ to the horizontal; c) The power spectrum determines the positioning of the tilt axis [Midgley2003].

When the tilt axis is positioned, the images can be aligned by tracking the movement of specific markers [Mastronarde2006]. The purpose is to use certain high-contrast details that are easy to identify, as will be spherical particles.

An alternative method, for example when no markers are available, is to use a cross-correlation alignment carried out sequentially image by image [Brandt2006]. However the cross-correlation method is essentially a measurement of the similarity between two objects, and the accuracy of this operation used as an alignment routine depends on the tilt increment between the successive projections: the higher the increment, the less accurate the alignment. Some correction can be made before the alignment such as proposed by Guckenburger: each projection is stretched in a direction perpendicular to the tilt axis by a factor $1/\cos\psi$, where ψ is the tilt angle [Guckenberger1982]. As a result, the change of shape of any object induced by the projection effect can be reduced and the spatial relationship between successive projections is better described.

For the reconstruction procedure, dedicated algorithms which have already been developed and applied according to the literature [Carazo2006]; here we give a rapid list of the major techniques that can be applied to tilting tomography:

- BP: the Back-Projection method is a real space reconstruction technique: any point in the euclidan space can be described by certain ‘rays’ passing through it which give rise to the various projections; the object can thus be restored by inversing these ‘rays’ from a sufficient number of projections from different angles: the superposition of all such back-projected ‘rays’ will define the shape of the original object. In practice, the projections from different angles are expressed in the Fourier space of the object, and then a tomogram is obtained by an inverse Fourier transform. [Herman1995] [Midgley2003]

- WBP: the Weighted Back-Projection algorithm came out to optimize the BP theory which produces artefacts due to a limited sampling: the points in the Fourier space are not equally separated which induces inaccuracy for details distant from the tilt axis. A weighting filter consisting in a radially linear function (from zero at the centre to some maximal value at the edge) can then be multiplied to the starting BP reconstruction in the Fourier space. This operation improves the frequency distribution (high frequencies near the edge) and thus removes the blurring in real space. [Radermacher2006]

- ART: the Algebraic Reconstruction Technique is a method which iteratively adds information to each pixel during the reconstruction procedure by comparing the projections of the current reconstructed volume with the experimental projections, and accounting for the differences to improve the quality of the final tomogram. [Herman1993] [Marabini1997]

- SIRT: the Simultaneous Iterative Reconstruction Technique is also an iterative method derived from ART, which compares all the theoretical and experimental projections at the same time. It requires more time than the ART method but is less sensitive to any noise present in the experimental projections because of the averaging at each voxel. Both ART and SIRT algorithms require a value for a relaxation coefficient which is close to the inverse of the number of acquired projections in order to control the speed of convergence to the optimized final volume. [Bangliang2000] [Benlekbir2009, thesis] [Chuang2012]

- SART: the Simultaneous Algebraic Reconstruction Technique is another implementation of the ART, based on a iterative method to solve the linear system described the reconstruction problem. This algorithm can generate a good reconstruction in only one iteration, because it uses the BP technique as a seed; this appears to be an important computational advantage over ART. [Andersen1984] [Wan2011]

Besides the most popular reconstruction algorithms mentioned above, new developments are currently produced in order to improve the reconstruction from both quality and rapidity points of view [Sandberg2003] [Fernández2008] [Xu2010a] [Xu2010b].

During this work, we have essentially used two sets of computer packages to perform reconstructions form the tilting tomography experiments. One is the commercial software suite of Gatan incorporated as a plug-in in the DigitalMicrograph software (Figure 1.43); it consists in three major modules: alignment of image series, volume reconstruction and a basic visualization function. The alignment part contains two modes: automatic and manual, they can both work without landmarks. The reconstruction can be realized in several different algorithms (WBP, SIRT, SART) conventionally using the central unit processor (CPU) or the processors of the graphic video board (GPU) which allows a significant speed improvement.

```
Welcome to DigitalMicrograph   24/02/2012  17:56:24
```

Figure 1.43: Screen copy of the Gatan Microscopy Suite: DigitalMicrograph (tomography version, 64 bits).

The second software that has be used is a free program developed by Cedric Messaoudi et al. and called TomoJ (*http://u759.curie.fr/en/download/softwares/TomoJ*) (Figure 1.44). It's an open source program based on the Java language; it allows the alignment of the image series without and with landmarks [Sorzano2009], and also the volume reconstruction with various algorithms (BP, WBP, ART, SIRT). This program works as a plug-in of ImageJ (*http://rsbweb.nih.gov/ij/*) and Fiji (*http://fiji.sc/Fiji*) software which are also well-known and efficient free image treatment software that provide all kinds of image processing, including image segmentation of special interest for the treatment of the tomograms.

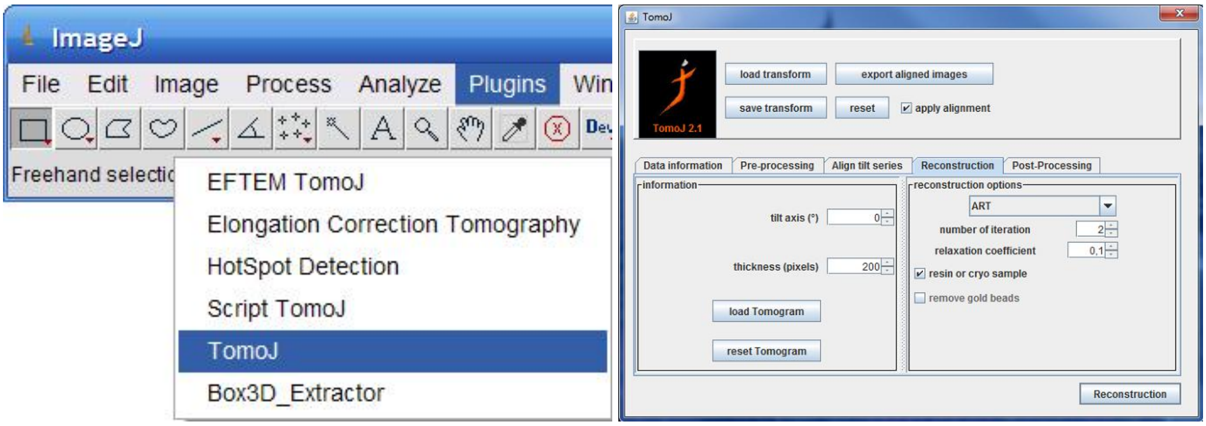

☑ apply alignment
tilt axis (°) 0
thickness (pixels) 200
ART
number of iteration 2
relaxation coefficient 0.1
☑ resin or cryo sample
☐ remove gold beads

Figure 1.44: TomoJ, a series alignment and reconstruction software solution working as a plugin of ImageJ [Messaoudi2007].

1.2.5.2 For FIB/SEM tomography

For this 'classic' tomography, the data treatment is relatively simpler. The series of images obtained by this technique needs no real reconstruction procedure like for tilting tomography series, but they may require a re-alignment due to drift problems encountered during the acquisition as already evoked. The image series could be re-aligned by the free programs Fiji and ImageJ [Timpel2010], but commercial solutions obviously exist (for example Avizo or Amira, which is a commercial software that can process images but also provide professional visualization tools). Most of these programs provide an alignment method without landmarks and based on a cross-correlation approach. Since

FIB/SEM tomography does not involve any tilting of the sample, the shapes of internal details is not affected by a projection effect and from this simple point of view, one may expect that cross-correlation alignments should produce more precision in comparison with tilting tomography.

To illustrate these purposes, Figure 1.45 shows several images extracted from a series acquired in a FIB/SEM tomography experiment on a specimen of polyurethane matrix reinforced by nanowires of iron carbide (PU/Fe_3C). As it can easily be seen, these images suffer a lateral drift evidenced by the 'motion' of the upper deposition layer and the scratch lines over, used as references, from one image to the other.

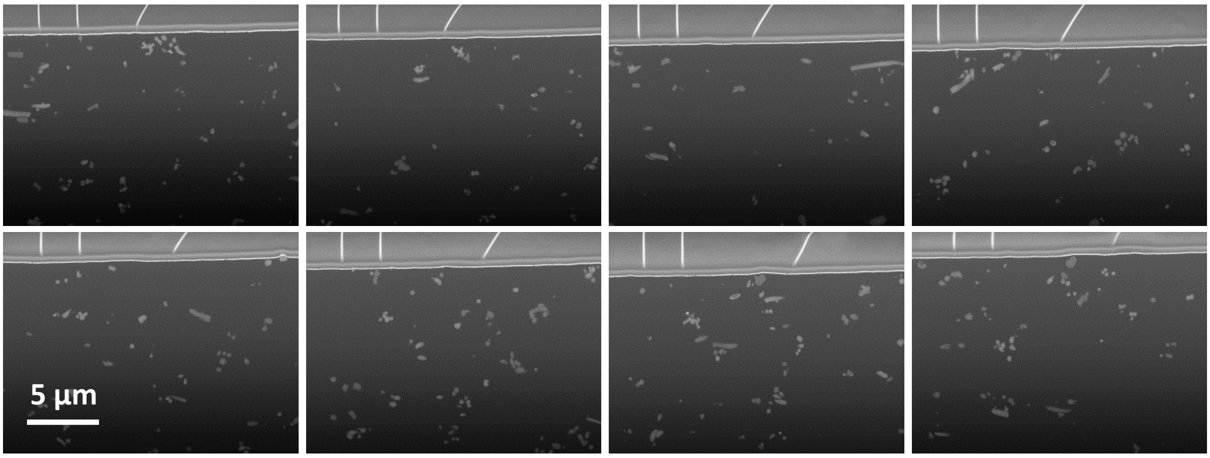

Figure 1.45: Original images extracted from a series obtained on a PNC. There are 50 images between every two neighbour images corresponding to nearly 35 minutes of experimental acquisition.

A re-alignment of these sections was performed with the Fiji software, and the resulting aligned images are reported in Figure 1.46. The black regions at the borders are the background generated by the alignment procedure: they have to be suppressed before the 3D visualisation (unavoidable cropping effect which reduces the field of view).

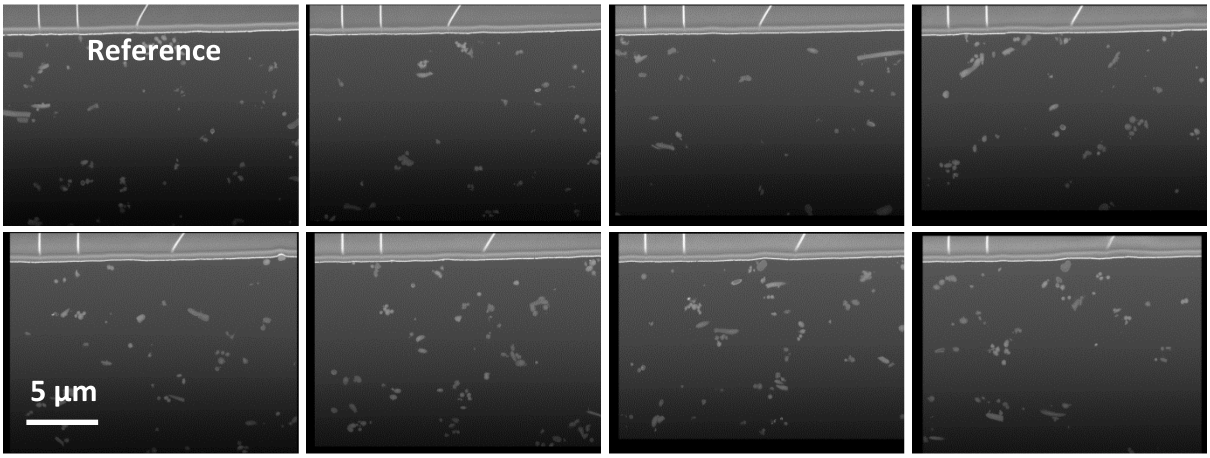

Figure 1.46: Same images as from Figure 1.45, when re-aligned with regard to the first one as reference (cross-correlation tool in Fiji).

Once the re-aligned stack is considered as correct, it may need to be segmented for the 3D visualization and quantification. This segmentation can be done using different strategies according to further desired treatments. Considering the case of the two-phase system PU/Fe_3C presented in Figure 1.45, the stack could easily be segmented as illustrated by the slice shown in Figure 1.47. The white objects are cut sections of Fe_3C nanowires, and all the black part that surrounds them is the polymer matrix.

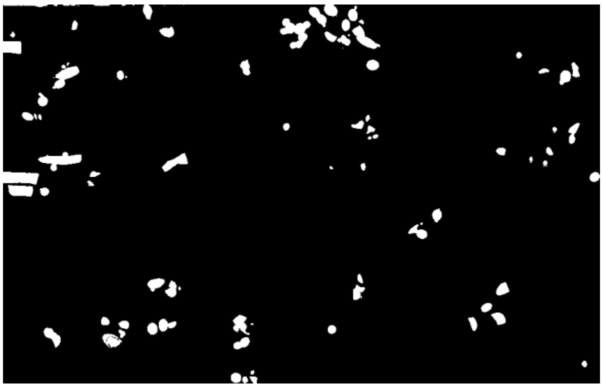

Figure 1.47: The segmented version of the first and also reference image of the series shown in Figure 1.45 (after cropping as produced by the re-alignment of the whole series).

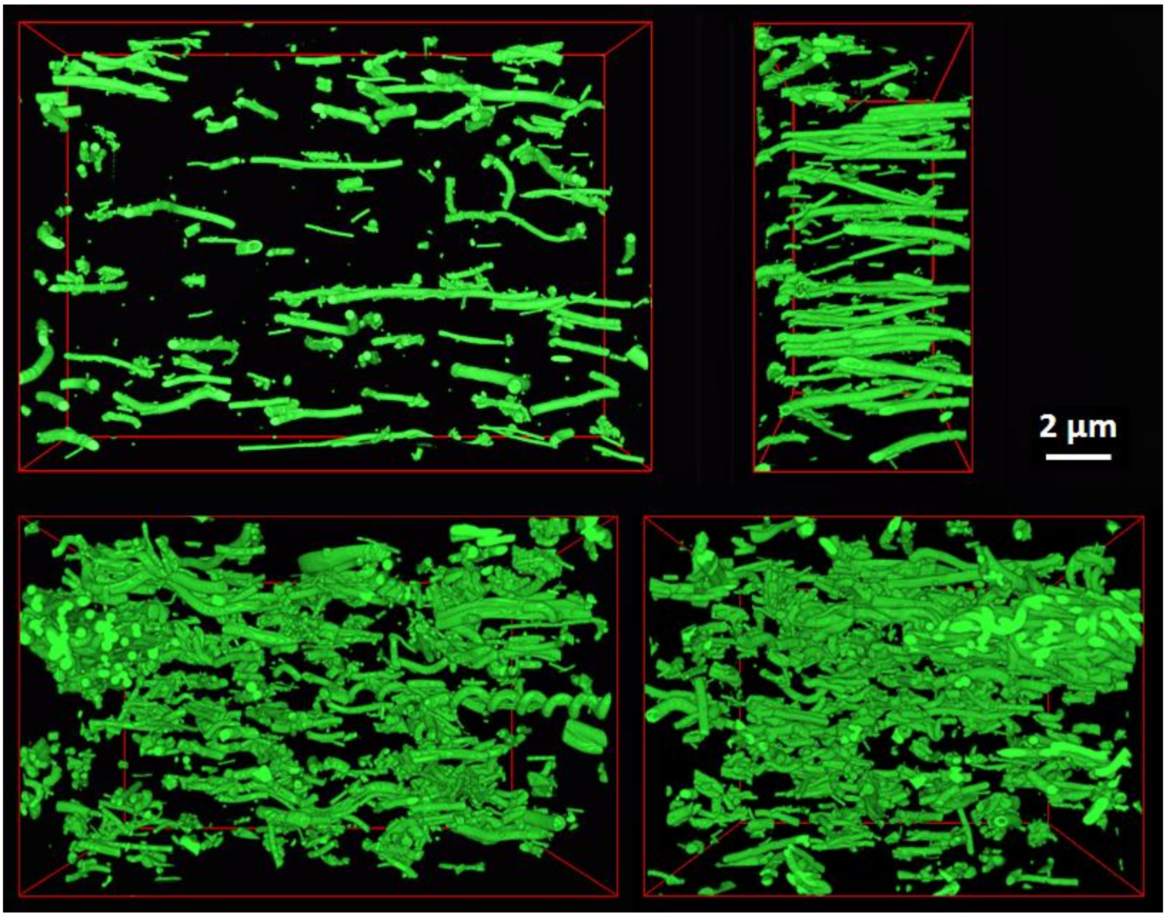

Figure 1.48: Surface rendering of the FIB reconstructed volumes from the PU-Fe3C 2.5 wt. % and 5 wt. % (respectively top and bottom rows) samples, projections on the left are front views, whereas projections on the right are side views. [Fiorido2013]

With the whole segmented stack of slices, the reconstructed volume could be visualized in 3D as shown in Figure 1.48. In this view, only the fillers can be seen since the grey level of the polymer matrix has been set to that of the black background. This system was studied in parallel to the main subjects treated in this thesis; in this particular case, the question was to estimate the quality of the dispersion of nanowires and quantify their volume fractions in two different materials. The values that could be measured form the reconstructed volumes indicate a significant difference (respectively about 1.21 % (2.5 wt. %) and 3.12 % (5 wt. %)).

Figure 1.49 illustrates another 'side-study'. A thin TiO_2 coating layer deposited onto a glass substrate contains silver nanoparticles that are in situ aligned under a controlled laser irradiation. A FIB/SEM 3D experiment was performed in order to confirm the alignment of the particles in 3D. The final stack of images was segmented into three levels: the white spheres are the silver nanoparticles which effectively show a clear alignment tendency, the grey flat layer is the TiO_2 film and the black background also including the glass substrate.

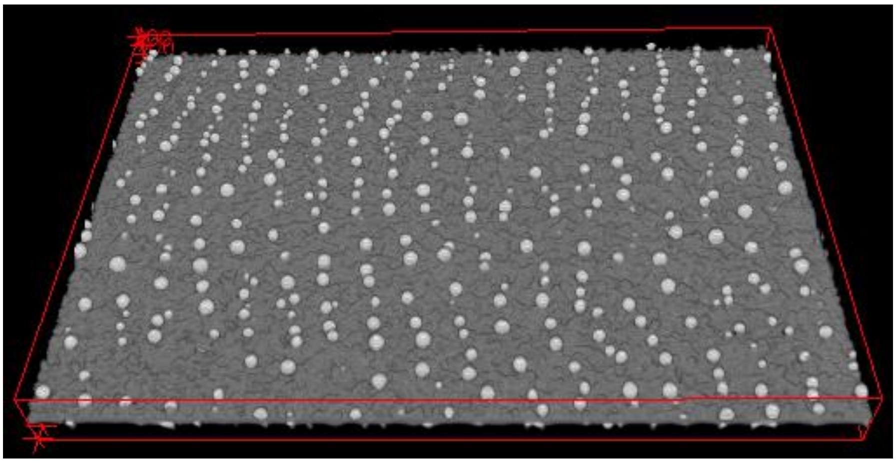

Figure 1.49: A reconstructed layer of TiO_2/Ag/glassy substrate sample.

1.3 General presentation of polymer nanocomposites

Polymer nanocomposites (PNCs) are formed by a polymer or copolymer matrix reinforced by a controlled dispersion of nano-fillers. These nano-fillers could be, for example, nanoparticles, nanotubes or nano-fibres (wires). No matter their overall shapes, they must have at least one dimension in the nanometre range to be considered as nano-fillers. As composite materials, PNCs belong to the multi-phase systems. The interest of these materials is that the physical and even chemical properties of the pure polymer matrix are significantly improved by the addition of nano-fillers, even when added in a little quantity [Bréchet2001].

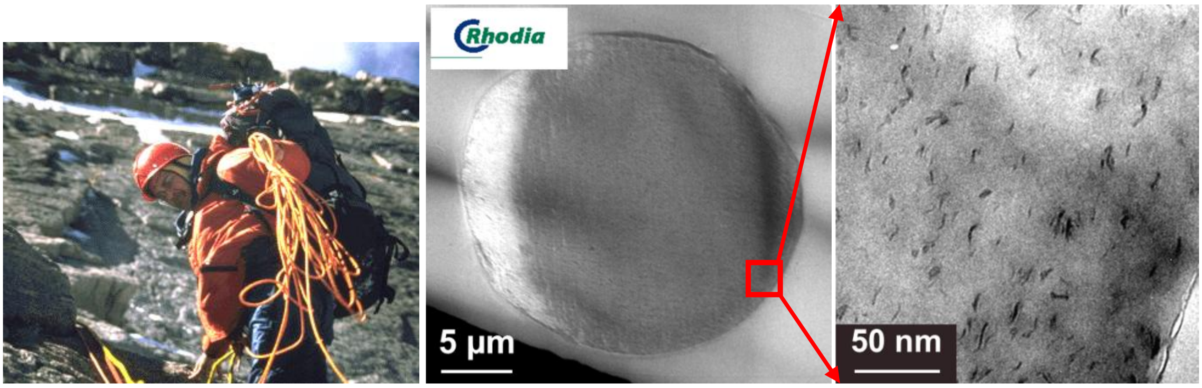

Figure 1.50: Nylon (polyamide PA6) strings, the mechanical properties of which are optimized by the addition of fillers (in the present case: montmorillonite lamellae as imaged in TEM) [Ibanes2004].

Figure 1.50 illustrates the example of nylon strings reinforced by some added mineral fillers. The mechanical performance is highly improved according to the tensile test results shown in Figure 1.51.

It also reveals that the nature of fillers is another controlling parameter, in addition to the volume fraction.

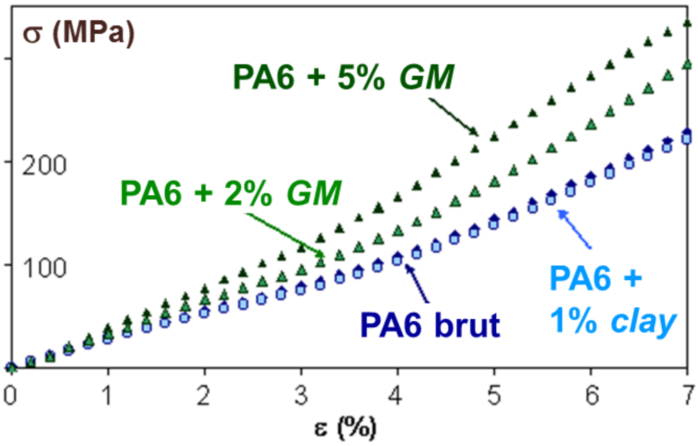

Figure 1.51: Increase in the Young's modulus of reinforced nylon as measured from tensile tests [Ibanes2004].

1.3.1 The shrinkage problem

A major issue concerning the tomography on polymer nanocomposites can be anticipated according to the already established evidences in the literature: it concerns the beam sensitivity of polymer-based materials under electron irradiation. As tilting electron tomography requires a large number of projections, the object will experience a long irradiation time, thus a high cumulative electron dose. This long exposure to the electron beam will easily damage the sample and then degrades the micro- or nanostructure, which will cause any 3D reconstruction meaningless [McEwen1995] [McEwen2002] [Hsieh2002] [Lucić2005]. The primary effects of the interaction of electrons with organic matter are inelastic scattering processes which produce an intense ionization and consequently break chemical bonds. This first level of damage causes secondary reactions, like the formation of free radicals and molecular fragments, and even chain scission, cross-linking, mass loss, heat generation and charge effects. It must also be stated that since polymers have generally a low glass transition temperature (T_g), they could also be damaged by the heat generated during the interaction between the incident electrons and the sample.

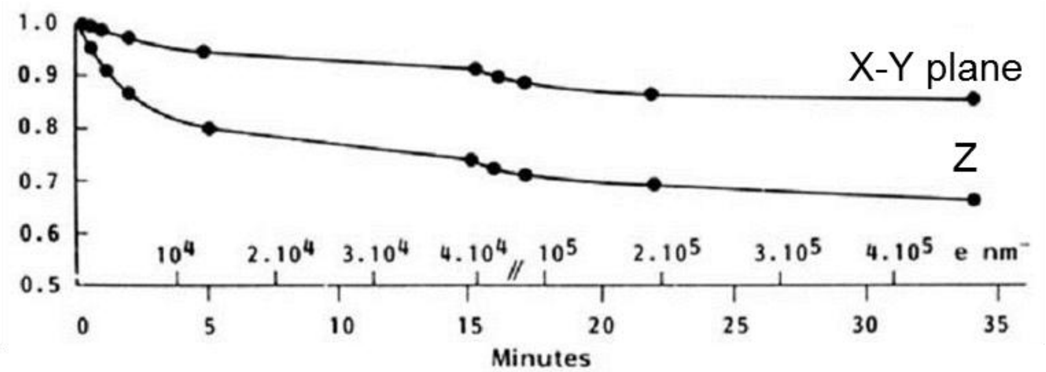

Figure 1.52: Measurement of shrinkage in three dimensions as a function of time with a certain electron dose in a soft polymer material [Luther2006].

All these effects may occur at various temperatures; the dominant effect is the mass loss experienced by the sample. It is always accompanied, or closely followed by a shrinkage of the sample (Figure 1.52). It has been demonstrated that the sensitivity of irradiation decreases while the carbon content increases in the polymeric samples.

As can be seen from Figure 1.52, there seems to be a saturation effect as the irradiation goes on. This means that from the point of view of the ‘stability’ of the microstructure, a 3D reconstruction is certainly possible. The question of the representativity of the reconstructed volume will be the important point.

A primary solution to prevent a dramatic shrinkage in tomography experiments is to reduce the experimental duration by increasing the tilt step or imaging speed and reducing the electron dose to minimize the damage. But this basic idea is generally not applicable in practice, because of a too poor signal-to-noise ratio according to the problem to be treated (especially in the case of nano-fillers in PNCs). It could decrease the resolution and contrast of the projections and eventually of the tomogram. In Figure 1.52, as the dose rate after 15 minutes is about 400 $e/nm^2/s$ compared to 50 $e/nm^2/s$ before, the sample shrinks more.

The beam damage can also be reduced by cooling the specimens to very low temperatures, as the liquid nitrogen (~ 98K) or liquid helium (~ 4K) temperatures [Iancu2006] [Bammes2010] in what can be called cryo-electron tomography (cryo-EM) [McEwen2002] [Bárcena2009]. Low temperatures protect the cooled specimens by slowing the irradiation effects and decreasing the magnitude and influence of the secondary chemical reactions. So this technique allows for imaging at higher electron doses with an improved resolution [Koster2006]. Van Marle et al. also found that there was more shrinkage for a sample cryo-cooled in the electron microscope than one cooled prior to insertion, this means that the microscopes vacuum may also play a role in the shrinkage.

Besides the two principal methods mentioned above, other considerations can be adopted to minimize the damage effects. Evaporated thin carbon films are often deposited on both sides of the specimen to improve the conductivity and reduce the drift [Jaffe1984]. The resistance to the electron dose is also improved despite of a loss of contrast. In addition, high electron accelerating voltages can decrease the inelastic scattering interactions. An improvement of 50% of the radiation resistance can be realized by changing the accelerating voltage from 100 kV to 200 kV, and this value could become six times better when going up to 1MV. Finally, the STEM imaging mode with automated methods to record tilt series in so-called ‘low-dose’ conditions can help [Aoyama2008].

From a very practical point of view, the shrinkage occurs early in the irradiation sequence, so the specimen can be pre-irradiated for a few minutes to produce a ‘controlled’ shrink and to arrive at a more stable configuration. In the case where the shrinkage level can be measured and corrected, reasonable measurements can be performed according to this strategy. However, there are numerous situations where is has no sense, especially if the shrinkage affects the parameter that is to be measured. We will see in the net two chapters that we did encounter the two different situations when (i) shrinkage correction could be performed post-mortem, and (ii) it produces a definitive modification of the nanostructure which could not be ‘de-convolved’ by any mean.

All the previous considerations refer to electron microscopy observations (SEM and TEM). Similar problems are expected under the ion beam in a FIB. Kim et al. have studied the FIB damage in polymer thin films, and the possible methods to limit this damage which is actually very significant [Kim2011].

References of chapter 1

[Adrien2007] Adrien J., Maire E., Gimenez N., and Sauvant-Moynot V. *Experimental study of the compression behaviour of syntactic foams by in situ X-ray tomography*. Acta Materialia (2007), vol.55, pp: 1667–1679.

[Andersen1984] Andersen A.H., and Kak A.C. *Simultaneous Algebraic Reconstruction Technique (SART): A superior implementation of the ART algorithm*. Ultrasonic Imaging (1984), vol.6, pp: 81–94.

[Angert2000] Angert I., Majorovits E., and Schröder R.R. *Zero-loss image formation and modified contrast transfer theory in EFTEM*. Ultramicroscopy (2000), vol.81, pp: 203–222.

[Aoyama2008] Aoyama K., Takagi T., Hirase A., and Miyazawa A. *STEM tomography for thick biological specimens*. Ultramicroscopy (2008), vol.109, pp: 70–80.

[Arslan2008] Arslan I., Marquis E.A., Homer M., Hekmaty M.A., and Bartelt N.C. *Towards better 3-D reconstructions by combining electron tomography and atom-probe tomography*. Ultramicroscopy (2008a), vol.108, pp: 1579–1585.

[Arslan2008] Arslan I., Walmsley J.C., Rytter E., Bergene E., and Midgley P.A. *Toward Three-Dimensional Nanoengineering of Heterogeneous Catalysts*. J. Am. Chem. Soc. (2008b), vol.130, pp: 5716–5719.

[Baldock2002] Baldock C., Gilpin C.J., Koster A.J., Ziese U., Kadler K.E., Kielty C.M., and Holmes D.F. *Three-dimensional reconstructions of extracellular matrix polymers using automated electron tomography*. Journal of Structural Biology (2002), vol.138, pp: 130–136.

[Bals2007] Bals S., Batenburg K.J., Verbeeck J., Sijbers J., and Van Tendeloo G. *Quantitative Three-Dimensional Reconstruction of Catalyst Particles for Bamboo-like Carbon Nanotubes*. Nano Lett. (2007), vol.7, pp: 3669–3674.

[Bammes2010] Bammes B.E., Jakana J., Schmid M.F., and Chiu W. *Radiation damage effects at four specimen temperatures from 4 to 100 K*. Journal of Structural Biology (2010), vol.169, pp: 331–341.

[Bangliang2000] Bangliang S., Yiheng Z., Lihui P., Danya Y., and Baofen Z. *The use of simultaneous iterative reconstruction technique for electrical capacitance tomography*. Chemical Engineering Journal (2000), vol.77, pp: 37–41.

[Bansal2006] Bansal R.K., Kubis A., Hull R., and Fitz-Gerald J.M. *High-resolution three-dimensional reconstruction: A combined scanning electron microscope and focused ion-beam approach*. Journal of Vacuum Science & Technology B: Microelectronics and Nanometer Structures (2006), vol.24, pp: 554.

[Bárcena2009] Bárcena M., and Koster A.J. *Electron tomography in life science*. Seminars in Cell & Developmental Biology (2009), vol.20, pp: 920–930.

[Baumeister1999] Baumeister W., Grimm R., and Walz J. *Electron tomography of molecules and cells*. Trends in Cell Biology (1999), vol.9, pp: 81–85.

[Benlekbir2009, thesis] Benlekbir S. *STEM-HAADF nanotomography : application to nanomaterials.* INSA de Lyon (2009). *http://theses.insa-lyon.fr/publication/2009ISAL0025*

[Benlekbir2009] Benlekbir S., and Epicier T. *STEM HAADF electron tomography of palladium nanoparticles with complex shapes*. Philosophical Magazine Letters (2009), vol.89, pp: 145–153.

[Bogner2005] Bogner A., Thollet G., Basset D., Jouneau P.-H., and Gauthier C. *Wet STEM: A new development in environmental SEM for imaging nano-objects included in a liquid phase*. Ultramicroscopy (2005), vol.104, pp: 290–301.

[Bogner2007] Bogner A., Jouneau P.-H., Thollet G., Basset D., and Gauthier C. *A history of scanning electron microscopy developments: Towards "wet-STEM" imaging*. Micron (2007), vol.38, pp: 390–401.

[Brandt2006] Brandt S.S. *Markerless Alignment in Electron Tomography.* In Electron Tomography, J. Frank, ed. (Springer New York, 2006), pp. 187–215.

[Bréchet2001] Bréchet Y., Cavaillé J.-Y., Chabert E., Chazeau L., Dendievel R., Flandin L., and Gauthier C. *Polymer Based Nanocomposites: Effect of Filler-Filler and Filler-Matrix Interactions*. Advanced Engineering Materials (2001), vol.3, pp: 571–577.

[Carazo2006] Carazo J.-M., Herman G.T., Sorzano C.O.S., and Marabini R. *Algorithms for Three-dimensional Reconstruction From the Imperfect Projection Data Provided by Electron Microscopy.* In Electron Tomography, J. Frank, ed. (Springer New York, 2006), pp. 217–243.

[Chuang2012] Chuang C.-C., Tsai J., Chen C.-M., Yu Z.-H., and Sun C.-W. *Convergence rate calculation of simultaneous iterative reconstruction technique algorithm for diffuse optical tomography image reconstruction: A feasibility study*. Optics Communications (2012), vol.285, pp: 2236–2241.

[Dalmas2007] Dalmas F., Cavaillé J.-Y., Gauthier C., Chazeau L., and Dendievel R. *Viscoelastic behavior and electrical properties of flexible nanofiber filled polymer nanocomposites. Influence of processing conditions*. Composites Science and Technology (2007), vol.67, pp: 829–839.

[Fernández2002] Fernández J.-J., Lawrence A.F., Roca J., García I., Ellisman M.H., and Carazo J.-M. *High-performance electron tomography of complex biological specimens*. Journal of Structural Biology (2002), vol.138, pp: 6–20.

[Fernández2008] Fernández J.-J., Gordon D., and Gordon R. *Efficient parallel implementation of iterative reconstruction algorithms for electron tomography*. Journal of Parallel and Distributed Computing (2008), vol.68, pp: 626–640.

[Fiorido2013] Fiorido T., Galineau J., Salles V., Seveyrat L., Belhora F., Cottinet P.-J., Hu L., Liu Y., Guiffard B., Brioude A., Epicier T., and Guyomar D. *Innovative organic/inorganic nanocomposites for actuators and magnetic sensors applications.* Advanced Functional Materials, *in progress*.

[Frangakis2006] Frangakis A.S., and Hegerl R. *Segmentation of Three-dimensional Electron Tomographic Images.* In Electron Tomography, J. Frank, ed. (Springer New York, 2006), pp. 353–370.

[Friedrich2005] Friedrich H., McCartney M.R., and Buseck P.R. *Comparison of intensity distributions in tomograms from BF TEM, ADF STEM, HAADF STEM, and calculated tilt series*. Ultramicroscopy (2005), vol.106, pp: 18–27.

[Gamo1996] Gamo K. *Nanofabrication by FIB*. Microelectronic Engineering (1996), vol.32, pp: 159–171.

[Giannuzzi1999] Giannuzzi L.A., and Stevie F.A. *A review of focused ion beam milling techniques for TEM specimen preparation*. Micron (1999), vol.30, pp: 197–204.

[Guckenberger1982] Guckenberger R. *Determination of a common origin in the micrographs of tilt series in three-dimensional electron microscopy*. Ultramicroscopy (1982), vol.9, pp: 167–173.

[Herman1993] Herman G.T., and Meyer L.B. *Algebraic reconstruction techniques can be made computationally efficient [positron emission tomography application]*. IEEE Transactions on Medical Imaging (1993), vol.12, pp: 600 –609.

[Herman1995] Herman G.T. *Image Reconstruction From Projections*. Real-Time Imaging (1995), vol.1, pp: 3–18.

[Hindson2011] Hindson J.C., Saghi Z., Hernandez-Garrido J.-C., Midgley P.A., and Greenham N.C. *Morphological study of nanoparticle-polymer solar cells using high-angle annular dark-field electron tomography*. Nano Lett. (2011), vol.11, pp: 904–909.

[Holzer2004] Holzer L., Indutnyi F., Gasser P.H., Münch B., and Wegmann M. *Three-dimensional analysis of porous BaTiO3 ceramics using FIB nanotomography*. J Microsc (2004), vol.216, pp: 84–95.

[Holzer2006] Holzer L., Muench B., Wegmann M., Gasser P., and Flatt R.J. *FIB-Nanotomography of Particulate Systems—Part I: Particle Shape and Topology of Interfaces*. Journal of the American Ceramic Society (2006), vol.89, pp: 2577–2585.

[Hsieh2002] Hsieh C.-E., Marko M., Frank J., and Mannella C.A. *Electron tomographic analysis of frozen-hydrated tissue sections*. Journal of Structural Biology (2002), vol.138, pp: 63–73.

[Hungría2009] Hungría A.B., Eder D., Windle A.H., and Midgley P.A. *Visualization of the three-dimensional microstructure of TiO2 nanotubes by electron tomography*. Catalysis Today (2009), vol.143, pp: 225–229.

[Iancu2006] Iancu C.V., Wright E.R., Heymann J.B., and Jensen G.J. *A comparison of liquid nitrogen and liquid helium as cryogens for electron cryotomography*. Journal of Structural Biology (2006), vol.153, pp: 231–240.

[Ibanes2004] Ibanes C., David L., De Boissieu M., Séguéla R., Epicier T., and Robert G. *Structure and mechanical behavior of nylon-6 fibers filled with organic and mineral nanoparticles. I. Microstructure of spun and drawn fibers*. Journal of Polymer Science Part B: Polymer Physics (2004), vol.42, pp: 3876–3892.

[Jaffe1984] Jaffe J.S., and Glaeser R.M. *Preparation of frozen-hydrated specimens for high resolution electron microscopy*. Ultramicroscopy (1984), vol.13, pp: 373–377.

[Jeanvoine2008] Jeanvoine N., Holzapfel C., Soldera F., and Mücklich F. *Microstructure Characterisation of Electrical Discharge Craters using FIB/SEM Dual Beam Techniques*. Advanced Engineering Materials (2008), vol.10, pp: 973–977.

[Jinnai2009] Jinnai H., and Spontak R.J. *Transmission electron microtomography in polymer research*. Polymer (2009), vol.50, pp: 1067–1087.

[Jornsanoh2008, thesis] Jornsanoh P. *Informations de volume en microscopie électronique à balayage : application à l'étude de la microstructure des matériaux et de son évolution sous traction.* INSA de Lyon (2008). http://theses.insa-lyon.fr/publication/2008ISAL0030

[Jornsanoh2011] Jornsanoh P., Thollet G., Ferreira J., Masenelli-Varlot K., Gauthier C., and Bogner A. *Electron tomography combining ESEM and STEM: A new 3D imaging technique*. Ultramicroscopy (2011), vol.111, pp: 1247–1254.

[Kaneko2005] Kaneko T., Nishioka H., Nishi T., and Jinnai H. *Reduction of anisotropic image resolution in transmission electron microtomography by use of quadrangular prism-shaped section*. J Electron Microsc (Tokyo) (2005), vol.54, pp: 437–444.

[Kano2002] Kano H., Jakobs S., Nagorni M., and Hell S.W. *Dual-color 4Pi-confocal microscopy with 3D-resolution in the 100 nm range*. Ultramicroscopy (2002), vol.90, pp: 207–213.

[Kato2007] Kato M., Ito T., Aoyama Y., Sawa K., Kaneko T., Kawase N., and Jinnai H. *Three-dimensional structural analysis of a block copolymer by scanning electron microscopy combined with a focused ion beam*. Journal of Polymer Science Part B: Polymer Physics (2007), vol.45, pp: 677–683.

[Kato2008] Kato M., Kawase N., Kaneko T., Toh S., Matsumura S., and Jinnai H. *Maximum diameter of the rod-shaped specimen for transmission electron microtomography without the "missing wedge."*Ultramicroscopy (2008), vol.108, pp: 221–229.

[Kawase2007] Kawase N., Kato M., Nishioka H., and Jinnai H. *Transmission electron microtomography without the "missing wedge" for quantitative structural analysis*. Ultramicroscopy (2007), vol.107, pp: 8–15.

[Kelly2007] Kelly T.F., and Miller M.K. *Invited Review Article: Atom probe tomography*. Review of Scientific Instruments (2007), vol.78, pp: 031101 –031101–031120.

[Kim2008] Kim H.S., Hwang S.O., Myung Y., Park J., Bae S.Y., and Ahn J.P. *Three-Dimensional Structure of Helical and Zigzagged Nanowires Using Electron Tomography*. Nano Lett. (2008), vol.8, pp: 551–557.

[Kim2011] Kim S., Jeong Park M., Balsara N.P., Liu G., and Minor A.M. *Minimization of focused ion beam damage in nanostructured polymer thin films*. Ultramicroscopy (2011), vol.111, pp: 191–199.

[Koning2009] Koning R.I., and Koster A.J. *Cryo-electron tomography in biology and medicine*. Annals of Anatomy - Anatomischer Anzeiger (2009), vol.191, pp: 427–445.

[Koster2000] Koster A.J., Ziese U., Verkleij A.J., Janssen A.H., and de Jong K.P. *Three-Dimensional Transmission Electron Microscopy: A Novel Imaging and Characterization Technique with Nanometer Scale Resolution for Materials Science*. J. Phys. Chem. B (2000), vol.104, pp: 9368–9370.

[Koster2006] Koster A.J., and Bárcena M. *Cryotomography: Low-dose Automated Tomography of Frozen-hydrated Specimens.* In Electron Tomography, J. Frank, ed. (Springer New York, 2006), pp. 113–161.

[Krueger1999] Krueger R. *Dual-column (FIB–SEM) wafer applications*. Micron (1999), vol.30, pp: 221–226.

[Kübel2005] Kübel C., Voigt A., Schoenmakers R., Otten M., Su D., Lee T.-C., Carlsson A., and Bradley J. *Recent advances in electron tomography: TEM and HAADF-STEM tomography for materials science and semiconductor applications*. Microsc. Microanal. (2005), vol.11, pp: 378–400.

[Lanzavecchia2005] Lanzavecchia S., Cantele F., Bellon P.L., Zampighi L., Kreman M., Wright E., and Zampighi G.A. *Conical tomography of freeze-fracture replicas: a method for the study of integral* *membrane proteins inserted in phospholipid bilayers*. Journal of Structural Biology (2005), vol.149, pp: 87–98.

[Leapman2004] Leapman R.., Kocsis E., Zhang G., Talbot T.., and Laquerriere P. *Three-dimensional distributions of elements in biological samples by energy-filtered electron tomography*. Ultramicroscopy (2004), vol.100, pp: 115–125.

[Li2006] Li J., Malis T., and Dionne S. *Recent advances in FIB–TEM specimen preparation techniques*. Materials Characterization (2006), vol.57, pp: 64–70.

[Liu2005] Liu J. *Scanning transmission electron microscopy and its application to the study of nanoparticles and nanoparticle systems*. J Electron Microsc (Tokyo) (2005), vol.54, pp: 251–278.

[Liu2012, EMC] Liu Y., Bogner-Van de Moortèle A., Epicier T., Sato K., and Konno T. *TEM and SEM tomography of polymer-based nanocomposites re-inforced by carbon nanotubes*. EMC 2012, Manchester (September 17-21, 2012), Vol. 2, PS 2.4, pp: 313-314.

[Loos2009a] Loos J., Sourty E., Lu K., Freitag B., Tang D., and Wall D. *Electron Tomography on Micrometer-Thick Specimens with Nanometer Resolution*. Nano Lett. (2009a), vol.9, pp: 1704–1708.

[Loos2009b] Loos J., Sourty E., Lu K., de With G., and v. Bavel S. *Imaging Polymer Systems with High-Angle Annular Dark Field Scanning Transmission Electron Microscopy (HAADF–STEM)*. Macromolecules (2009b), vol.42, pp: 2581–2586.

[Lu2010] Lu K., Sourty E., Guerra R., Bar G., and Loos J. *Critical Comparison of Volume Data Obtained by Different Electron Tomography Techniques*. Macromolecules (2010), vol.43, pp: 1444–1448.

[Lucić2005] Lucić V., Förster F., and Baumeister W. *Structural studies by electron tomography: from cells to molecules*. Annu. Rev. Biochem. (2005), vol.74, pp: 833–865.

[Lück2010] Lück S., Sailer M., Schmidt V., and Walther P. *Three-dimensional analysis of intermediate filament networks using SEM tomography*. J Microsc (2010), vol.239, pp: 1–16.

[Luther2006] Luther P.K. *Sample Shrinkage and Radiation Damage of Plastic Sections.* In Electron Tomography, J. Frank, ed. (Springer New York, 2006), pp. 17–48.

[Maire2001] Maire E., Buffière J.Y., Salvo L., Blandin J.J., Ludwig W., and Létang J.M. *On the Application of X-ray Microtomography in the Field of Materials Science*. Advanced Engineering Materials (2001), vol.3, pp: 539–546.

[Maire2007] Maire E., Colombo P., Adrien J., Babout L., and Biasetto L. *Characterization of the morphology of cellular ceramics by 3D image processing of X-ray tomography*. Journal of the European Ceramic Society (2007), vol.27, pp: 1973–1981.

[Marabini1997] Marabini R., Rietzel E., Schroeder R., Herman G.T., and Carazo J.M. *Three-Dimensional Reconstruction from Reduced Sets of Very Noisy Images Acquired Following a Single-Axis Tilt Schema: Application of a New Three-Dimensional Reconstruction Algorithm and Objective Comparison with Weighted Backprojection*. Journal of Structural Biology (1997), vol.120, pp: 363–371.

[Mastronarde2006] Mastronarde D.N. *Fiducial Marker and Hybrid Alignment Methods for Single- and Double-axis Tomography.* In Electron Tomography, J. Frank, ed. (Springer New York, 2006), pp. 163–185.

[McEwen1995] McEwen B.F., Downing K.H., and Glaeser R.M. *The relevance of dose-fractionation in tomography of radiation-sensitive specimens*. Ultramicroscopy (1995), vol.60, pp: 357–373.

[McEwen2002] McEwen B.F., Marko M., Hsieh C.-E., and Mannella C. *Use of frozen-hydrated axonemes to assess imaging parameters and resolution limits in cryoelectron tomography*. Journal of Structural Biology (2002), vol.138, pp: 47–57.

[Menard2011] Menard L.D., and Ramsey J.M. *Fabrication of Sub-5 nm Nanochannels in Insulating Substrates Using Focused Ion Beam Milling*. Nano Lett. (2011), vol.11, pp: 512–517.

[Merli2003] Merli P.., Morandi V., and Corticelli F. *Backscattered electron imaging and scanning transmission electron microscopy imaging of multi-layers*. Ultramicroscopy (2003), vol.94, pp: 89–98.

[Messaoudi2007] Messaoudi C., Boudier T., Sorzano C.O.S., and Marco S. *TomoJ: tomography software for three-dimensional reconstruction in transmission electron microscopy*. BMC Bioinformatics (2007), vol.8, pp: 288.

[Midgley2003] Midgley P.A., and Weyland M. *3D electron microscopy in the physical sciences: the development of Z-contrast and EFTEM tomography*. Ultramicroscopy (2003), vol.96, pp: 413–431.

[Miller2005] Miller M.K. *Atom Probe Tomography.* In Handbook of Microscopy for Nanotechnology, N. Yao, and Z.L. Wang, eds. (Springer US, 2005), pp. 227–246.

[Ortalan2009] Ortalan V., Herrera M., Morgan D.G., and Browning N.D. *Application of image processing to STEM tomography of low-contrast materials*. Ultramicroscopy (2009), vol.110, pp: 67–81.

[Ostadi2010] Ostadi H., Rama P., Liu Y., Chen R., Zhang X.X., and Jiang K. *3D reconstruction of a gas diffusion layer and a microporous layer*. Journal of Membrane Science (2010), vol.351, pp: 69–74.

[Penczek1995] Penczek P., Marko M., Buttle K., and Frank J. *Double-tilt electron tomography*. Ultramicroscopy (1995), vol.60, pp: 393–410.

[Radermacher2006] Radermacher M. *Weighted Back-projection Methods.* In Electron Tomography, J. Frank, ed. (Springer New York, 2006), pp. 245–273.

[Rau2007] Rau C., Crecea V., Liu W., Richter C.-P., Peterson K.M., Jemian P.R., Neuhäusler U., Schneider G., Yu X., Braun P.V., et al. *Synchrotron-based imaging and tomography with hard X-rays*. Nuclear Instruments and Methods in Physics Research Section B: Beam Interactions with Materials and Atoms (2007), vol.261, pp: 850–854.

[Rubanov2004] Rubanov S., and Munroe P.. *The application of FIB milling for specimen preparation from crystalline germanium*. Micron (2004), vol.35, pp: 549–556.

[Salvo2003] Salvo L., Cloetens P., Maire E., Zabler S., Blandin J.., Buffière J.., Ludwig W., Boller E., Bellet D., and Josserond C. *X-ray micro-tomography an attractive characterisation technique in materials science*. Nuclear Instruments and Methods in Physics Research Section B: Beam Interactions with Materials and Atoms (2003), vol.200, pp: 273–286.

[Sandberg2003] Sandberg K., Mastronarde D.N., and Beylkin G. *A fast reconstruction algorithm for electron microscope tomography*. Journal of Structural Biology (2003), vol.144, pp: 61–72.

[Schneider2011] Schneider P., Meier M., Wepf R., and Müller R. *Serial FIB/SEM imaging for quantitative 3D assessment of the osteocyte lacuno-canalicular network*. Bone (2011), vol.49, pp: 304–311.

[Sinha Ray2010] Sinha Ray S. *A new possibility for microstructural investigation of clay-based polymer nanocomposite by focused ion beam tomography*. Polymer (2010), vol.51, pp: 3966–3970.

[Sorzano2009] Sorzano C.O.S., Messaoudi C., Eibauer M., Bilbao-Castro J.R., Hegerl R., Nickell S., Marco S., and Carazo J.M. *Marker-free image registration of electron tomography tilt-series*. BMC Bioinformatics (2009), vol.10, pp: 124.

[Sueda2010] Sueda S., Yoshida K., and Tanaka N. *Quantification of metallic nanoparticle morphology on TiO2 using HAADF-STEM tomography*. Ultramicroscopy (2010), vol.110, pp: 1120–1127.

[Talbot1996] Talbot C.G. *A new application-specific FIB system architecture*. Microelectronic Engineering (1996), vol.30, pp: 597–602.

[Tan2011] Tan J.P.Y., Tan H.R., Boothroyd C., Foo Y.L., He C.B., and Lin M. *Three-Dimensional Structure of CeO2 Nanocrystals*. J. Phys. Chem. C (2011), vol.115, pp: 3544–3551.

[Thomas1994] Thomas D., Schultz P., Steven A.C., and Wall J.S. *Mass analysis of biological macromolecular complexes by STEM*. Biol. Cell (1994), vol.80, pp: 181–192.

[Timpel2010] Timpel M., Wanderka N., Murty B.S., and Banhart J. *Three-dimensional visualization of the microstructure development of Sr-modified Al–15Si casting alloy using FIB-EsB tomography*. Acta Materialia (2010), vol.58, pp: 6600–6608.

[Utsunomiya2003] Utsunomiya S., and Ewing R.C. *Application of high-angle annular dark field scanning transmission electron microscopy, scanning transmission electron microscopy-energy dispersive X-ray spectrometry, and energy-filtered transmission electron microscopy to the characterization of nanoparticles in the environment*. Environ. Sci. Technol. (2003), vol.37, pp: 786–791.

[Wan2011] Wan X., Zhang F., Chu Q., Zhang K., Sun F., Yuan B., and Liu Z. *Three-dimensional reconstruction using an adaptive simultaneous algebraic reconstruction technique in electron tomography*. Journal of Structural Biology (2011), vol.175, pp: 277–287.

[Ward2007] Ward E.P.W., Yates T.J.V., Fernández J.-J., Vaughan D.E.W., and Midgley P.A. *Three-Dimensional Nanoparticle Distribution and Local Curvature of Heterogeneous Catalysts Revealed by Electron Tomography*. J. Phys. Chem. C (2007), vol.111, pp: 11501–11505.

[Weyland2002] Weyland M. *Electron Tomography of Catalysts*. Topics in Catalysis (2002), vol.21, pp: 175–183.

[Weyland2004] Weyland M., and Midgley P.A. *Electron tomography*. Materials Today (2004), vol.7, pp: 32–40.

[Weyland2006] Weyland M., Yates T.J.V., Dunin-Borkowski R.E., Laffont L., and Midgley P.A. *Nanoscale analysis of three-dimensional structures by electron tomography*. Scripta Materialia (2006), vol.55, pp: 29–33.

[Woodward2010] Woodward J.D., and Sewell B.T. *Tomography of asymmetric bulk specimens imaged by scanning electron microscopy*. Ultramicroscopy (2010), vol.110, pp: 170–175.

[Xu2010a] Xu F., Xu W., Jones M., Keszthelyi B., Sedat J., Agard D., and Mueller K. *On the efficiency of iterative ordered subset reconstruction algorithms for acceleration on GPUs*. Computer Methods and Programs in Biomedicine (2010a), vol.98, pp: 261–270.

[Xu2010b] Xu W., Xu F., Jones M., Keszthelyi B., Sedat J., Agard D., and Mueller K. *High-performance iterative electron tomography reconstruction with long-object compensation using graphics processing units (GPUs)*. Journal of Structural Biology (2010b), vol.171, pp: 142–153.

[Yaguchi2008] Yaguchi T., Konno M., Kamino T., and Watanabe M. *Observation of three-dimensional elemental distributions of a Si device using a 360°-tilt FIB and the cold field-emission STEM system*. Ultramicroscopy (2008), vol.108, pp: 1603–1615.

[Yakushevska2007] Yakushevska A.E., Lebbink M.N., Geerts W.J.C., Spek L., van Donselaar E.G., Jansen K.A., Humbel B.M., Post J.A., Verkleij A.J., and Koster A.J. *STEM tomography in cell biology*. Journal of Structural Biology (2007), vol.159, pp: 381–391.

[Zampighi2005] Zampighi G.A., Zampighi L., Fain N., Wright E.M., Cantele F., and Lanzavecchia S. *Conical tomography II: A method for the study of cellular organelles in thin sections*. Journal of Structural Biology (2005), vol.151, pp: 263–274.

[Zhang2012, thesis] Zhang T. *Imagerie multi-résolution par tomographie aux rayons X : application à la tomographie locale en science de matériaux.* Institut National Polytechnique de Grenoble - INPG, *not yet public on-line*.

2 Nanocomposites P(BuA-*stat*-S)/MWNTs

2.1 Presentation of the system

2.1.1 Motivation of the study

One specific system which has been recently studied in the laboratory concerns the reinforcement of a copolymer matrix with multiwall carbon nanotubes (MWCNTs) [Dalmas2005]. As will be seen below, different elaboration routes were employed, leading to different results in terms of mechanical and electrical properties. We have undertaken a 3D analysis of such materials in order to get more information about the interactions of the MWNTs. We have mainly focused our approach on two aspects: firstly, trying all possible tomography techniques in order to get the most reliable 3D reconstructions; secondly, quantifying the fraction of contacts between MWNTs in order to correlate the 3D microstructure with the electrical conduction, which was expected to be improved compared to the pure copolymer matrix.

In the research group PVMH (*Polymères, Verres et Matériaux Hétérogènes*) of laboratory MATEIS, there is already an available system of polymer nanocomposites that interests us and could be a good candidate to electron tomography: this system was elaborated by Florent Dalmas and his supervisors in the frame of his work as PhD student in PVMH. By adding carbon nanotubes they intended to reinforce the mechanical resistance and electrical conductivity of the copolymer matrix.

2.1.2 Elaboration of the material

We summarize here the main features regarding the elaboration route of the system that we have studied, namely an amorphous statistical copolymer poly (styrene-*co*-butyl acrylate) matrix reinforced by multi-walled carbon nanotubes as fillers, designated hereafter as P(BuA-*stat*-S)/MWNTs.

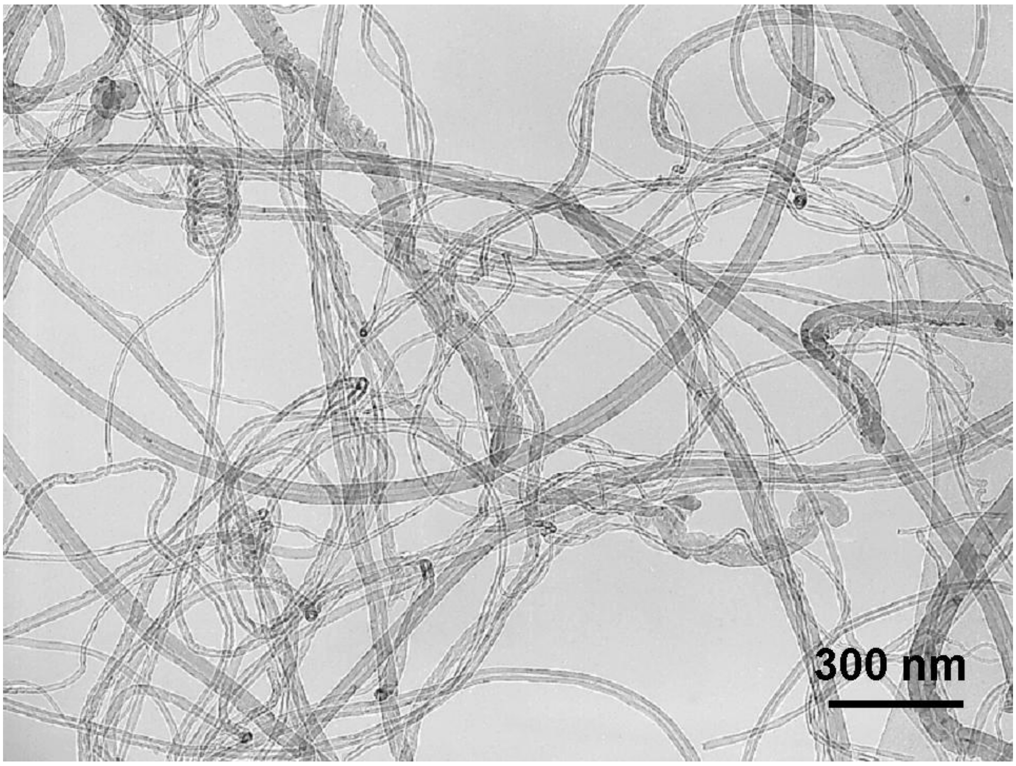

Figure 2.1: TEM observation of multi-walled carbon nanotubes after purification in nitric acid. [Dalmas2005]

Firstly, the Multi-Walled Carbon Nano-Tubes were fabricated by *Institut de Physique de la Matière Complexe* (IPMC) of *Ecole Polytechnique Fédérale de Lausanne* (EPFL). They are compounded from the catalytic decomposition of acetylene at 720 °C on supported cobalt/iron catalyst [Couteau2003]. Afterwards different sonication, filtering and washing steps were performed in order to obtain purified MWNTs without any metallic catalysts, as shown in Figure 2.1. This micrograph exhibits long and entangled MWNTs (mean length around 8 µm). Their diameter distribution is estimated by analysing TEM images to be between 8 nm and 105 nm with a mean value around 32 nm. Such sizes indicate the multiwall nature of these nanotubes [Dalmas2007] [Dalmas2005, thesis].

In order to be prepared for the composite processing, the purified nanotubes were dispersed in a distilled water solution of 1.2 g L^{-1} sodium dodecyl benzene sulfonate (SDBS: $C_{18}H_{29}SO_3Na$) surfactant; the quality of the dispersion was attested by analyses in environmental scanning electron microscopy (ESEM) using a home-made device which allows the observation of aqueous latex in low-voltage STEM [Bogner2005] [Bogner2007].

In the meanwhile, the latex of polymer matrix was prepared by the emulsion copolymerization of styrene (35 wt. %) and butyl acrylate (65 wt. %) at the *Laboratoire de Chimie et Procédés de Polymérisation* (LCPP) of *École Supérieure de Chimie Physique Électronique Lyon* (CPE) according to a detailed procedure given in [Dalmas2005]: basically, an anionic [$C_{12}H_{25}O(CH_2CH_2O)_4SO_3Na$] and a non-ionic [$C_{12}H_{25}O(CH_2CH_2O)_{19}H$] surfactant mixture of a micellar aqueous solution provided the environment for the polymerization. Then a surfactant-stabilized poly(styrene-co-butyl acrylate) suspension, P(BuA-*stat*-S), was obtained containing 43 wt. % spherical polymer particles with an average diameter of (145 ± 11) nm.

To finally process the composite, two methods were applied:
(1) The so-called evaporated films or **E materials** were produced by drying the mixture in an aluminium mold with a Teflon coating sealed in a vacuum drying oven at 35 °C. During five days, the water evaporated slowly to form the film (i.e. polymer particles coalescence);
(2) The suspension mixture was freeze-dried to sublimate water and obtain a compact soft powder after 45 minutes thermal stabilisation. Then the film-forming was done by pressing the prepared powder at 100 °C for 5 minutes under 1 MPa. This second type of nanocomposites was referred as **FP** (freeze-dried and pressed) **materials**.

2.1.3 Physical characterizations of the P(BuA-*stat*-S)/MWNTs E and FP nanocomposites

Several measurements were performed in order to characterize both types of materials. At first, DSC has shown the influence of the fillers content and the elaboration route on the P(BuA-*stat*-S) matrix's glass transition temperature (T_g): the FP materials exhibited a T_g equal to 262 K lower than that for E materials (266 K), which was attributed to a difference in the spatial distribution of surfactants that was known for deucing the polymer T_g.

Then, DMA measurements were done to reveal the elastic behaviour and the mechanical reinforcement induced by the fillers as illustrated in Figure 2.2. It can further be noted that E materials are slightly more efficiently reinforced than FP ones. It was suggested that this difference in the mechanical behaviour is related to the fraction and the quality of MWNTs contacts and entanglements [Dalmas2007].

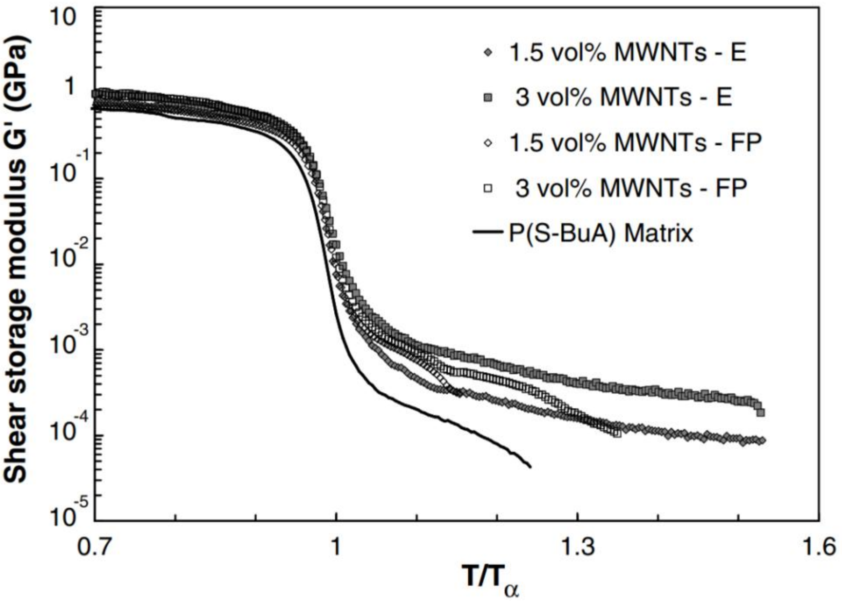

Figure 2.2: Storage shear modulus G' as a function of normalized temperature for the pure P(BuA-*stat*-S) matrix and composites filled with MWNTs, T/T_α is referred to T_g. [Dalmas2007]

Finally, electrical conductivity measurements as reported in Figure 2.3 indicate that E materials are always more conductive than FP ones whatever the fillers volume fraction between 0.2 % and 3 %.

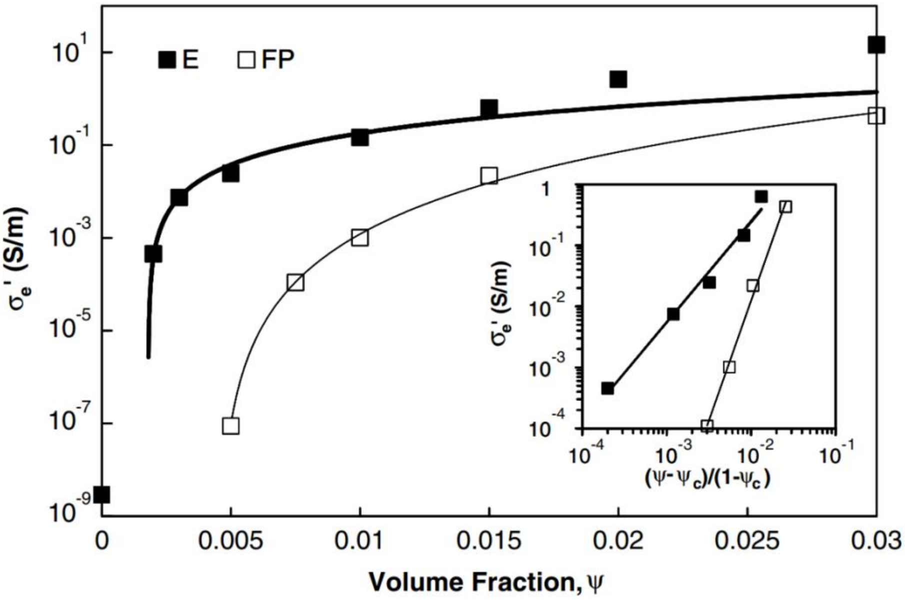

Figure 2.3: Real part of the AC electrical conductivity at 1 Hz for different nanotubes contents in E materials and FP materials, in comparison with predictions of statistical percolation theory (solid lines). [Dalmas2007]

Those measurements shown in Figure 2.2 and in Figure 2.3 indicate differences in the fillers distribution and interactions between both E and FP materials as schematically shown in Figure 2.4.

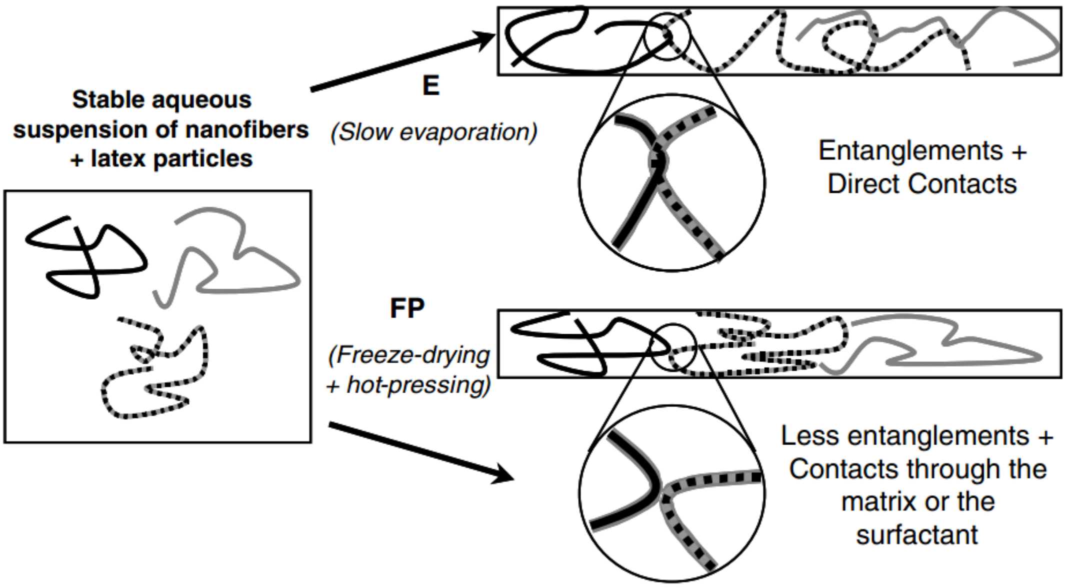

Figure 2.4: The possible influence of processing conditions on entanglements and contacts generations. [Dalmas2007]

In the slow evaporation 'E' process, the rearrangement of the nano-fillers leads to a completely relaxed structure in which entanglement contacts are created between well-dispersed long and flexible carbon nanotubes. In the opposite way, the FP process first froze the filler particles in the polymer suspension and then hot-pressed the mixed powder. In this mixture, the rearrangement of nano-fillers was strongly limited. So the tubes remain mainly isolated from each other with only possible simple contacts between them. Furthermore, several theoretical studies demonstrate that simple contacts between nanotubes through the matrix and the surfactant, such as suspected in the FP materials, are poorly conductive resulting in a weaker electrical efficiency. In addition, the possible presence of surfactant at the filler-filler interfaces decreases the electrical conductivity independently of the volume fraction of fillers which obviously also control this property according to the percolation theory.

In our work, we aimed at providing quantitative 3D information for a better understanding of the differences between the 2 processed materials. To facilitate their comparison, we choose the same volume fraction of fillers for both, i.e. 3 % of MWNTs. As we have presented in chapter 1.2, we can access to different microscopes where different tomography approaches can be undertaken. It is indeed interesting to apply all techniques to this subject, because imaging carbon nanotubes in, essentially, a carbon-based polymer matrix is a challenge in terms of resolution, contrast and absence of damage. We have thus performed various electron tomography experiments on the 2 kinds of materials.

2.2 TEM tomography results

2.2.1 STEM-HAADF, 200kV, JEOL 2010F

STEM-HAADF tomography was developed on the JEOL 2010F microscope available at CLYM during a recent thesis in the MATEIS laboratory [Benlekbir2009, thesis]. According to the need for a good resolution and contrast in order to image properly the MWNTs, we decided to start our experiments on this instrument. Furthermore, it was already stated that STEM-HAADF imaging is not sensitive to diffraction effects, which might be an advantage to suppress the strong diffraction contrast of

MWNTs seen edge-on in the thin foils, as can be seen in Figure 2.5. The comparison of conventional TEM-BF and STEM-HAADF images shows moreover that the matrix contrast is slightly smoother in the HAADF image, which may help in terms of noise during the 3D reconstruction.

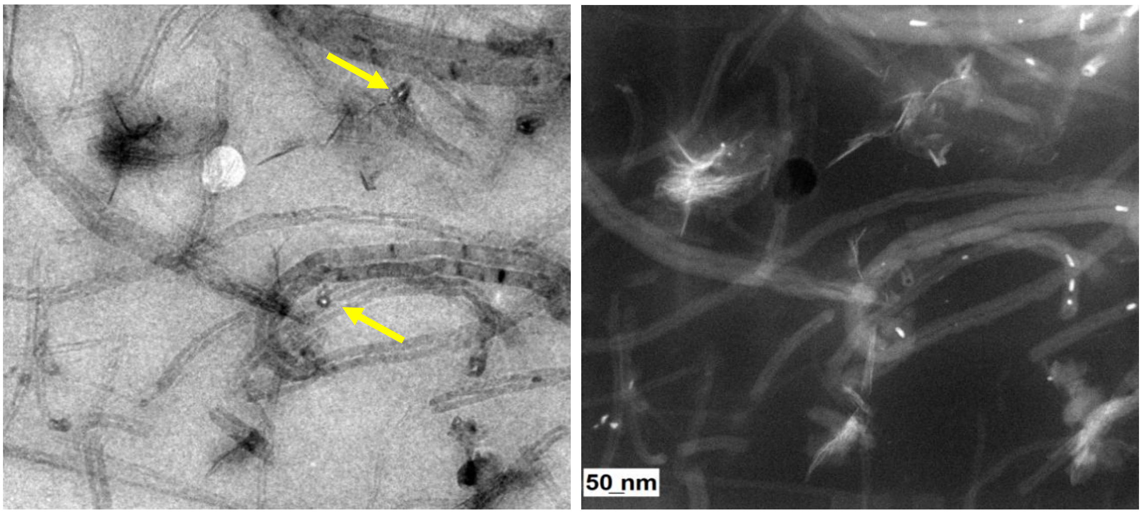

Figure 2.5: Microstructure of the evaporated P(BuA-*stat*-S)/MWNTs sample as imaged at 200 kV in CTEM (left) and HAADF-STEM (right). Note that strong contrast arises from the edge-on MWNTs in the CTEM image (arrows).

As for all the tomography experiments carried out on this system, adequate thin foils for TEM were prepared by cryo-ultramicrotomy performed at CTµ (*Centre Technologique des Microstructures, University of Lyon 1*). Sections of about 200 nm thick were collected on classical TEM copper grids covered by a thin and electron-transparent carbon film as in Figure 2.6.

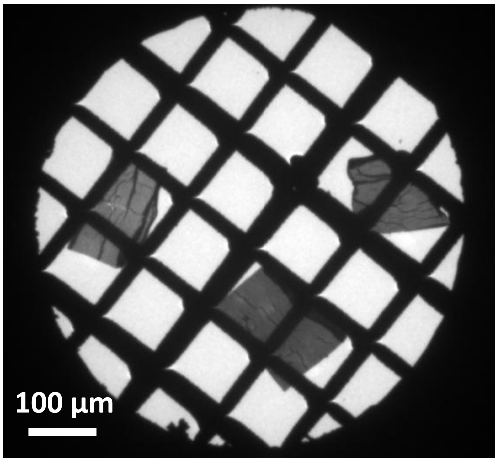

Figure 2.6: Low magnification image of the P(BuA-*stat*-S)/MWNTs sections prepared by cryo-ultramicrotomy, viewed in the bright field (BF) mode (TEM JEOL 2010F of CLYM-Lyon).

2.2.1.1 Images series and related tomograms

The home-made specimen holder which was developed at MATEIS for tomography in the TEM JEOL 2010F has already been shown in sub-sections 1.1.2.1 and 1.2.1.3 [Benlekbir2009, thesis]. It was used to obtain all tomographic series, as the one illustrated in Figure 2.7.

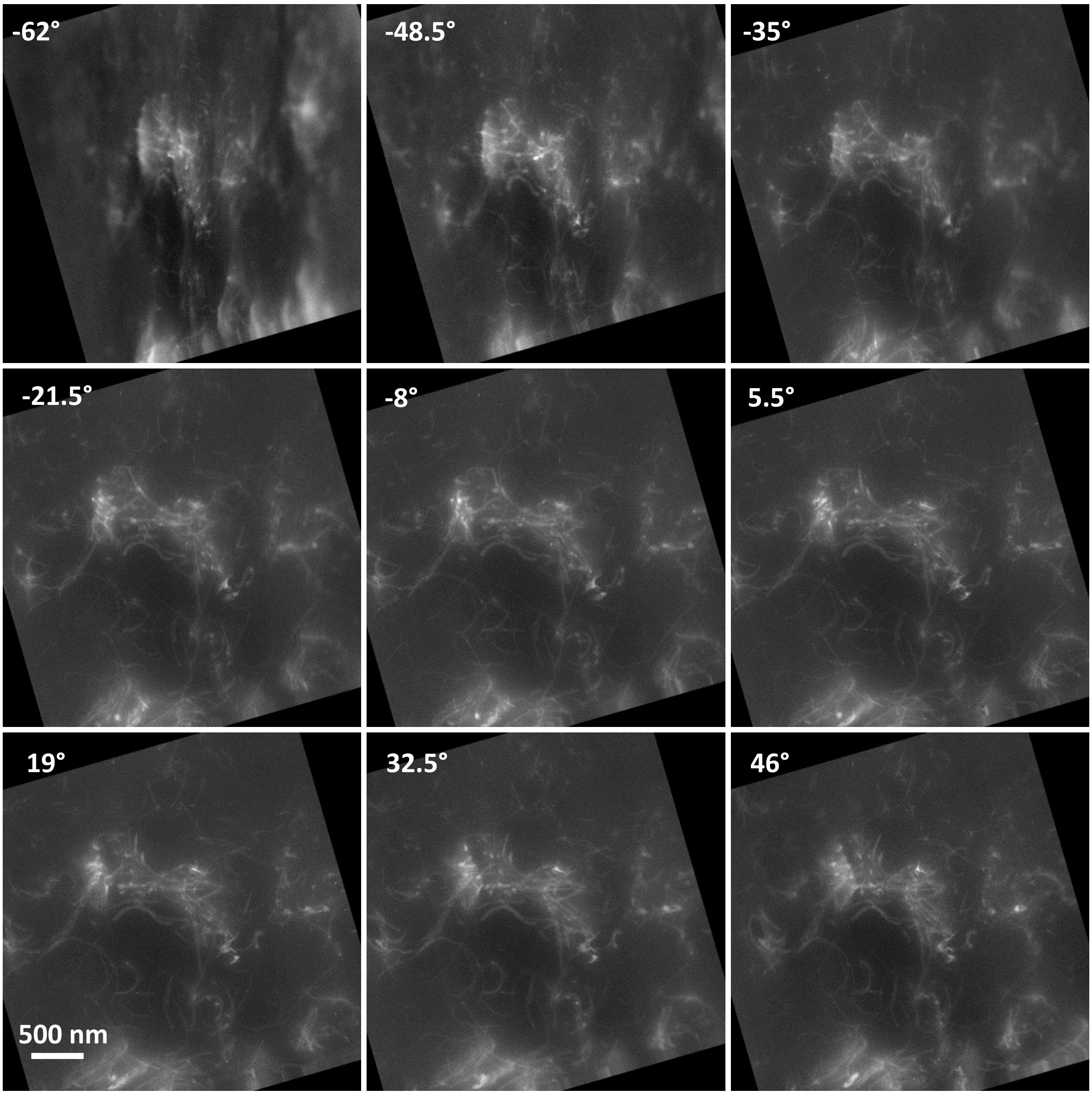

Figure 2.7: Images from an aligned projection series obtained in the STEM-HAADF imaging mode.

This original series of images was acquired from - 62° to 55° with a tilting increment of 1.5°. The contrast was normalized to the whole aligned series, and it appears good enough to allow the CNTs to be clearly distinguished from the polymer matrix; the very bright white points are the metal catalyst particles. On these micrographs recorded at a relatively low magnification, it is not easy to resolve the walls of CNTs, but as stated in 2.1, the important point to be studied in this material is the quantification of contacts between the nanotubes. So, the volume, then the magnification, was adjusted to have as many fillers as possible in the field of view, which leads to an obvious compromise between contrast and resolution.

The images were aligned and reconstructed by the SIRT algorithm in Digital Micrograph. The photo shown in Figure 2.8 is a rendering of the related tomogram, where white objects are mostly the reconstructed CNTs; due to threshold difficulties, some catalyst particles and noise are also present in the reconstruction.

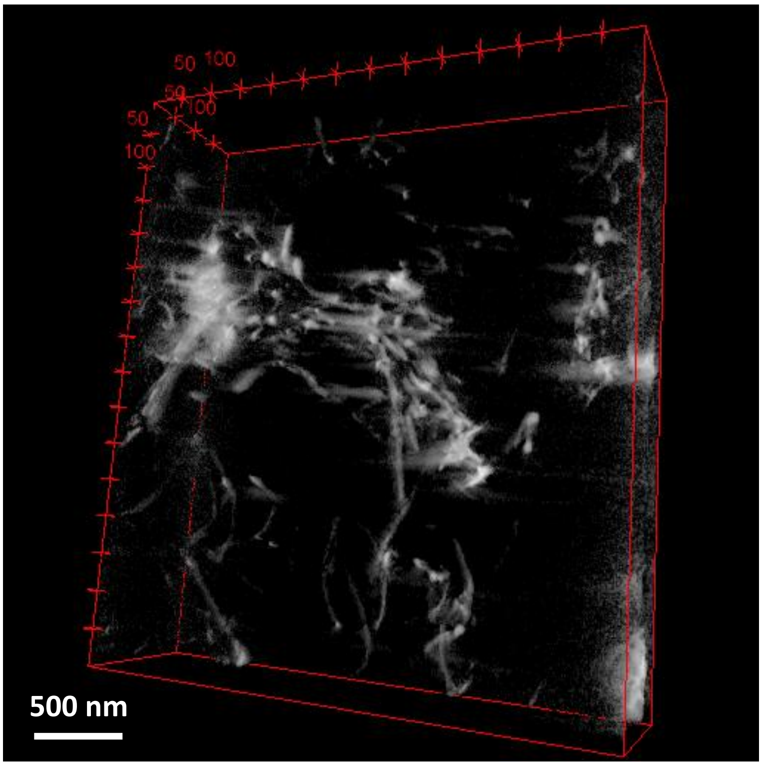

Figure 2.8: Volume rendering of the tomogram reconstructed from the image series shown in Figure 2.7 (GPU SIRT algorithm in Digital Micrograph and visualization with '3D Viewer' in Fiji).

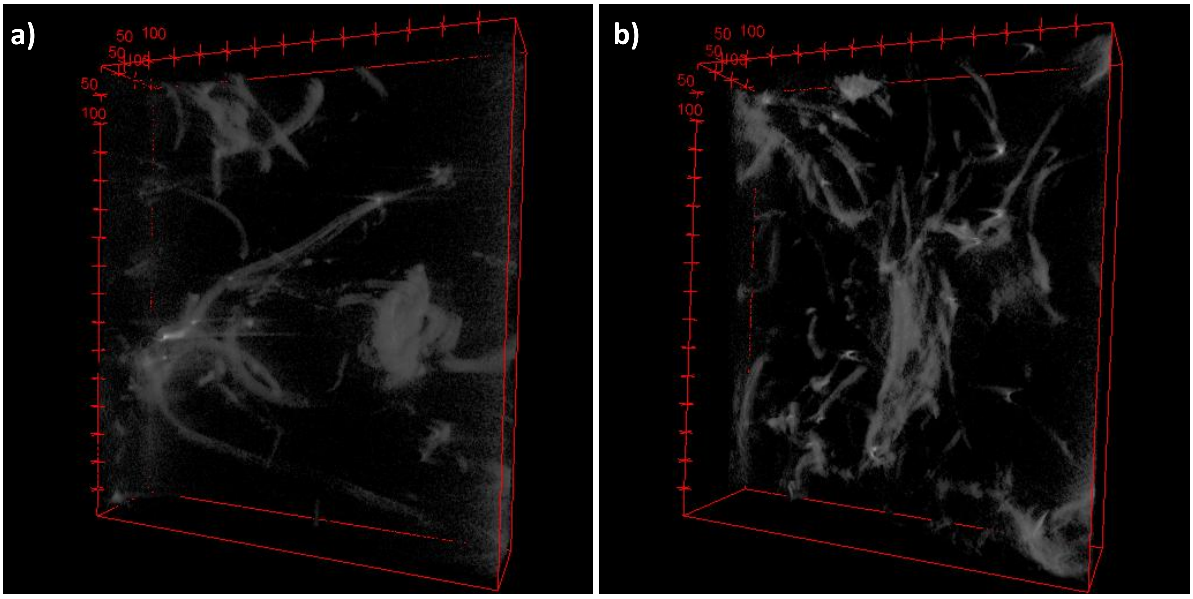

Figure 2.9: Volume rendering of other tomograms obtained from STEM-HAADF experiences in the JEOL 2010F TEM.

Some other projection series have also been acquired: Figure 2.9 a) concerns a reconstructed volume from a series with a 2° step between a ± 51° tilting range, and Figure 2.9 b) is related to a series acquired between 52.5° and - 64.5° with a 1.5° increment.

2.2.1.2 Encountered shrinkage problem

Both during and after this experiment, an unexpected phenomenon was noticed: the shrinkage of the polymer matrix.

Figure 2.10 illustrates this effect by comparing the images obtained at different angles, after their automatic alignment and rotation, in order to position the tilt axis vertically. If we adjust the origin on Y (vertical axis) on the trajectory followed by the end of a CNT close to half the height of the image, we clearly notice that the catalyst particle in the upper part of the images moves towards bottom, whereas the catalyst particle in the lower part moves towards top. According to the alignment and positioning of the tilt axis, the Y coordinate of any detail during the tilt sequence should remain constant. This is not what we see here, although it might be difficult to detect the problem in the absence of such markers (i.e. catalyst nanoparticles). We have then to conclude that the material has shrinked during the TEM irradiation. In spite of several tries, it was however not possible to reconstruct a reasonably 'good' volume form these data, as illustrated by Figure 2.8: it is obvious that this is due to the more or less continuous distortion induced during the acquisition of the series and caused by the shrinkage effect.

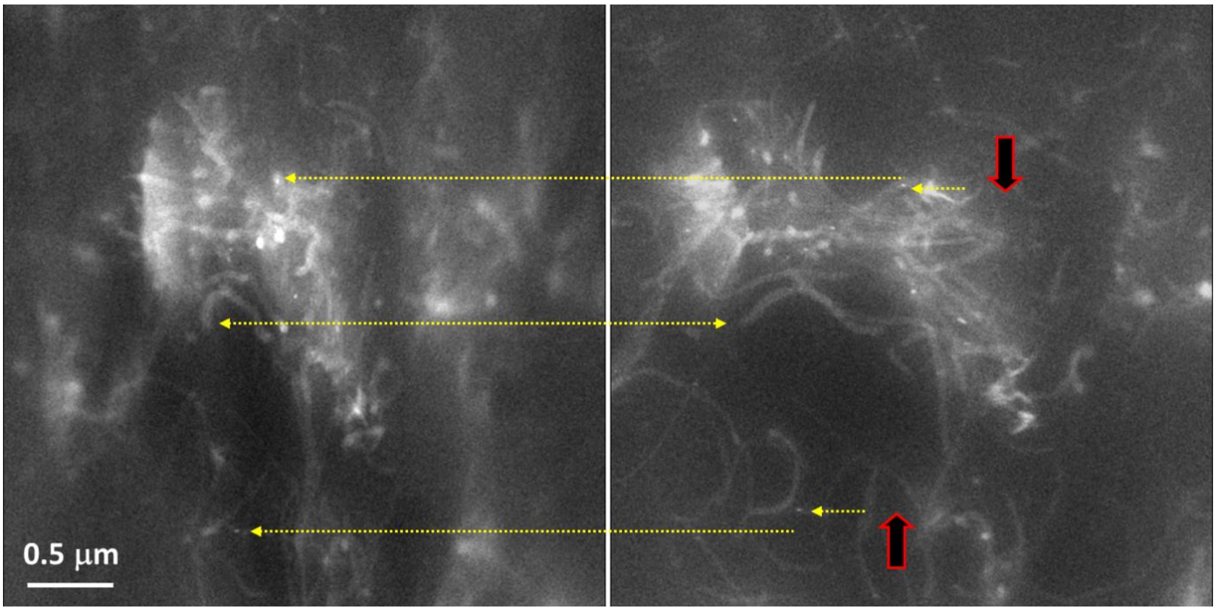

Figure 2.10: Images at - 53° (left) and + 37° (right) from the aligned series as in Figure 2.8 (the tilt axis is vertical and centred in the images). The two red arrows indicate the vertical motion of the trajectories of different details which illustrate the shrinkage effect.

A better evidence of the shrinkage effect is then obtained by the following experiment, performed on thicker cryo-ultramicrotomic sections (thickness of 500 nm).

As shown in Figure 2.11, one fresh zone containing some CNTs but a lot of metal catalyst nanoparticles was irradiated for 5 minutes at 200 kV in the STEM-HAADF mode (without tilting). During the beginning of the irradiation sequence, we have observed a rapid deformation of the region of interest (simply by eye inspection of the relative positions of the particles). Near the end of the sequence, we had the feeling that the deformation speed was considerably reduced. The superposition of the starting and ending microstructures as transparent layers clearly evidences the deformation which appears to be more of less isotropic and thus can be described as a shrinkage of all details roughly towards the centre of the image.

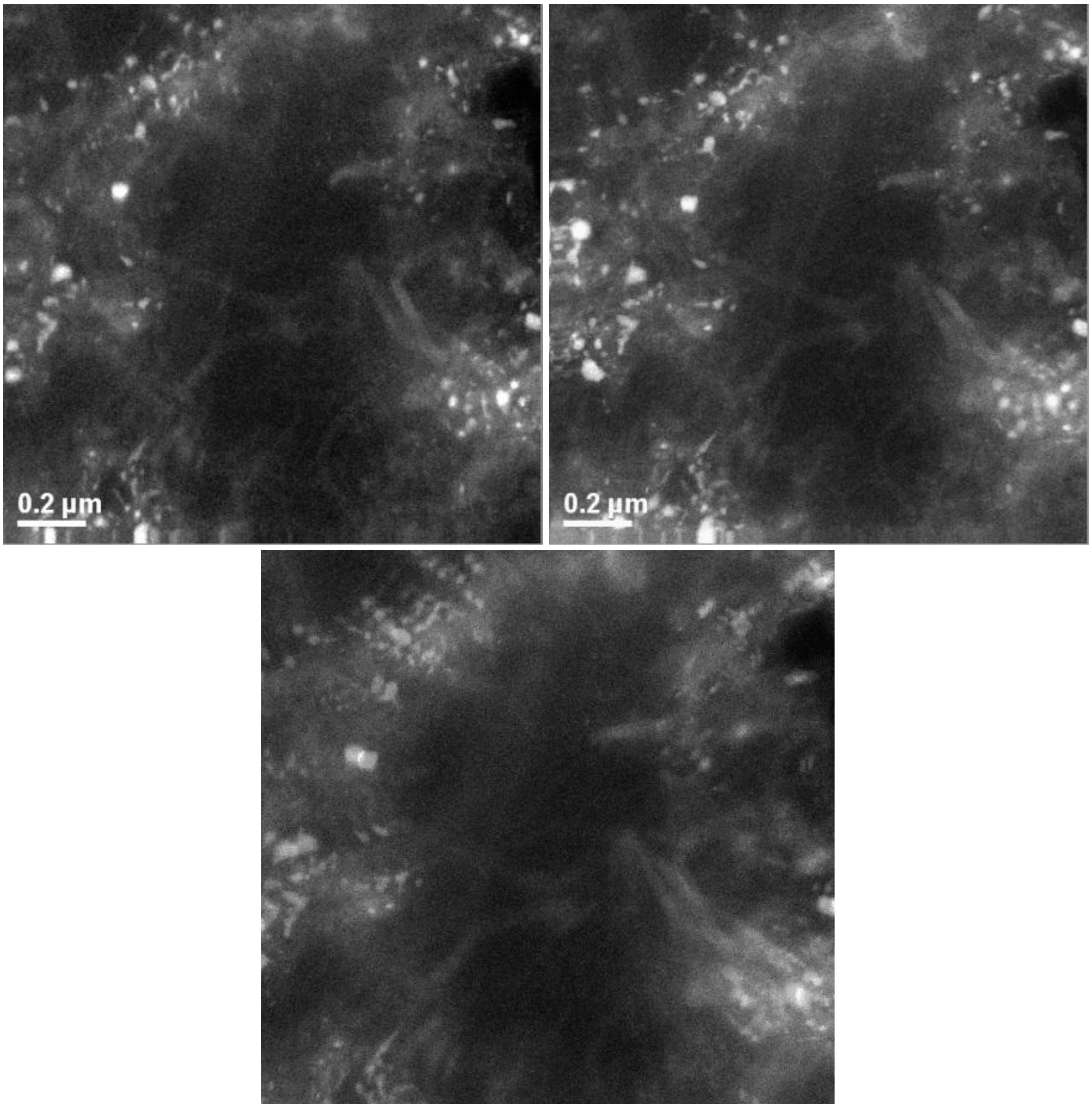

Figure 2.11: First (top left) and last (top right) image of a 5 minutes video recorded for a freeze-dried section in STEM-HAADF mode at 200 kV, 25 frames stored per second. Below: superposition of the two images showing the shrinkage effect.

The trajectories of some particles has been tracked and extracted every 100 images of a video recorded at a speed of 25 frames/second. These particles are positioned with red marks in Figure 2.12. The diagram on the right shows the positions of each particle with respect to the barycentre calculated in each extracted image. The most central particle is almost immobile, whereas all peripheral particles move roughly in the direction of the barycentre.

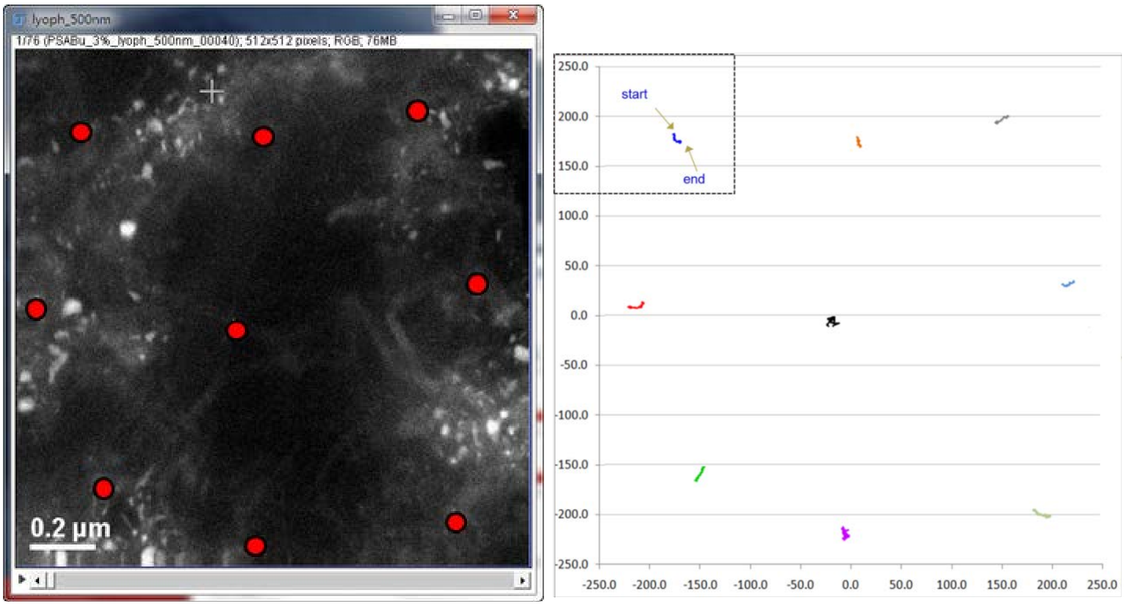

Figure 2.12: Display of the motion of catalysts nanoparticles during the irradiation in the TEM (STEM mode, 200 kV).

This first experiment was confirmed with others. Indeed we have checked different operating conditions regarding the high voltage (200 and 100 kV) and the imaging mode (STEM-HAADF or conventional TEM in Bright Field - TEM BF -) on other evaporated sections. The results are shown from Figure 2.13 to Figure 2.16 (presentation similar to Figure 2.12).

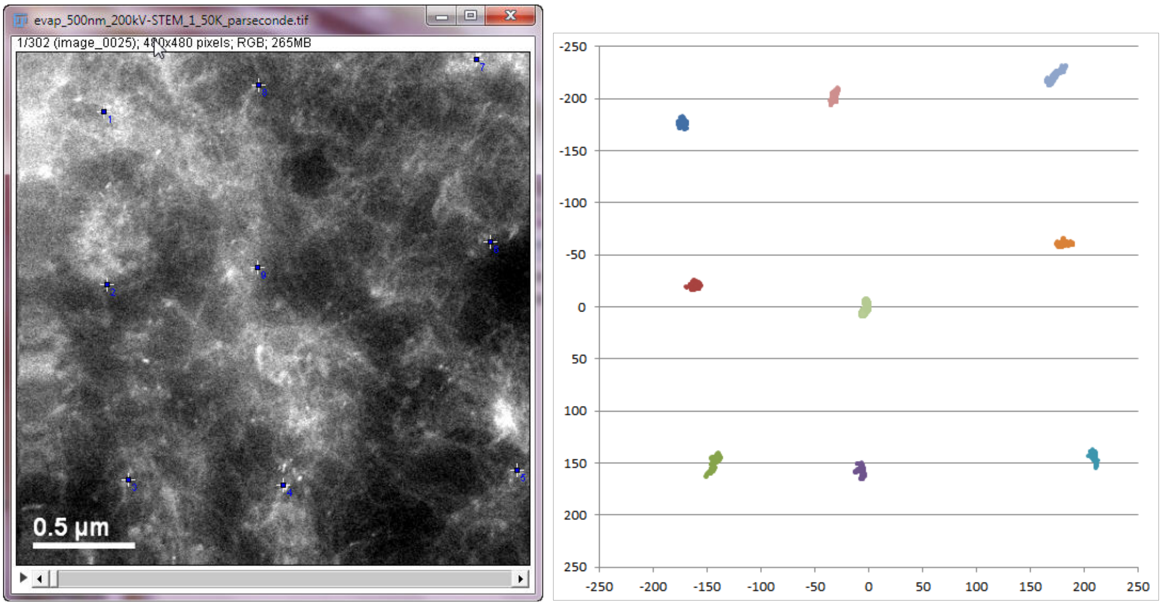

Figure 2.13: Shrinkage test for an evaporated section irradiated during 5 minutes in STEM-HAADF mode at 200 kV.

As a matter of fact, these tests performed in different imaging modes of TEM confirm that there is indeed an effect of shrinkage in such polymer-based materials. We can of course assume that regions with a high density of fillers might appear more resistant regarding the shrinkage problem; however, we do not intend to restrict our study to such regions, which could be non-representative of the global dispersion of these fillers.

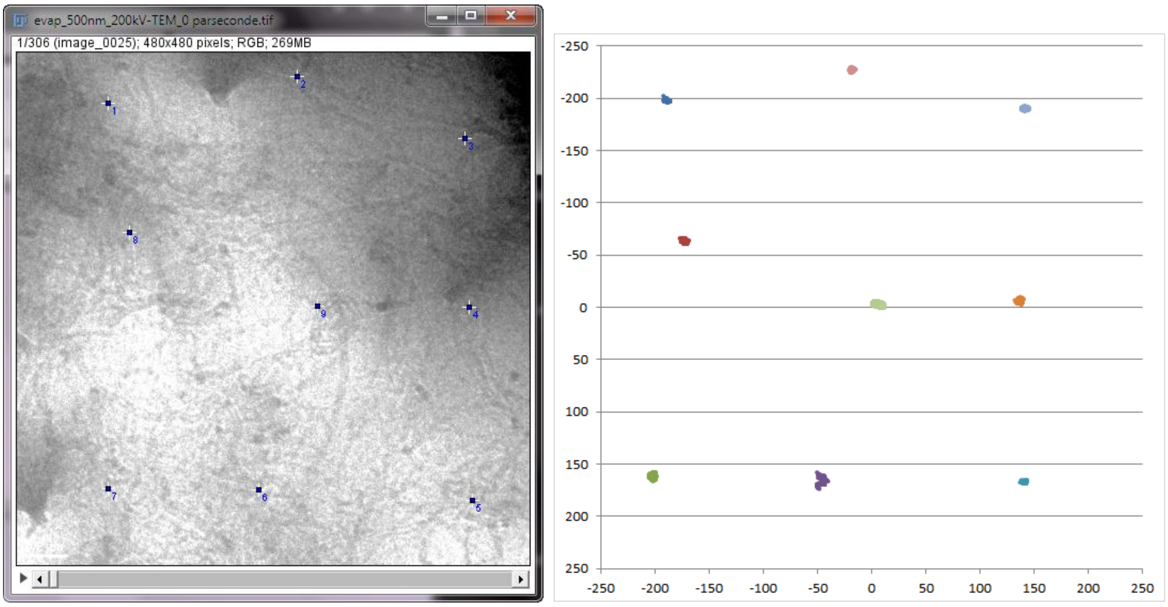

Figure 2.14: Shrinkage test for an evaporated section irradiated 5 minutes in TEM-BF mode at 200 kV.

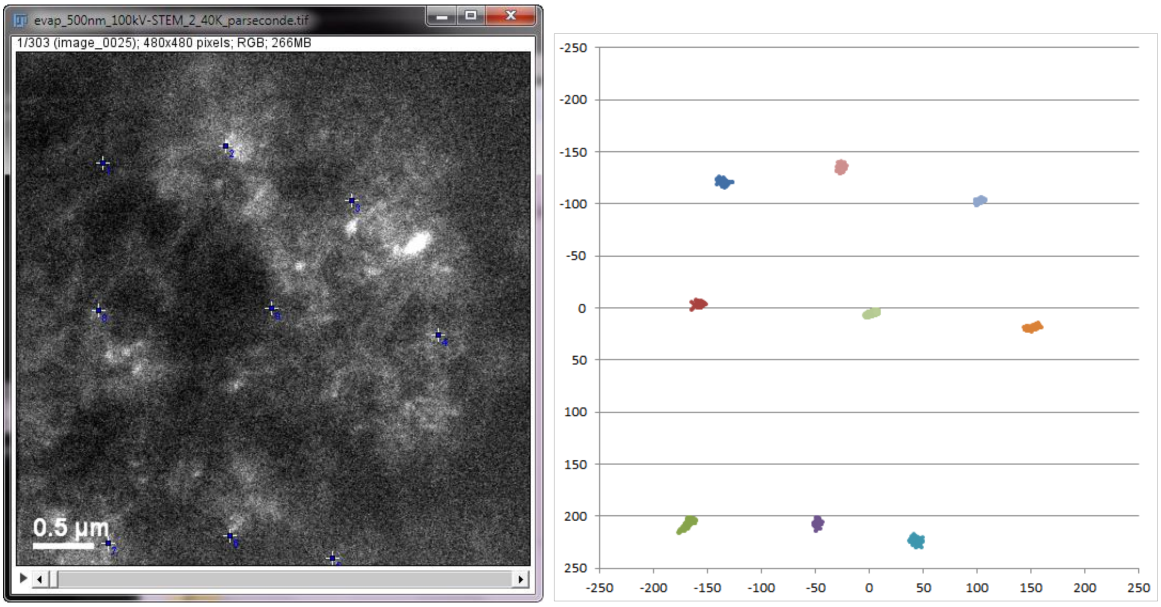

Figure 2.15: Shrinkage test for an evaporated section irradiated 5 minutes in STEM-HAADF mode at 100 kV.

According to the literature as discussed in § 1.3, this shrinkage problem is quite normal during TEM imaging of soft materials such as polymers and polymer-based composites. The main problem we are facing here is that 3D experiments require a long exposure to the electron beam, and any shrinkage during this observation would degrade the quality of the reconstructed tomograms, and maybe, make reconstructions even to be impossible. Then, it is necessary to avoid or correct this deformation in the original image series to obtain true and relevant tomograms.

We have thus undertaken a specific study of the shrinkage effect thanks to the numerous catalysts particles present in the nanocomposites, they constitute good markers to follow the 3D evolution, i.e. the deformation of the polymer matrix during tomographic acquisitions.

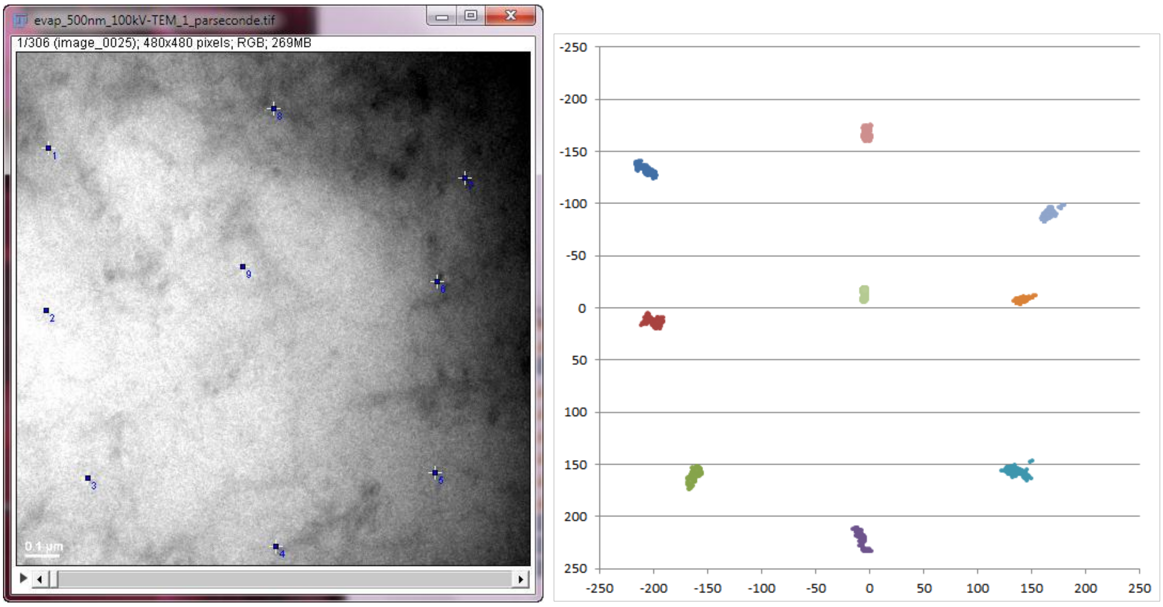

Figure 2.16: Shrinkage test for an evaporated section irradiated 5 minutes in TEM-BF mode at 100 kV.

2.2.1.3 Towards an in-situ 3D study of the shrinkage in polymer nanocomposites

Based on previous considerations, a method for studying the shrinkage in the tomographic series is proposed as follows: we intend to follow the projected trajectory (X_α, Y_α) of some particles (markers) as a function of the tilt angle α. According to the large number of experimental data for each particle (i.e., an almost unlimited number of tilt positions), we can easily determine its starting 3D position (X_0, Y_0, Z_0) and refine numerically this position assuming a homogeneous contraction (shrinkage) effect, which will be parameterized in order to match the experimental data. Since the contraction will concern all particles simultaneously, the procedure will treat all trajectories as a whole, and identify the best solution on the basis of a computer optimization based on a least-mean square routine.

In practice, this is achieved according to the following steps:
1) After the acquisition of one tilting series, images are first aligned without taking into account of any possible deformation of the polymer matrix. The tilt axis is oriented along the Y axis and the origin is assumed to be the centre of the image. This position will be optimized later.

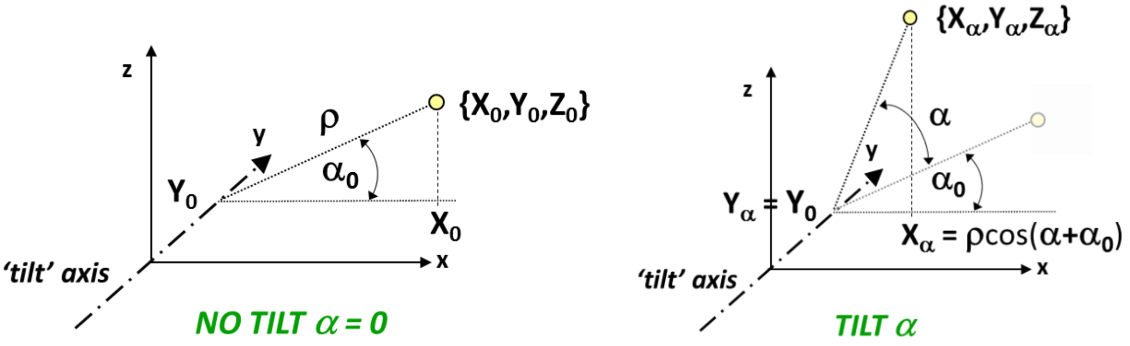

Figure 2.17: The coordinates of one point in the material before and after a tilting when there is no deformation. α is the tilt angle and α=0 means the section is in flat position.

2) The coordinates in pixels (X_α^i, Y_α^i) of experimental projections at several tilt angles α are recorded for a given number of markers (index *i*) identified in the material itself. Their original 3D starting

position at zero tilt (X_0^i, Y_0^i, Z_0^i) are then calculated from a simple linear regression as illustrated in Figure 2.17. If a particle (or any object represented by its mass centre) is located at the position (X_0, Y_0, Z_0) at zero tilt, it can be characterized by its polar coordinates ρ and α_0: the initial elevation angle. Obviously, these 3D parameters are unknown. After tilting by an angle α (without shrinkage), the position of the object becomes (X_α, Y_α, Z_α) according to the following simple relations:

$$\boldsymbol{X_\alpha = \rho \cos(\alpha + \alpha_0)}$$

$$\boldsymbol{Y_\alpha = Y_0}$$

$$\boldsymbol{\rho = (X_0^2 + Z_0^2)^{1/2} = (X_\alpha^2 + Z_\alpha^2)^{1/2}}$$

$$\boldsymbol{\tan(\alpha_0) = Z_0/X_0}$$

$$\boldsymbol{\tan(\alpha + \alpha_0) = Z_\alpha/X_\alpha}$$

If no shrinkage occurs, the curve $X_\alpha = f[cos(\alpha + \alpha_0)]$ must be a straight line; thus, a simple linear regression allows deducing α_0 and ρ by maximizing R^2, the coefficient of linear regression. This starting position will be used as a seed in a next step, i.e. the optimizing procedure.

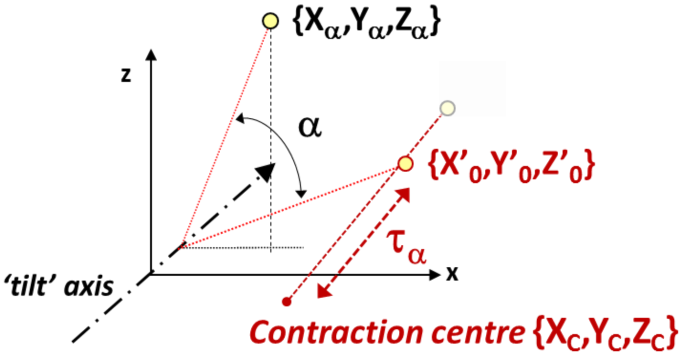

Figure 2.18: The coordinates of one point suffered shrinkage when tilted by an angle α.

3) We then assume an isotropic deformation, describe it by a strain level (τ in %) of any point with respect to an assumed fixed origin, i.e. a deformation centre C_{def}, as shown in Figure 2.18.

In our model, the deformation is isotropic at any given irradiation time i.e. a given tilt angle, which means that $\tau = \tau_\alpha$ must be fixed. Note that at this point we do not impose any constraint on the value of τ which can represent either a dilatation (τ > 100 %) or a contraction (τ < 100 %), nor we impose that the various τ_α at different tilts are correlated. The exact location of the deformation centre is refined in a classical Monte-Carlo method: a large number of random positions C_{def} are generated, allowing the positions ($X'^i_\alpha, Y'^i_\alpha, Z'^i_\alpha$) (deduced from ($X^i_\alpha, Y^i_\alpha, Z^i_\alpha$) after applying the strain level τ_α) of each marker to be calculated; the 'best average' τ_α is obtained after minimizing the quantity:

$$Q = \sum \{ [(\boldsymbol{X'^i_\alpha})_{calc} - (\boldsymbol{X^i_\alpha})_{exp}]^2 + [(\boldsymbol{Y'^i_\alpha})_{calc} - (\boldsymbol{Y^i_\alpha})_{exp}]^2 \}^{1/2}$$

(i.e. the sum of Euclidian distances between the calculated and experimental projections)
This whole Monte-Carlo simulation procedure is represented in the algorithm shown in Figure 2.19.

4) A final procedure is applied, to account for the optimization of the tilt axis position. According to point 1), the tilt axis was refined with the 'no deformation' hypothesis. To increase the accuracy of our procedure, we have run the different steps reported in Figure 2.19 (points 2) and 3)) with the

allowance of a slight misalignment of the tilt axis (i.e. in plane rotation θ). The final set of deformation levels (τ_α) is finally that which gives the lowest value for the error factor Q. Regarding the tilt axis, the optimum was obtained with a re-alignment of less than 2°.

```
Starting linear regressions of $X^i_{\alpha_j} = \rho^i\cos(\alpha^i_j+\alpha^i_0)$ and $Y^i_{\alpha_j} = f(\alpha^i_j)$ to get SEEDS for $\{X^i_0,Y^i_0,Z^i_0\}$
Loop over random CENTRES $\{X^k_C, Y^k_C, Z^k_C\}$
    Loop over angles $\alpha_j$
        Loop over 'markers' i
            adjust contraction/dilatation factor $\tau^i_j$ to force $\{X^i_{\alpha_j}, Y^i_{\alpha_j}\}_{calc.} = \{X^i_{\alpha_j}, Y^i_{\alpha_j}\}_{exp.}$
        End loop
        Average contraction/dilatation factor $\tau_j$ at angle $\alpha_j$
    End loop
    Calculate Euclidian ERROR between calculated and experimental projections
    and store best CENTRE (lowest error)
End loop
```

Figure 2.19: The general simulation algorithm for the shrinkage study.

From a practical point of view, the curve $\tau_\alpha = f(\alpha)$ gives directly the variation of τ versus time because the acquisition was performed with an almost constant tilting 'speed'.

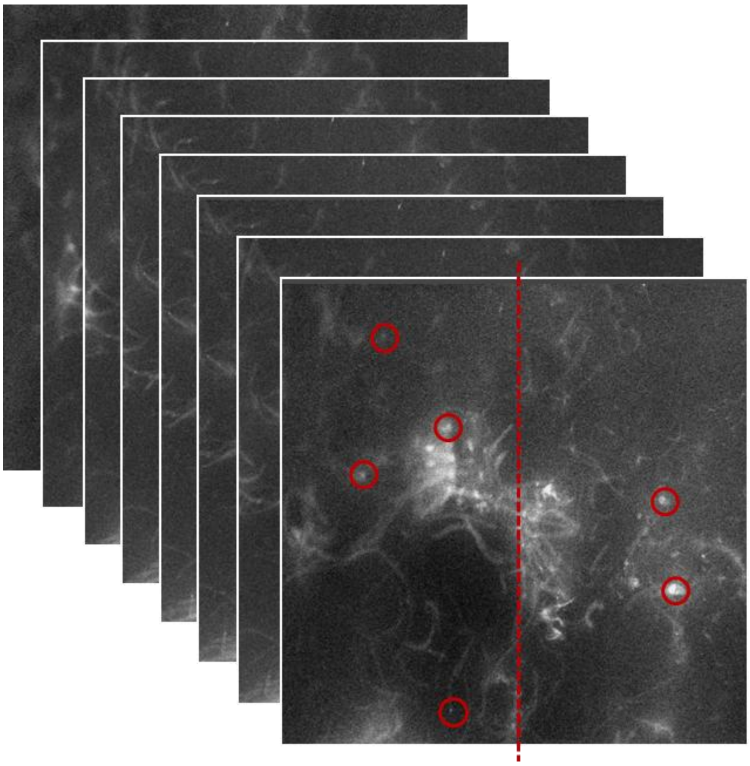

Figure 2.20: Example of markers to be used for the trajectory tracking in an aligned tomographic series of projections, with tilting axis along the Y axis (red dotted line in the middle of the image frame).

This approach has been applied to the first experimental tilt sequence shown in Figure 2.7 of 2.2.1.1. 9 trajectories have been tracked (see Figure 2.20) over 14 tilt angles; 20 × 10^6 random deformation centres have been tested [Liu2011, SFμ].

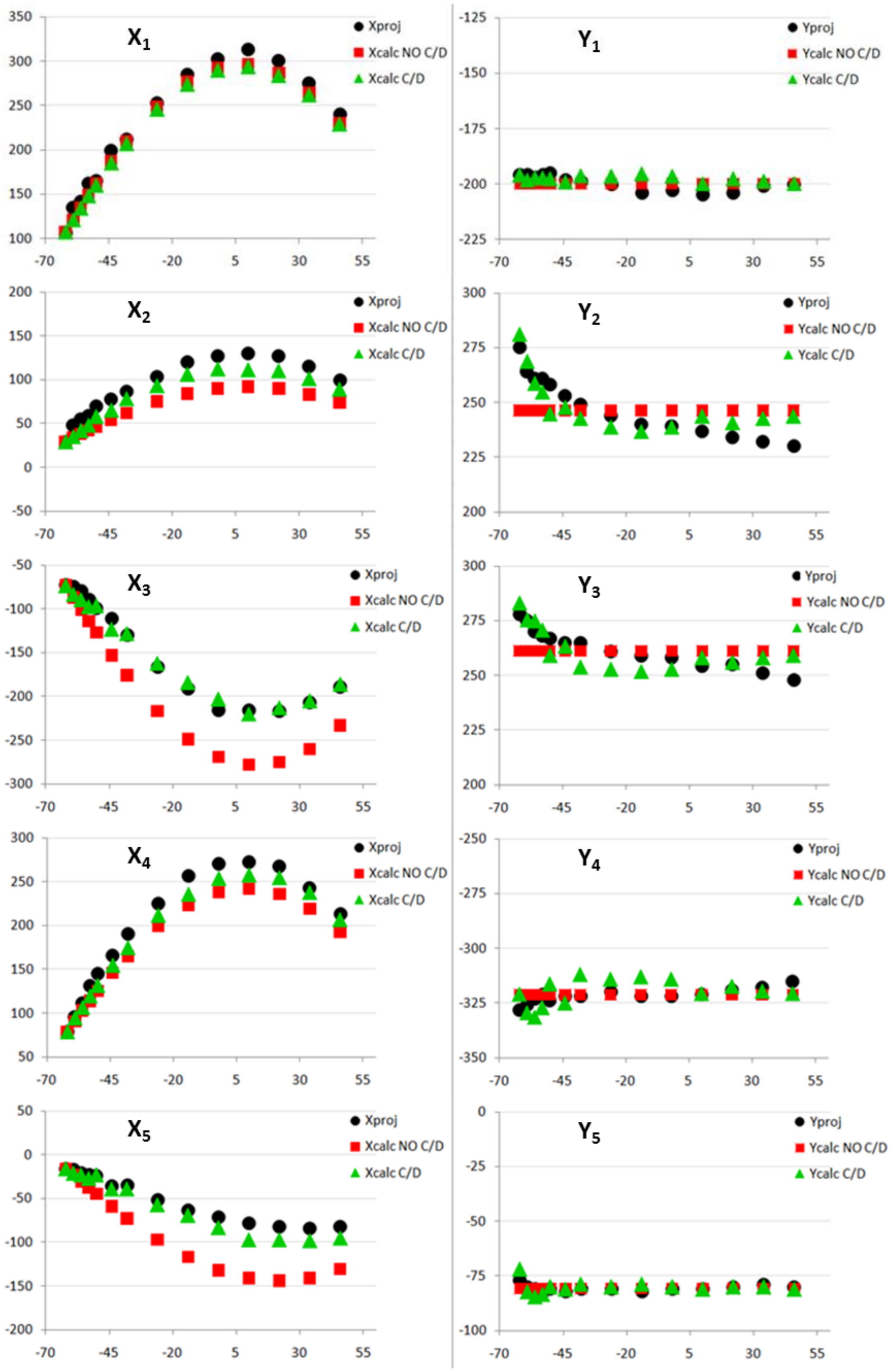

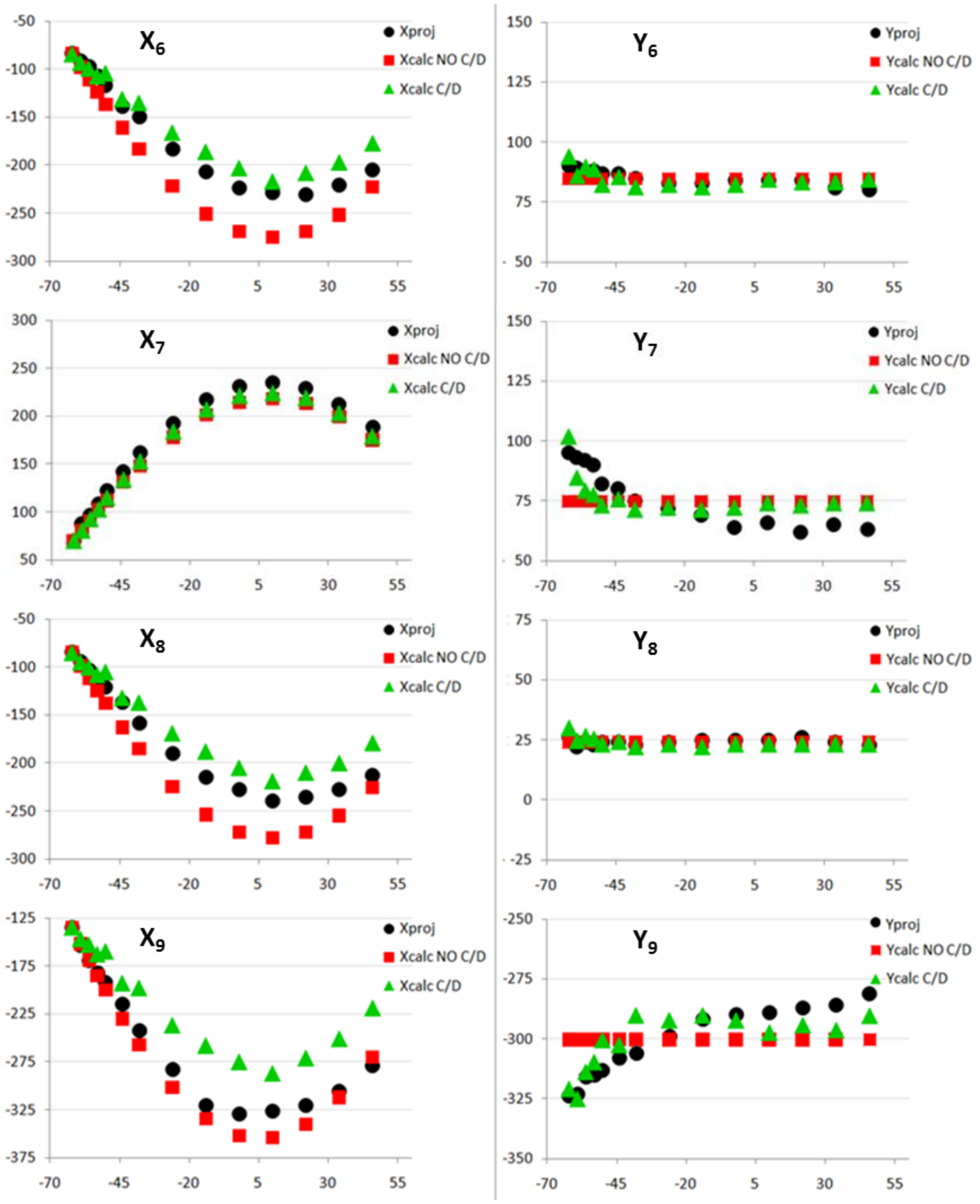

Figure 2.21: Analysis of 9 trajectories over 14 angular positions with the application of the best calculated τ . The evolution of X coordinate vs. tilt angle (α on the horizontal axis) is shown on the left and Y on the right. Black circles are the experimental marker coordinates; red squares are the calculated ones supposing no deformation, and green triangles are the final calculated coordinates accounting for a deformation with the best mean value of τ refined independently for each tilt angle. [Liu2011, SFμ]

Figure 2.21 shows the results of the trajectory analysis based on 9 markers chosen for their good visibility and contrast over the whole series of 14 tilting angles with an increment of 7.5°. The evidence of a deformation during the experiment is obtained from the evolution of the Y coordinate, which should remain constant (since Y is along the tilt axis) if no shrinkage occurs, as shown by the calculated points red squares) in this hypothesis; clearly, this is not the case for all markers (dark circles showing experimental data). These diagrams show essentially that for each marker, accounting for a deformation improves the match for all trajectories, although it remains imperfect, probably due to the main limitation of our model, i.e. an isotropic contraction / dilatation versus a single central point.

The final curve reported in Figure 2.22 shows the evolution of τ_α versus α. We see two very interesting and relevant features:

- τ_α remains lower than 100 %, which means a shrinkage, rather than a dilatation
- The variation of τ_α is continuous and monotonic, showing a saturation effect: after the first 40°, the shrinkage seems to stop, which means that the microstructure is stabilized. This is exactly what was obtained in the literature [Luther2006].

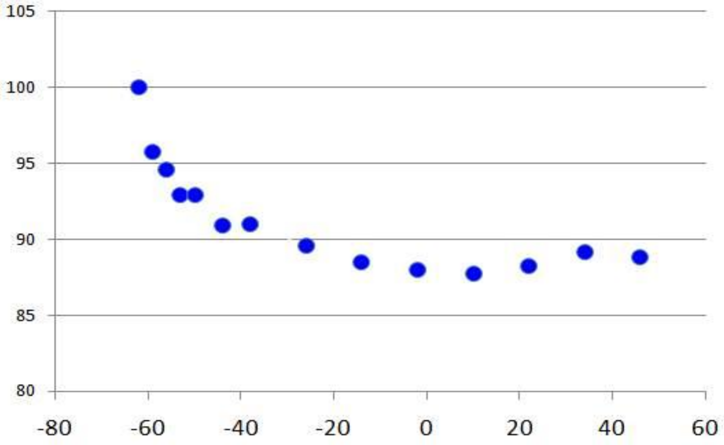

Figure 2.22: 3D measurement over a tomographic projection series in STEM-HAADF assuming a homogeneous shrinkage (τ in % vs. tilt angle in °).

Several conclusions can be drawn out form this study:

- We clearly evidence the stabilization of the shrinkage with time, which provides a good indication of the pre-irradiation time which would make a tomographic experiment consistent from the strict point of view of the stability of the microstructure.
- The present approach provides a mean to correct the 3D deformation of the object during a long 3D acquisition. If smart cross-correlation based routines are used, such as Digital Image Correlation techniques (for a general presentation, see [Hild2013]), it is *in principle possible* to analyse tomographic projections without identifying true markers, but working on the local texture of the micrographs. Then from the evolution of trajectories of local areas covering the whole field of view, it is *in principle possible* to correct the deformations and reconstruct a more realistic volume. This gives an interesting perspective for realizing a dedicated algorithm to implement this strategy.
- Obviously, we can wonder about the true representativity of such experiments, which would then be carried out on a 'modified microstructure' (since after shrinkage). This might be of a great importance in the present case, since the shrinkage effect could cause more contacts between CNTs than initially existing in the 'true microstructure'. In other situations concerning polymer nanocomposites reinforced by fillers, the problem may just be to quantify this shrinkage effect, in order to get a correct volume fraction of the fillers. This is what we will be facing to in the third chapter of the present work.

Because of the third point above, we have decided to perform less aggressive experiments, either a low voltage or at the liquid nitrogen temperature.

Experiments carried out at low voltage will concern both TEM (see section 2.2.2) and SEM (section 2.3) approaches. TEM Work under cryogenic conditions will be described in section 2.2.3.

2.2.2 EFTEM, C_s-corrector, 80 kV, FEI TITAN

According to the first STEM-HAADF experiments and the initial study of the shrinkage problem in P(BuA-*stat*-S)/MWNTs shown in the previous sub-sections 2.2.1.2 and 2.2.1.3, it appears that 200 kV in the TEM is too energetic. In the frame of the ElyT-lab. (*www.elyt-lab.com*) collaboration between University of Lyon and Tohoku University at Sendai, Japan, we have conducted tomographic experiment at 80 kV using a C_s-corrected TITAN microscope from FEI[1]. The interest of this instrument for the present work is twofold: i) because of the imaging C_s-corrector, a good spatial resolution is kept even at low voltage, and with a high-gap pole pieces enabling the large tilting amplitude as required for tomography; ii) thanks to the energy 'Gatan Imaging Filter' (GIF) installed on the microscope, we could record zero-loss filtered images with a good contrast, despite the high relative thickness of our ultramicrotomic slices when observed at 80 kV (Figure 2.23).

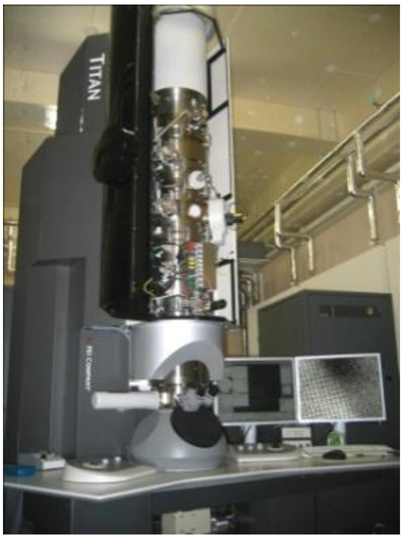

Figure 2.23: View of TEM of FEI TITAN with C_s-corrector.

The last point (ii) is spectacularly demonstrated by Figure 2.24. A section of FP material was observed in both conventional Bright Field (BF, unfiltered) and Energy-Filtered TEM (EFTEM) mode at 80 kV. With a slice cut to about 200 nm with the ultramicrotom, the projected thickness is simply doubled when tilted at 60°. This very important thickness at 80 kV leads to a totally blurred contrast of the conventional BF image, owing to the very poor density difference between the CNTs and the matrix. In the case of EFTEM imaging, a reasonably good visibility of the CNTs is retrieved when getting rid of the inelastic scattering as permitted by the GIF (so-called 'zero-loss' images, where an energy window of about 20 eV in width is centred on the zero-loss elastic peak). It should be mentioned that the STEM mode could not be applied because the use of energy filter requires working in the BF mode.

According to this, the tomography acquisition was entirely recorded in the EFTEM mode; a series of projections was acquired between ± 62° with a tilt increment of 2°, as illustrated in Figure 2.25. Although the filter brings a good contrast compared to unfiltered imaging, it was moreover required to enhance the visibility of the CNTs by a constant, and relatively large under-focus of 5 µm. Under-focussing TEM images leads to significant Fresnel contrast which enhances the difference in atomic densities between different parts of the object, then improves the overall contrast.

---

[1] The assistance of Dr. K. Sato (IMR, Tohoku University) for conducting these experiments is gratefully acknowledged.

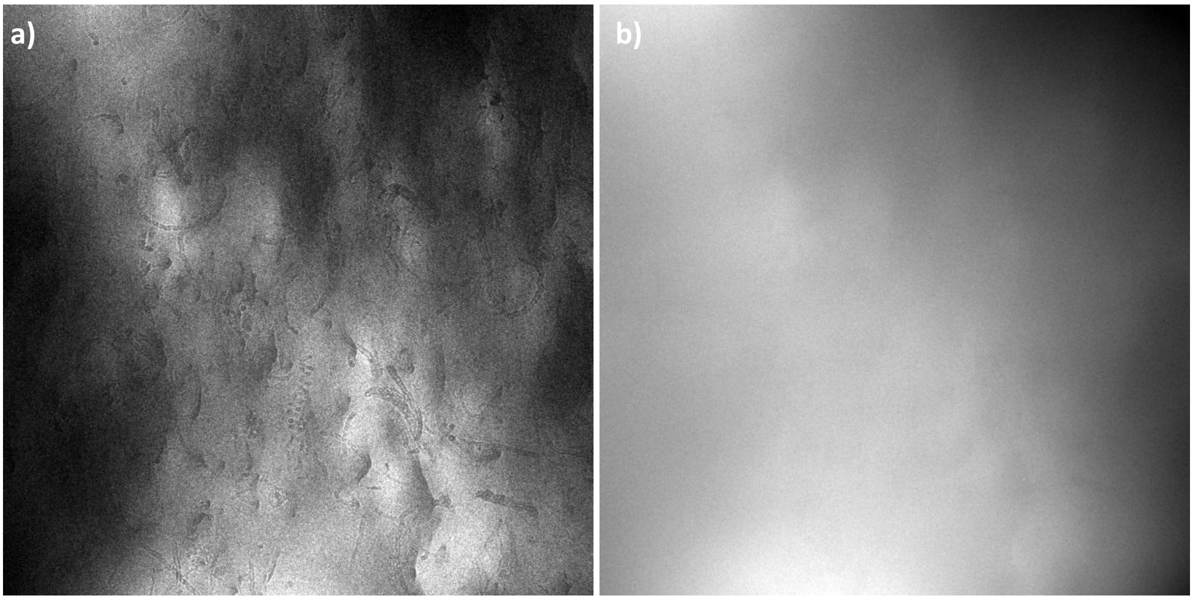

Figure 2.24: Images obtained with defocus of - 5 µm at 60° of tilt. a) EFTEM image; b) CTEM image.

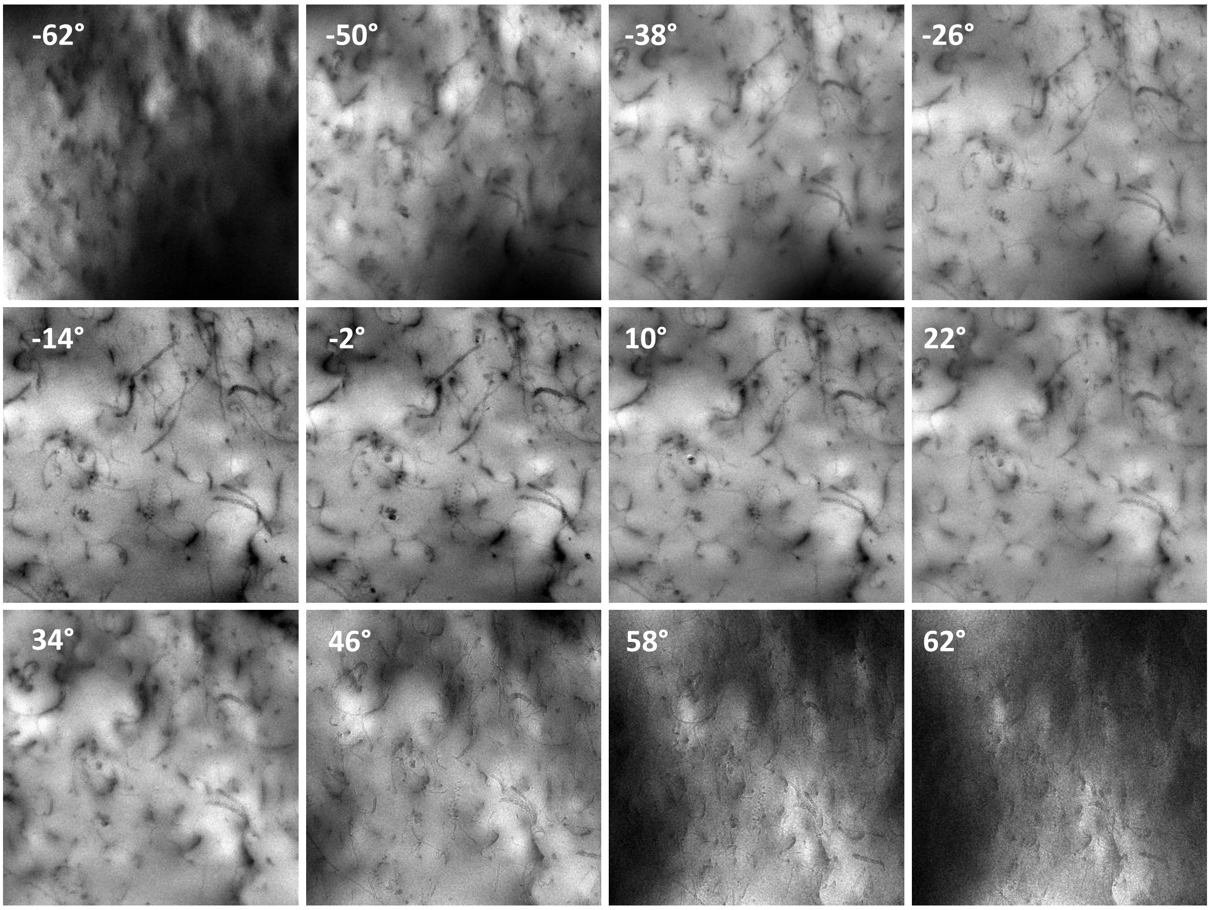

Figure 2.25: Illustration of a typical EFTEM series of images obtained at 80 kV with defocus of 5 µm (FEI-TITAN microscope, Tohoku University, Sendai-Japan).

Despite the advantages of energy-filtered and low voltage, we did still encounter some difficulties in this experiment, which are then discussed in the nest sub-section. Due to the conditions in which this experiment was performed during a visit to Japan, it was not possible to reproduce the acquisition with a better accuracy, and we then had to try to correct the available data.

2.2.2.1 Different strategies and corrections

Before the reconstruction of the series of EFTEM projections shown in Figure 2.25, there are some issues to be addressed for getting 'correct' tomograms.

The first one is, as before, the shrinkage problem. Actually, the target region was irradiated at zero tilt during 5 minutes to wait for a complete stabilization of the polymer matrix. Although this may induce an undesirable contraction of the microstructure, it was judged necessary to proceed in this way in order to allow a good 3D reconstruction. Indeed, it appeared to be insufficient since a specific check performed after the first half of the total acquisition revealed a little but existing shrinkage effect.

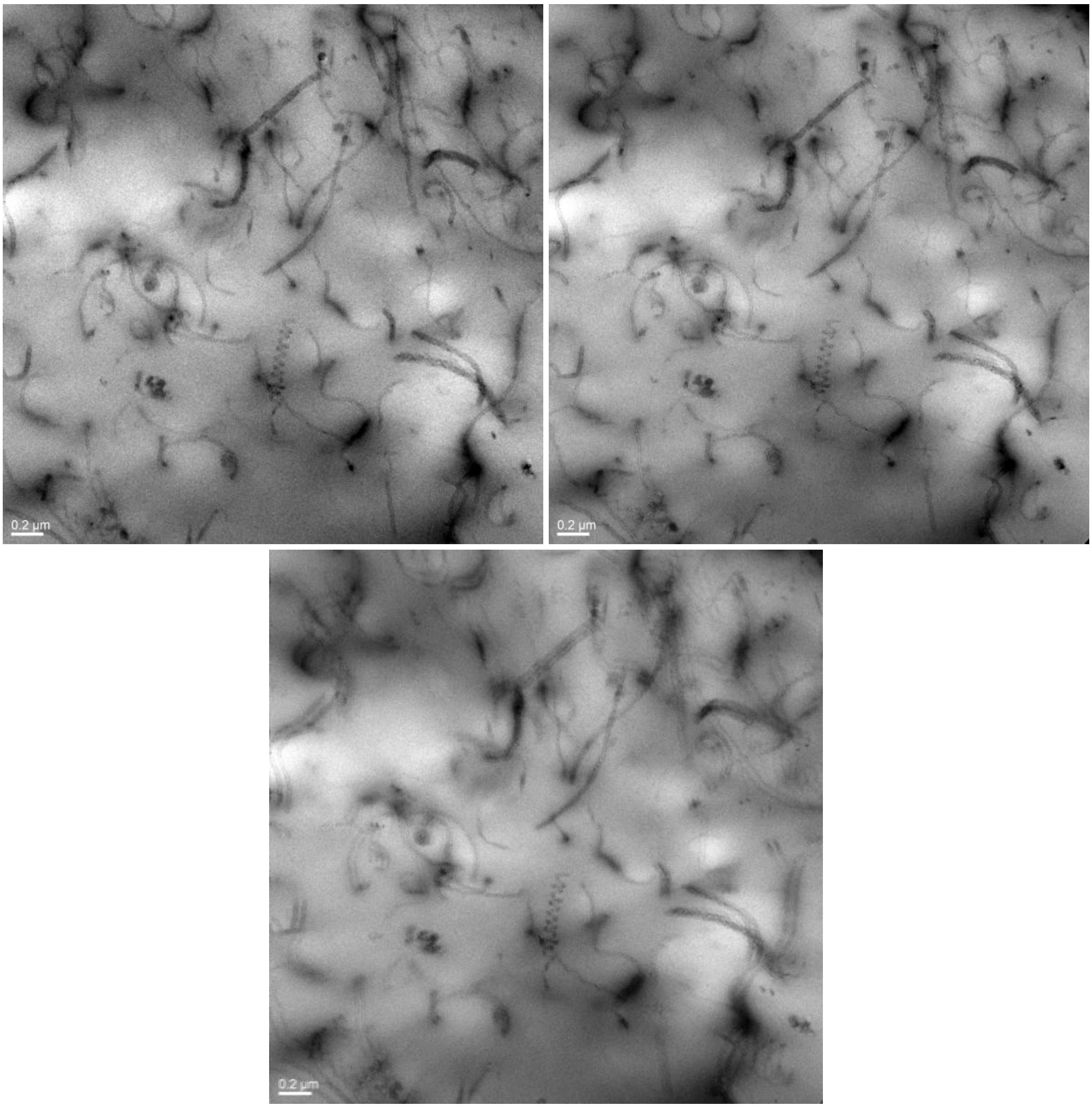

Figure 2.26: Images at 0° before (top left) and after (top right) tomographic acquisition of negative tilts and their superposition (below) (after centring).

This is shown in Figure 2.26: the initial micrograph at 0°, obtained after the irradiation and before the tomographic acquisition, is compared to a 0° image recorded after the all negative tilts. When both images are superimposed, a 'blurring' effect is produced, which is due to the deformation between the two microstructures. When the central feature (e.g. the 'spiral-shaped' CNT) is aligned, we see that the first image is as if recorded at a slightly larger magnification, which indicates a detectable shrinkage. This means that despite our pre-irradiation, a residual shrinkage occurred, which could be estimated in the present case to about 3 %. Although weak, this effect should be corrected to allow a 'good' 3D reconstruction.

Indeed a second problem was encountered, which is, in practice, also concerned by a similar correction.

As announced in the beginning, the whole series was acquired at a defocus of - 5 µm, which was determined as a reasonable value to bring a sufficient contrast for low tilt angles. When tilting at large angles, typically more than 50°, we realized that the contrast became very low, owing to the drastic thickness increase as illustrated in Figure 2.27.

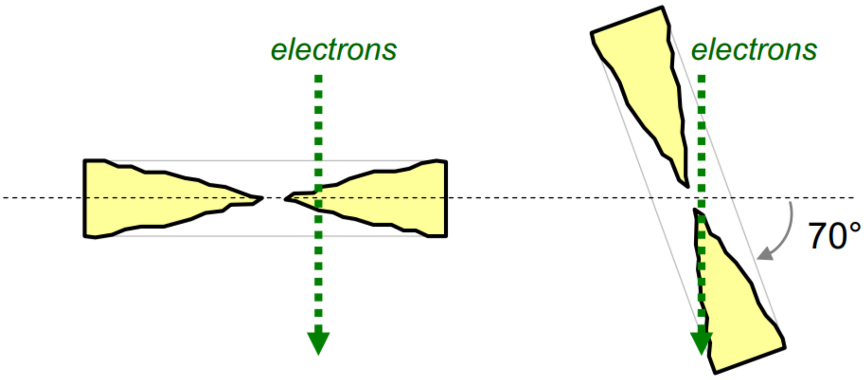

Figure 2.27: Illustration of the drastic thickness increase at high tilting angle for tomographic acquisition.

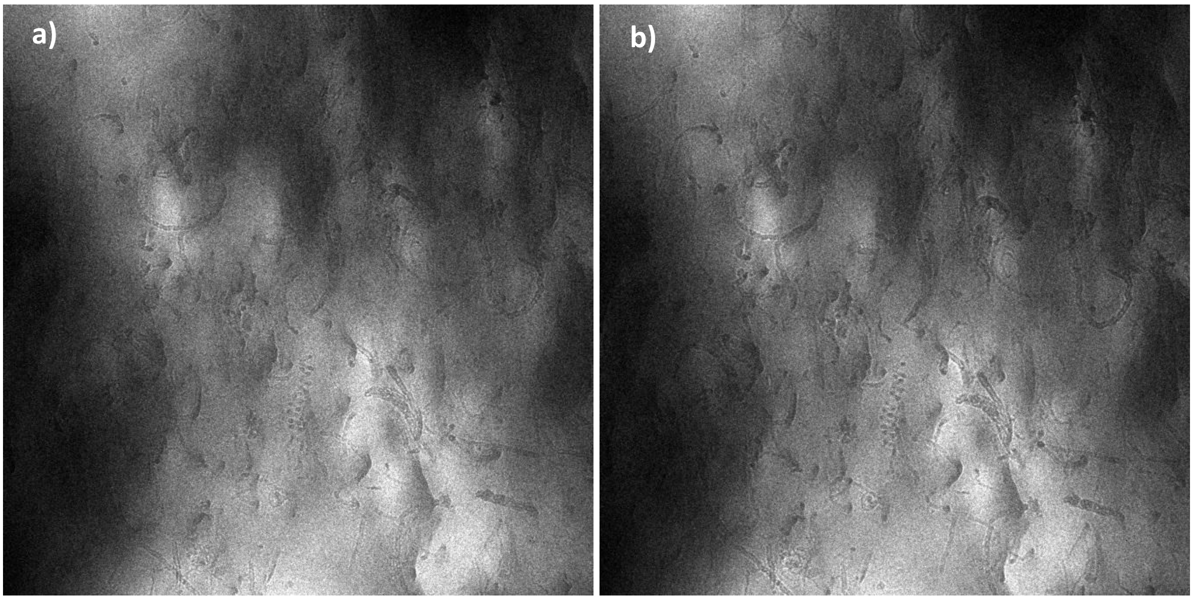

Figure 2.28: EFTEM images after tilting at 60°; a) defocus equal to - 5 µm; b) defocus - 13 µm.

As shown in Figure 2.28, the higher defocus at - 13 µm could really offer a better contrast, but at the same time, introduce slight changes in magnification and in-plane rotation, due to difference in the excitation of the objective lens. This well-known effect is more clearly demonstrated in Figure 2.29 and Figure 2.30, where the same region is observed in bright field and STEM-HAADF with the JEOL 2010F microscope. In Figure 2.29, the bright field image was recorded at almost Gaussian (0) defocus, and the size of the green dotted frame passing through the edge-on section of 3 CNTs is identical to that observed in the HAADF image. When under-focussing the bright field image (Figure 2.30), a stronger (better) contrast is produced for the CNTs, but the local magnification and rotation have changed by respectively about 10 % and 2°, as expected when a significant excitation changes of the imaging lens is produced.

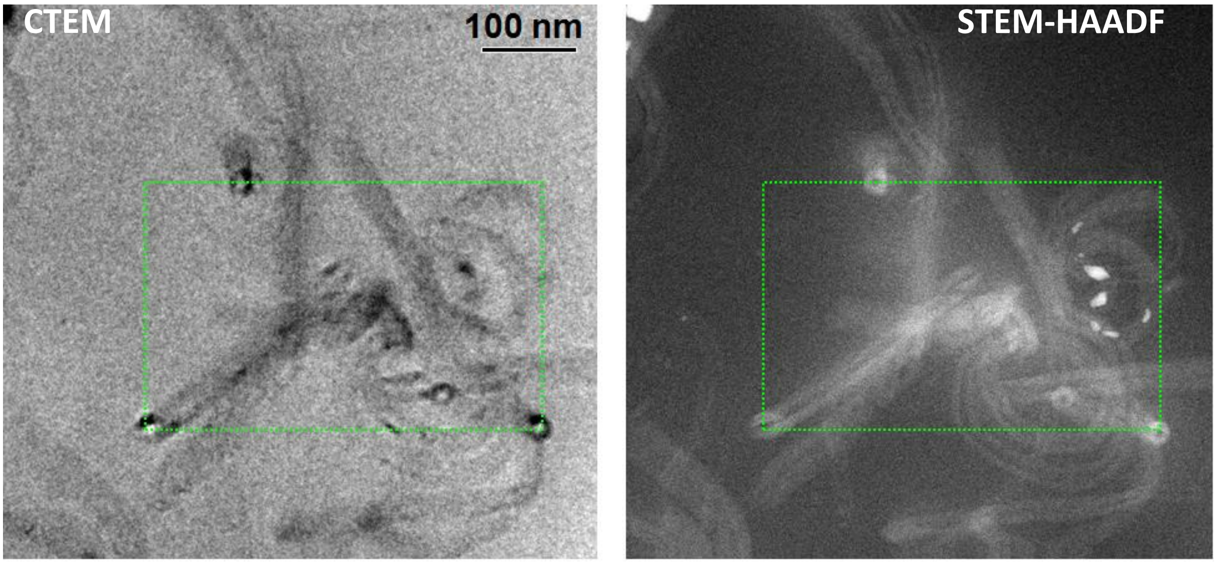

Figure 2.29: Same region of a polymer-CNTs nanocomposites observed in bright Field CTEM at Gaussian focus and STEM-HAADF modes (JEOL 2010F, 200 kV).

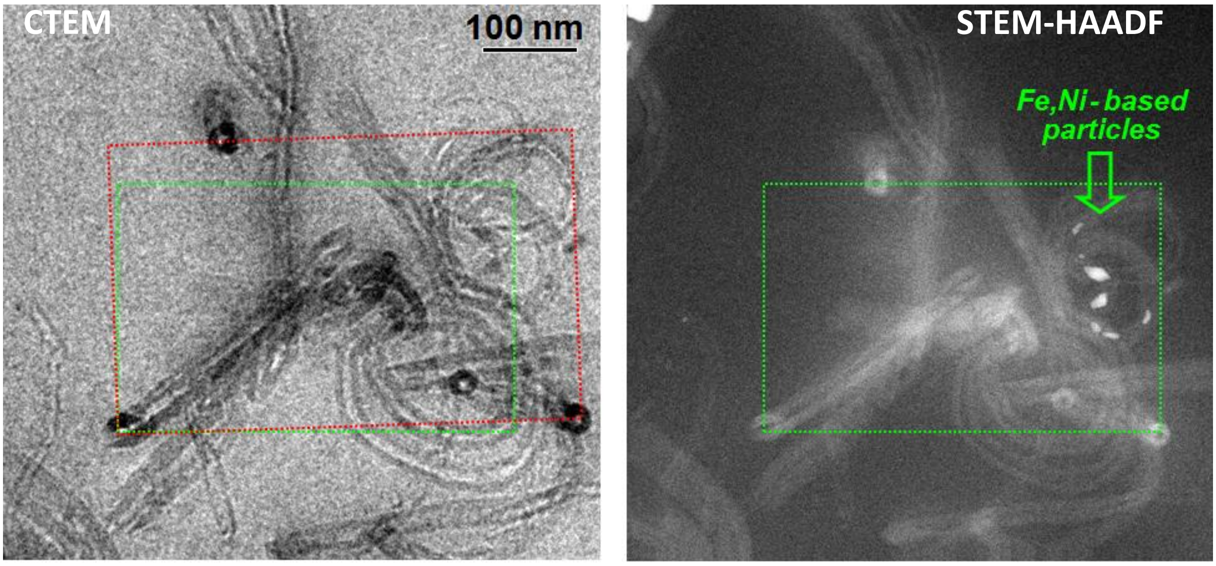

Figure 2.30: Same as Figure 2.29 when the BF image has been under-focused by a few µm: note that the original green frame has been enlarged and slightly rotated (red dotted frame).

According to this, correcting images taken at a - 13 µm defocus to 'realign' them according to the -5 µm series requires to measure the magnification and rotation changes in order to modify consistently the images. This is illustrated by Figure 2.31. The magnification factor (ρ) and rotation angle (α) have been determined from a simple tracking of identical features in both images, and a numerical refinement, based on the calculation of the Euclidian error between the '- 13 µm' corrected and '- 5 µm' initial positions has been performed to end up with the optimal unique set of values permitting the best superimposition of the corrected - 13 µm onto the original - 5 µm.

In this way, all images with relatively poor contrast recorded at - 5 µm at large tilt angles could be replaced by the corrected - 13 µm.

It is interesting to note that this geometrical correction is similar to that required to account and correct from the shrinkage effect in the simplest way. From a practical point of view, the shrinkage effect evidenced in the first part of the series (recorded at negative tilt angles) has thus been corrected in a similar way. It was further checked that no further shrinkage could be measured while acquiring the positively tilted images.

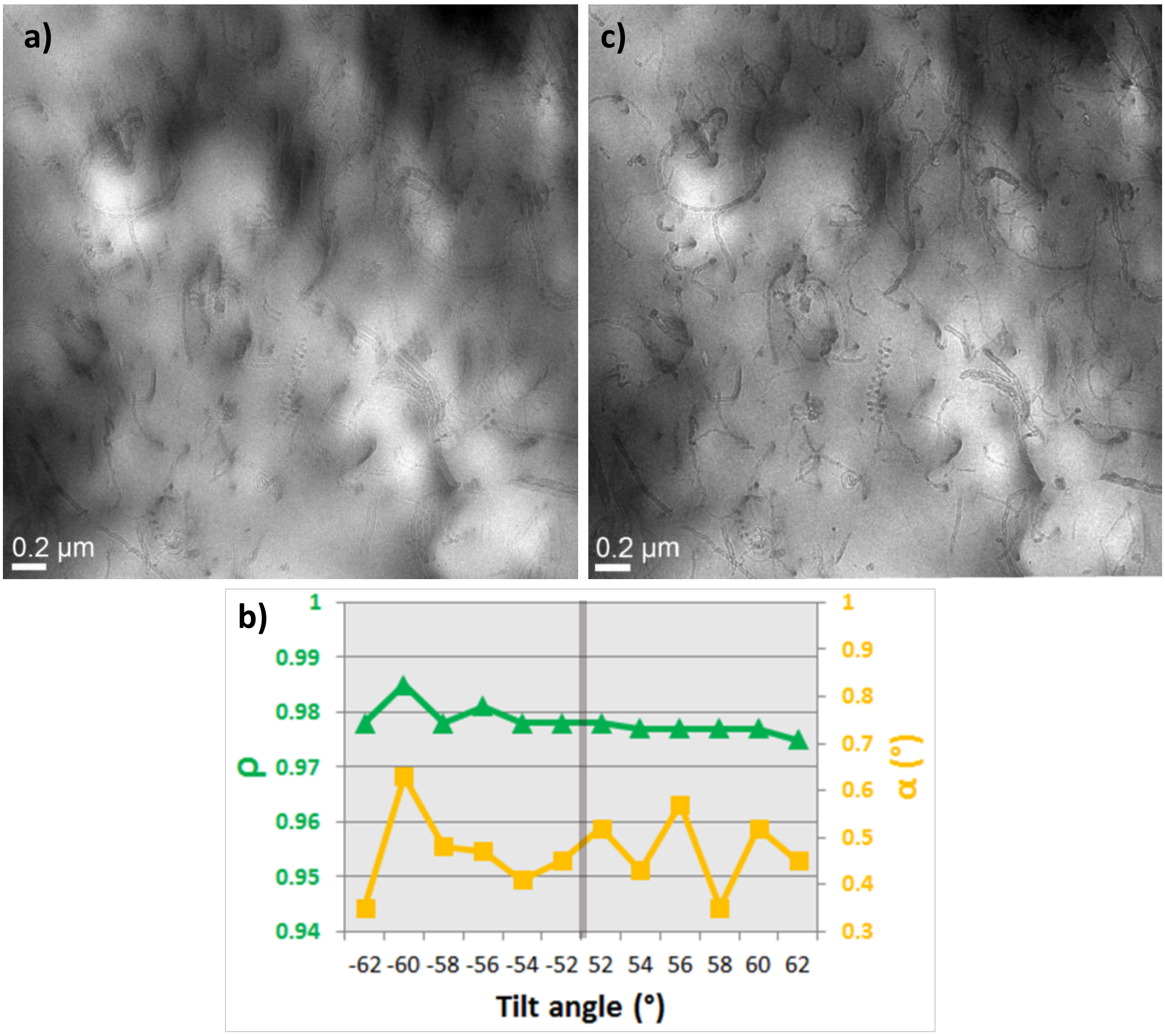

Figure 2.31: Correction of the magnification and rotation changes due to defocus change at high tilt; a): example of overlapping of images at 50° with defocus of - 5 µm and - 13 µm; b): quantitative measurements of magnification factor (ρ) and rotation angle (α) allowing to match the - 5 µm and - 13 µm images at high tilt angles; c): overlap of the 'resized' image at - 13 µm and the original - 5 µm micrograph, according to the correction parameters ρ and α applied to the initial - 13 µm image at 50°.

From the above, we can compare 3 different reconstructions:

- The first one (indeed labelled *3* in the following) can be obtained from the raw series recorded at - 5 µm.
- The second one (*2*) is mixing original images at - 5 µm at low tilt, and original - 13 µm at high tilts.
- The third (*1*) is similar to the second one, but uses corrected - 13 µm images at high tilts.

This comparison is shown in the next sub-section.

2.2.2.2 A comparison of three reconstructed tomograms

Figure 2.32 shows a perspective view of the three tomograms reconstructed according to the strategy presented above. The tomograms are displayed in reverse contrast which leads to a better visibility. From a simple visual inspection, it is hard to appreciate any difference, especially regarding the quality of the reconstructions. In order to evaluate this, we did re-project these volumes in some orientation and measure intensity profiles across nanotubes in order to define a contrast and resolution based criterion. In Figure 2.33, all tomograms are projected at rotation angles 0°, - 20° and 30° (like experimental micrographs from the original series). One typical tube section was then selected, and its contrast level calculated from the intensity measurements in all 9 projections.

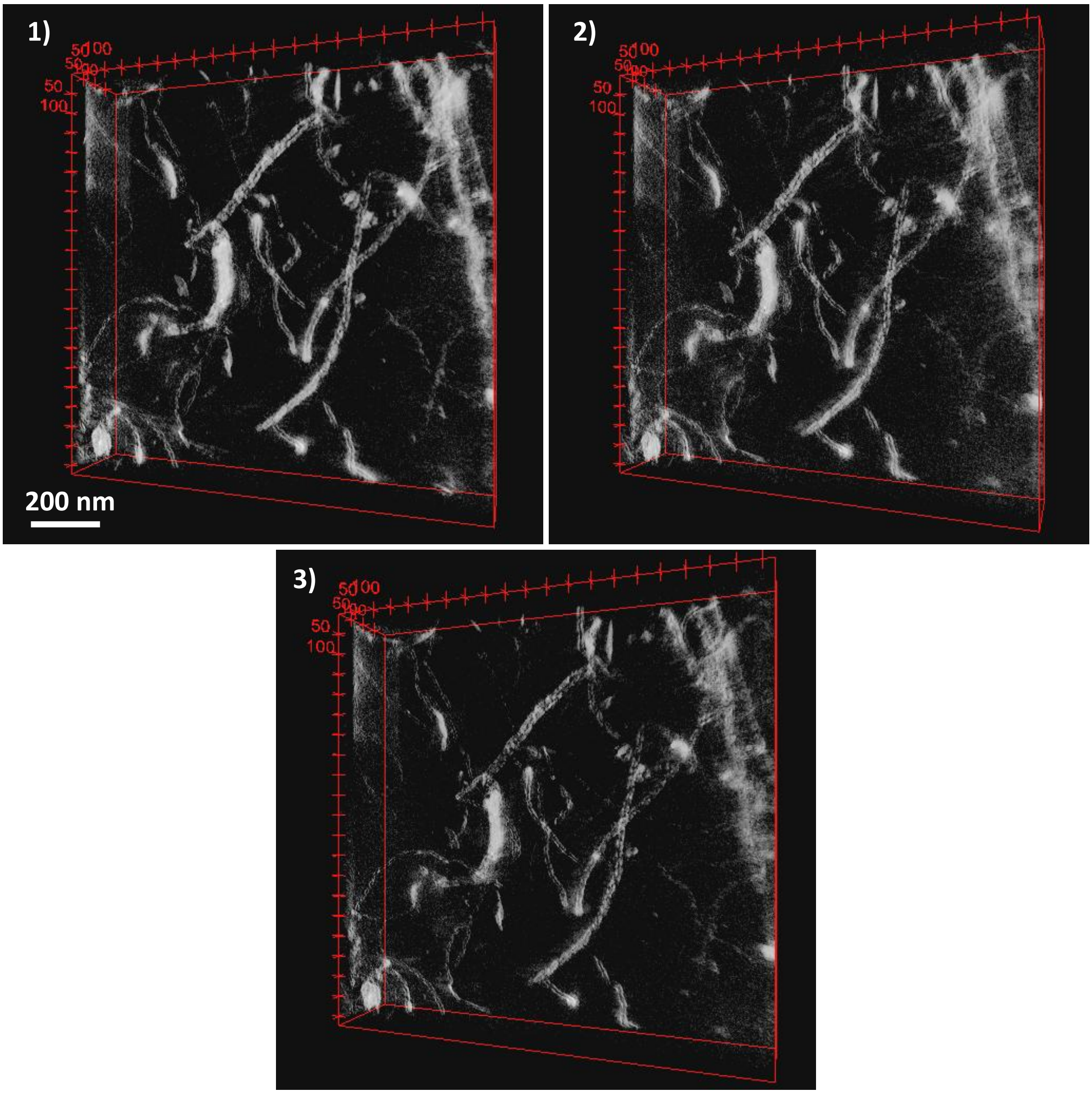

Figure 2.32: Volume rendering of tomograms. 1) Reconstruction from series with defocus-corrected images at high tilts, 2) reconstruction from series with original defocus (- 13 µm) images at high tilts, 3) reconstruction from series with normal images at a fixed defocus value (- 5 µm).

Intensity profiles along 'lines' shown in Figure 2.33, are presented in Figure 2.34. From this, a contrast criterion was calculated between the intensity level of the walls of the selected nanotube (with brighter intensity) and the core of the nanotube (darker level). These relevant contrasts are plotted in Figure 2.35. As we can see from there, the tomogram No.*1* exhibits a slightly better contrast for each projection. Obviously, the contrast is linked to the resolution since a low contrast between the outer and central parts of the CNTs will decrease the visibility of their inner structure.

To get a better statistical view, several other nanotubes sections have been analysed in the same way, as illustrated in Figure 2.36, where all calculated contrast values are normalized in the same range. Then the average values of all measured sections for each tomogram are shown in Figure 2.37. As we can see, the first tomogram which was reconstructed from the image series associated with focus-corrected images is slightly better than the other two. However, we should state that this improvement is not essential in the present case. [Liu2012a]

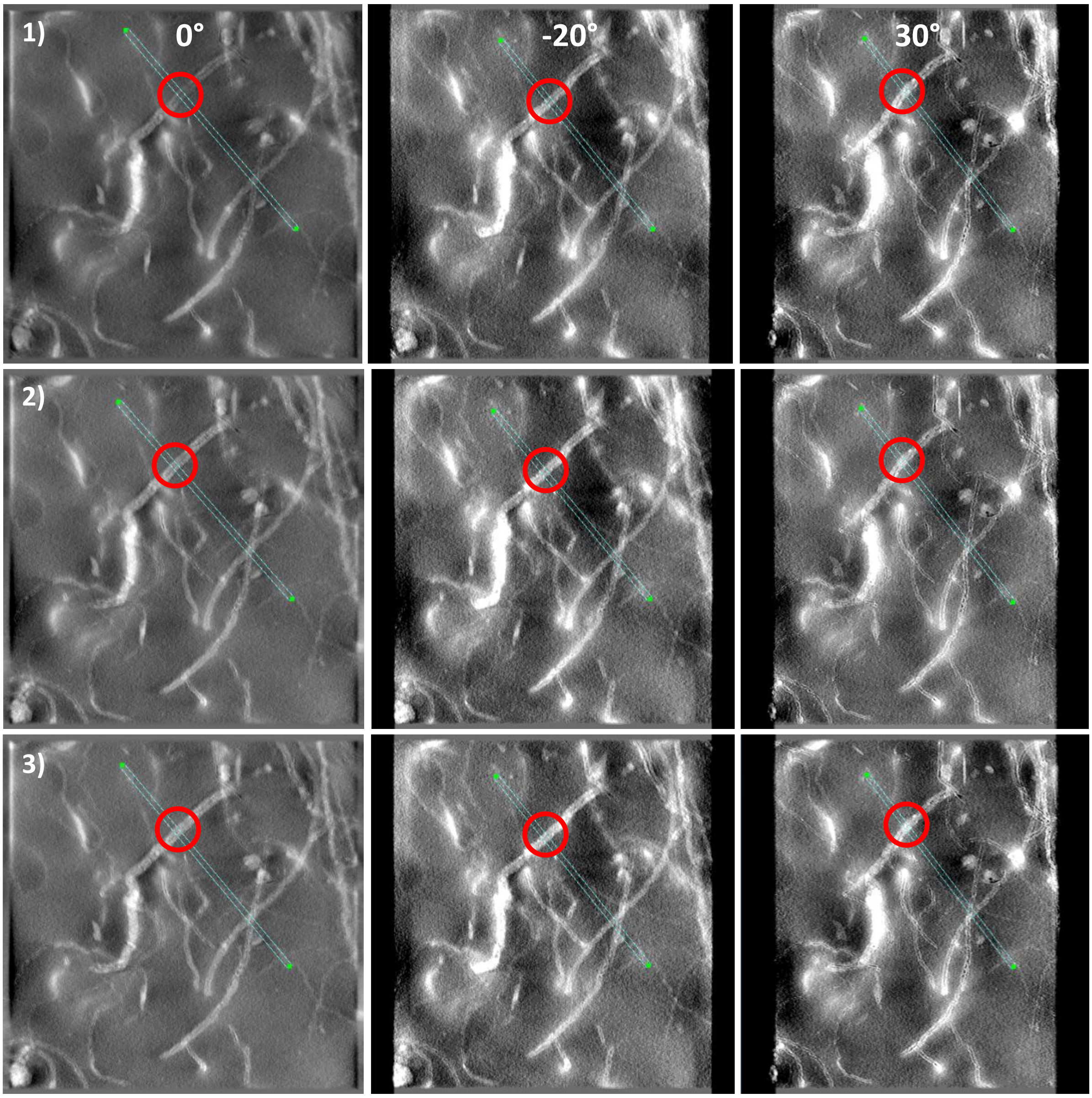

Figure 2.33: Tomogram projections at 0°, - 20° and 30° of *1)* reconstruction from series with focus-corrected images at high tilts, *2)* reconstruction from series with original defocus (- 13 µm) images at high tilts, *3)* reconstruction from series with normal images at a fixed defocus value (- 5 µm). The light frame shows the intensity profile that has been extracted on each projections to define the contrast of the nanotube section circled in red.

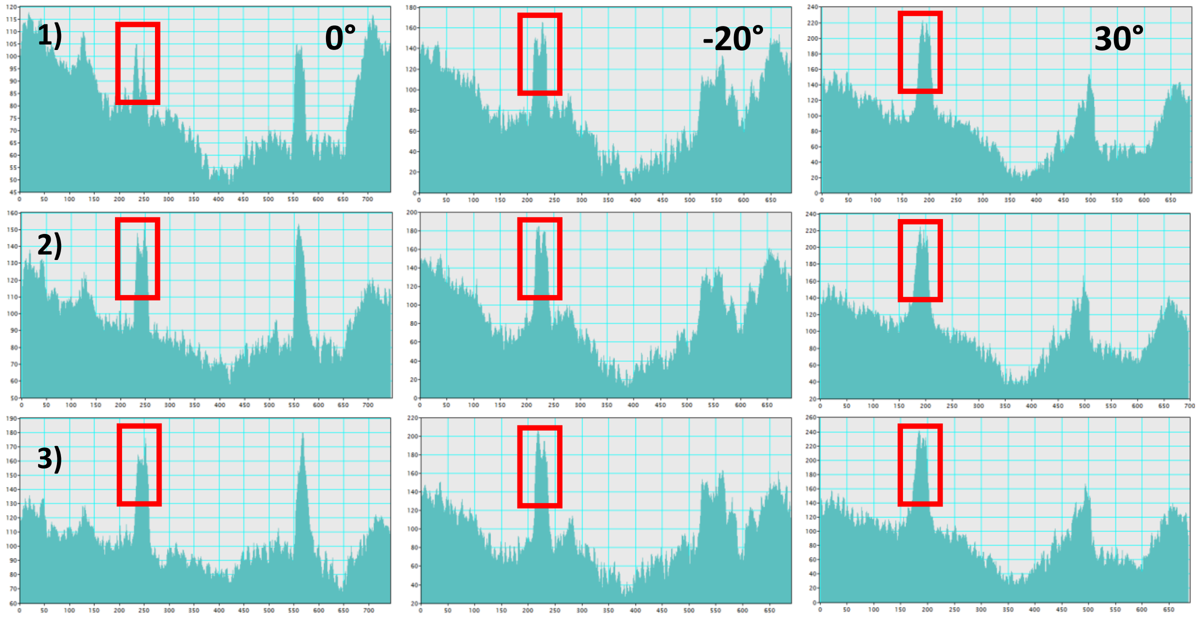

Figure 2.34: Grey level measurements of the chosen nanotube section on all tomogram projections of Figure 2.33.

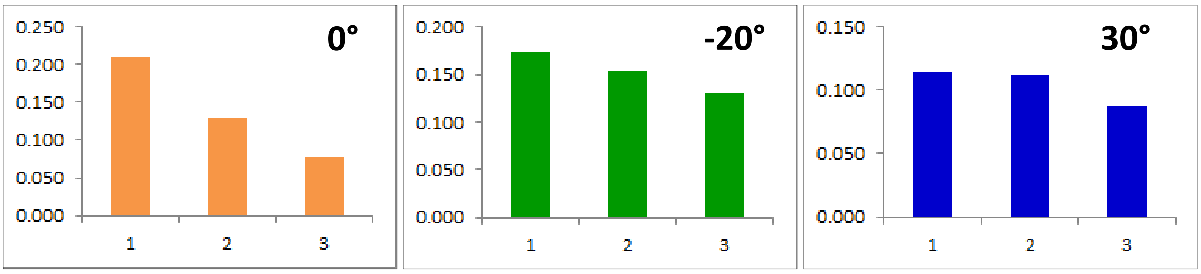

Figure 2.35: Calculated contrasts based on the measurements from Figure 2.34.

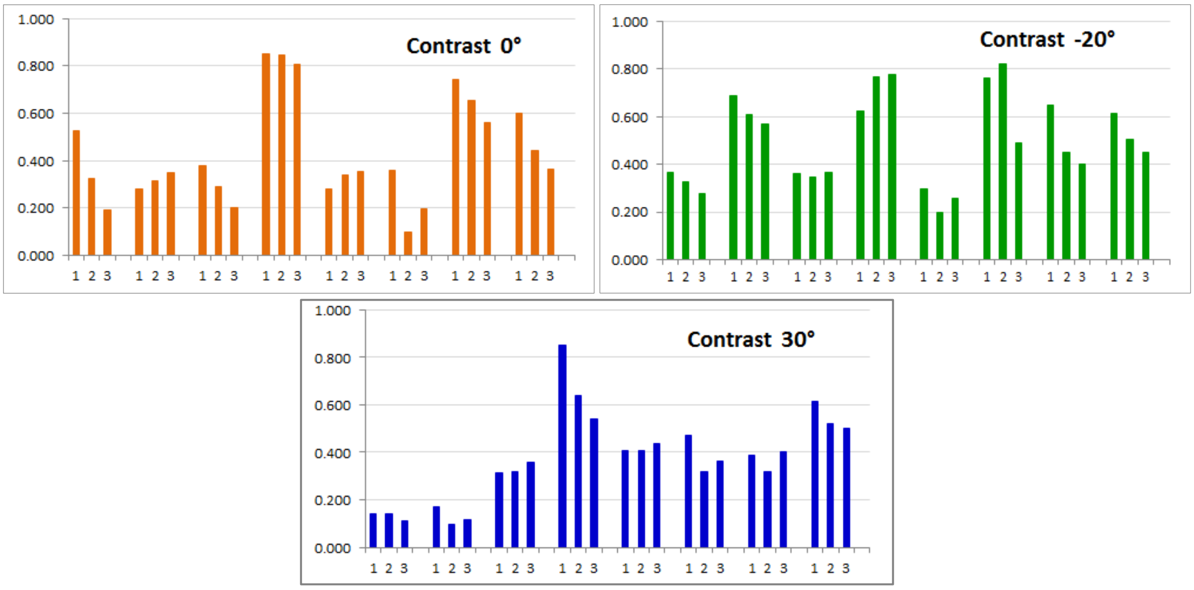

Figure 2.36: Examples of statistical contrast calculations done on several nanotube sections in the three tomograms *1*, *2* and *3*.

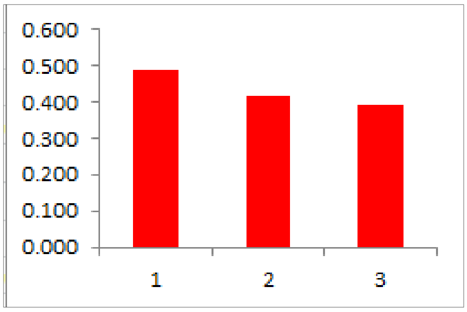

Figure 2.37: Overall average contrast calculated from the data shown in Figure 2.36 for the three tomograms' projections.

2.2.3 Cryo-EFTEM, 200kV, JEOL 2200FS

As mentioned in sub-section 2.2.1.2, observing soft materials like polymer and polymer nanocomposites at low temperature should improve the resistance of the sample during the long tomographic acquisition (whatever the acceleration voltage). We did not have a cooled specimen holder compatible with the high tilt capability required for tilting tomography on the JEOL 2010F instrument at CLYM. A test experiment was thus performed on the JEOL 2200FS microscope (Figure 2.38) at *Institut Curie* in Orsay[2]; this instrument was not only equipped with a low temperature stage permitting the in-situ congelation of samples at the temperature of liquid nitrogen, but also equipped with a Gatan Imaging Filter permitting the acquisition of energy-filtered (zero-loss) images, as performed in section 2.2.2.

Figure 2.38: View of the JEOL 2200FS of *Institut Curie* in Orsay.

The acquisition of the tilting sequence was performed automatically using a commercial software from the JEOL company: after having chosen a region of interest (manual procedure), the program manages to obtain images with auto-detection of best brightness and contrast conditions, and to tilt the sample according to a predefined angular increment. During the acquisition, the user can always pause the process to proceed to some adjustments if necessary.

For our experiments, the image series were obtained at 200 kV with zero-loss filtering for both E (Evaporated) and FP (Freeze-Pressed) materials.

---

[2] Sergio Marco and Cedric Messaoudi are greatly thanked for their assistance in this experiment.

Figure 2.39 concerns an EFTEM projection series of E material obtained from - 65.43° to 64.97° using the Saxton scheme with a basic increment of 2°. Its related volume is displayed in Figure 2.40. There are also some other reconstructions done for the E material, as shown in Figure 2.41.

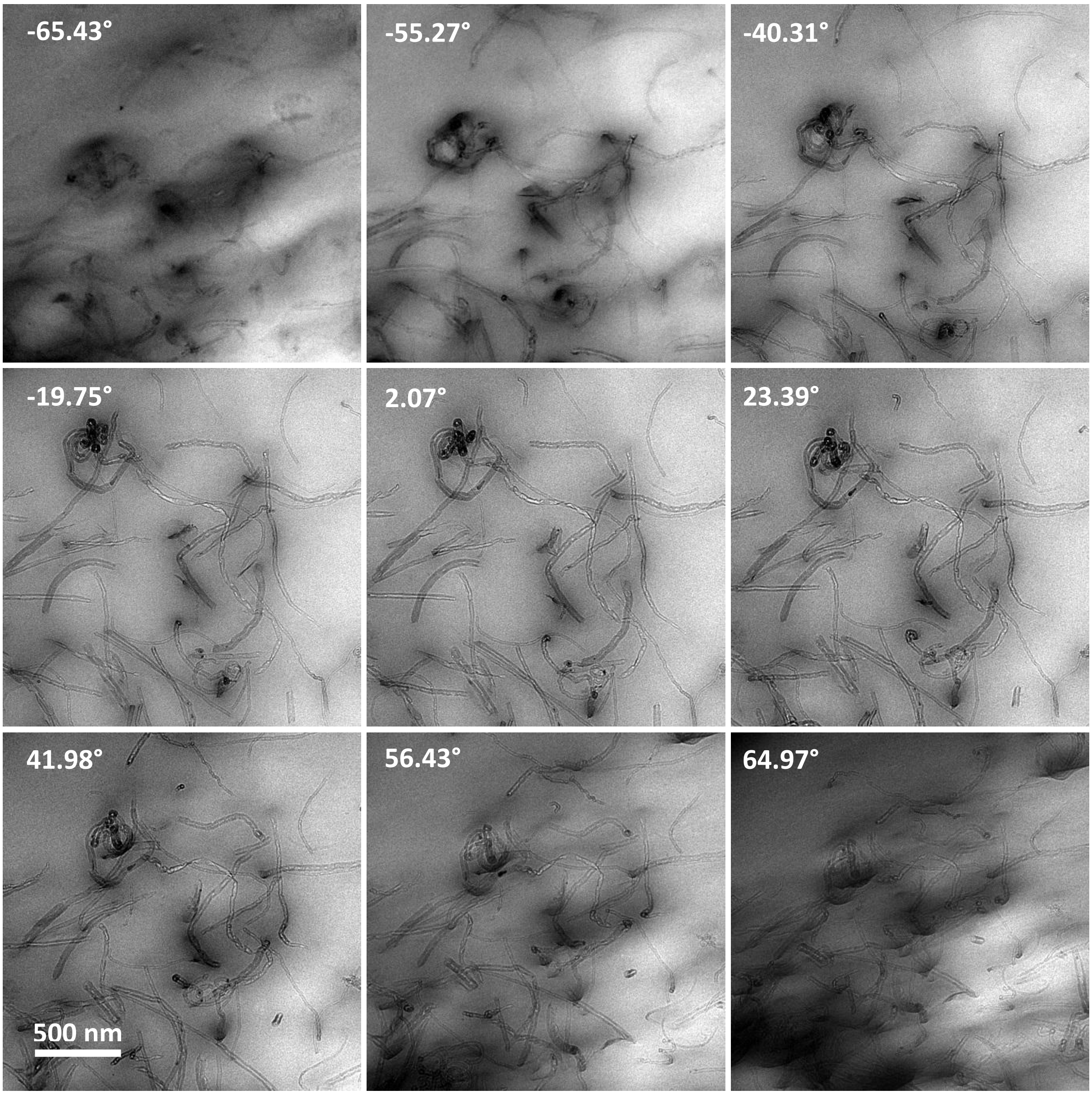

Figure 2.39: Zero-loss images from a projection series of E material.

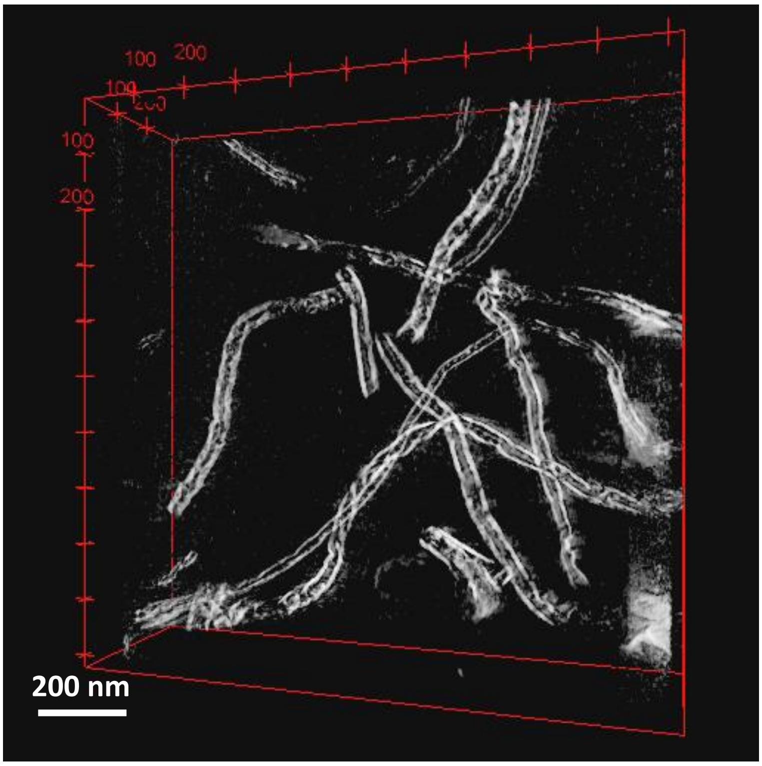

Figure 2.40: Rendering of the tomogram reconstructed using related image series of Figure 2.39.

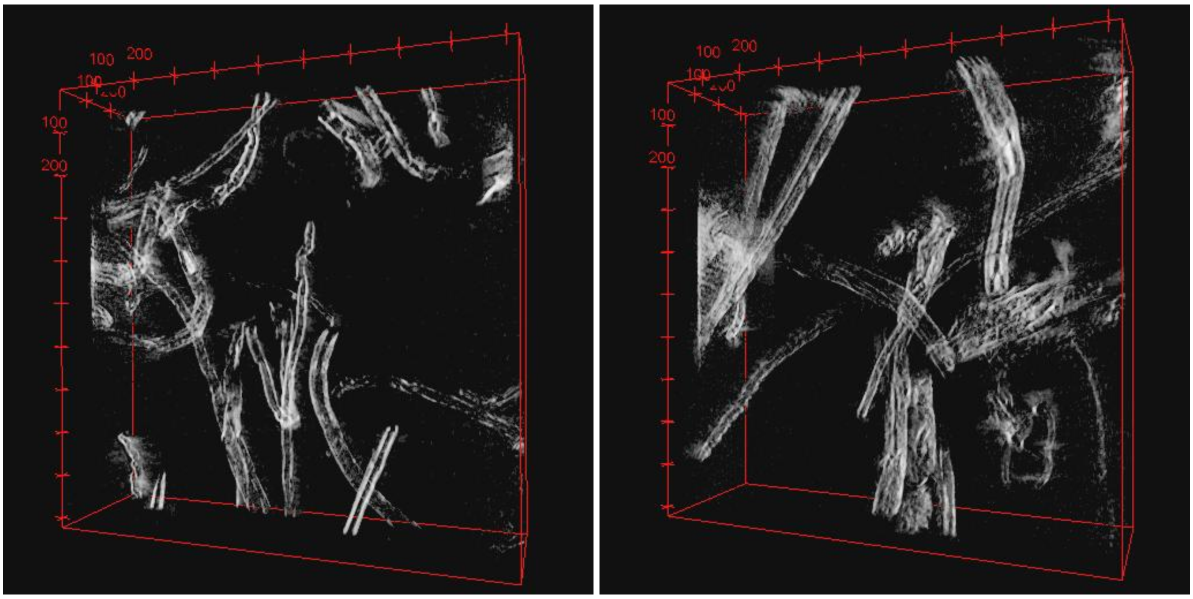

Figure 2.41: Some other tomograms of E material.

Figure 2.42 shows some images of an original EFTEM projection series for FP material, from - 55.07° to 54.16° in Saxton scheme with also a basic increment of 2°. The related reconstruction is shown in Figure 2.43.

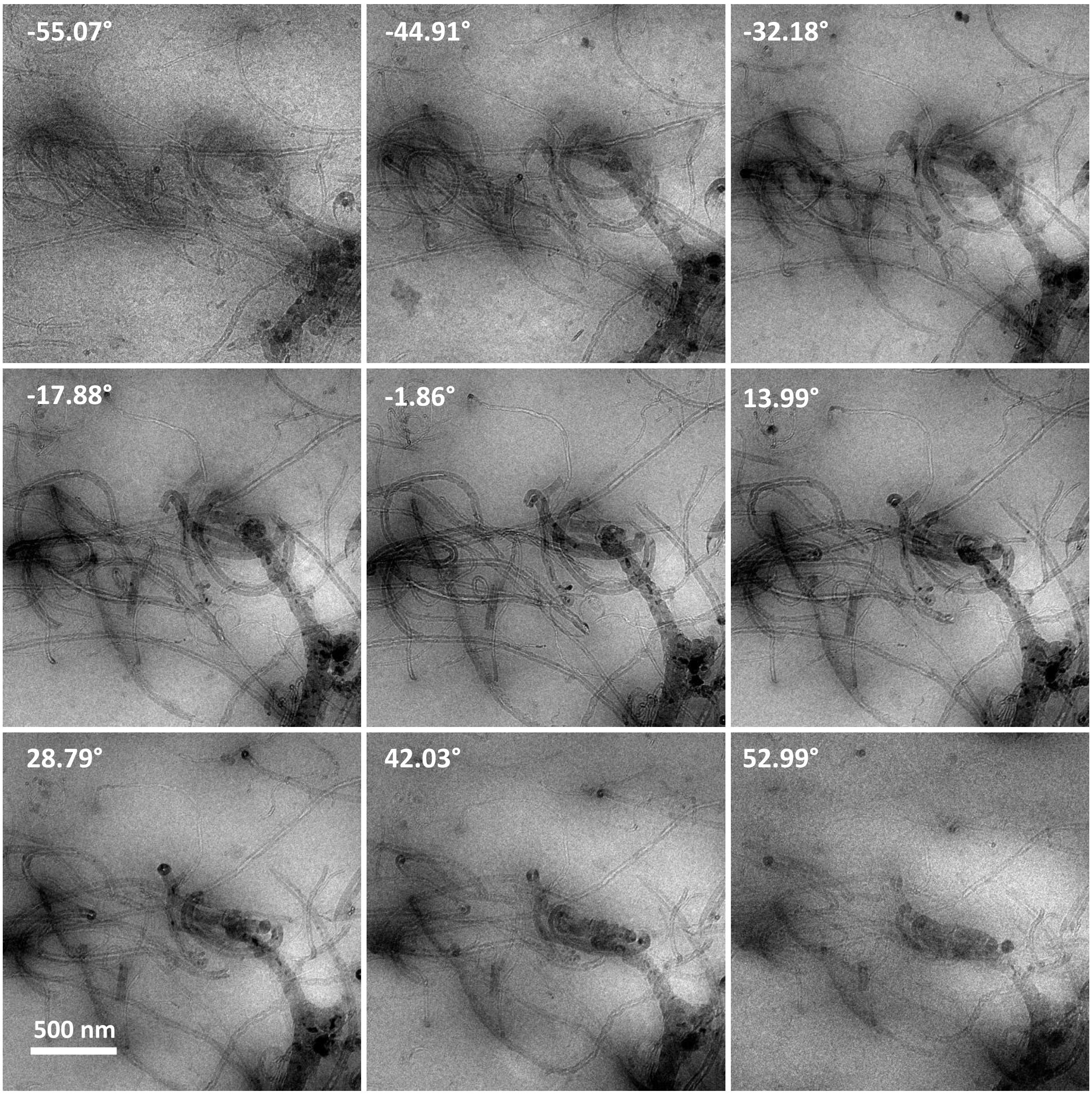

Figure 2.42: Zero-loss images from a projection series of FP material.

As we can see from all previous figures (Figure 2.39 to Figure 2.43), the quality of those zero-loss filtered series seems to be very good. Actually, they look better, in terms of resolution and contrast, than what was obtained in the two previous TEM tomography approaches. The resolution and contrast are excellent without much diffraction contrast (just a little for the extremities of the tubes); from a practical point of view it should also be added that they lead to easier reconstructions. It presents especially the great advantage of an apparent reduction of the irradiation damages producing the undesirable shrinkage effect; indeed, the samples appear very stable and the pre-irradiation was not required.

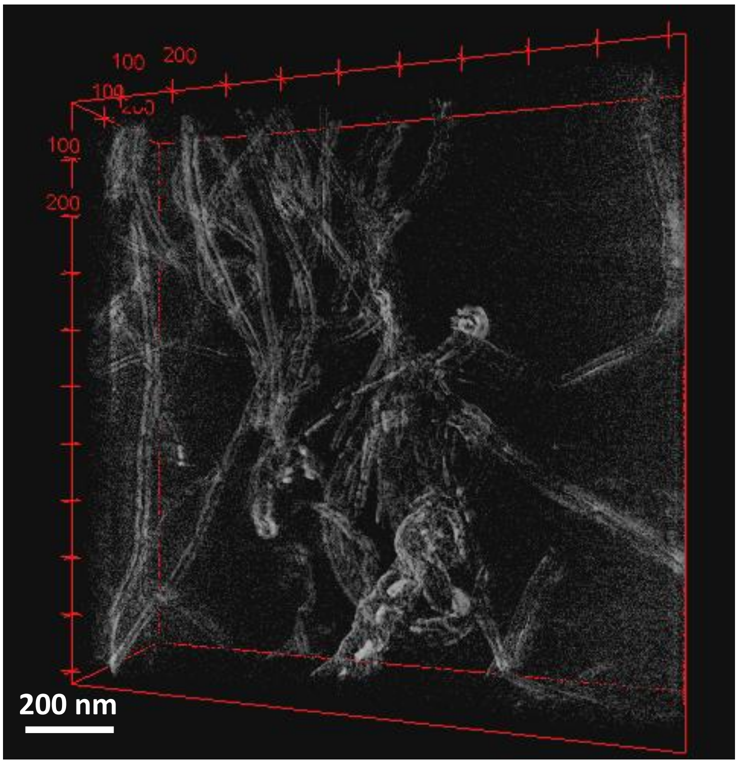

Figure 2.43: Rendering of the tomogram reconstructed using related image series of Figure 2.42.

2.3 Results of SEM tomography

The availability of the transmission mode in modern SEMs opens the way to tilting tomography in the so-called 'low-voltage' STEM (LV-STEM) [Jornsanoh2011]. The advantage is at least threefold:

- SEM is easier to handle, compared to TEM.
- SEM works at much lower voltage than TEM, which is a priori favourable in the case of beam sensitive materials, like polymer or polymer-based nanocomposites.
- When working with an Environmental SEM like it is available with the ESEM XL30 microscope installed at CLYM, we may suppress the charging effects as usually encountered with non-conductive materials.

A dedicated system was recently developed at MATEIS in order to allow tilting tomography to be easily performed in the SEM [Jornsanoh2008, thesis]; it was thus of a great interest to perform such low voltage tilting experiments on our materials, and compare them with the results obtained in classical TEM.

2.3.1 Tomo-STEM®, 30 kV, FEI ESEM XL30

As shown in 1.2.2.1, our SEM tomography uses a home-made tomography stage (called 'Tomo1') which contains 3 parts: 1) motor system for rotation; 2) eucentric system for letting the tilt axis pass in the centre of the sample section; 3) detection system for collecting transmitted electrons to form projection images.

With the help of a little pincer, TEM grids of ultramicrotomic sections can be mounted, which means that same grids could be used both in TEM tomography and then SEM tomography. Thanks to our environmental SEM which has a large sample chamber, this tomography stage can be settled in the microscope. Implicitly, the idea of this technique came from the 'Wet-STEM' mode developed in Agnès Bogner's thesis [Bogner2005].

Before tomography experiment, the sample sections of 200 nm (prepared by cryo-ultramicrotomy and mounted on TEM grids) were usually first observed in STEM mode in ESEM using another home-made sample holder developed in MATEIS, in order to test the penetrability of electrons throughout the sections under relatively low energy electrons. Figure 2.44 shows the experimental STEM setup within the ESEM showing the grid installed in a flat position. Two experimental images at low and high magnification are shown in Figure 2.45.

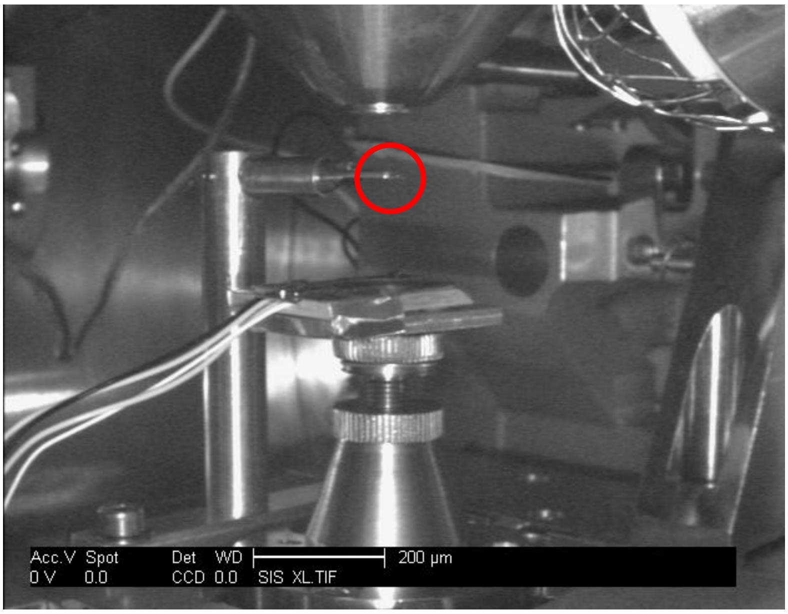

Figure 2.44: Illustration of the 'static' STEM montage in ESEM. The sample grid is visible in the red circle.

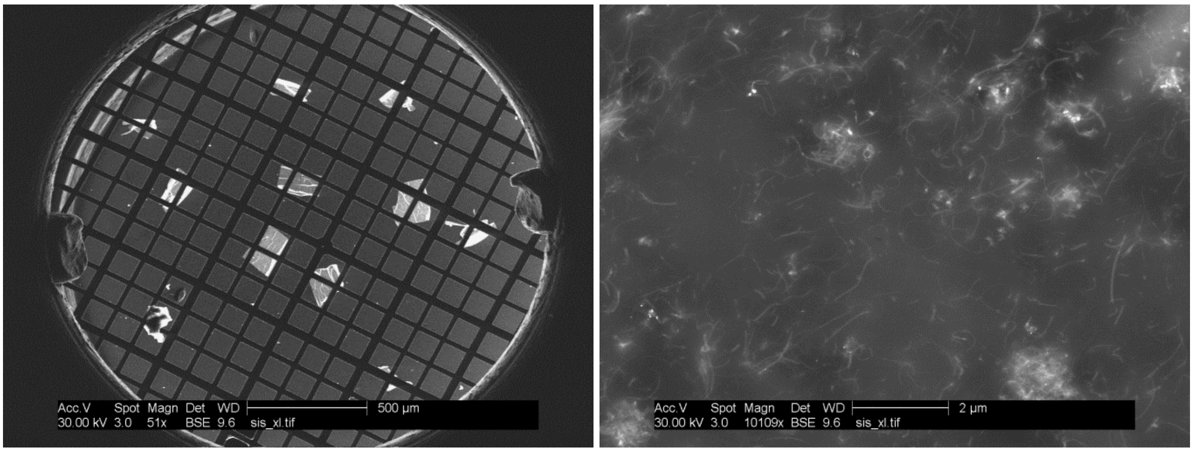

Figure 2.45: STEM mode in ESEM: a low-mag image of the grid (left) and a higher-mag image of a small area in a section (right).

After the installation of the grid on the tomography stage, the eucentric should be adjusted in order that a chosen sample section remains always in the field of view and in focus when being tilted during the experiment. This procedure is done by using an optic microscope and before installing the stage into ESEM. Images series were obtained for both E material and FP material, as shown in Figure 2.46 and Figure 2.48; they were acquired from - 70° to 60° with a tilting increment of 2°. Their corresponding tomograms are visualised as in Figure 2.47 and Figure 2.49.

As we can see from the projection images and the volume reconstructions, the STEM images in ESEM exhibit a large field of view and a reasonable good contrast between the nanotubes and the polymer matrix.

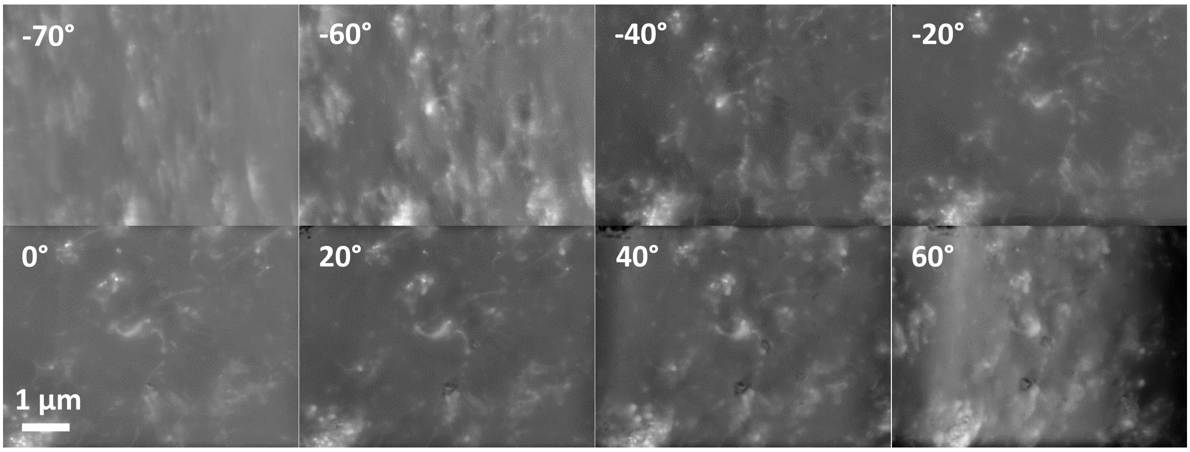

Figure 2.46: A series of low-voltage STEM projections from the E material.

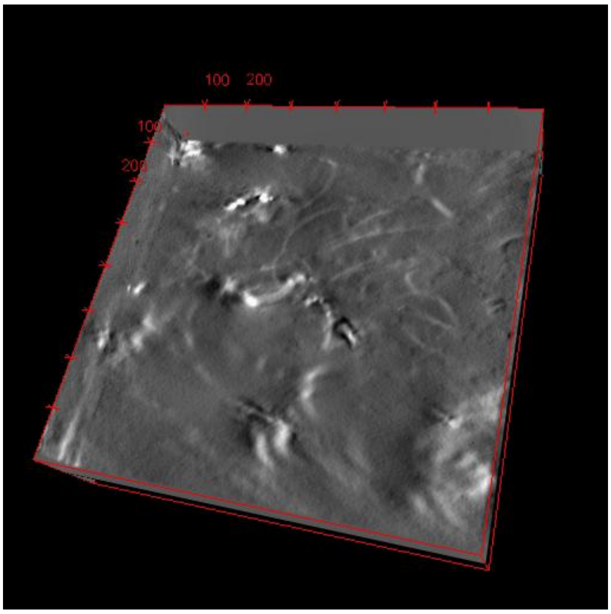

Figure 2.47: Reconstructed tomogram related to the series in Figure 2.46.

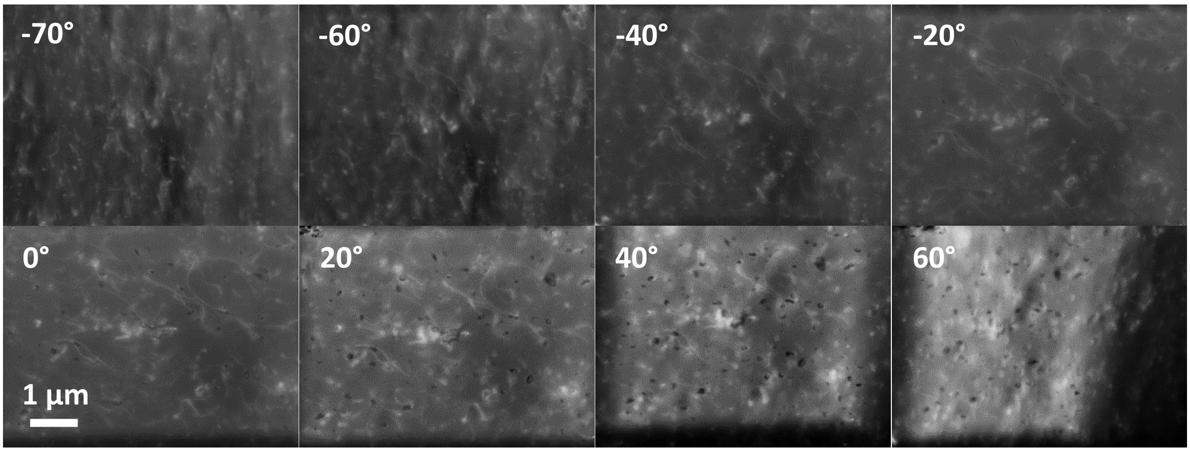

Figure 2.48: A series of low-voltage STEM projections from the FP material.

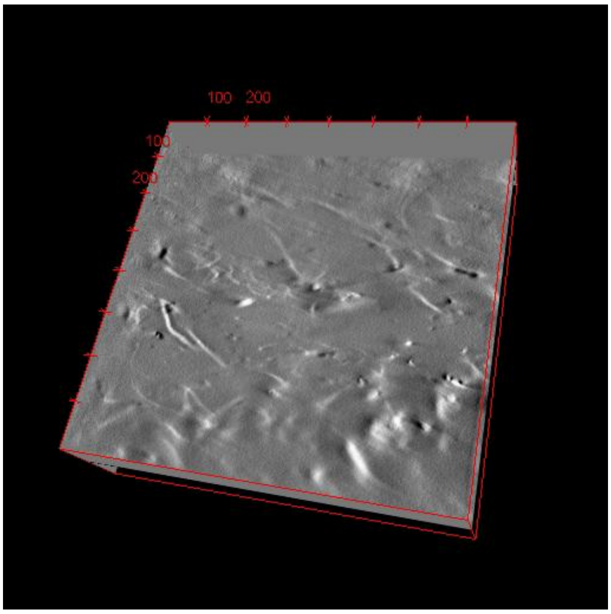

Figure 2.49: Reconstructed tomogram related to the series in Figure 2.48.

However, this approach presented some drawbacks:

- The major problem that we did encounter was a serious contamination during the (long) tilting experiment.
- Although reasonable, the contrast is not as good as in TEM tomography (and it was further affected by the contamination).

Finally, the resolution was relatively limited since in all series we could almost not resolve the CNT walls in the 3D reconstructions.

According to the collaboration existing between INSA de Lyon and the Tohoku University in Sendai, Japan, the last limitation reported just above has motivated an experiment using the cold FEG, high resolution Hitachi SEM microscope installed at IMR, Tohoku (*http://www.imr.tohoku.ac.jp/en/*). These experiments are reported in the next sub-section.

2.3.2 STEM in SEM, 30kV, Hitachi S5500 Cold-FEG

A second series of SEM tomography was then realised in the S5500 Hitachi SEM at Tohoku University in Japan (Figure 2.50; see also section 1.2.2.2)[3]. The main interests of this instrument is that (i) for the STEM mode, it directly accepts TEM specimen which are indeed mounted on a TEM specimen holder of good mechanical stability, and (ii) the cold FEG system provides an excellent spatial resolution. However, it suffers the problem of limited tilt amplitude of ± 40° due to the limited space available in the chamber below the objective lens.

---

[3] The assistance of Professor T. Konno (IMR, Tohoku University) is gratefully acknowledged for these experiments.

Figure 2.50: General view of the S5500 Hitachi microscope at Tohoku University (Sendai, Japan); on the right side, the tip of TEM specimen holder (compatible with the STEM mode in the SEM) is shown.

Several images series were then obtained at 30 kV between ± 40° with a tilting step of 1° for both E and FP materials, as shown in Figure 2.51 to Figure 2.56.

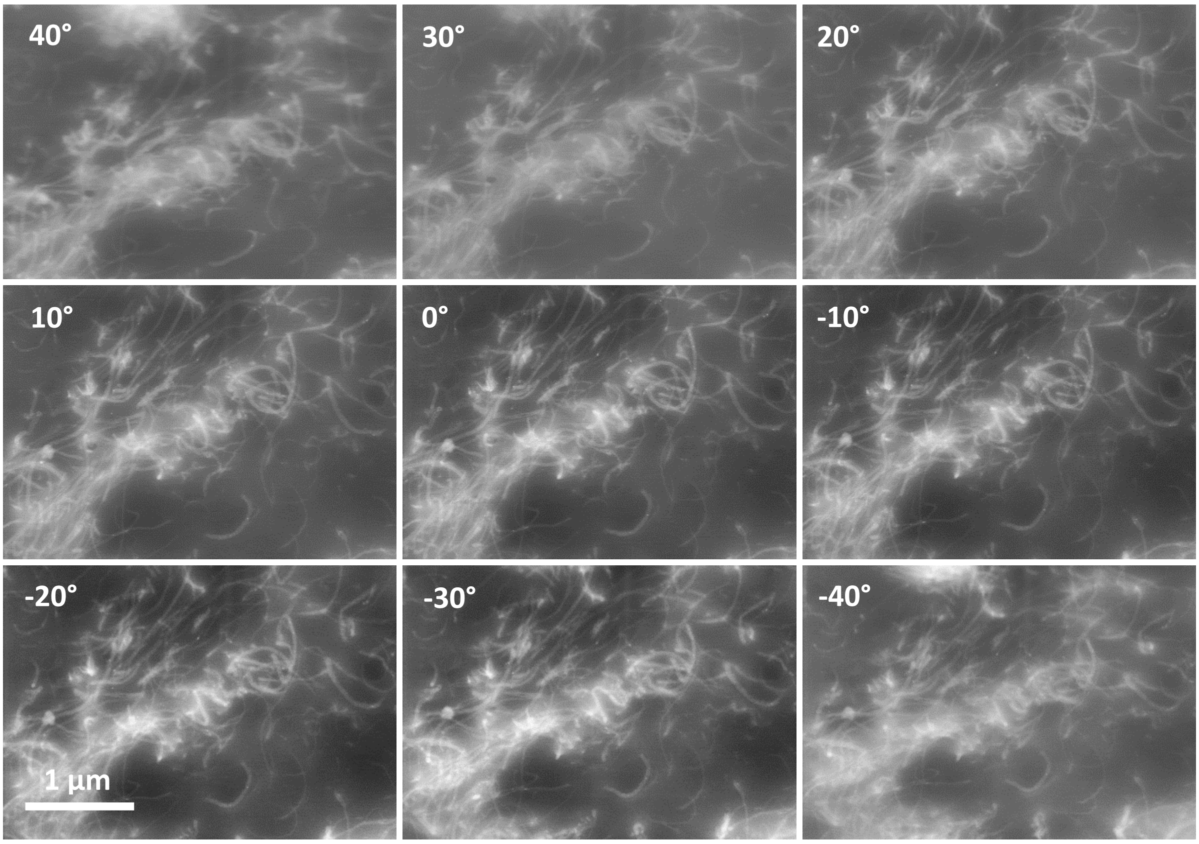

Figure 2.51: A series of STEM projections from the E material.

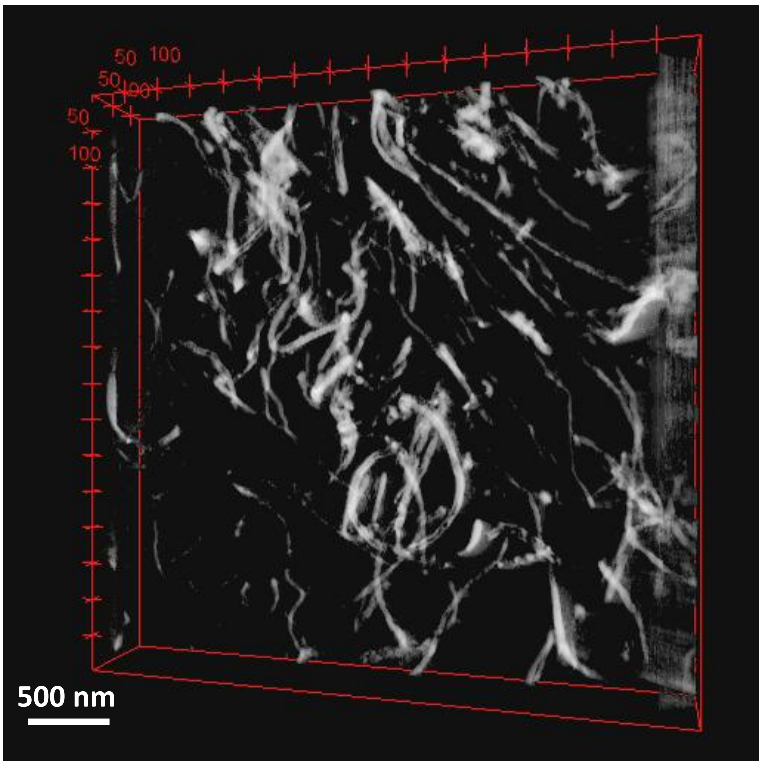

Figure 2.52: Reconstructed tomogram related to the series shown in Figure 2.51.

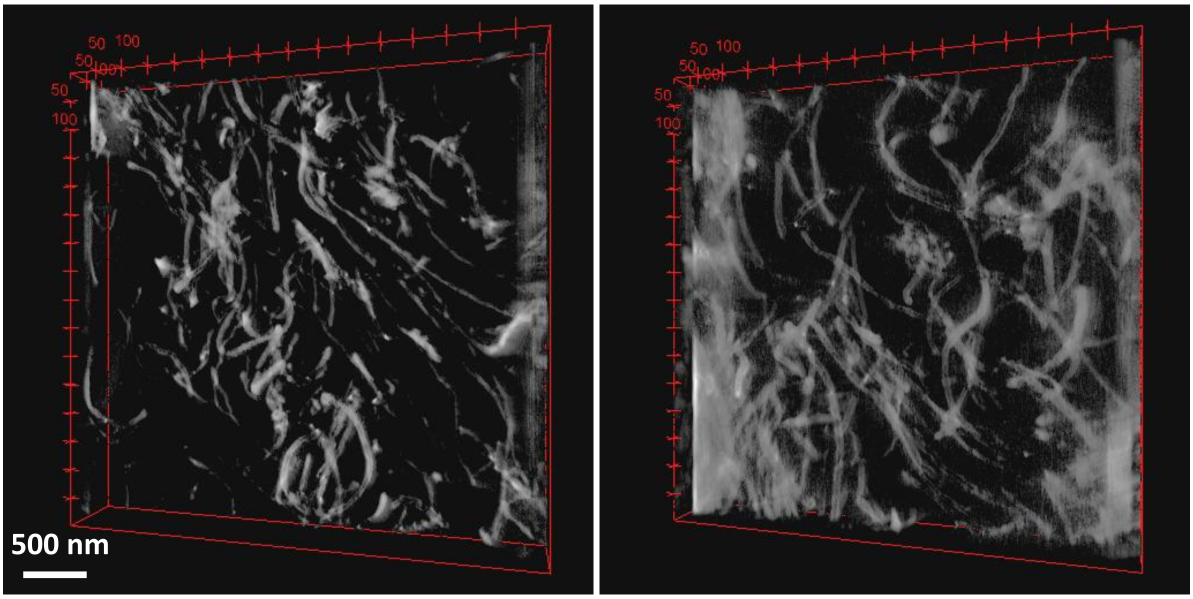

Figure 2.53: Illustrations of other reconstructions done for E material.

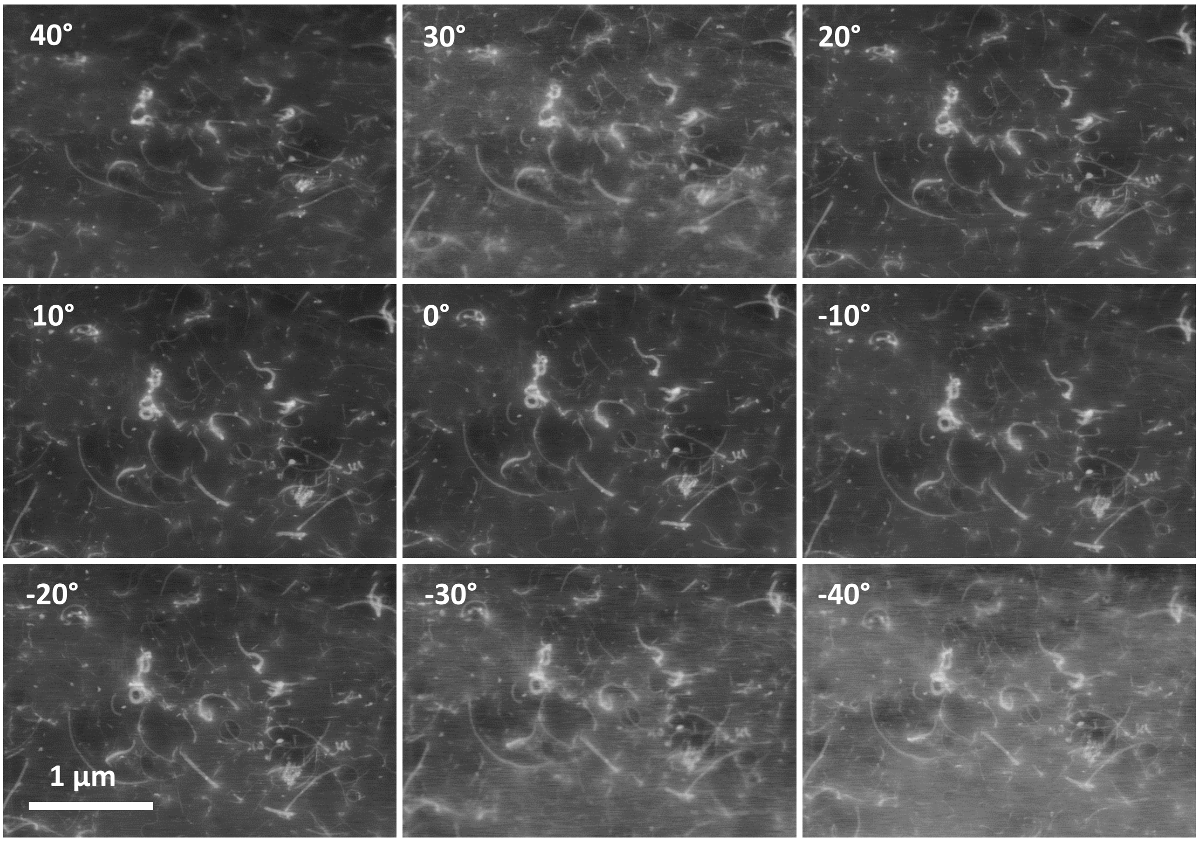

Figure 2.54: A series of STEM projections from the FP material.

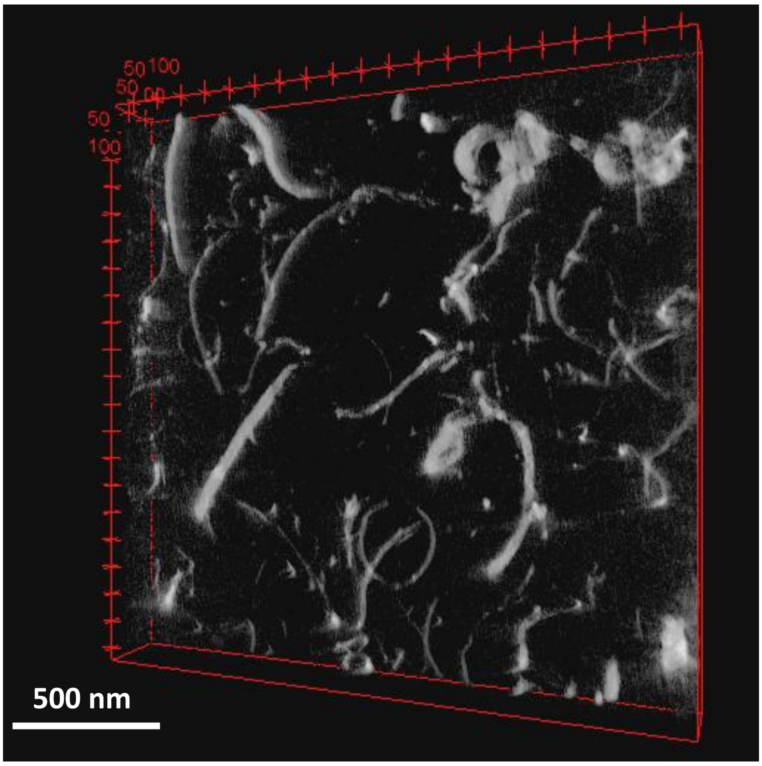

Figure 2.55: Reconstructed tomogram related to the series shown in Figure 2.54.

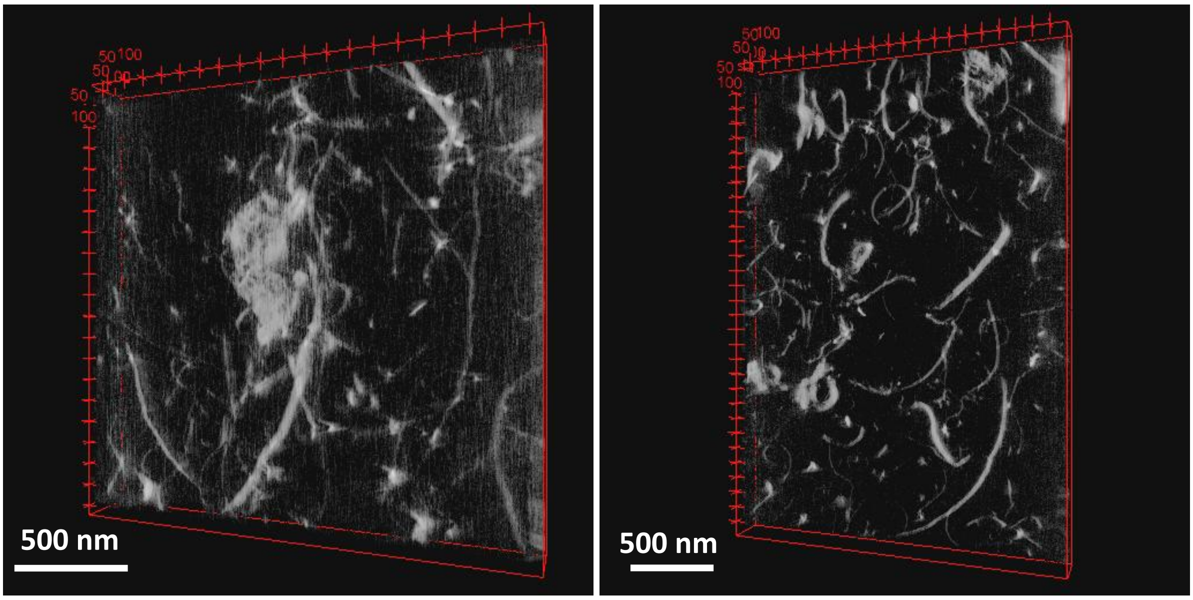

Figure 2.56: Illustrations of some other reconstructions done for FP material.

As expected, the comparison of present results (Figure 2.51 to Figure 2.56) with the data acquired in the ESEM (Figure 2.46 to Figure 2.49 in sub-section 2.3.1) indicates that SEM tomography in the cold FEG instrument provides a better contrast and resolution than in the ESEM. More importantly, the reconstruction quality doesn't look like to be significantly affected by the smaller tilt amplitude (then the larger 'missing wedge' [Midgley2003]) possible in the Hitachi unit, i.e. ± 40°.

We also tried to observe a 'thick' sample, i.e. a section of 500 nm thickness from the E material; one example of reconstruction is reported in Figure 2.57. Although it is still possible to detect most of CNTs, it can be estimated that the quality is not as good as what was obtained with thinner sections. Although the thicker specimen presents the advantage of a greater volume (then, a better statistic), we did not insist in this direction but concentrated on 200 nm samples.

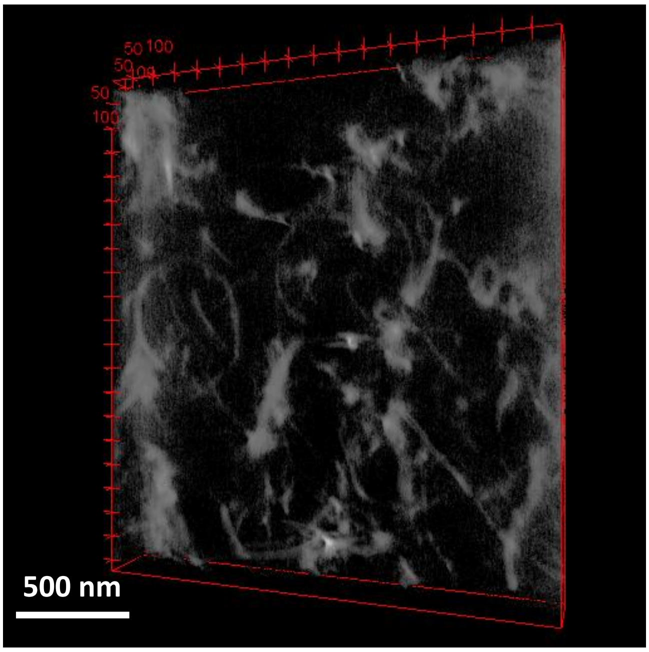

Figure 2.57: Rendering of the reconstruction from a section about 500 nm thick from E material.

2.4 First try of FIB/SEM tomography, 30kV/1kV, Zeiss NVision40

The last instrument available to perform nano-tomography is the FIB/SEM double column microscope of Carl Zeiss (see § 1.1.2.3) recently available at CLYM-Lyon. The newly installed machine and the basic tomography experiment were already presented in § 1.2.3.

Compared to tilting tomography in SEM or TEM, tomography in FIB offers the tremendous advantage of a true tomographic approach, i.e. the 'slice-and-view' approach (see § 1.2.3) [Holzer2004]. This method does not suffer the limitation of the 'missing wedge' as in any tilting tomography in reduced tilting amplitude. According to this, we intended to test the capability of the FIB tomography in the context of the CNTs-polymer nanocomposites concerned by the present chapter.

An 'E' material sample was then investigated in the FIB/SEM system. Unfortunately, this sample appeared to be a bad candidate for the technique. Figure 2.58 is a typical section of the volume analysed in 3D; as it can easily be seen, the nanotubes' ends could be distinguished, but their contrast is relatively low as compared to the polymer matrix. Indeed, a good contrast was obtained for some details, i.e. the metal catalyst particles (appearing as bright dots in Figure 2.58), of poor interest in the context of our study (except for alignment purposes for example). Furthermore, we could not avoid 'waterfall' (or called curtaining, [Orloff2003] [Ishitani2004] [Giannuzzi2005]) effect most probably associated with the presence of numerous catalyst nanoparticles.

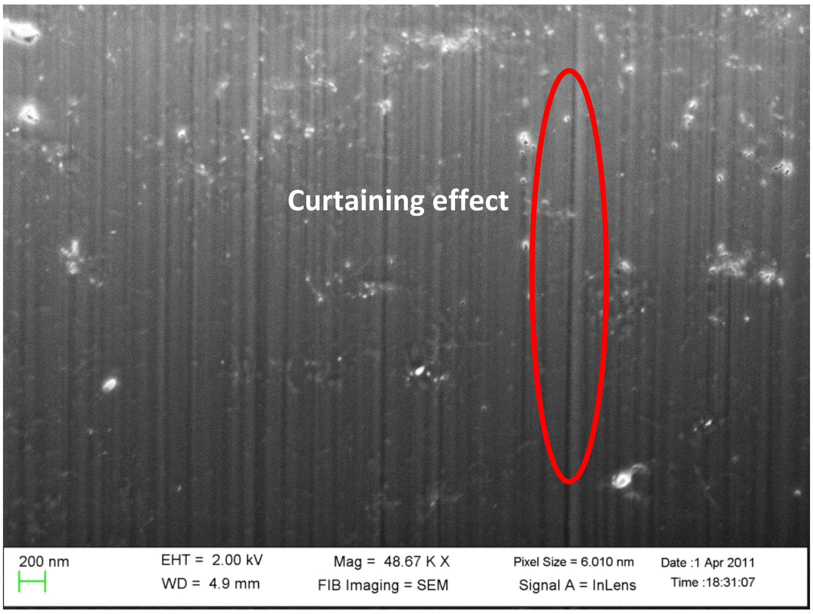

Figure 2.58: Typical SE image of a FIB-milled section of E material.

This poor imaging quality is made more obvious by the comparison with surface imaging in SEM. Figure 2.59 shows cryo-fractured surfaces observed in a Supra 55VP SEM from Carl Zeiss, where nanotubes are properly resolved even at low voltage.

But this difference in quality is not really surprising. Firstly, the Supra 55 VP works in the so-called variable pressure (VP) mode, which allows to greatly eliminate charging effects, which was not possible under high vacuum conditions in the FIB. Secondly, it must be considered that the FIB produces fresh flat surfaces when using the ion beam, which certainly does not help to bring contrast in the present case, since all CNTs are essentially perfectly cut at level of the surface. In the case of surfaces produced by cryo-fracture, it can be postulated that some part of the CNTs may emerge from the surface, which thus gives rise to a topographic contrast.

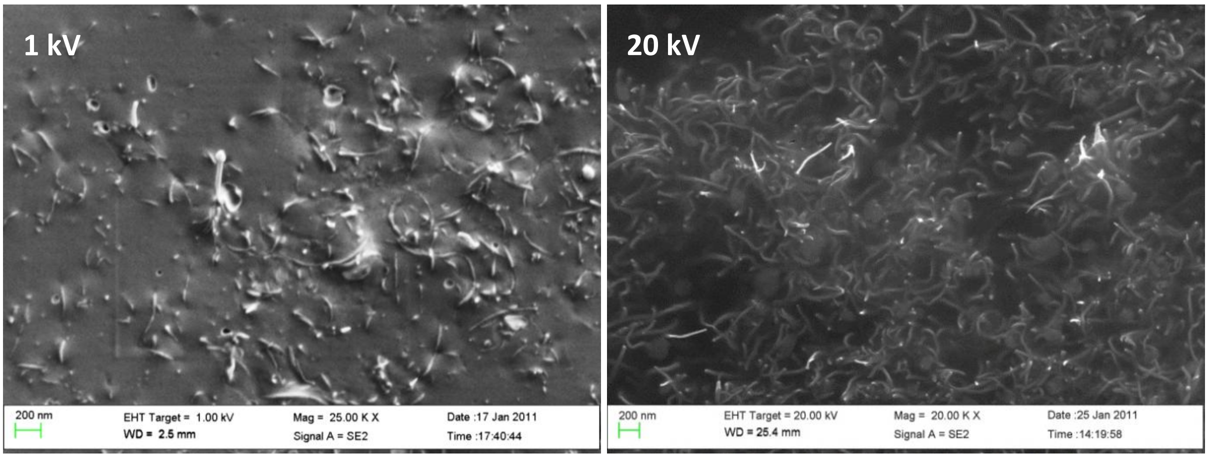

Figure 2.59: SE images obtained from a cryo-fractured ‘E’ sample in a classical SEM.

Furthermore, it was observed that the copolymer matrix easily deformed under the combined action of the ion and electron beams in the FIB. In Figure 2.60 a), a fresh area of a sample has just been prepared for a ‘slice and view’ procedure. The top surface exhibits a perturbed contrast due to a classical partial re-deposition of milled matter [Holzer2004] [Uchic2007] [Lasagni2008]. Figure 2.60 b) shows the same area after ion beam cleaning under low current polishing conditions: the lateral ‘walls’ of the area have clearly been deformed, which is indeed the evidence of a significant shrinkage of the matrix.

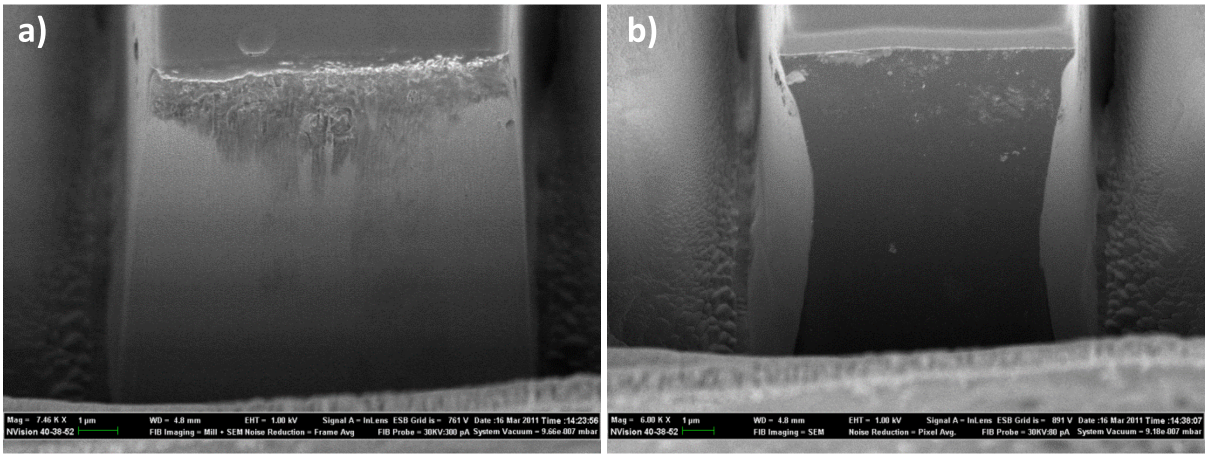

Figure 2.60: a) Typical zone of interest after cavity milling; b) polished and cleaned section (lower current milling in comparison with cavity milling) exhibiting a significant shrinkage effect.

Clearly this shrinkage will be a drastic problem in any 3D experiment, as it was in the case of TEM tilting tomography (see sections 2.2.1.2 and 2.2.1.3). In the TEM, we did observe that some pre-irradiation could stabilize the material, but it was not easy to do the same in the FIB (the shrinkage appears to be continuous during the continuous FIB slicing). More importantly, the aim of the 3D approach here is to characterize the fillers’ interactions, which will be totally affected by any dimensional changes of the matrix as evidently produced by its shrinkage.

A possible solution could be to try FIB experiments at low temperature (using a cryo-FIB/SEM system as for biological applications) in order to go under the matrix T_g of about - 7°C. However such equipment was not easily accessible at the time of the present work, and it would not have ‘solved’ the problem of the weak imaging contrast between the nanotubes and the copolymer.

According to these statements, we could not take profit of the FIB in the case of these CNTs-polymers nanocomposites. We will however see in the following chapter that FIB tomography was fortunately possible for the second system studied in the present work.

2.5 Quantification of contacts between CNTs

2.5.1 Comparison of experimental results of TEM and SEM tomography

The initial aim of studying these polymer-based materials is to quantify the CNTs contacts so as to understand the different physical properties between the two differently processed materials as discussed in 2.1. In order to achieve this goal, different electron tomography experiments were performed.

TEM tomography offers good contrast and resolution of the CNTs, but indeed this quality might be disadvantageous regarding the aim of the study: if we compare TEM tomograms (i.e., Figure 2.32, Figure 2.41, Figure 2.43) with SEM ones (Figure 2.52, Figure 2.53, Figure 2.55), it is seen that the internal structure of the CNTs (the presence of walls) is not clearly revealed in the SEM micrographs, whereas they are obviously nicely imaged in the TEM ones. Indeed this ‘lack’ of resolution in SEM can help considering the quantification procedure: since we essentially aim at quantifying the contacts between tubes, we need to binarize images and isolate the CNTs as rough cylinders, which will be more easier with the SEM micrographs compared to the TEM micrographs. Another drawback of TEM is that it provides less easily low magnification images, which is not favourable from a statistical point of view. According to this last argument, the FIB/SEM tomography would be the best choice because of the ‘unlimited’ volume reconstruction and the SEM-level resolution. But as reported in the previous sub-section, it was not possible to obtain reasonably good results on these polymer-based systems.

2.5.2 Development of a dedicated analysis of CNTs contacts

From the above, we will focus on SEM image series. In order to carry out the quantification of the interactions between CNTs, we have checked whether we could find any existing program of plugin enabling the counting of the surface contacts between objects which a high aspect ratio like the present CNT fillers. Since we did not find any reasonable solution, we have developed a home-made program in language Visual Basic, based on a pseudo-3D approach. This program proceeds in 3 steps:

- Firstly, segmented and binary SEM tomogram slices are treated so that the CNTs are described as wavy ‘cylinders’, as shown in Figure 2.61. Obviously, the quality of these segmented images is not perfect, but it will be shown in Figure 2.62 that a reasonable threshold can easily eliminate most of the noise. Each detected single cylinder is then numerically painted in a random colour, based on its geometrical continuity. This process is iterated until almost all cylinders are judged to be detected, according to a test on the failure to detect new cylinders during random tries (Figure 2.62 a)).

- In a second step, the contact between tubes is measured according to the intersection between their representative cylinders: in Figure 2.62 b), all tubes are shown in red whereas their intersections are displayed in green; from this ‘colour’ criterion, the contact areas are measured in pixels, and the surface fraction of contacts is thus calculated for each slice of the tomogram.

- The process is repeated for all segmented slices of one tomogram, and then the final average contact fraction of the whole reconstructed volume is obtained.

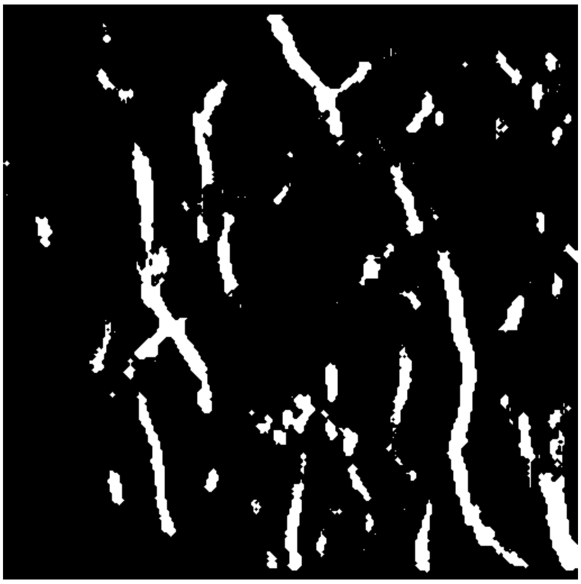

Figure 2.61: One segmented slice of a SEM tomogram to be used as input data for the quantification program.

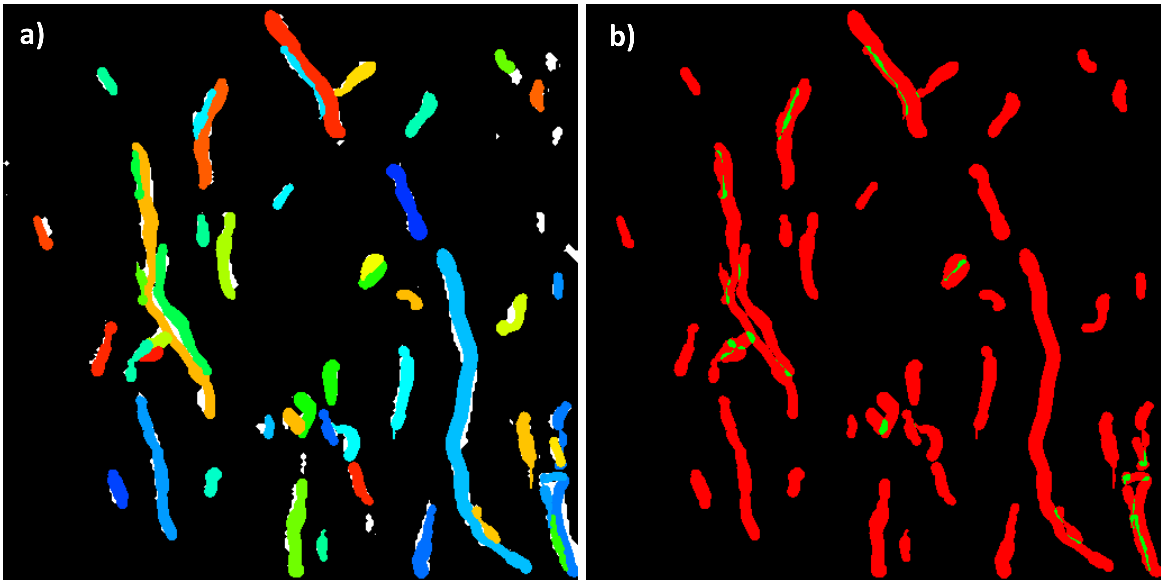

Figure 2.62: a) Tubes are detected and painted in colors in a 2D tomogram slice; b) surfaces of tubes (in red) and of their intersections (in green) serve to calculate the surface fraction of contacts.

Obviously this approach suffers a large number of drawbacks:

- The procedure is actually a 2D approach and not a 3D approach. We started with a fully 3D procedure but have to abandon the idea because of the computing time needed for a true 3D treatment. Moreover it is believed that this 2D approach is not a real problem since, the surface of each contact is simply discretized according to the voxel size (6 to 10 nm): this would be a serious problem for an absolute quantification, but not strictly for comparing two materials.
- As can be seen from Figure 2.62 a), the 'filling' of the real CNT projections as cylinders is not perfect, but we could not reduce this inaccuracy because of the noise level of the starting images.

- The contact surface is measured as an intersection of surfaces rather than a real contact surface; again, we believe that this error is similar in both materials and would not affect the comparison between their respective microstructures.

In order to give some additional information, we report here some details about the algorithms used during these calculations:

A first routine intends to describe a given cylinder as a 'broken line'. For the determination of one single cylinder, the starting point is a random 'white' pixel P_i which is a seed to fill the tube (cylinders are white in binary images). From this first position, another pixel P_{i+1} within a distance l_i is chosen at random: if this second pixel is also white (Figure 2.63 a)), then the process will continue to find a third pixel P_{i+2}, assuming we are travelling inside a single tube / cylinder (for this purpose, the amplitude l_i can be adjusted in order to avoid 'jumping' from one tube to another). This trial-and-error procedure is repeated so that the tube is described as a broken line; to avoid the backward propagation of this line, a simple test is made insuring that $P_iP_{i+2} > P_iP_{i+1}$ (Figure 2.63 b); some 'bad' tries are nevertheless accepted with a very low probability in order to describe properly heavily bent cylinders). An adjustable number of inefficient tries to propagate the line is the way to detect an extremity of the current tube. Then, the propagation is oriented in the opposite direction (compared to the last increments) in order to fill the remaining part of the cylinder: the second block indicates the second extremity, which means a complete description of the current cylinder.

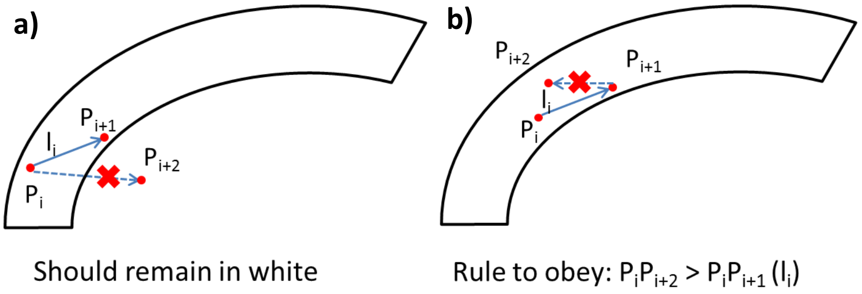

Figure 2.63: Pixel validation process for single 'cylinder' detection. a) All selected pixels should remain in the 'cylinder' of which the grey value is 1 (white level in binary images). b) Rule of distances between successive pixels to make sure that the propagation goes forward and not backward.

A second routine aims at measuring the width of the detected tube. Considering a given number of successive propagation points P_i as shown in Figure 2.64 a), the program proceeds to a linear interpolation which defines the perpendicular direction along which the width of the tube R can be measured by searching the first black pixel on each side. Then, the successive points P_i are linked with a segment of width R, which paints and defines the current cylinder as schematically represented in Figure 2.64 b).

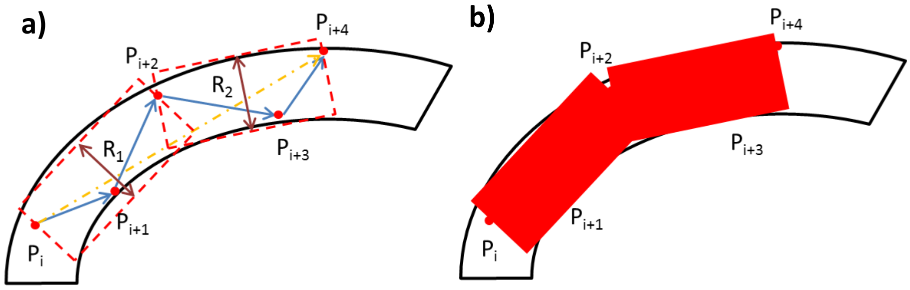

Figure 2.64: Tube determination process. a) Segments defining a tube; b) brief schema of the identified tube.

A specific case corresponds to the situation described by Figure 2.65 where two cylinders cross each other on a single slice. This geometry is actually not very probable since the slice thickness is only a few nanometers. However, depending upon the way the tubes are identified, one may end up with a different surface area (see Figure 2.66). Since very few tubes are much curved (see Figure 2.1), we add a criterion limited the angle α made by the new segment $P_{i+2}P_{i+3}$ with respect by the previous one $P_{i+1}P_{i+2}$ in order to force the propagation in the right tube.

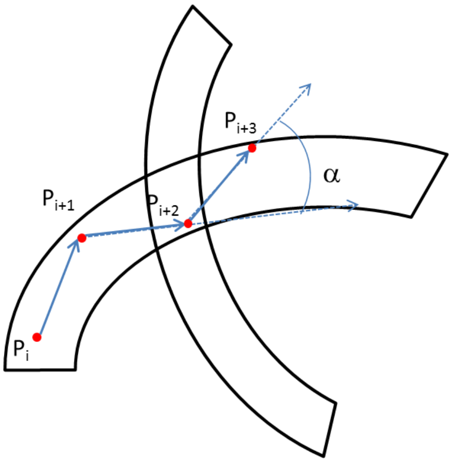

Figure 2.65: Pixel detection in the case of two crossed tubes: the angle α is limited.

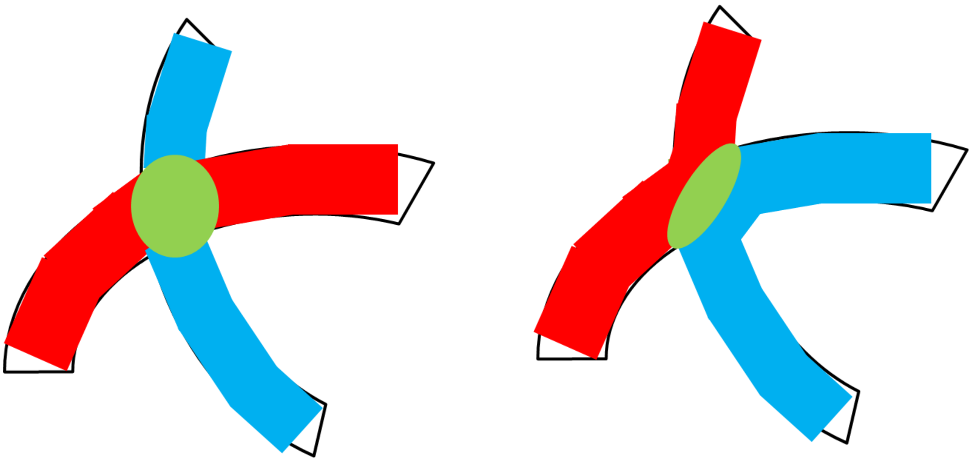

Figure 2.66: different intersection (green surface) between 2 superimposed tubes, depending upon their respective identification.

2.5.3 Results of simulations and discussion

More than ten SEM tomograms were 'sliced' and treated with this program for both materials. The results are reported in Table 2.1.

	Vol. % tubes	**Contacts/tubes ratio**	Surf. % contacts
E material	7.29 %	**2.37 %**	0.16 %
FP material	4.53 %	**3.71 %**	0.19 %

Table 2.1: Quantification of CNTs contacts [Liu2012, EMC].

A first comment concerns the fact that the volume fraction of tubes is higher than expected (3 %) for both materials. This is certainly due to a non-arbitrary selection of areas with significant amounts of fillers. Moreover, SEM microstructures in Figure 2.67 show a denser amount of fillers in the E material as compared to the FP material, consistently with our measurements. And since the E material is better at conducting (see sub-section 2.1.3), one may have naively expected that it contains more CNTs contacts. But this is not the case: the FP material contains more contacts either by the ratio of contacts vs. all detected tubes (3.71 % to 2.37 %) or the absolute measured surfaces (0.19 % to 0.16 %; this last measurement is certainly not very significant regarding the transport properties).

As already said, our measurements are certainly not very accurate, in addition to the previous limitations, we can add that the total analysed volumes remain very limited (about 4 µm^3). However, the analysis was performed in the same way on two kinds of samples treated under identical conditions, which makes us believe that it remains reasonable to use these conclusions for comparing both samples. Our findings can thus at best only be used to qualify some general trend: they indeed tend to indicate that the conduction efficiency of contacts in the FP material is less than in the E material, which confirms a previous suggestion of the sample elaborator [Dalmas2007].

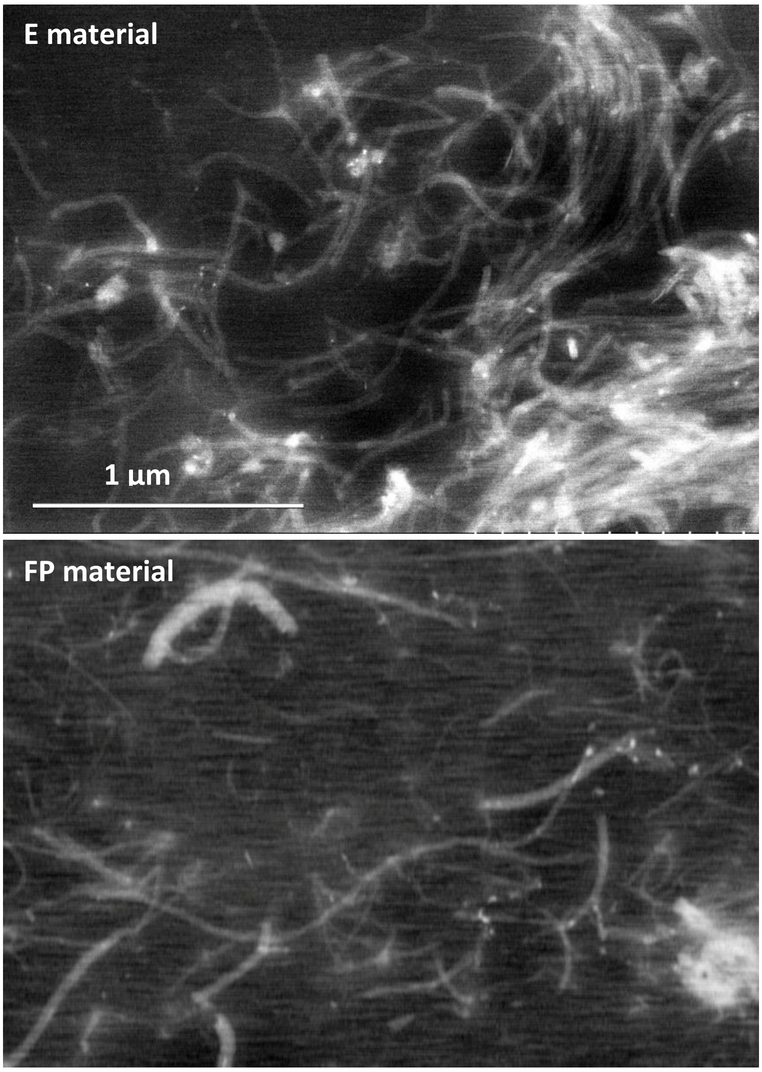

Figure 2.67: Low-voltage (30kV) STEM images in a SEM of both materials.

2.6 Conclusions and perspectives of the chapter

For TEM tomography, a classical 200 kV STEM-HAADF tomography experiment was first carried out. With proper verifications, shrinkage of the polymer matrix has been encountered. Therefore, a method for studying this undesirable effect has been proposed. As already stated in sub-section 2.2.1.3, an interesting perspective can be deduced from our preliminary approach: under certain favourable conditions, it could be possible to correct the projections from the shrinkage by an advanced image analysis using Digital Image Correlation (DIS) techniques in order to track local deformations of the material from one projection to another.

Next, EFTEM tomography (zero-loss filtering) at a relative low voltage (80 kV in a TEM) was performed. A short pre-irradiation of the sample was done before the tomographic acquisition in order to stabilize its microstructure. A small shrinkage effect was however detected for the first part of the series (images at negative tilt angles). The corresponding deformation was then manually corrected, which was shown to lead to some improvement (although not very significant) of the final 3D reconstruction. At this stage it should be emphasized that zero-loss images appear to be essential to optimise the contrast on such samples containing elements with similar atomic masses.

In the end, further zero-loss observations at 200 kV were performed on samples cooled down to the temperature of liquid nitrogen. They gave quite nice results in terms of resolution and identification of CNTs, but could not be used in the course of this study because of lack of sufficient results for a representative and comparative study.

All TEM tomographic results obtained in different instruments and imaging modes show good contrast and resolution between the CNTs and the polymer matrix; however the better conditions were clearly corresponding to the EFTEM series performed on cooled samples. A final optimization in the case of polymer nanocomposites such as those studied here, could be to perform such low temperature EFTEM experiments at low voltage, say 80 or even 60 kV as permitted in modern advanced microscopes. Although TEM tomography can offer good reconstructions for the characterisation of carbon nanotubes in the copolymer matrix, this quality did not help for the main objective of our study, consisting in quantifying the fraction of contacts between CNTs in both E and FP samples: we thus preferred to use results from SEM (low-voltage STEM) tomography for an easier treatment of data.

For SEM tomography, the relatively low electron acceleration tension is an advantage for soft materials, since undesirable beam irradiation effects are reduced. And so does the resolution. For this reason, larger reconstructed volumes can be obtained by simply working at lower magnification without sacrificing the resolution. We did perform valuable experiments in a high resolution SEM (Hitachi model installed at Tohoku University, Sendai, Japan); however, the tilting amplitude was restricted to ± 40°, which is not optimal for a titling tomography. Current developments in an ESEM performed at MATEIS should improve the existing montage available in this laboratory, and hopefully permit better 3D acquisition in a near future.

Regarding FIB/SEM tomography: this technique is certainly the most powerful one when a resolution lower than a few nanometres is not required, since it permits to analyse quite large volumes more easily than any other approaches, without any complicated sample preparation. It could however not be applied in the present case since the contrast between the CNTs and the polymer matrix was too low to allow reasonable reconstructions. Also, the problem of shrinkage of the polymer matrix was found to be difficult to control in this case (this point will be re-investigate in the next chapter devoted to a second type of polymer nanocomposites). A cryo-stage would certainly be of a great help to reduce or avoid shrinkage, as well as the undesirable 'curtaining' effect.

References of chapter 2

[Benlekbir2009, thesis] Benlekbir S. STEM-HAADF nanotomography : application to nanomaterials. INSA de Lyon (2009). *http://theses.insa-lyon.fr/publication/2009ISAL0025*

[Bogner2005] Bogner A., Thollet G., Basset D., Jouneau P.-H., and Gauthier C. *Wet STEM: A new development in environmental SEM for imaging nano-objects included in a liquid phase*. Ultramicroscopy (2005), vol.104, pp: 290–301.

[Bogner2007] Bogner A., Jouneau P.-H., Thollet G., Basset D., and Gauthier C. *A history of scanning electron microscopy developments: Towards "wet-STEM" imaging*. Micron (2007), vol.38, pp: 390–401.

[Couteau2003] Couteau E., Hernadi K., Seo J.W., Thien-Nga L., Miko C., Gaal R., and Forro L. *CVD synthesis of high-purity multiwalled carbon nanotubes using CaCO3 catalyst support for large-scale production*. Chemical Physics Letters (2003), vol.378, pp: 9–17.

[Dalmas2005, thesis] Dalmas F. *Composites à matrice polymère et nano-renforts flexibles : propriétés mécaniques et électriques.* Institut National Polytechnique de Grenoble - INPG. *http://tel.archives-ouvertes.fr/tel-00012111*

[Dalmas2005] Dalmas F., Chazeau L., Gauthier C., Masenelli-Varlot K., Dendievel R., Cavaillé J.Y., and Forró L. *Multiwalled carbon nanotube/polymer nanocomposites: Processing and properties*. Journal of Polymer Science Part B: Polymer Physics (2005), vol.43, pp: 1186–1197.

[Dalmas2007] Dalmas F., Cavaillé J.-Y., Gauthier C., Chazeau L., and Dendievel R. *Viscoelastic behavior and electrical properties of flexible nanofiber filled polymer nanocomposites. Influence of processing conditions*. Composites Science and Technology (2007), vol.67, pp: 829–839.

[Giannuzzi2005] Giannuzzi L.A., Kempshall B.W., Schwarz S.M., Lomness J.K., Prenitzer B.I., and Stevie F.A. *FIB Lift-Out Specimen Preparation Techniques. In Introduction to Focused Ion Beams, L.A. Giannuzzi, and F.A. Stevie, eds.* (Springer US), pp. 201–228.

[Hild2013] Hild, F., Roux, S. *Imagerie 3D en mecanique des materiaux*. Section *Correlation d'images volumiques*. Publisher traite MIM (Hermes), (2013).Ed. Buffiere, J.-Y., Maire, E..

[Holzer 2004] Holzer L., Indutnyi F., Gasser P.H., Münch B., and Wegmann M. *Three-dimensional analysis of porous BaTiO3 ceramics using FIB nanotomography*. J Microsc (2004), vol.216, pp: 84–95.

[Ishitani 2004] Ishitani T., Umemura K., Ohnishi T., Yaguchi T., and Kamino T. *Improvements in performance of focused ion beam cross-sectioning: aspects of ion-sample interaction*. J Electron Microsc (Tokyo) (2004), vol.53, pp: 443–449.

[Jornsanoh2008, thesis] Jornsanoh P. *Informations de volume en microscopie électronique à balayage : application à l'étude de la microstructure des matériaux et de son évolution sous traction.* INSA de Lyon (2008). *http://theses.insa-lyon.fr/publication/2008ISAL0030*

[Jornsanoh2011] Jornsanoh P., Thollet G., Ferreira J., Masenelli-Varlot K., Gauthier C., and Bogner A. *Electron tomography combining ESEM and STEM: A new 3D imaging technique*. Ultramicroscopy (2011), vol.111, pp: 1247–1254.

[Lasagni2008] Lasagni F., Lasagni A., Engstler M., Degischer H.P., and Mücklich F. *Nano-characterization of Cast Structures by FIB-Tomography*. Advanced Engineering Materials (2008), vol.10, pp: 62–66.

[Luther2006] Luther P.K. *Sample Shrinkage and Radiation Damage of Plastic Sections.* In Electron Tomography, J. Frank, ed. (Springer New York, 2006), pp. 17–48.

[Liu2011, SFµ] Liu Y., Bogner A., Epicier T. *Shrinkage study in polymer nanocomposites during electron tomography.* 12th Conference of SFµ, Strasbourg (June 27 to July 01, 2011), P-SC-12, pp: 254-255.

[Liu2012a] Liu Y., Bogner A., Epicier T., Sato K. *Energy-filtered TEM tomography of a CNTs@polymer nanocomposite.* Interdisciplinary Symposium on 3D Microscopy, Les Diablerêts, Suisse (March 5-8, 2012), S7, pp: 65-66.

[Liu2012, EMC] Liu Y., Bogner-Van de Moortèle A., Epicier T., Sato K. and Konno T. *TEM and SEM tomography of polymer-based nanocomposites reinforced by carbon nanotubes.* EMC 2012, Manchester (September 17-21, 2012), Vol. 2, PS 2.4, pp: 313-314.

[Midgley2003] Midgley P.A., and Weyland M. *3D electron microscopy in the physical sciences: the development of Z-contrast and EFTEM tomography*. Ultramicroscopy (2003), vol.96, pp: 413–431.

[Orloff2003] Orloff J., Swanson L.W., and Utlaut M.W. *High Resolution Focused Ion Beams: Fib and Its Applications : The Physics of Liquid Metal Ion Sources and Ion Optics and Their Application to Focused Ion Beam Technology,* Springer, (2003).

[Uchic2007] Uchic M.D., Holzer L., Inkson B.J., Principe E.L., and Munroe P. *Three-dimensional microstructural characterization using focused ion beam tomography*. MRS Bulletin (2007), vol.32, pp: 408–416.

3 Nanocomposites P(BuA-*stat*-MMA)/SiO_2

3.1 Presentation of the system

The second polymer-based system that we have studied is a silica-latex nanocomposites consisting in a statistical copolymer matrix made of butyl acrylate (BuA) and methyl methacrylate (MMA) (see Figure 3.1) latex reinforced by silica nanoparticles (NPs). This system was elaborated at LVCN (*Laboratoire des Colloîdes, Verres et Nanomatériaux*) of Montpellier 2 University [Tatou2011] [Oberdisse2006] [Oberdisse2007] [Genix2012].

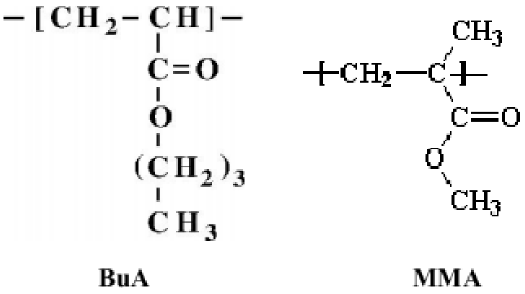

Figure 3.1: Structure of BuA and MMA.

3.1.1 Elaboration of the material

The preparation of this system involved a colloidal suspension of silica and copolymer nanoparticles. The polymer latex is from Rhodia company; the copolymer nanoparticles are hydrophobic and stabilized by a ring of hydrophilic acrylic acid in the latex. Figure 3.2 shows the sample preparation: after the mixture of both suspensions of nanoparticles, the mixed suspension is dried at 65° which constitutes a slow evaporation procedure during 5 days and leading to the film formation.

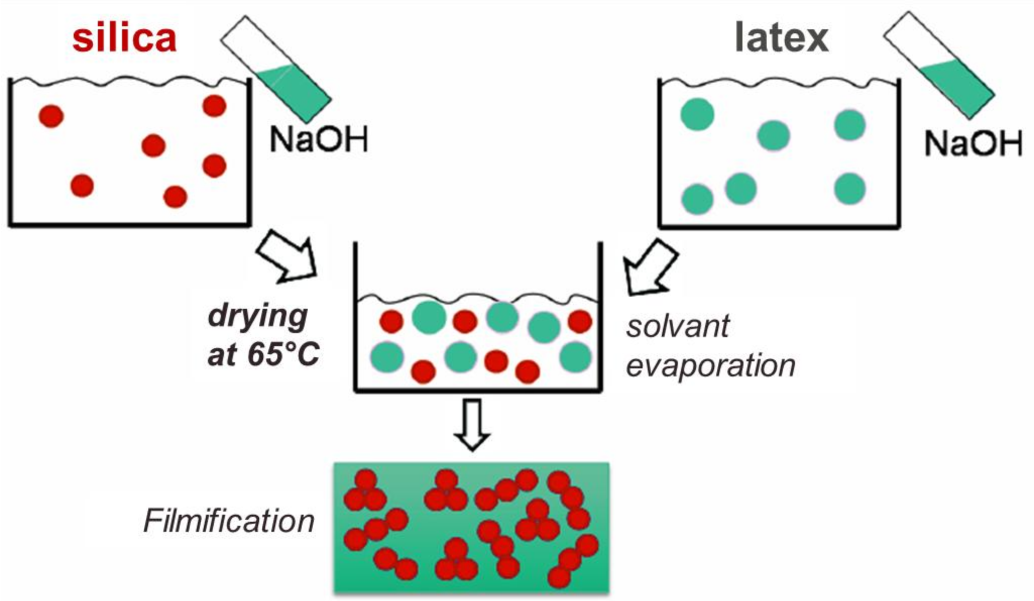

Figure 3.2: The preparation of the silica/polymer nanocomposites film. [Tatou2010, thesis]

The dispersion of silica nanoparticles (with a volume faction of 1 to 5 percent) was first characterized by small angle neutron scattering (SANS) which further allowed the shape and size of those fillers to be measured [Tatou2011]. The radius of the spherical nanoparticles was estimated to be about 8 nm (mean diameter of 16 nm). The final organization of silica fillers could be controlled by the pH value of the mixed solution. This is shown in Figure 3.3 with showing the example of a series of materials with 1 % silica nanoparticles and different pH values; the agglomeration level increased while the pH value of the suspension decreases (i.e. the acidity increases).

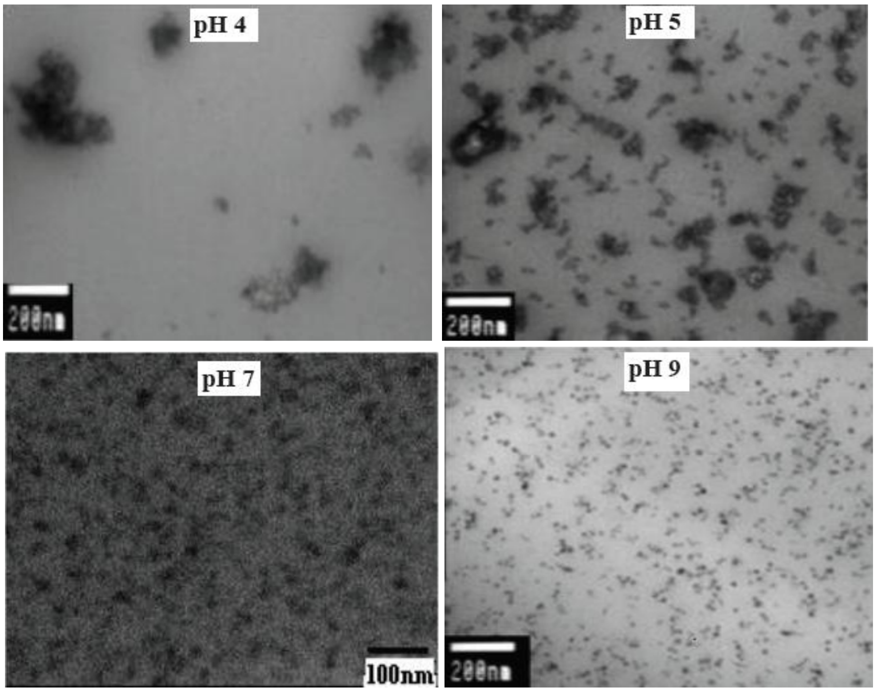

Figure 3.3: Series of nanocomposites with 1 % silica: the agglomeration level is influenced by the pH value (from [Tatou2011]).

3.1.2 Motivation of this study

The reinforcement of mechanical properties, especially rheological ones, of a pure polymer by nanoparticles is believed to be related to the interactions between particles or aggregates in the systems of interest [Tatou2011]. Former characterization tests and numeric simulations were done to verify this hypothesis [Papon2012] [Oberdisse2006] [Oberdisse2007]. In this context, electron tomography appears to be a good way to characterize the 3D dispersion of the nanoparticles and characterize both the size distribution and the aggregates structure of these fillers. Indeed such polymer nanocomposites based on a matrix reinforced by (aggregates of) spherical nanometric particles constitute an interesting test for a multi-scale 3D characterization using different electron tomography techniques (FIB, SEM and TEM).

Figure 3.4 shows the microstructure of 4 materials on which we have performed tomography experiments: two samples with 1 % silica and elaborated under pH values respectively equal to 5 and 9, and two samples containing 5 % silica with also different pH values. In all cases the nanoparticles appeared to be well dispersed in the final materials. In order to check this, we realized first some classical SEM observations on sections of the films produced by cryo-fracture.
Micrographs in Figure 3.5 were taken in a variable pressure Supra 55 from Carl Zeiss and installed in MATEIS laboratory. The low voltage mode was used to avoid charging effects since the materials are not conductive. As can be observed, the sections of the materials with the lower pH (5) are more flat than the ones with pH 9, no matter what the filler volume fraction is, which could be related to their higher aggregates concentration. From these images, it seems reasonable to consider that the dispersion of the filling particles is homogeneous in all samples; we will see later on that the tomography analysis by 3D-FIB confirms this tendency in a more quantitative way. They also show that a reasonable contrast is obtained in the SEM mode between the nanoparticles and the polymer matrix.

From these microstructures, it is very clear that in the systems elaborated under basic conditions (PH 9), the silica nanoparticles are mostly isolated, whereas under acid conditions (PH 5), they form aggregates. Since we aim at measuring both volume fractions and structure of the possible aggregates, we first have to discuss about the experimental conditions that would be needed to get quantitative and representative results.

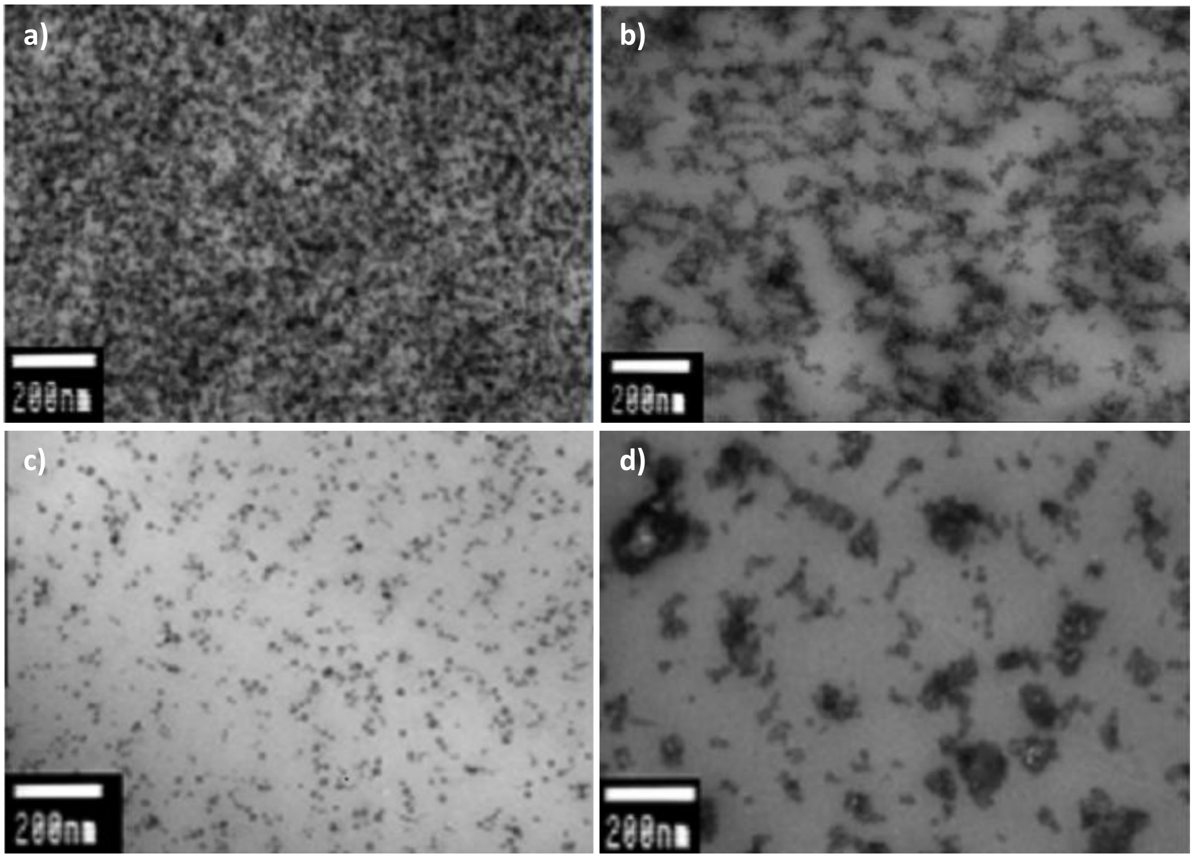

Figure 3.4: TEM microstructures of 4 samples selected for tomography experiments. a) M49, 5 % pH 9; b) M57, 5 % pH 5; c) M82, 1 % pH 9; d) M86, 1 % pH 5 (from [Tatou2010, thesis]).

3.1.3 Strategy regarding experiments

3.1.3.1 Is the SEM / FIB resolution sufficient?

The first constraint is obviously to resolve correctly the individual particles. According to their mean diameter (i.e. 16 nm), and expected relatively spherical shape, SEM imaging appears to be sufficient. Figure 3.6 and Figure 3.7 show SEM micrographs recorded respectively in the low-voltage STEM mode in an ESEM, and SEM mode in a FIB. In both cases, isolated single particles are easily resolved. The first STEM-ESEM image has a size of 1280 x 960 pixels and corresponds to a magnification of 40 K; the pixel size is 2.4 nm and the field of view is then 3.072 x 2.304 µm². This numerical resolution is thus largely sufficient to resolve single particles of a few nanometres in size. The same conclusion yields for the SEM-FIB image, with a size of 3072 x 2304 pixels, and so a field of view of 6 x 4.6 µm²: in this case, the pixel size is smaller and equal to 2 nm.

From these images however, we may doubt that it would be possible to resolve properly the internal structure of aggregates revealed in the materials elaborated under acid conditions (that is suggested in TEM images from Figure 3.4b) and d), and SEM images in Figure 3.6 and Figure 3.7).

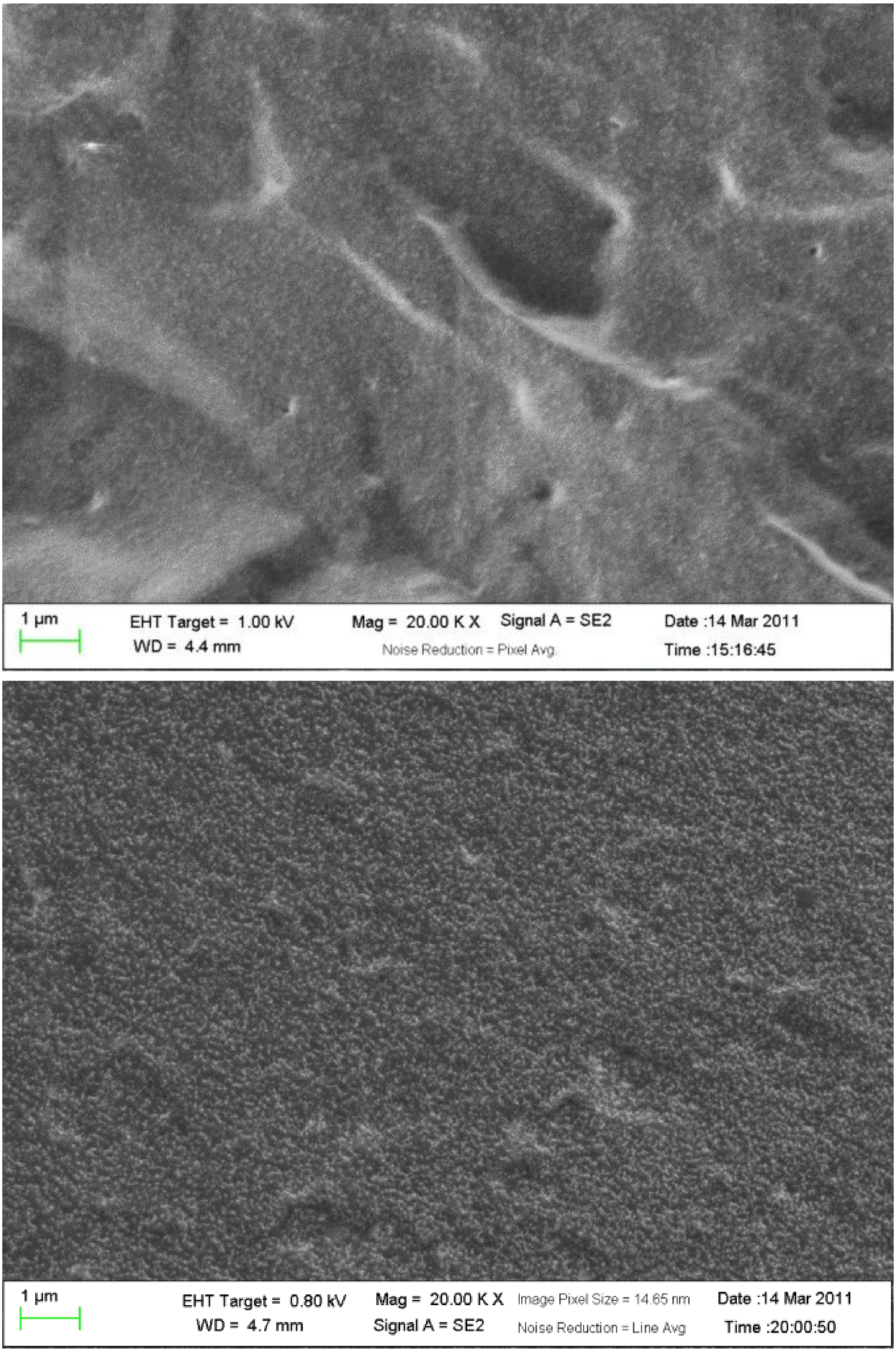

Figure 3.5: SEM images of cryo-fractured surfaces; top: M49, 5 % pH 9; bottom: M57, 5 % pH 5. (White points are silica particles or aggregates.)

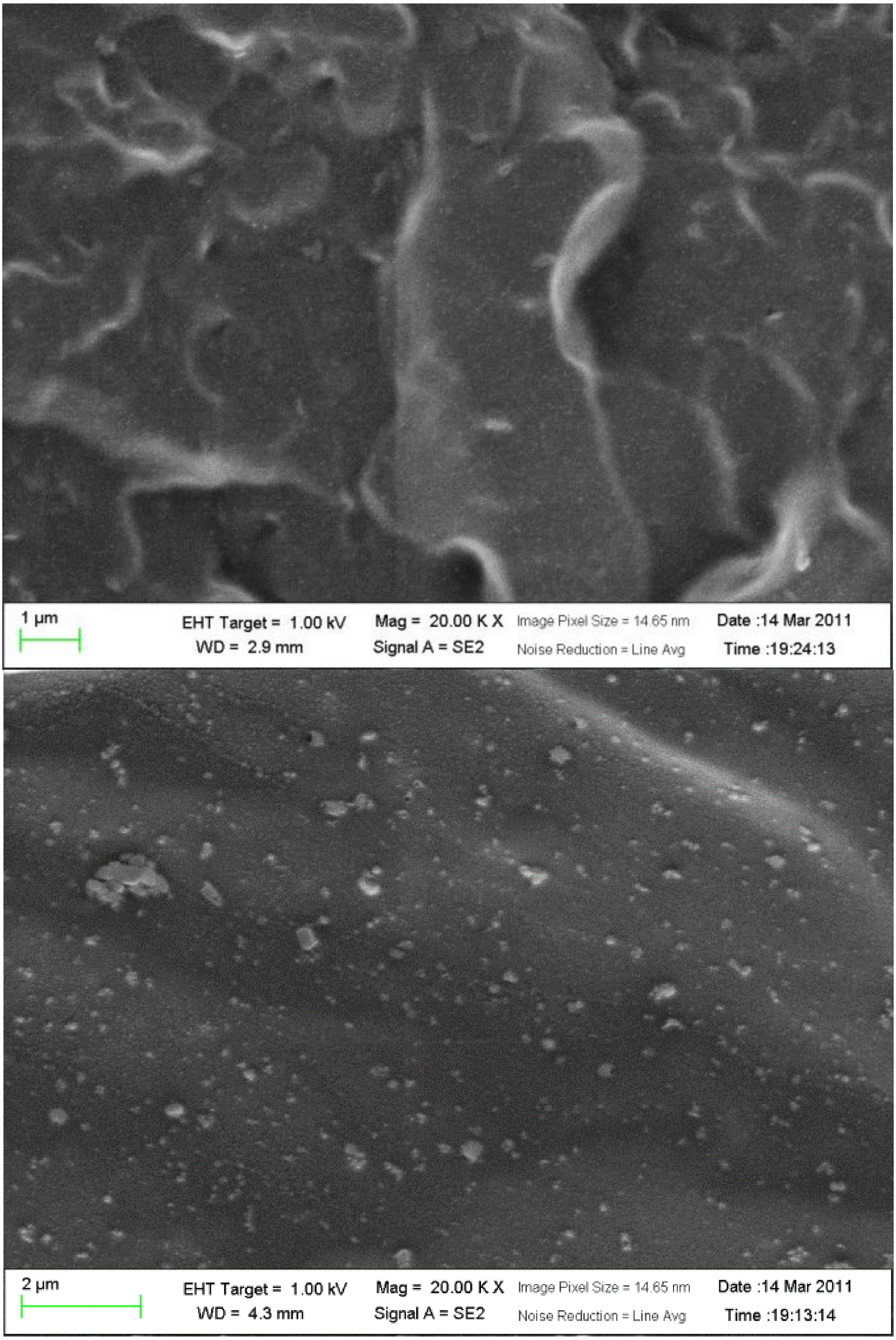

Figure 3.5 (continued): Top: M82, 1 % pH 9; bottom: M86, 1 % pH 5. (White points are silica particles or aggregates.)

Figure 3.8 is a schematic representation of the organization of the aggregates; clearly, the size of 'voids' between particles, which is indeed the polymer matrix embedded within the aggregates, can be too small to be correctly resolved in our SEM images. Thus, when evaluating the volume fraction of the silica particles, any error in the measurement of the density of these aggregates would probably lead to a significant error of the mean volume fraction. This problem does not concern the materials elaborated under basic conditions, for which we may expect than FIB tomography or low-voltage STEM tomography in the ESEM would be sufficient to get a correct estimation of the volume fraction. However it is highly preferable to adjust the same conditions for studying all samples, and the strategy employed will then be dictated by the most severe constraints imposed by the aggregates.

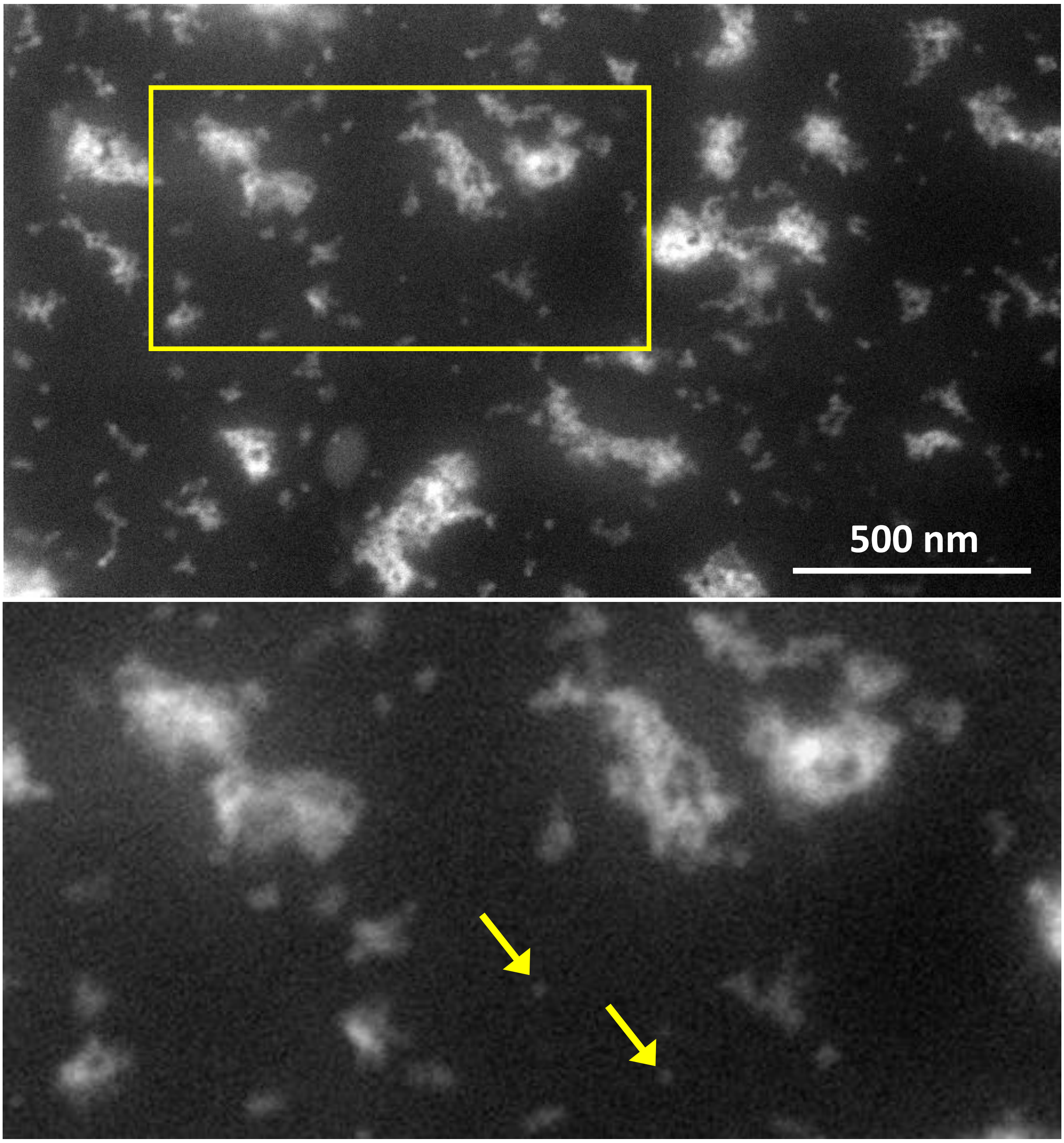

Figure 3.6: Low-voltage STEM image of a 200 nm thick ultramicrotomic section of the M86 sample. The frame in the top image is enlarged at bottom; arrows indicated isolated single silica particle, with a measured size equal to 16 nm. Note that most aggregates, seen here in projection over a 200 nm thickness, are clearly not fully dense.

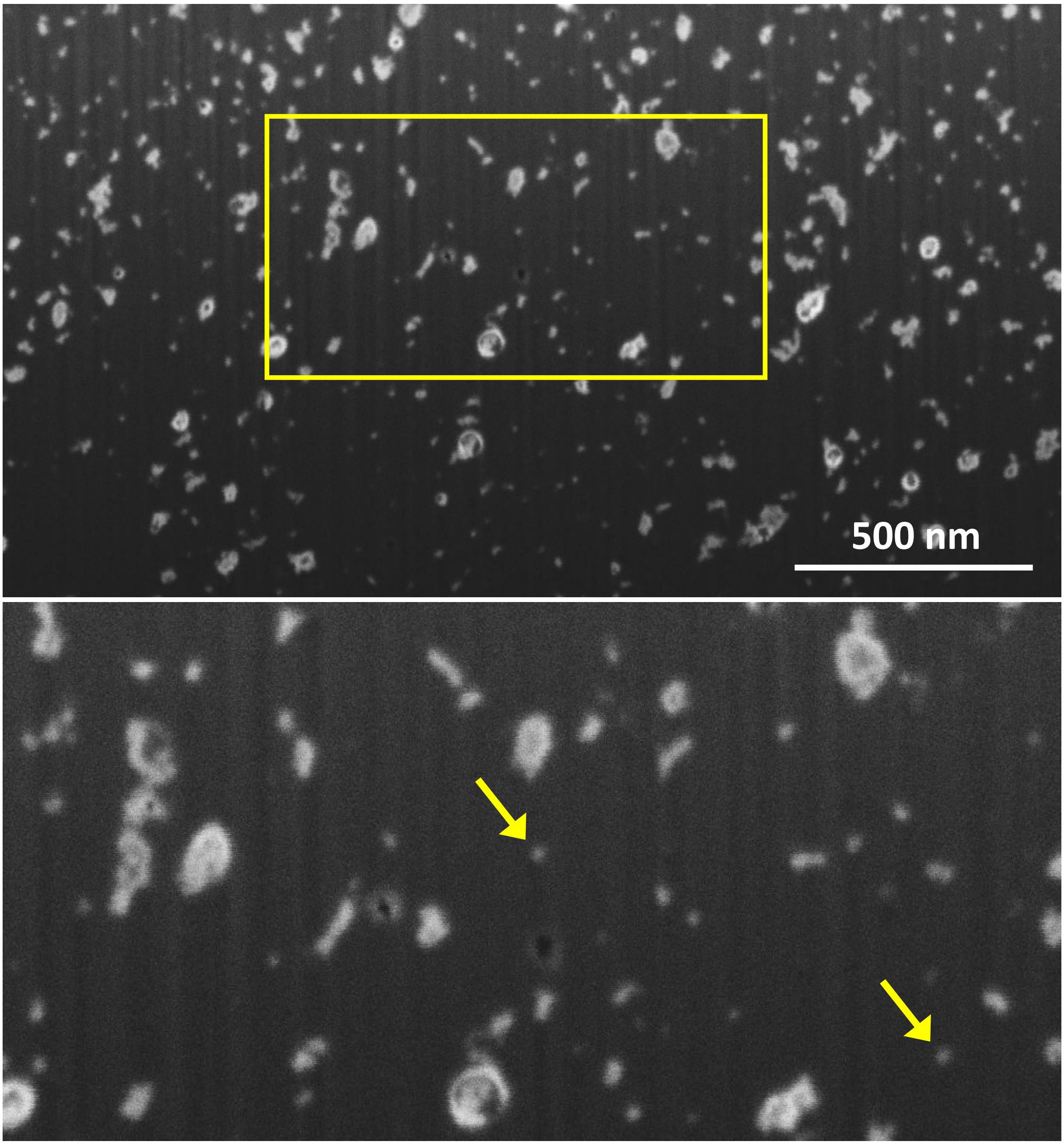

Figure 3.7: Same as Figure 3.6 for a SEM picture taken after slicing in the FIB instrument. Compared to Figure 3.6, aggregates look smaller because the image reflects only the surface. Because of the FIB cut, sections of particles, smaller than their diameter, are also resolved.

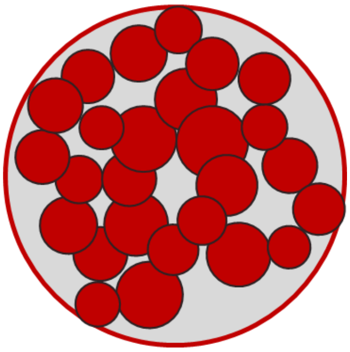

Figure 3.8: Sketch of the structure of aggregates in the M86 and M57 samples elaborated under pH 5.

According to this, we have two different possible strategies: the first one is to improve the magnification of SEM and FIB images in order to get the better resolution and resolve the “hidden” matrix within aggregates. The second option is to perform tomography under low-resolution conditions, but sufficient to resolve isolated particles (and obviously aggregates), and combine these results with TEM tomography at higher resolution to quantify properly the volume fraction inside the aggregates.

The first approach is in fact illusive for several reasons. Whatever the problems linked to the sample itself, the resolution of SEM (and SEM in the FIB) is typically of the order of 2 nm, which might be insufficient, and cannot certainly be preserved in 3D because of errors in the alignment of the image stack. Secondly, the main problem is the ‘z’ resolution during the FIB acquisition. Several attempts have been tried, which have shown that it is not realistic to get slices smaller than about 6 nm for these types of materials. Finally, getting a better resolution (if this would have been possible) would increase drastically the time of the experiment, and/or reduce the size of the explored volume, which might be a severe limitation in terms of the representativity of the experiments (this point will be specially addressed in section 3.1.3.3).

Based on these arguments, we have chosen the second approach. We will present the FIB results in section § 3.2, then the TEM results in § 3.3. According to what was already said above, there is no need for TEM tomographic approach for samples without aggregates, since it is expected that isolated particles should be correctly measured in SEM/FIB micrographs. But before, we still have to define our experimental conditions. Our preliminary tests indicate that ‘easy’ conditions are the following: images size equal to 2048 * 1536 pixels, pixel size of 4 nm and z ‘resolution’ equal to 10 nm (i.e. the slice thickness is 10 nm, a reasonable condition to attain with a rather good stability and reproducibility). Since these conditions are slightly worse than those used in Figure 3.6 and Figure 3.7, we must check if they are sufficient from the resolution point of view. This is done in the next sub-section 3.1.3.2. In addition and as already mentioned above, we will then have to test the validity of these conditions in terms of representativity of our measurements. This will be discussed in the sub-section 3.1.3.3.

3.1.3.2 Resolution of the images versus size of the particles

Reminding that we aim at measuring particles as small as a few nanometres (the average size of the distribution is around 16 nm as reported by [Tatou2011], see § 3.1.1), the main question is to know whether our measurements with a given pixel size will be sufficient. The resolution of the SEM imaging mode in a modern instrument such as the NVision 40 used in this study is not a limiting factor to *detect* particles down to the nanometric level in the nanocomposites considered in this work. What is more limiting is the magnification and size of numerical images that will be acquired, which lead to a given pixel size which might be too large for a reasonable ‘sampling’ of small particles. Moreover, the elementary thickness of matter removed at each step during the slice-and-view sequential acquisition of images is also a limiting factor.

For practical reasons, we have chosen to acquire micrographs of 2048*1536 pixels, with a resolution of 4 nm in the X-Y plane, and a voxel length along the Z direction equal to 10 nm. The X-Y size is indeed mostly defined by the magnification in order to get a sufficiently large area which will allow to analyse a statistically representative volume (as discussed later in sub-section 3.1.3.3), even after cropping due to image alignment and drift. The Z-resolution, or voxel length, is defined by the thickness of matter removed by the ion beam. Owing to the nature of the materials of interest (i.e. a polymer matrix), the stability of the whole system during the 3D sequence, we deduced from preliminary measurements that about 8 to 10 nm is a reasonably good and confident value in order to keep a sufficient resolution and a reasonably small number of slices (then reasonable acquisition time) to explore a sufficient volume.

Then, according to a voxel value of 4x4x10 nm^3, the question of measuring particles with a diameter of a few nanometres is really relevant. A similar question was already discussed in previous 3D works by FIB [Holzer2006].

Figure 3.9 shows how we can consider the SEM image of a particle sampled by the scan of the beam.

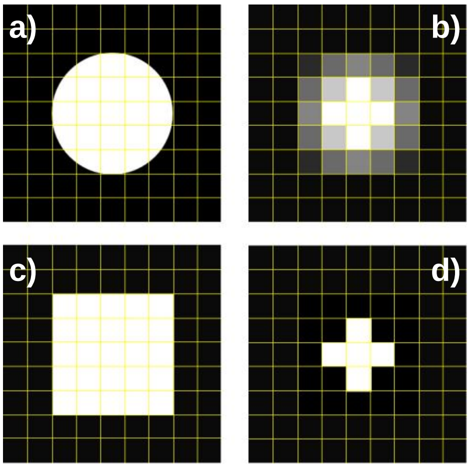

Figure 3.9: 'Sampling' of a nanoparticle in SEM numerical images (see text for details): a) ideal 2D 'white' particle shown on a pixel grating ('black' background); b) same as a) when the intensity of each pixel is proportional to the particle surface contribution; c) segmented version of b) when the threshold is chosen equal to the smallest pixel intensity of the particle; d) same as c) when the threshold is the highest intensity of the particle.

On the left-hand side, the particle is shown as if the SEM signal was fully continuous and not sampled on the digital image; on the right-hand side, we have represented the image of the particle when it is sampled on the pixels grating, according to the intuitive principle that each pixel will have an intensity proportional to the particle surface contribution. From such images, it is obvious that the final size of each particle will depend upon the numerical treatments applied to the micrographs. Typically, a binary segmentation followed by a classical erosion-dilatation will be realized, as illustrated in Figure 3.10. This is especially true for small particles which will be sampled on a very small number of pixels (voxels), with the consequence that their size could be easily flawed after the numerical treatment: during the segmentation process, we may increase the size of the particles if we choose a too low threshold value (as demonstrated in Figure 3.9 c)), or decrease it if the threshold value is too high (Figure 3.9 d)). Then, the erosion-dilatation process can make the final situation even worst.

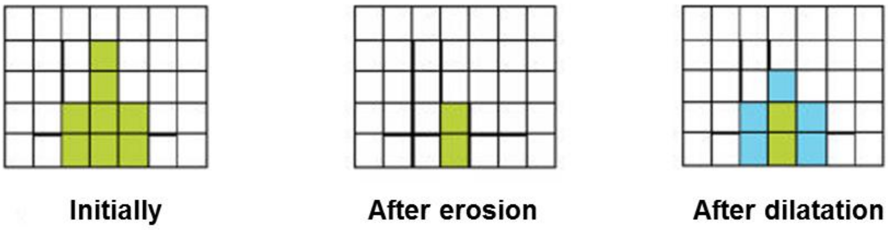

Figure 3.10: Illustration of the erosion and dilatation treatment on segmented binary images [Deschanel2005, thesis].

In 3D, the situation is even more complex than what is depicted in Figure 3.9 owing to the fact that the voxel size is not isotropic.

Considering all these problems, we must re-emphasize that the main goal of our approach is to measure the *mean* volume fraction, and not really the exact size distribution of the particles. Then, we have adopted the following strategy:

- On the basis of the contrast process described in Figure 3.9, we have run numerical simulations of representative volumes of matrix where a known volume fraction of particles, with a known mean size and distribution, has been generated on a computer.
- These 3D simulations were treated with the Fiji© program (*http://fiji.sc/Fiji*), where the segmentation, erosion-dilatation operations have been performed and adjusted in order to retrieve a reasonable value of the known volume fraction.
- The parameters for all image treatments deduced from this simulation approach were then applied to the experimental sets of data.

Results of these simulations are illustrated in Figure 3.11. The analysis of the 'raw' volume gives a real volume fraction of 1.27 % (slightly different from the input value of 1 % owing to the numerical procedure to generate the particles). After optimizing the segmentation, we arrived at a value of 1.16 %; and the final values after erosion and dilatation is 1.06 %. These values are smaller than the true value, simply because the erosion-dilatation of small objects, i.e. objects defined over a small number of voxels, is known to minimize their size, as qualitatively illustrated in Figure 3.10.

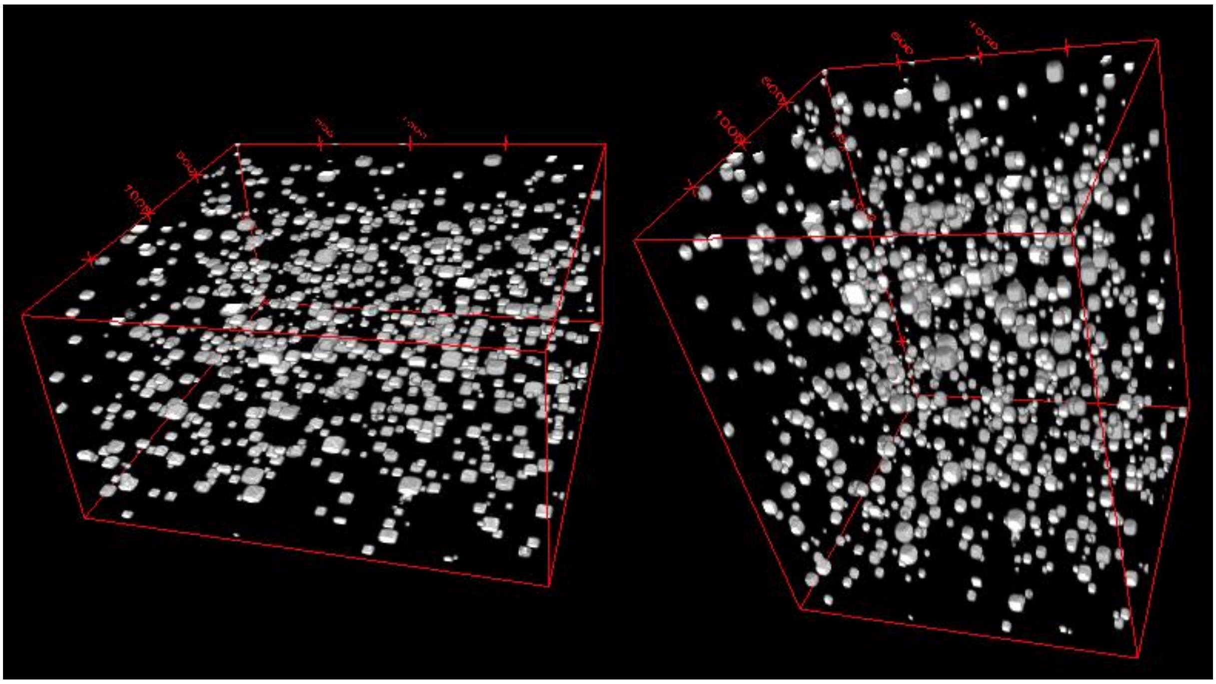

Figure 3.11: Volume equivalent to the M86 sample numerically generated with a 1 % volume fraction (actually, 1.27 %) of particles according to the following Gaussian distribution: mean diameter equal to 16 nm, FWHM of 8 nm. Left: representation of the volume with 500 * 500 * 250 isotropic voxels (silica particles appear to be compressed along Z because of the different scale along this direction, compared to the (X, Y) plane); right: same volume when correctly 'stretched' (the dimensions along X, Y and Z are corrected from the voxel size equal to 4 * 4 * 10 nm^3).

From these results, we can consider that our treatment, based on the experimental conditions that have been chosen for the 3D FIB experiment (i.e. the (X, Y) 'resolution' of 4 nm/pixel, and the Z-'slicing resolution' of 10 nm), cannot provide a relative accuracy better that about 16 %. This may be considered as a 'poor' accuracy, but the absolute value remains very reasonable (a volume fraction of 1 % would be measured in the interval 0.84 – 1.16 %).

3.1.3.3 Statistical representativity

The question of the representativity of the studied volumes is the following: what is the minimum volume that is to be considered in order to obtain a meaningful measurement of the volume fraction? This question is relevant in the case of the small volume fractions (i.e. expected around 1 %).

To consider this problem, we have run numerical simulations where a homogeneous, and ideally mono-disperse population of spherical 16 nm (expected mean size) silica particles has been distributed in a volume, or numerical cubic box, with a given and variable size. For each analysis, the average measured volume fraction of silica has been deduced according to several tries (about 1000 calculations). From these numerical results, the volume fraction deduced with a confidence interval of 95 % has further been calculated for each total 'box'. Results are illustrated by Figure 3.12 and Table 3.1.

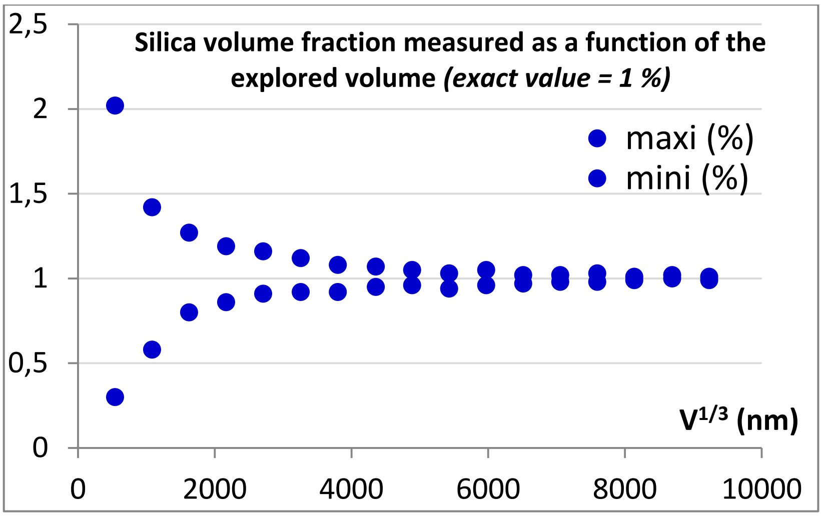

Figure 3.12: Numerical estimation of the volume fraction of a mono-disperse homogeneous population of silica spherical particles (with a diameter equal to 16 nm) distributed in a variable volume V: for each volume, the minimum and maximum values obtained among 1000 simulations are plotted.

size (nm)	542	1083	1625	2167	3258	5429	5971	6512	7596	8137	9233
Measurement (fraction in %)	1+/- 0.08	1+/- 0.06	1+/- 0.04	1+/- 0.04	1+/- 0.03	1+/- 0.03	1+/- 0.02	1+/- 0.02	1+/- 0.02	1+/- 0.01	1+/- 0.01

Table 3.1: Measurement of the volume fraction as a function of the size of the edge length of the explored cubic volume within a 95 % confidence interval.

These data show that volumes with a cube edge size as small as 2 µm allow the exact volume fraction to be approached with a 4 % relative accuracy within a 95 % confident interval. Moreover, all values measured for such a volume range between 0.83 and 1.14 % (minimal and maximal values) which remains relatively close to the exact value.

This conclusion is also important from the point of view of evaluating the homogeneity of the distribution of the silica particles, which can be appreciated through the dispersion between measurements from several such volumes.

However, we chose much larger volumes to be even more confident in the statistical representativity of our measurements. All FIB series have thus consisted in the acquisition of SE images from about 500 slices with a size of 2048 * 1536 pixels, and a pixel size of 4 nm. We will see in the following section that crop and re-alignment have finally lead to final surfaces ranging between 770x970 and 920 * 1220 pixels. According to a depth resolution in Z (that is the slice thickness) equal 10 nm, volumes consisting of 500 slices with the previously mentioned area, between 45 and 87 μm^3 were explored and analysed at the end; these volumes were consequently much larger that the 2x2x2 = 8 μm^3 volume required for the 4 % relative accuracy mentioned above (e.g. Table 3.1).

3.1.3.4 Summary

The previous sub-sections have established that the conditions selected for the FIB 3D experiments are sufficient in order to (i) resolve the individual isolated particles, (ii) analyze properly the volume fraction of homogenous distributions of isolated particles, (iii) be representative from a statistical point of view.

Main conditions and conclusions are as follows:
- 3D FIB series of SEM micrographs were recorded with an initial size of 2048 x 1536 pixels, and a pixel size of 4x4 nm^2.
- 'Slice-and-view' sectioning was performed with a slice thickness ranging between 6 and 10 nm; about 500 slices were recorded for each 3D sequence.
- Volumes of about 50 μm^3 were explored; these volumes are consequently much larger than the 8 μm^3 which was defined as an acceptable minimum volume for a good statistical representativity.
- According to the voxel size of about 4x4x10 nm^3, and the strategy used for image treatment of the 3D volumes (segmentation and erosion/dilatation), a relative accuracy of about 16 % is expected for the final volume fractions measured from the FIB approach.

We must emphasize that samples exhibiting aggregates of particles require an additional analysis at higher resolution than that permitted with the FIB, so that the internal structure of the aggregates (the embedded 'hidden' matrix) is correctly measured.

Keeping this in mind, we can proceed with the 3D acquisition in FIB/SEM.

3.2 FIB/SEM tomography, 30kV/1kV, Zeiss NVision40

The newly installed FIB/SEM double column system of CLYM-Lyon was already presented in chapter 1.2.3, and an 'unsuccessful' first try of the P(BuA-*stat*-S)/MWNTs system was shown in chapter 2.4.

The sample preparation for the FIB tomography is relatively simple, since, in a first step, we essentially need to mount a piece of material on a stub like for any conventional SEM observation. In this respect, this preparation is much easier than for TEM and SEM tomography where ultramicrotomic sections have to be cut as already performed (see chapter 2). Thus, a small piece of material is sticked with silver sticking lacquer on a dedicated SEM sample support. For the FIB experiments, the surface of the sample should be metallized to avoid undesirable charging effect during the observations: in order to conduct the charging electrons, the glued sample was silver coated at their profiles to create 'conducting pathways' between the surface of the sample and the surface of the support, which were finally covered with a thin layer of gold about 10 - 15 nm thick deposited in a conventional gold evaporator (see prepared samples in Figure 3.13).

Figure 3.13: Samples prepared for FIB/SEM tomography.

3.2.1 Problems and proposed solutions

Before exhibiting the results, experimental difficulties and their potential solutions should be discussed: even during the initial ‘rough’ abrasion of the cavity prior to the real 3D acquisition, the experimental conditions, like the milling strategy and geometry, scanning speed, choice of imaging detector, have to be optimized.

The first problem we encountered was related to the milling conditions, i.e. the ionic current used to mill the sample. As shown in Figure 3.14, a high ionic current of 6.5 nA, as classically used for most materials machined with the FIB in the CLYM context, leads to a drastic damage of the zone of interest and makes it collapse.

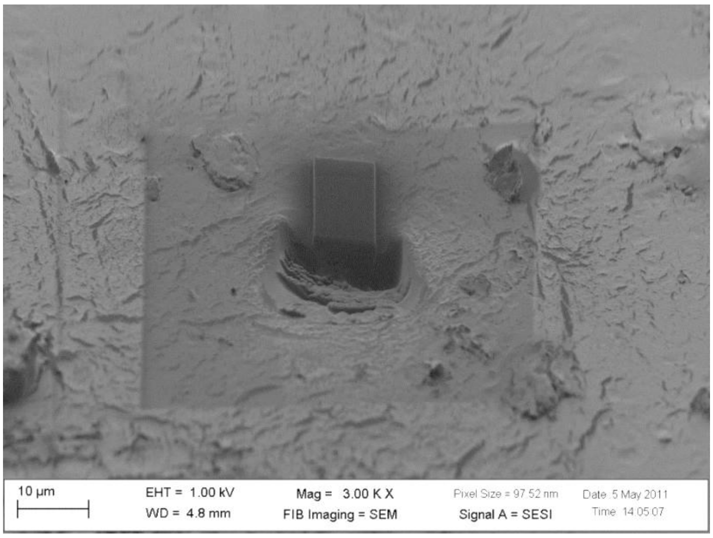

Figure 3.14: Consequence demonstration of a bad choice of the milling ion current.

After reducing the milling current to about 1.5 nA, further important issues appeared. Figure 3.15 exhibits a prepared zone after a long ‘slice and view’ acquisition which demonstrates three major experimental problems.

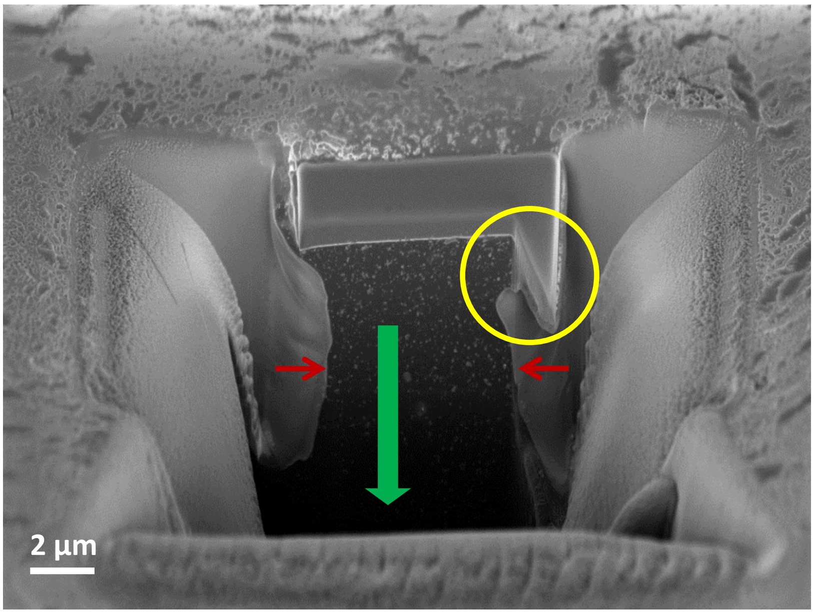

Figure 3.15: Image obtained after a complete 'slice and view' procedure which demonstrates three problems encountered: 1) the long green arrow shows the continuous fading of the brightness and contrast due to a shadowing effect of the 'In-lens' detector; 2) the circle (yellow) indicates a significant drift of the sample (see § 3.2.1.2 for details); 3) a shrinkage in X dimension is indicated by the two red arrows.

3.2.1.1 The shadowing effect

Preliminary tests showed that the best contrast in the SEM mode of the ZEISS Nvision40 microscope was obtained with the 'In-lens' detector, compared to any other imaging mode on this instrument (i.e. SESI: Secondary Electron Secondary Ion detector and EsB: Energy and angle selective BSE detector). To avoid charging effect and minimize the shrinkage problem (see section 3.2.1.3) for soft materials like our polymer nanocomposites, the voltage of SE imaging used in our tomography experiments was decreased to 1 kV; it can be specified that the 'In-lens' detector of the ZEISS 'Gemini' electronic columns is the most adapted for a better resolution at low voltage. However under these conditions, the 'In-lens' detector easily suffers from any shadowing effect, that is any obstacle that can limit the collection angle for incoming electrons. In the classical geometry of a FIB tomography experiment, the forefront cavity performed to prepare the viewing area produces such a shadowing in its lower part, due to the 'wall' of matter in front of the cavity. As can be seen from Figure 3.16, the acquired image is much darker at the lower part than at the top.

Experimentally, if we want to avoid this problem, the solution could be milling a bigger, more importantly, much larger cavity in the Z direction. More space in front of the zone of interest could keep the signal trajectories free from being blocked by the forefront wall, especially for signals generated at the low part of the section. But this situation will take much more time for the milling procedure, especially for soft materials because they couldn't stand high ionic current. So if we sometimes look for a big volume to reconstruct, we have to mill large cavities to escape from this shadowing effect and also the re-deposition effect, which make the preparation time too long and occupying a too important part compared to the 'slice and view' procedure.

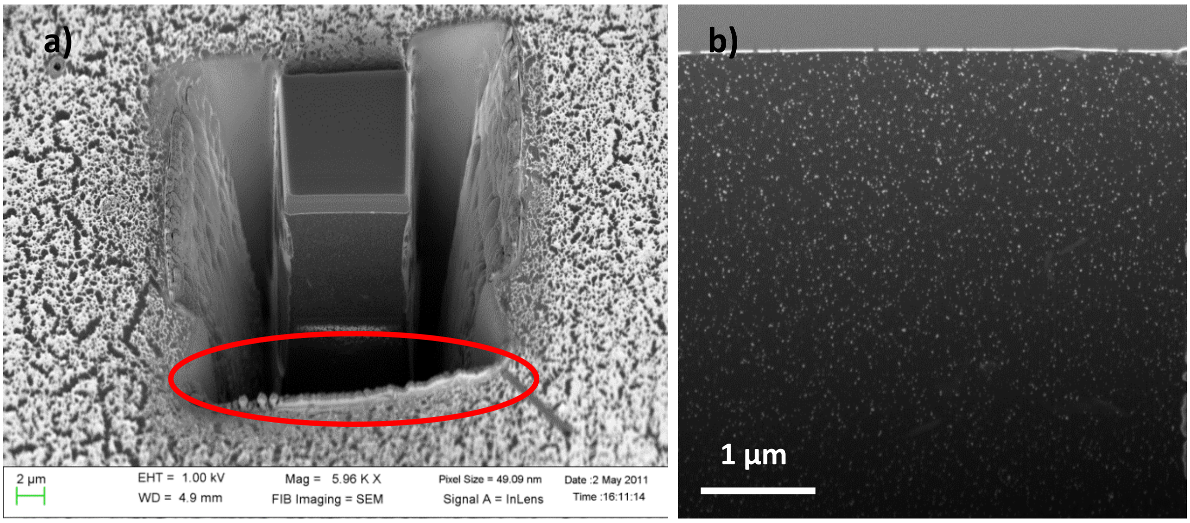

Figure 3.16: One zone ready for tomography acquisition. a) The wall of cavity blocking signals for 'In-lens' detector is circled in red. b) A resulted image from shadowing effect. The brightness decreases along with the depth of the section.

Besides, this problem doesn't affect much the imaging but mostly the post treatment of the slices. Once the stack of images was obtained, it would be first re-aligned and then segmented to be binary for visualization and quantification. This brightness and even contrast altering in the frame of image would be a serious issue for some automatic threshold adjustment tools. As illustrated in Figure 3.17, a small slice of 500*500 pixels is pulled out from the original aligned image stack (Figure 3.17 a)), brighter points are the silica nanoparticles and the grey part all around them is the polymer matrix. We first segment this small cropped slice and get a rather good result with an originally available binary segmentation tool (Figure 3.17 b)). However some little details at the lower part of the slice are missing after this rapid segmentation, so the existence of this shadowing effect is so confirmed and needs to be corrected. Then, once again, the segmentation was tried with the same software to keep the missing details of the first time, however too much noise was also induced at the higher part of the frame (Figure 3.17 c)). Thus other more intelligent segmentation resources were expected to resolve this situation, if we don't want to extend the experience duration by increasing the size of the cavities.

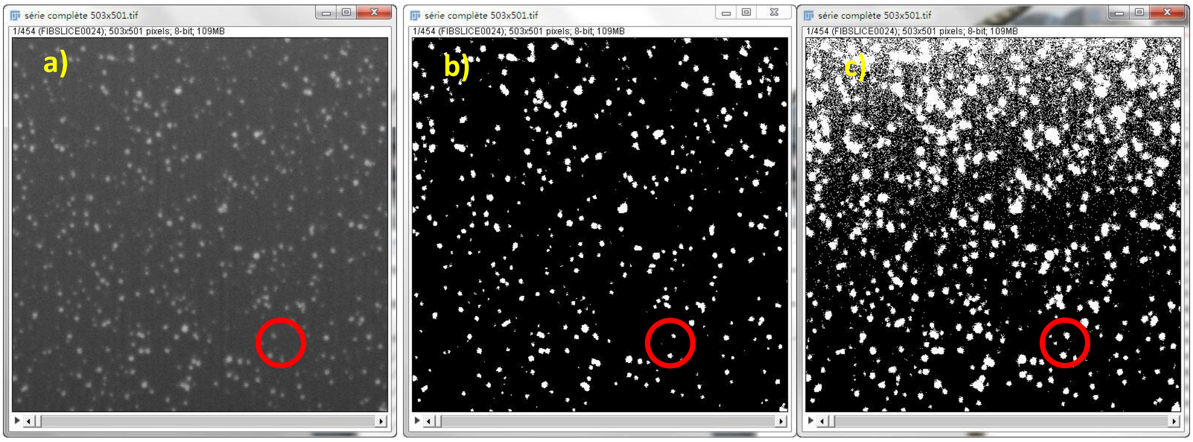

Figure 3.17: a) One 500 * 500 slice cropped from the aligned image stack; b) a quick automatic segmentation of the cropped slice; c) another automatic segmentation trying to preserve the details in the lower part of image.

A Fiji plugin called 'Trainable Segmentation' ([*http://fiji.sc/wiki/index.php/Trainable_Segmentation Plugin#*](http://fiji.sc/wiki/index.php/Trainable_Segmentation_Plugin#)) was found to be capable for segmenting this kind of image slices with a slight brightness and contrast variance. As suggested by the name of this program, the user can adjust the way to associate an interval of grey levels to a given phase in a manual training procedure. This process is thus repeated as many times as required in order to include all the nanoparticles in a unique class, without introducing too much noise.

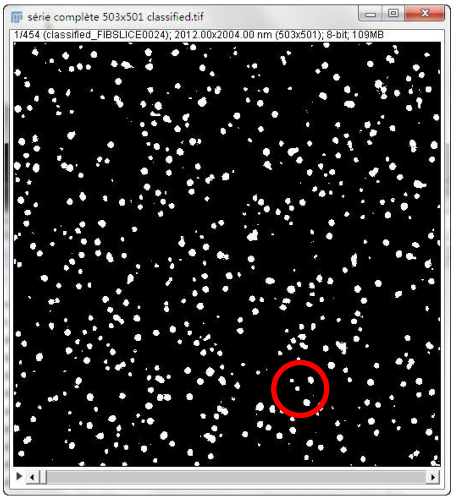

Figure 3.18: A good segmentation result provided by the 'Trainable segmentation' plugin within Fiji.

Figure 3.18 shows a result obtained with this program. In comparison with Figure 3.17 b) and c), this approach clearly gives much better results in terms of (i) particle identification and separation, (ii) noise reduction. Once the training classifier has been optimized on one single image, it can be applied to segment the image stack to be used for the 3D visualization. We have also used an advanced version of this kind of segmentation tool, i.e. the 'Advanced Weka Segmentation' plugin (*http://fiji.sc/wiki/index.php/Advanced_Weka_Segmentation*) which can train the classifier on the whole images stack, which will be much more accurate in the case where there is a contrast change in the stack. In the present case, the quality of results was found to be sufficient with the faster and easier 'Trainable Segmentation' routine.

3.2.1.2 Drift during 3D experiment

The second issue is the sample drift during 3D experiments. Figure 3.19 illustrates this problem; we extracted 12 slices from a series of 3 hours acquisition. A clear continuous drift is revealed, which could have led to a complete exit of the area of interest from the field of view after a longer acquisition sequence. In the case of a severe drift, the final alignment of images once the series has been completed can lead to a drastic cropping effect of the area of interest.

Typically, this alignment procedure is performed with the help of a cross-correlation procedure. There is a lot of software based on the 'cross-correlation' algorithm which can be used to re-align a tomographic stack. As previously mentioned in the Introduction section (§ 1.2.5.2), we have used either free Fiji plugins or a commercial solution to perform this alignment.

In the case of Figure 3.20, aligning all images with respect to the first one of the series shows that the last slice contains only 67 % of the initial surface of the first section; it may obviously be anticipated that after a very long acquisition time, the region common to all images could be null if no live correction is operated.

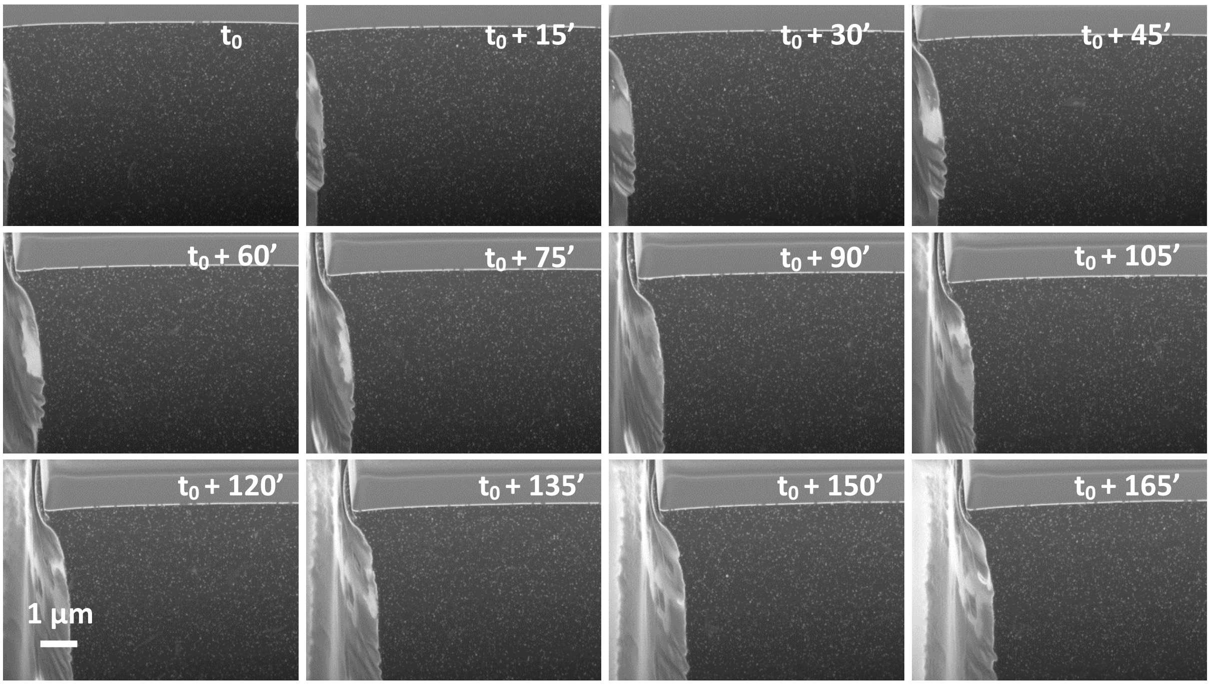

Figure 3.19: FIB/SEM slices extracted at 15 mins interval from a M82 stack.

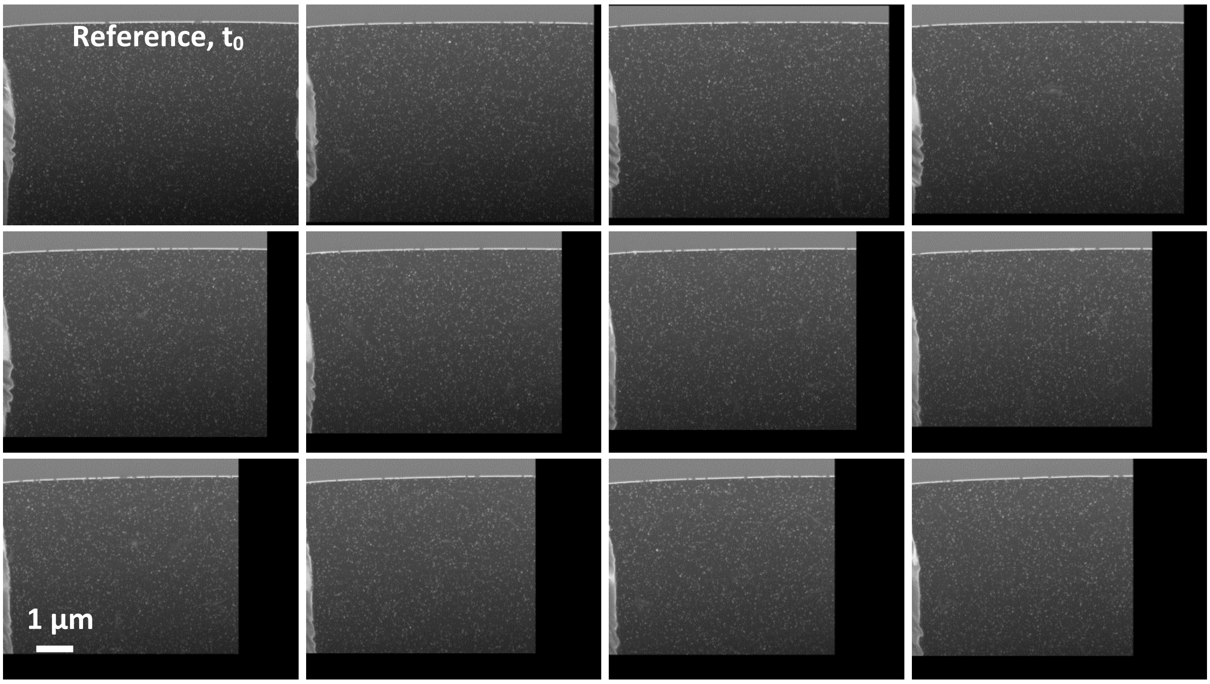

Figure 3.20: The same slices from Figure 3.19 which are aligned according to the first one.

More generally it can be anticipated that the sample drift occurs ‘in 3D’ and not only in the (X, Y) section imaged during the slice-and-view sequence. Drift along the Z direction produces an additional problem, which is a blurring of images due to a loss of focus. Such drifts may have different origins; they can be due to (i) the influence of the beam(s) on the sample (in the case of easily damaged and/or charging materials), (ii) mechanical instabilities of the sample on its support, or the stage itself, (iii) any kind of environmental electromagnetic perturbation. All these causes can apply simultaneously to cause the final drift. Nevertheless, it can and needs to be corrected especially in case of long stack acquisitions. There is a lot of software, free and commercial, that is based on the algorithm ‘cross-correlation’ to re-align a tomographic stack for correction of drift and translation in

2D, but those programs don't work very well if a stack is too large. Also, they will not be fully efficient when the drift is too important despite of long treatment duration.

Thus, manual live drift correction is generally performed. Firstly, the focus is readjusted if needed in the case of a serious drift in the Z direction. Normally the focus is automatically synchronized with the change of working distance (WD) caused by the slice removal at each 'slicing' step (see § 1.2.3.2), but obviously this does not correct any drift along Z. As for the lateral (X, Y) drift, we can correct it visually by adjusting the 'Beamshift' settings of the electron beam (this electronic correction means that the sample stage is not actually displaced, which would have more chances to produce a mechanical instability). After the complete acquisition, the alignment tools previously mentioned are still used to ultimately correct any residual drift.

The main problem of the live alignment is that it requires a constant presence in front of the instrument if it has to be performed manually. During his thesis at CLYM, H. Yuan has developed a home-made program to correct automatically the sample drift and focus loss in real time during the FIB/SEM tomography experiments.

We have been contributing to some experimental tests to optimize this procedure [Liu2012b]. An example of the (X, Y) drift correction is shown in Figure 3.21 and Figure 3.22, where images are extracted from a 'slice and view' experience on a Ni alloy sample [Yuan2012]. The home-made program was fist turned on and then off to visualize the efficiency of the correction in the presence of a continuous drift.

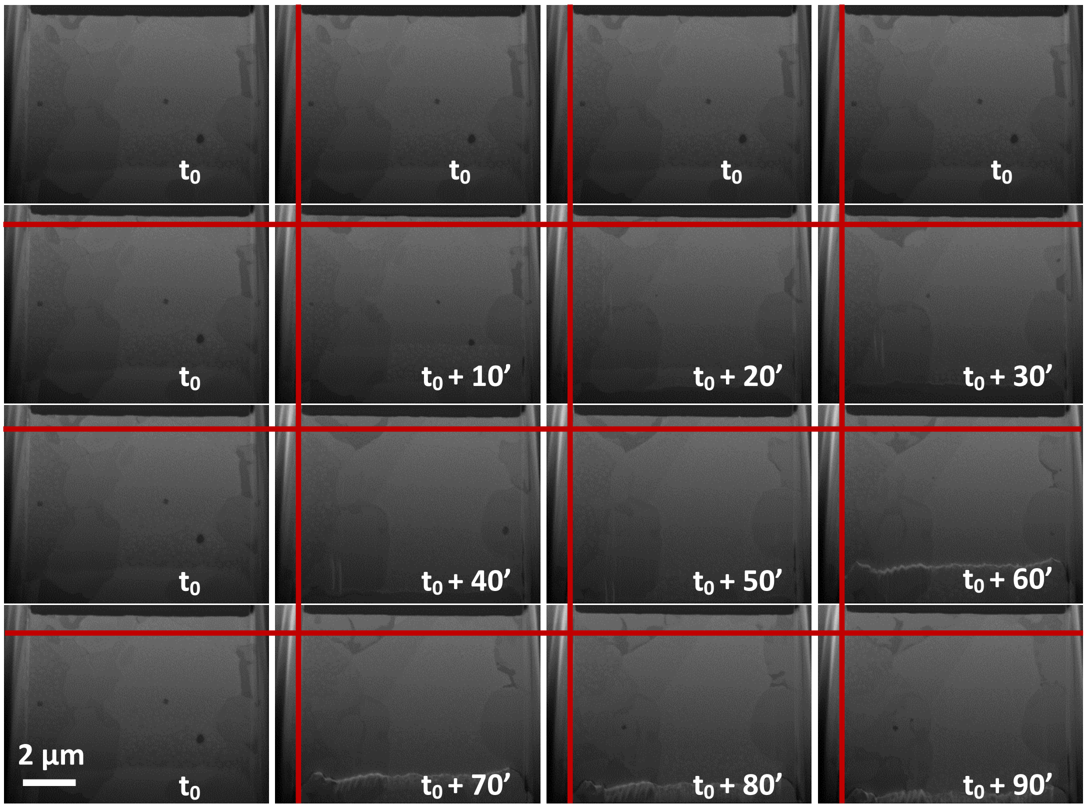

Figure 3.21: Reduced image series from a FIB/SEM tomography on a Ni alloy with the *in-situ* drift correction program running. The initial (reference at time t$_0$) image is repeated in the first row and column, the other ones being recorded at different times (as indicated). Red lines are guides for the eye indicating the left position of the carbon deposited layer as a reference marker, and proving the absence of any significant drift. [Yuan2012]

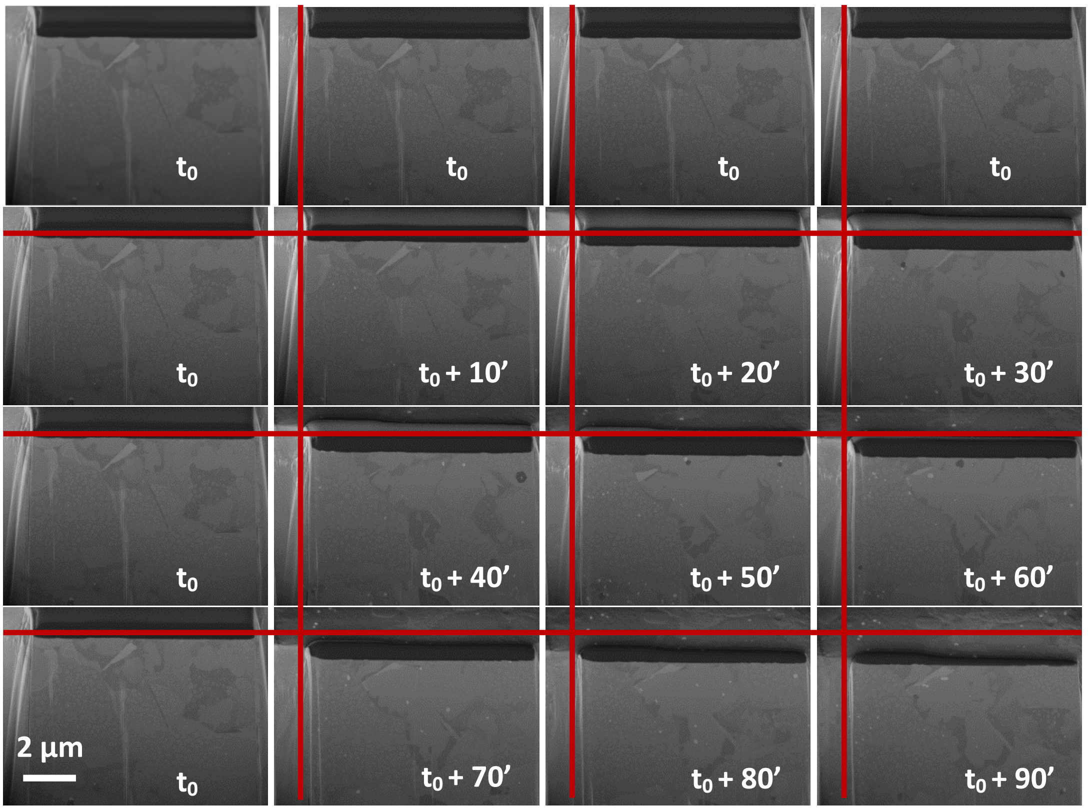

Figure 3.22: Same montage as in Figure 3.21 while the live correction is switched off. [Yuan2012]

Figure 3.23 shows the curves of the 'Beamshift' variations in both X and Y directions versus time (in seconds). Before point P the correction is applied as indicated by deviations from linearity in both curves (see Figure 3.21). After P the live correction is stopped (see Figure 3.22); the Y curve shows a perfectly linear variation caused by the internal Zeiss procedure adjusting automatically the WD parameter, whereas the X curve does not shows any variation since no Zeiss correction is applied. It can be noted that the rough linearity of both X and Y curves during the active correction step indicate a continuous and regular drift of the sample. Presently this program is still under further development and optimization (H. Yuan, thesis in progress).

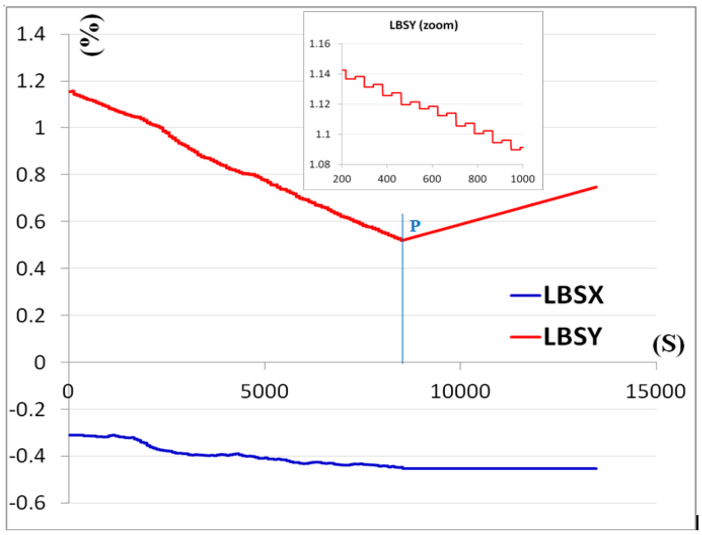

Figure 3.23: The recorded movement of the incident electron beam represented by 'Beamshift' as a function of time. The first part before the point P corresponds to the in-situ correction of acquisition in Figure 3.21 and the second part after is the acquisition non-corrected as in Figure 3.22. [Yuan2012]

3.2.1.3 The matrix shrinkage

As already presented in the previous chapter on P(BuA-*stat*-S)/MWNTs, polymers and the polymer matrix of nanocomposites are very beam sensitive, and they shrink easily under irradiation. In the current study, the polymer matrix P(BuA-*stat*-MMA) also shrinks gradually during the tomography process. Figure 3.24 shows two images recorded at the beginning and at the end of a short 'slice and view' acquisition on the M86 sample: horizontal red arrows clearly point out a spectacular shrinkage of the lateral 'walls'.

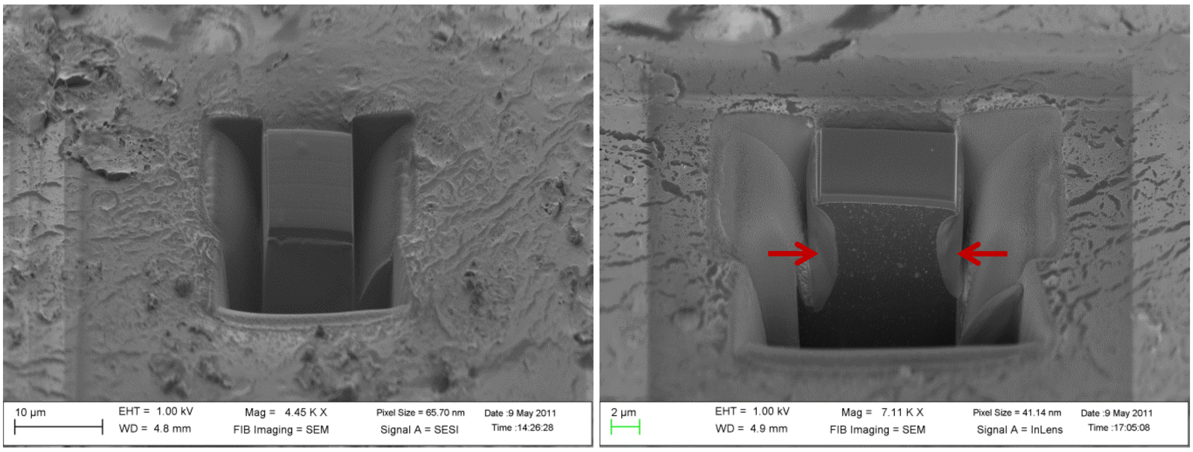

Figure 3.24: Evidence of the shrinkage effect: two images of the same zone of interest at the beginning and at the end of a short tomography acquisition.

Although this shrinkage problem is expected to affect drastically the measurements of the silica volume fraction, we have decided in a first step to analyze all samples according to the classical 3D geometry depicted in Figure 3.24. Doing so, we will account for the shrinkage by estimating the variation of the volume matrix to correct our measurements.

This estimation is illustrated in Figure 3.25. Assuming that the contraction in the Z direction of the sample remains negligible and that the volume changes as the area of the section changes, the shrinkage rate $\tau_{\text{shrinkage}}$ can be directly expressed as:

$$\tau_{\text{shrinkage}} = V_{\text{final}}/V_{\text{reference}} = S_{\text{final}}/S_{\text{reference}}$$

Where the subscripts 'final' and 'reference' refer to the final and initial volumes (or surfaces as shown in Figure 3.25) respectively. Values deduced from Figure 3.25 are 74 % and 70 % respectively for images b) and c). According to these values, it can be assumed that the shrinkage level does not significantly evolve during the 3D slice-and-view sequence. This finding is in agreement with the previous statement, that the shrinkage of polymers under the electron beam is rapidly stabilized with time at a given beam dose rate (see § 1.3.1) [Luther2006].

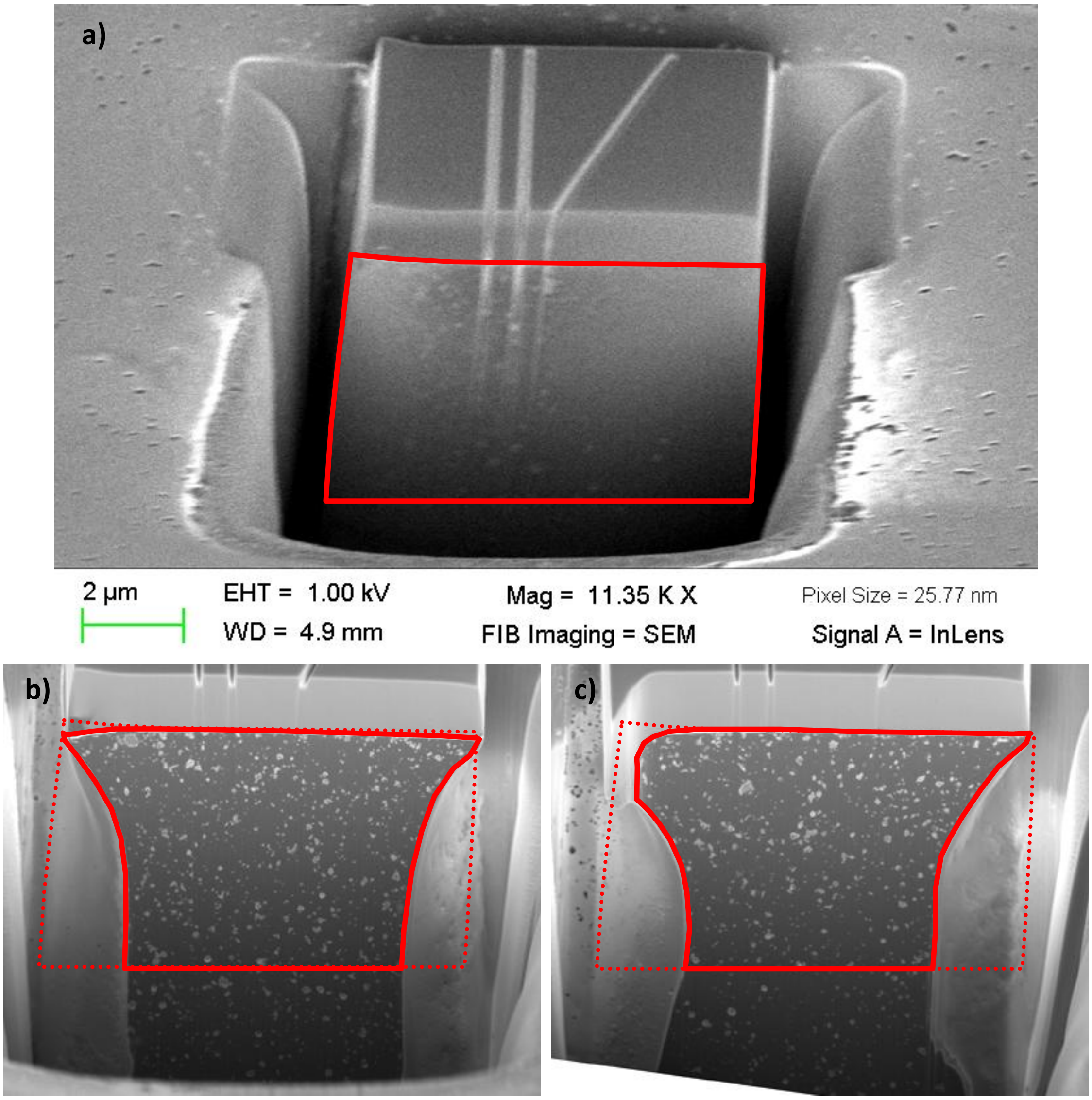

Figure 3.25: Estimation of the matrix shrinkage during a typical 3D experiments (case of the M86 sample). a) section of the 'wall' at the very beginning of the series, the frame in red delimitates the front surface; b) - c) same as a) after removing about 100 and 200 slices respectively (thickness about 8 nm in this case). The reference surface is shown in dotted line, whereas the shrunk surfaces are delimited by the red heavy lines.

According to this, Table 3.2 reports the measurements performed for all samples; these values will then be used to correct the final measurements of the silica volume fraction (see below).

Sample	**Average shrinkage level** $\tau_{\text{shrinkage}}$ **(%)**
M82	80
M49	82
M86	70
M57	79

Table 3.2: Measurement of the shrinkage values for the different samples during 3D FIB acquisitions.

At this point, it must be claimed that these results are very approximate, and it is obvious that avoiding the shrinkage would be a much better solution. This strategy will be developed in the section 3.4 through the optimization of the sample geometry on one of the four samples that we have been studying here; however, the comparison of all materials according to the usual geometry depicted in Figure 3.24 and Figure 3.25 is worth being presented now.

3.2.2 First series of results

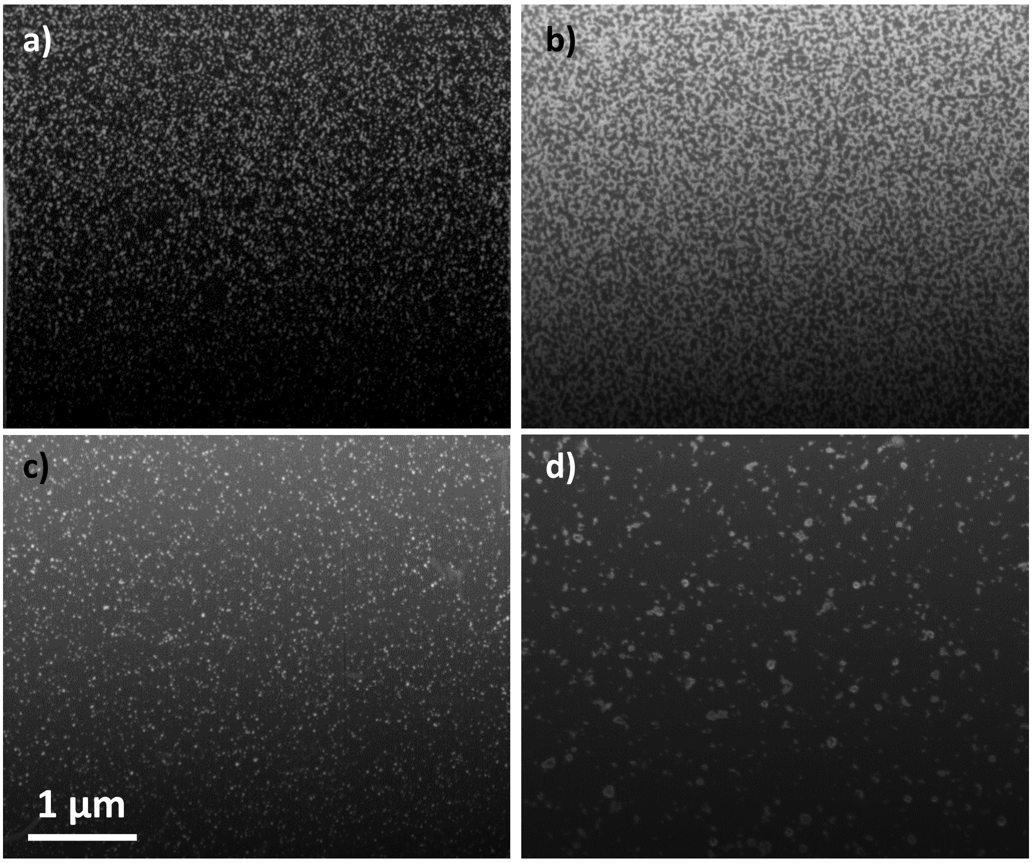

Figure 3.26: Examples of images extracted from the tomographic series of all 4 samples (area 4.6 * 3.9 μm^2); a) M49, 5 % pH 9; b) M57, 5 % pH 5; c) M82, 1 % pH 9; d) M86, 1 % pH 5. Note that the distribution of silica particles appears to be relatively homogeneous in all cases.

In Figure 3.26, we report raw SEM micrographs obtained during the 3D acquisitions of all samples studied in the present work. We can note that the dispersions of the nanoparticles seem to be homogeneous and in good correlation with the microstructures depicted in the TEM projections from Figure 3.4, or the SEM images in Figure 3.5. As already stated in § 3.1.3.2, all the original slices are 2048*1536 pixels SE images, with an 'in-plane' resolution of 4 nm, and a Z 'slice resolution' of 10 nm, corresponding to the thickness of matter removed at each FIB slicing step.

Figure 3.27 shows 3D visualizations of the reconstructions concerning the 4 samples. To get them, obtained image series were re-aligned to correct the drift that was even firstly adjusted during the experiments, and then cut out into smaller sections of about 500*500 pixels for harmonizing the binary representations (white for silica NPs and black for the polymer matrix).

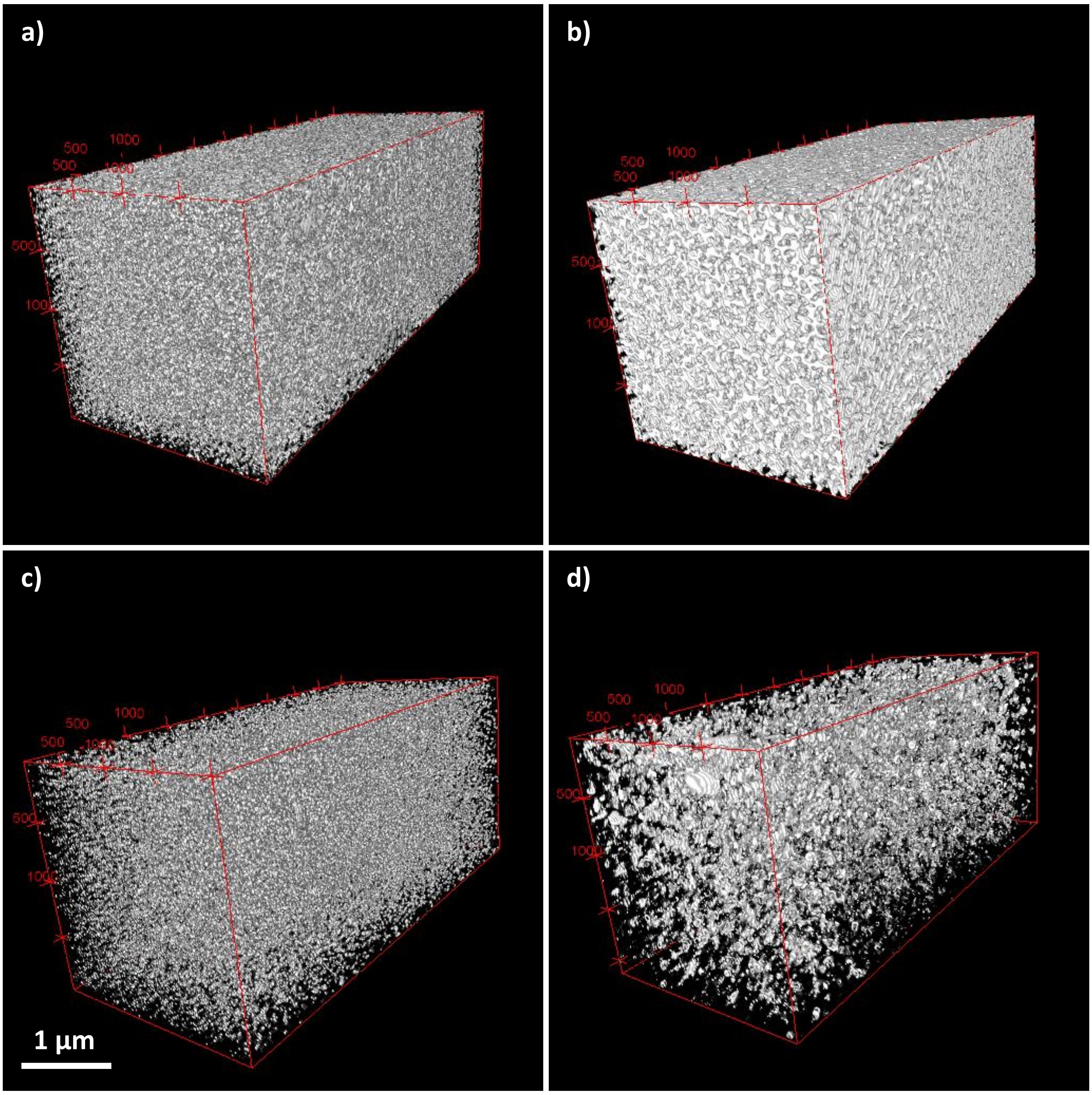

Figure 3.27: 3D visualizations (performed with the plugin "3D volume viewer" of the Fiji program) of reconstructed volumes from the first series of FIB/SEM tomography experiments. 500 * 500 pixels sections shown were selected from original series of 500 images of 2048 * 1536, voxel size of 4 * 4 * 10 nm^3; a) M49, 5 % pH 9; b) M57, 5 % pH 5; c) M82, 1 % pH 9; d) M86, 1 % pH 5.

In Table 3.3, volume fraction of silica NPs for the 4 materials calculated from the 3D reconstruction shown in Figure 3.27 are listed together with other parameters. As previously mentioned, two classical image treatments have been performed according to the optimization realized on simulations, as reported in Figure 3.11: (i) a segmentation allowing the NPs and polymer matrix phases to be separated; (ii) an erosion-dilatation operation, mainly aiming at suppressing residual noise (i.e. isolated pixels considered as belonging to the NPs class). Clearly, these treatments lead to volume fractions much higher than expected for all the samples. When we apply the contraction correction as described in section 3.2.1.3 (see Table 3.2), we get reasonable volume fractions for the samples elaborated under basic conditions (PH9), but not for samples elaborated under acid conditions (PH5).

Let us discuss about possible reasons for this discrepancy. One may argue that these results could be partially flawed because of statistical errors due to a non-representative volume. We should recall that the volumes analysed in Table 3.3 (between 45 and 87 µm^3) are much larger that the minimal volumes required for getting a 4 % accuracy in the measurement of the volume fraction (8 µm^3, as discussed in 3.1.3.3 and Table 3.1).

Sample	Final volume after shrinkage	Analysed volume (µm^3)	**Silica volume fraction (%)**			**Elaboration conditions**	
			After segmentation + erosion-dilation	**After shrinkage correction**	***Expected value***	pH	Aggregates?
M82	80 %	82	1.7 %	**1.4 %**	***1 %***	9	no
M49	82 %	61	5.0 %	**4.1 %**	***5 %***	9	no
M86	70 %	45	8.0 %	**5.6 %**	***1 %***	5	yes
M57	79 %	87	31.6 %	**25.0 %**	***5 %***	5	yes

Table 3.3: First calculation of volume fractions of silica in all 4 reconstructions (see text for details).

Moreover, we can further test the assumption of a homogenous distribution by comparing measurements obtained from different sub-volumes of about 8 µm^3: this has been briefly performed on sample M86, where the 5.6 % mean value measured form the large volume does perfectly correspond to several values measured from sub-volumes. Results shown in Table 3.4 attest the homogeneity of the distribution of the NPs. In conclusion, the disagreement between our measurements (5.6 %) and the expected value of 1 % in that case cannot be attributed to a limiting statistical representativity of our measurements.

1	2	3	4	5	6	**Average**	σ
5.1 %	5.5 %	5.8 %	5.3 %	5 %	5.8 %	**5.4 %**	0.27 %

Table 3.4: Measurements of the NPs volume fraction from 6 different 8 µm^3 sub-volumes in the M86 sample (the last column shows the dispersion), to be compared to the mean value measured on the large volume (5.6 %).

According to the above discussion, we have to admit that the overestimated values obtained for the two samples with aggregates are linked to this specific microstructure. This was already suggested by the discussion (see § 3.1.3) about the internal structure of aggregates, which do contain a non-negligible contribution of 'hidden' polymer phase.

As expected, we need to try tomographic experiments with a better resolution than that allowed by the 3D-FIB approach. Although we tried 'tilted tomography' in the SEM (Transmission mode), we will not present these results since they do not exhibit any resolution improvement compared to the 3D FIB experiments. Consequently, we will report directly results obtained in TEM tomography; because of time constraints, it was only possible to realize an experiment on the M86 sample (1 %, pH 5).

3.3 TEM tomography, STEM-HAADF, 200kV, JEOL 2010F

3.3.1 Experimental conditions

About 200 nm thick films of M86 material were prepared by cryo-ultramicrotomy and deposited on a conventional TEM grid. Samples were first observed at 200 kV in the JEOL 2010F (Filed Emission Gun) microscope at CLYM. In the TEM mode, we have the choice to acquire the tomographic tilt series either in Conventional Bright Field (BF) imaging or in the HAADF mode (see § 1.2.1.3). Figure 3.28 shows that a good contrast is obtained between the nanoparticles and the matrix in both imaging modes. It also shows obviously that the resolution is correct for imaging both particles and the internal structure of the aggregates; for comparison, we report in Figure 3.29 a typical SEM/FIB micrograph to highlight the resolution improvement of TEM vs. SEM.

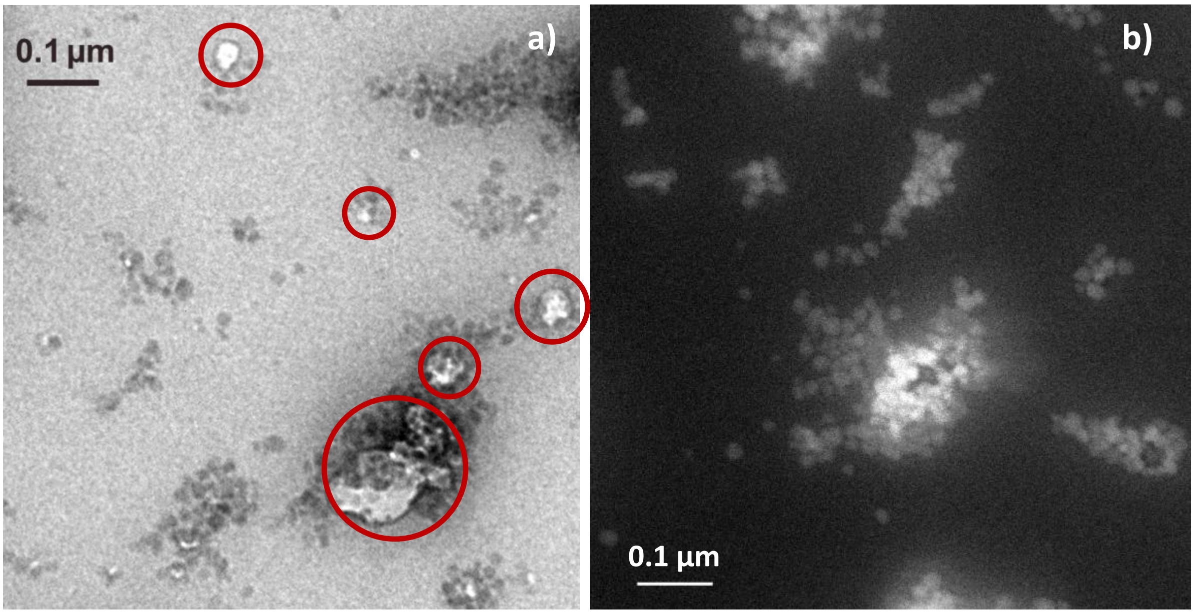

Figure 3.28: Images of M86 at a) Conventional BF mode; b) STEM-HAADF mode.

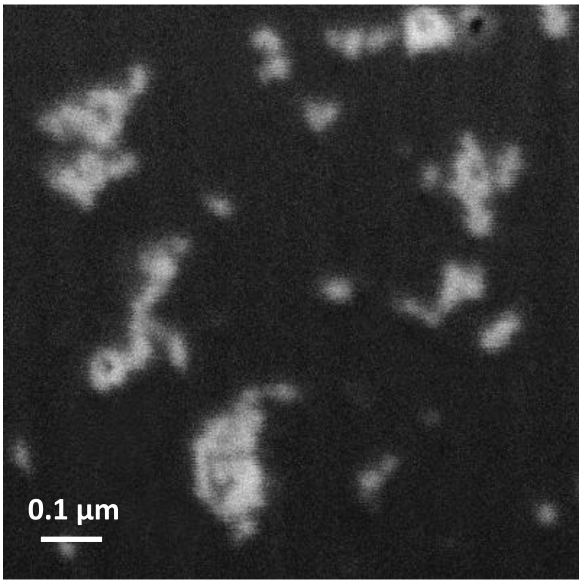

Figure 3.29 : SEM/FIB image of M86 (to be compared with TEM micrographs - same magnification - of Figure 3.28).

Coming back to the BF image in Figure 3.28, we notice a significant amount of voids, especially in large aggregates, which are not present in the HAADF micrograph (taken from another area; note that in the STEM, voids should appear darker than any matter). This effect has been followed in situ in the microscope by recording a video, clearly showing that voids appear during electron beam irradiation, as illustrated by some frames extracted from the video sequence in Figure 3.30. We have checked a lower high voltage, but did not observe a significant improvement at 100 kV. The interesting feature here is that this damage systematically occurs in the aggregates, which indicates a 'weaker' matrix in the polymer-silica interfacial region. We did not investigate this effect in deeper details, and we chose to perform 3D experiments in the HAADF mode in order to safely ignore this problem.

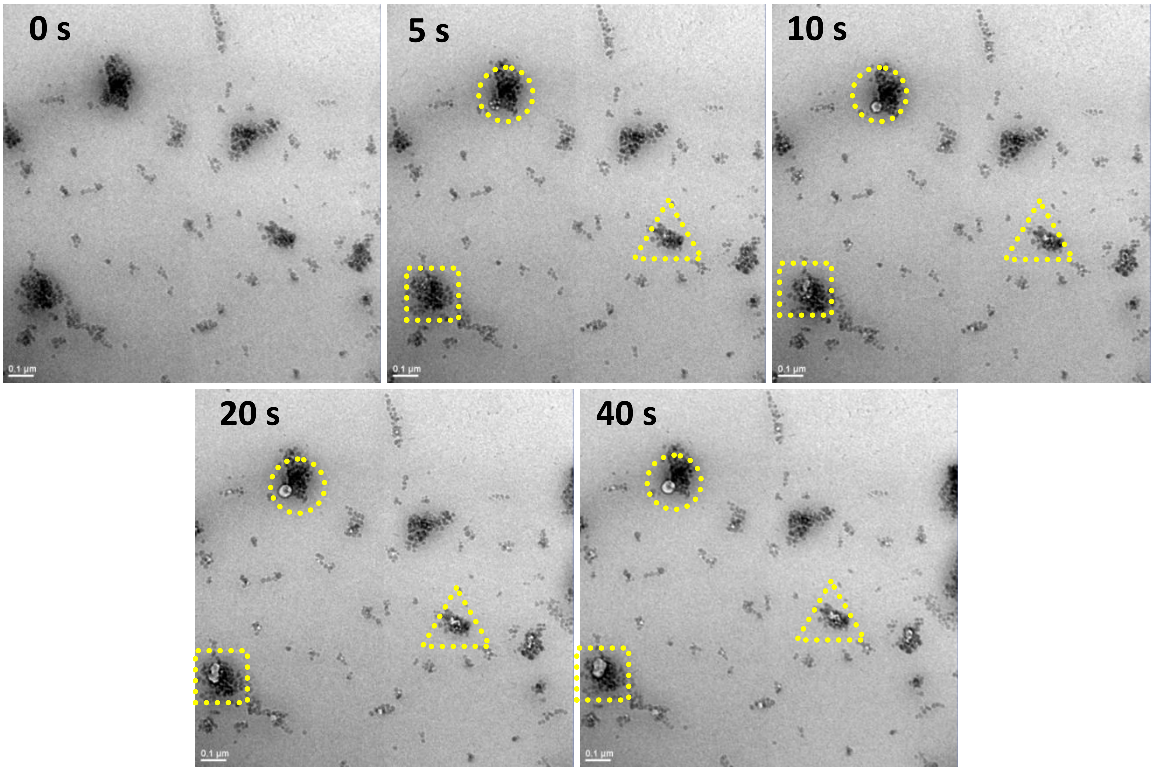

Figure 3.30: Images extracted from a video recorded in BF mode for demonstrating the creation of voids. The first image corresponds to a 'fresh' un-irradiated area brought under the electron beam after a fast displacement of the sample.

3.3.2 Tomographic reconstruction of aggregates

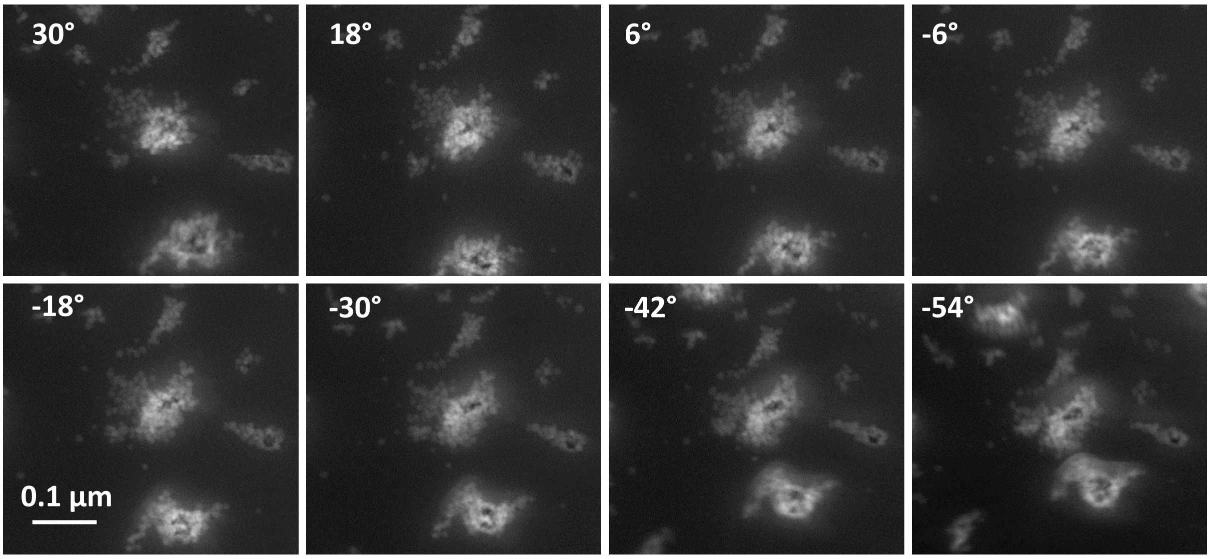

Figure 3.31: Projections obtained in STEM-HAADF of M86 from a tilting series between 30° and - 58° with a tilt step of 4°.

A series of projection was then acquired from 30° to - 58° with a tilt step of 4°. This constitutes a small series for tilted tomography, but the idea was to minimize the time under the electron beam. In addition, the tilt amplitude was also partly limited by mechanical constraints in this specific case.

Figure 3.31 reports some micrographs from the tilted series; note that interspaces between individual silica nanoparticles in the different aggregates were properly resolved. Figure 3.32 exhibits the reconstructed tomogram.

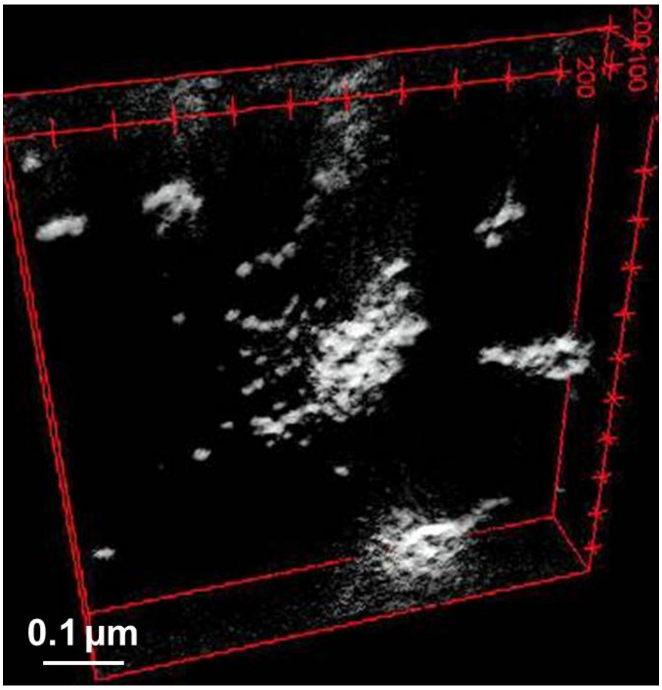

Figure 3.32: 3D representation of the tomogram reconstructed from the projection series corresponding to Figure 3.31.

3.3.3 Refinement of the silica volume fraction measurement

From the reconstruction of the tilting series obtained in STEM-HAADF mode, the internal structure of the aggregates is revealed and can thus be quantified. The idea is to measure the actual silica volume fraction τ_{SiO_2} inside these aggregates, in order to correct the values of silica volume fraction calculated from the FIB/SEM tomography results reported in Table 3.3.

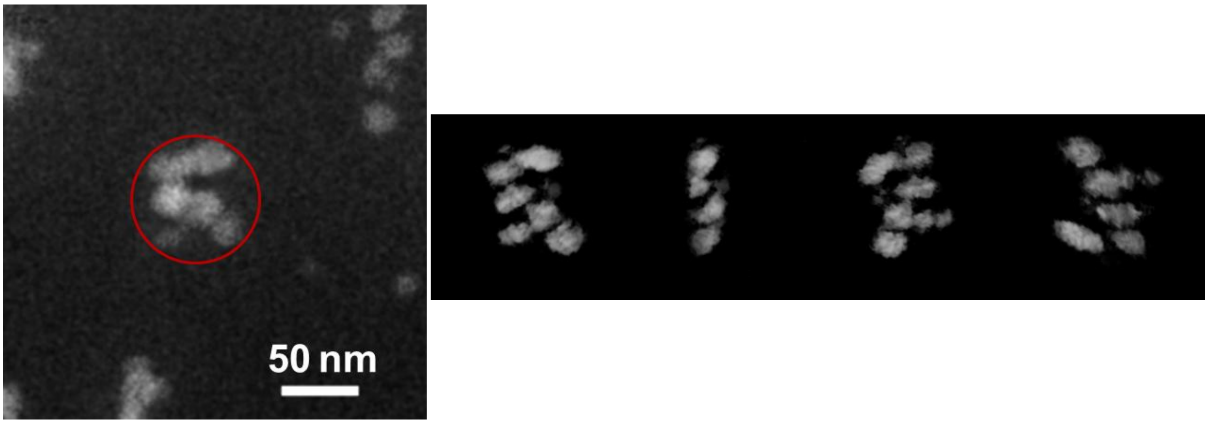

Figure 3.33: Typical aggregate selected in the HAADF image series; the red circle indicates the aggregate envelope (in 2D).

This was performed by selecting numerous aggregates (like the one shown in Figure 3.33), and measuring the ratio between the volume of silica nanoparticles and the overall volume of the aggregate itself, as illustrated by its visual envelope in Figure 3.33. In order to increase the statistics, we did select sub-volumes within larger ones for a better description of the smallest volumes (see for example in Figure 3.33: when the volume is seen under different projections, the definition of the overall aggregates volume is somewhat delicate).

Although this induces a large scatter of the results as show in Figure 3.34, it is seen that a reasonable constant value of 20 % can be confidently deduced for τ_{SiO_2} from these measurements.

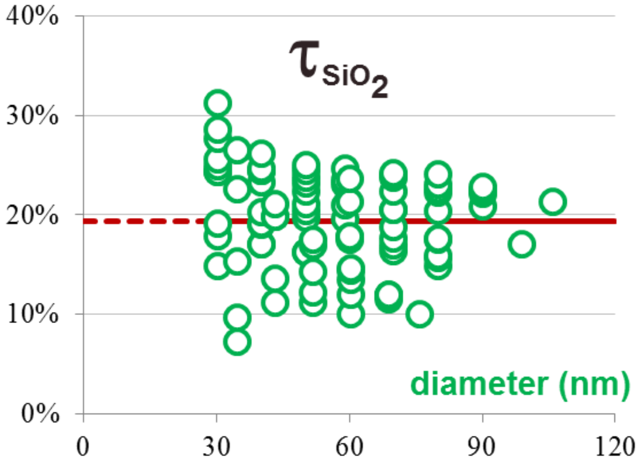

Figure 3.34: Volume fractions of silica NPs in aggregates as a function of the aggregates' diameter.

According to this evaluation, we can correct the volume fraction of silica NPs in the M86 sample as measured from the FIB/SEM tomography.

Let's write the apparent volume fraction measured in SEM/FIB as:

$$F_{SEM/FIB} = V_{SiO_2} / V_{total}$$

In this basic relation, V_{total} is the total explored volume, and V_{SiO_2} is the measured silica volume, made of two contributions: the volume occupied by isolated particles $V_{isolated}$ and the silica volume within the aggregates $V_{aggregates}$:

$$V_{SiO_2} = V_{isolated} + V_{aggregates}$$

According to the microstructure of the M86 sample (and the M57 as well), we may anticipate that the volume constituted by isolated nanoparticles is negligible compared to the volume measured from the aggregates:

$$V_{SiO_2} \approx V_{aggregates}$$

From the TEM tomography, we can deduce that the 'true' silica volume $V_{\text{'true' silica}}$ is much lower than V_{SiO_2} measured by 3D-FIB since we have:

$$V_{\text{'true' silica}} = \tau_{SiO_2} V_{aggregates}$$

So finally, the corrected and actual volume fraction of silica in sample M86 is given by:

$$F_{corrected}(M86) = \tau_{SiO_2} V_{aggregates} / V_{total} = \tau_{SiO_2} F_{SEM/FIB}$$

From Table 3.3, the measured volume fraction for M86 was $F_{SEM/FIB}$ = 5.6 %, which leads to a corrected value of 5.6 % * 20 %, i.e. 1.1_2 %. This result suffers from a relatively large inaccuracy, since (i) we have established that the relative error of the SEM/FIB measurement is about 16 % (see 3.1.3.2), and (ii) we can easily estimate the accuracy of the evaluation of τ_{SiO_2} to be about ± 5 %. All things considered, this gives 1.16 ± 0.46 % as a final result. Remembering that the value deduced from the synthesis is 1 %, we finally find a reasonably good quantification when considering the correction due to the hidden matrix within aggregates.

Assuming the same value for τ_{SiO_2} in the M57 sample (because of lack of time, the corresponding TEM tomography could not be performed with this second material elaborated under acid conditions - i.e. pH 5 -), we can correct the value of 25 % as reported in Table 3.3 from the FIB/SEM experiment as:

$F_{corrected}$(M57) = 5.20 ± 2.05 %

This again is in very good agreement with the expected value from the synthesis conditions, i.e. 5 %.

3.4 Improved geometry to avoid the matrix shrinkage

One last point that we would like to check concerns the correction of the shrinkage effect of the polymer matrix. It is induced, as presented, during the FIB/SEM experiments by the usual geometry of the cavities machined in the sample, in order to prepare a front surface adequate to the 3D slice-and-view experiment (see section 3.2.1.3 and for example Figure 3.24).

In the results reported previously, a shrinkage ratio of about 80 % was systematically observed (see Table 3.2). In order to reduce this effect, we have to strengthen the central part of matter to be used for the 3D analysis, which is actually weakened by the 'U-shape' cavity in the usual geometry. Figure 3.35 shows the newly adopted geometry. The main difference with the 'U-shape' cavity is that no excavation is performed on the laterals side of the central zone to be used for the 3D sequence. It can further be seen that the front cavity is much wider and longer in the Z direction than in the case of the usual U-shape' cavity (reported for comparison in the right hand part of Figure 3.35). Doing so is to (i) simply avoid the re-deposition of milled matter onto the very central region of interest, and (ii) optimize the signal collection (i.e. minimize shadowing effects) when using the 'Inlens' detector of our Zeiss FIB instrument.

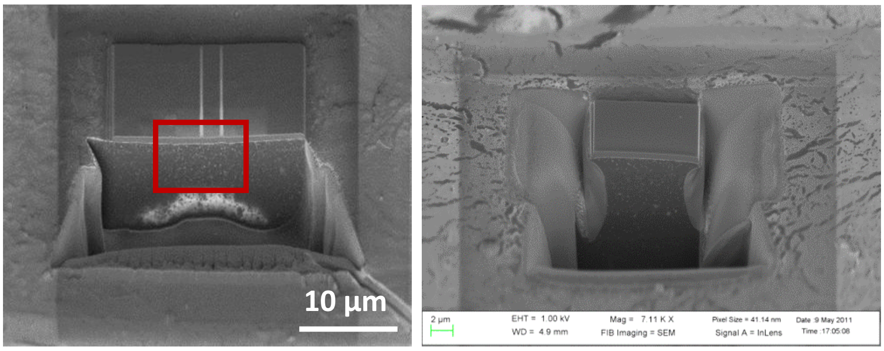

Figure 3.35: Left: adopted geometry of a new cavity for reducing the shrinkage effect; the classical 'U-shape' cavity (see Figure 3.24) is reported on the right for comparison. The imaging field is marked by a red frame.

To test this geometry, two image stacks were acquired on the M86 and M57 samples (elaborated with pH 5).

In the case of the M86 samples, 515 images were acquired; a segmented volume with a 500 * 500 pixels² section series is visualized in Figure 3.36. The measurement of the silica volume fraction without any shrinkage estimation and correction gives a value of 5.01 %, much less than the 'raw' value of 8 % (see Table 3.3) before the shrinkage correction in the case of the 'U-shape' geometry. Obviously, this value remains roughly five times larger than the expected value of 1 %, because of the 'hidden matrix effect' discussed in the previous section 3.3.3 (after correction by the factor τ_{SiO_2} of about 20 %, we end up with the correct volume fraction of about 1 %).

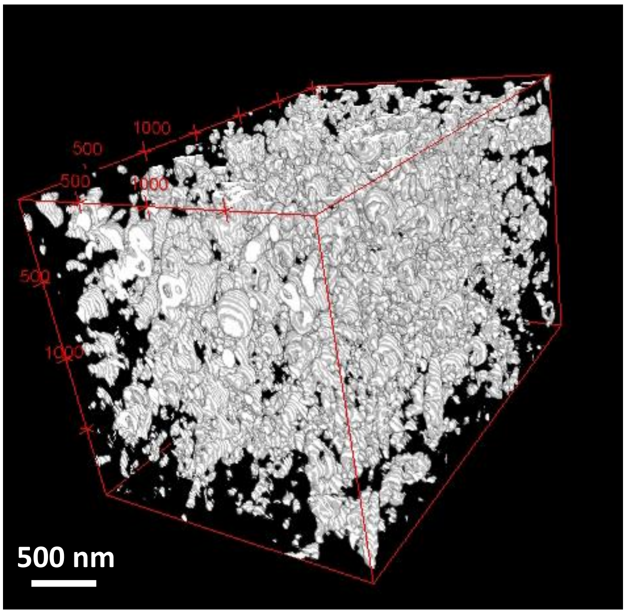

Figure 3.36: 3D visualization of a 500 * 500 segmented stack of 515 slices corresponding to Figure 3.35 (left).

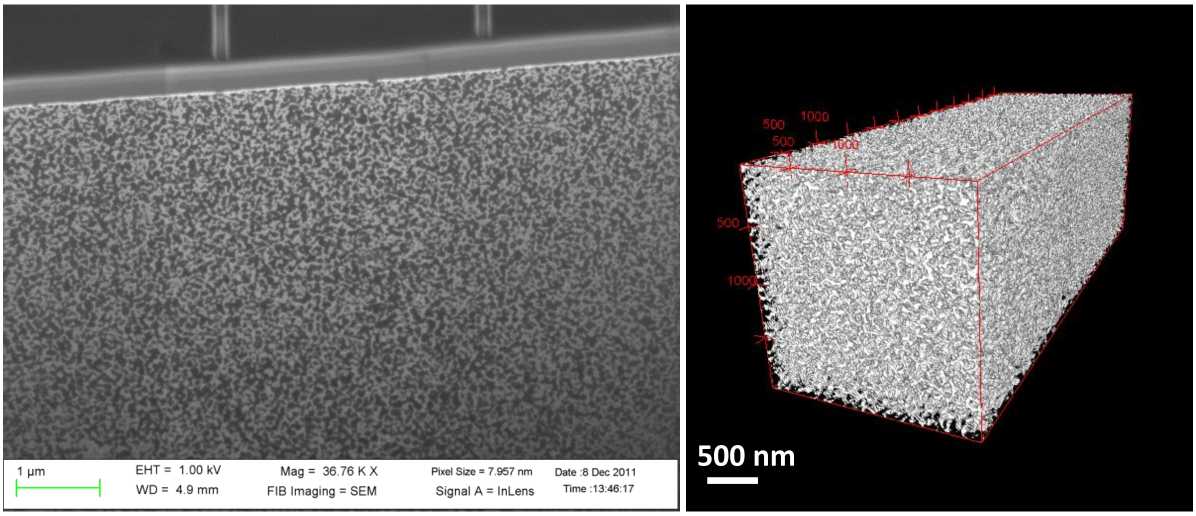

Figure 3.37: 3D FIB analysis of sample M57 with the new geometry of the front cavity; left: typical micrograph; right: 3D representation of a segmented stack of 495 slices (section of 500 * 500 pixels²).

In the case of the M57 sample illustrated by Figure 3.37, the quantification of the silica volume fraction gives a value of 26.6 %. As for the M86 sample, this value is much less than the 'raw' value of 31.6 % (see Table 3.3) before the shrinkage correction in the case of the 'U-shape' geometry. Then, applying the correction factor τ_{SiO_2} leads to a final value of about 5.33 %, assuming again that most of the silica volume is comprised in the aggregates. This is in very reasonable agreement with the expected quantity of 5 %.

From these measurements, we can conclude that the new geometry for preparing the 3D FIB experiment mostly eliminate the shrinkage of the matrix that was induced by the collapse of the lateral walls in the usual configuration shown in Figure 3.24.

3.5 Conclusions and perspectives of the chapter

The present chapter was devoted to the quantitative analysis of the microstructure of statistical poly methyl methacrylate-co-butyl acrylate (P(BuA-*stat*-MMA))/SiO_2 nanocomposites constituted by a dispersion of silica particles, with an average size of about 16 nm (and a narrow distribution) in a polymer matrix obtained under different elaboration (i.e. pH) conditions. These samples were elaborated at LVCN (*Laboratoire des Colloîdes, Verres et Nanomatériaux*) of Montpellier 2 University and characterized in both TEM and by SANS [Tatou2011] [Oberdisse2006] [Oberdisse2007] [Genix2012].

The aim of our approach was to test whether 3D electron microscopy techniques could be applied for a quantitative measurement of the volume fraction of the reinforcing silica particles. According to the elaboration conditions, different volume fractions and organizations of the particles were expected. Table 3.5 completes previous Table 3.3 and summarizes the results.

Sample	Analysed volume (μm^3)	**Silica volume fraction (%)**				**Elaboration conditions**	
		After segmentation + erosion-dilation	**After shrinkage correction**	**After correction of the aggregates density**	***Expected value***	pH	Aggregates?
M82	82	1.7 %	**1.4 %**	***1.4 %***	***1 %***	9	no
M49	61	5.0 %	**4.1 %**	***4.1 %***	***5 %***	9	no
M86	45	8.0 %	**5.6 %**	***1.2 %***	***1 %***	5	yes
M57	87	31.6 %	**25.0 %**	***5.20 %***	***5 %***	5	yes

Table 3.5: Final results concerning the volume fractions of silica in the 4 studied P(BuA-*stat*-MMA)/SiO_2 nanocomposites (see Table 3.3 and text for details).

After all required corrections, it is seen that reasonable (if not good) measurements can be obtained, but the process is still complicated:

- During 3D FIB acquisition, polymers are known to experience a severe shrinkage which has to be estimated and corrected, or ideally avoided. For the latter case, we have adapted the geometry of the excavation to be performed by the FIB on the surface of the material in order to prepare an adequate area for the tomographic slice-and-view approach. A cooled stage could probably be a good mean to improve the sample stability in operation.
- Due to the limitation of the SEM resolution (in the nanometre range), and more seriously, that of the FIB approach (a few nanometres in the best case because of the voxel size according to the desired field of view, magnification and slice thickness during the successive FIB abrasions), the 3D FIB analysis could not resolved properly fine details as they were encountered in the case of samples where silica aggregates form (that is, in the present case, acid elaboration conditions).

- To complete the analysis from the spatial resolution point of view, TEM nano-tomography was required. This has imposed to prepare ultramicrotomic sections as for a classical TEM observation. During TEM, conventional bright field imaging was shown to produce significant damage at the matrix-particles interfaces within the silica aggregates. Fortunately, the STEM-HAADF mode appeared to be much less aggressive and successful tilting tomography sequences could be recorded.
- In this particular case, tilting tomography in the SEM (Transmission mode), although slightly easier to undertake compared to TEM nano-tomography, could not bring better results than the FIB approach, simply because of the intrinsic resolution limit of SEM imaging.
- Finally, the most stringent issue during this analysis is perhaps the image treatment part. It was shown that the way the tomograms were filtered greatly influence the final measurements and great attention has to be paid in order to get representative results. With the aid of computer simulations based on modelled microstructures, we were able to adjust the segmentation and erosion/dilatation parameters.

All things considered, we can conclude that a relative accuracy not better than 16 % could be obtained in the present measurements. This may appear as a poor value, but according to the typical volume fractions used in such nanocomposites (usually no more than a few percent), this does not lead to a great absolute error. However, and in complement of more ‘mesoscopic’ or ‘local’ approaches (like SAXS or SANS and TEM respectively), the FIB-SEM approach which was applied here offers a good compromise in terms of statistical representativity of the volumes explored, the possibly of visualizing the homogeneity of the particle distribution, and a real space 3D reconstruction of the microstructure. It is thus a good complementary tool to cross-check results obtained from other methods.

References of chapter 3

[Deschanel2005, thesis] Deschanel S. *Dynamique des précurseurs de la rupture des matériaux hétérogènes : application aux mousses polymères vitreuses.* GEMPPM, INSA de Lyon (2005). http://theses-search.insa-lyon.fr/notice/view/default%3AUNIMARC%3A141656

[Genix2012] Genix A.-C., Tatou M., Imaz A., Forcada J., Schweins R., Grillo I., and Oberdisse J. *Modeling of Intermediate Structures and Chain Conformation in Silica-Latex Nanocomposites Observed by SANS During Annealing*. Macromolecules (2012), vol.3, pp: 1663-1675.

[Holzer2006] Holzer L., Muench B., Wegmann M., Gasser P., and Flatt R.J. *FIB-Nanotomography of Particulate Systems—Part I: Particle Shape and Topology of Interfaces*. Journal of the American Ceramic Society (2006), vol.89, pp: 2577-2585.

[Liu2012b] Liu Y., Yuan H., Bogner A., Van de Moortèle B., Epicier T., *"Tri-3D" Tomography in FIB, SEM and TEM: Application to Polymer Nano-Composites"*. Interdisciplinary Symposium on 3D Microscopy, Les Diablerêts, Suisse (March 5-8, 2012), S4, pp: 43-44.

[Luther2006] Luther P.K. *Sample Shrinkage and Radiation Damage of Plastic Sections.* In Electron Tomography, J. Frank, ed. (Springer New York, 2006), pp: 17–48.

[Oberdisse2006] Oberdisse J. *Aggregation of colloidal nanoparticles in polymer matrices*. Soft Matter (2006), vol.2, pp: 29–36.

[Oberdisse2007] Oberdisse J., Hine P., and Pyckhout-Hintzen W. *Structure of interacting aggregates of silica nanoparticles in a polymer matrix: Small-angle scattering and Reverse Monte-Carlo simulations*. Soft Matter (2007), vol.3, pp: 476–485.

[Papon2012] Papon A., Montes H., Lequeux F., Oberdisse J., Saalwächter K., and Guy L. *Solid particles in an elastomer matrix: impact of colloid dispersion and polymer mobility modification on the mechanical properties*. Soft Matter (2012), vol.8, pp: 4090–4096.

[Tatou2010, thesis] Tatou M. *Nanocomposites modèles silice-latex : Etude des propriétés rhéologiques et de la structure des charges et des chaînes par Diffusion de Neutrons aux Petits Angles.* Université Montpellier 2 (2010). http://www.theses.fr/2010MON20179/document

[Tatou2011] Tatou M., Genix A.-C., Imaz A., Forcada J., Banc A., Schweins R., Grillo I., and Oberdisse J. *Reinforcement and Polymer Mobility in Silica–Latex Nanocomposites with Controlled Aggregation*. Macromolecules (2011), vol.44, pp: 9029–9039.

[Yuan2012] Yuan H., Van de Moortèle B., Epicier, T. and Menard, J.-C. *Live correction of drifts during 3D-FIB experiments.* EMC 2012, Manchester, UK (17-21 September, 2012), Vol. 2, pp: 135-136.

4 Conclusions and perspectives

4.1 Preliminary remarks

First of all, before beginning this chapter, we intend to remind the initial aim of this work.

MATEIS is a multi-materials laboratory, with a dedicated research team focussed on *Polymers, Glasses and Heterogeneous Materials* (PVMH). Part of its activities concern polymer nanocomposite (PNC), which are essentially composite systems made of a polymer matrix in which a controlled, or as controlled as possible, distribution of nano-fillers is added in order to improve some of the physical, macroscopic properties of the material as compared to the pure polymer matrix [Dalmas2007].

On another hand, MATEIS comprises also a research team dedicated to the use of microscopy techniques, namely the *Structure, nano- and Microstructure* group (SNMS). This team is directly involved in the CLYM (*Centre Lyonnais de Microscopie*), which owns several electron microscopes, among which a FEG-TEM, an Environmental SEM (ESEM) and a dual beam FIB-SEM unit.

The idea of this work was to explore the possibility of these electron microscopy techniques for the 3D characterization of PNCs. In this context, '3D' means essentially getting quantitative information about the size, morphology, distribution and interactions of the fillers within the matrix, and correlating these features with the macroscopic properties and the elaboration processes in order to optimize the use and the performances of these materials.

Hence, the initial goals of our research were:

- Perform TEM and ESEM titling tomography and FIB-SEM 'slice-and-view' tomography on different polymer nanocomposite materials, in order to explore the possibilities of these techniques in terms of 3D quantification of the fillers distribution.
- Compare these techniques and determine their relative advantages and drawbacks; search for possible optimization solutions if limitations are encountered.

This strategy has been applied to two kinds of polymer nanocomposite systems: P(BuA-*stat*-S)/MWNTs (§ 2.1, [Dalmas2005]) and P(BuA-*stat*-MMA)/SiO_2 (§ 3.1, [Tatou2011]). Different electron tomography techniques have been applied to study these materials, especially to quantify the fillers and their interactions.

We will summarize and discuss the results that have been obtained during this study, by first giving some general comments about the techniques (respectively: tilting TEM tomography in § 4.2.1, tilting SEM tomography in § 4.2.2 and FIB-SEM tomography in § 4.2.3. Then, we will discuss the results deduced from the quantification performed on the tomograms in § 4.2.4. Then, final perspectives will be gathered in the last section of this report in § 4.3.

4.2 Concluding remarks

4.2.1 TEM tomography

As already mentioned in the first introductive chapter, electron tomography is classically performed using tilting series in a Transmission Electron Microscope (§ 1.2.1). In our case, we could easily access a FEG-TEM (see Figure 1.4) operating at 200 or 100 kV, and enabling both conventional imaging (bright field) and STEM-HAADF imaging. Tomography experiments in the HAADF mode were performed on both PNC systems (see § 2.2.1 and § 3.3).

4.2.1.1 STEM-HAADF tomography

As most of the TEM tomographic experiments reported in the literature (see § 1.2.1.3), we performed first STEM-HAADF experiments. STEM-HAADF is a required method when studying crystalline materials to avoid diffraction effects during tilting which will invalidate the projection requirement (see § 1.2.1, [Midgley2003]). However, our systems were poorly crystallised (indeed, not really crystallized except the carbon nanotubes which induced very minor diffraction effects depending upon the orientation of the tubes with respect to the electron beam), and STEM-HAADF was not strictly required. Nevertheless, we noticed a reasonable contrast and its better control compared to bright field TEM (see Figure 2.5 and § 4.2.1.2). Furthermore, we also noticed a greater resistance to the irradiation in the STEM mode compared to the conventional imaging mode (see Figure 3.28). In order to complete this, we have performed a tilting experiment at a lower voltage that is not permitted in our FEG-TEM (i.e. 80 kV in the EFTEM mode, see § 4.2.1.2).

For **P(BuA-*stat*-S)/MWNTs**, several projection series were acquired between ± 65° with a tilt increment of 1.5° or 2°. The main problem that we encountered was the shrinkage of the polymer matrix during observation. This classical effect is indeed one of the major issues when observing polymer material under an electron beam [Luther2006]. According to the fact that our instrument was not specifically equipped with low dose routines, neither with a cryo-holder compatible with high tilt experiments, the essential parameter that we could adjust was the high voltage. Even at 100 kV, shrinkage was detected (see § 2.2.1.2). This is an important issue for obtaining reliable reconstruction of the original material.

This problem has led us to quantify the shrinkage during the exposure to the electron beam. Video sequences could be acquired, and tracking of natural markers (i.e., catalysts nanoparticles used for the elaboration of carbon nanotubes) allowed the strain to be measured in 2D. It has further been shown that this deformation could be, in principle, followed in 3D during the tilting experiment. A numerical trial-and-error approach, based on the hypothesis of a homogeneous (isotropic) shrinkage has been developed (see sub-section 2.2.1.3).

The first result was to allow the degree of shrinkage to be evaluated; then it could have been possible to detect the moment when the microstructure is sufficiently stabilized in order to perform a reasonable reconstruction. **A second result** concerned a possible strategy for an 'a priori' correction of the shrinkage before running the numerical reconstruction step. This point will be re-discussed in the Perspectives section § 4.3.

For **P(BuA-*stat*-MMA)/SiO$_2$**, several TEM tomography series were also acquired. It will be shown that TEM tomography nicely completed FIB results by offering the required resolution in order to understand discrepancies when quantifying the volume fraction of added particles from the FIB results only. Again, we encountered degradation effects of the material under the electron beam, but sufficiently 'small' to allow reasonable 3D reconstruction. To minimize their effect, we indeed reduce the acquisition time by increasing the angular step during the series (typically, images were obtained between ± 60° with a tilt increment of 4°). A resolution of a few nanometres could be achieved, although the experimental conditions were thus not perfect.

From this approach, we were able to quantify properly the volume fraction of fillers for different materials; however, numerous treatments were required, which will be summarized in sub-section 4.2.4.

4.2.1.2 EFTEM tomography (C$_s$-corrected tomography and cryo-tomography)

The question of contrast between the STEM-HAADF and Conventional TEM modes was evoked in the previous sub-section. Polymer-based nanocomposite systems such as those studied in the present work are not ideal candidate for HAADF imaging, because most atomic species have low weights, and thus do not produce great scattering at high angles. This is particularly true for the P(BuA-*stat*-S)/MWNTs materials, essentially composed of carbon (nanotubes) embedded into a carbon-based matrix! From this point of view, it was interesting to test conventional TEM imaging but using zero-loss filtered images (see Figure 2.24). In this Energy-Filtered mode, inelastic electrons contributing essentially to noise in the micrographs is suppressed since images can be recorded only with elastic electrons. This greatly improves the contrast and further permits to work with lower voltage: diminishing the voltage is equivalent to virtually increase the sample thickness, thus increase the inelastic contribution, which is the noise. At low voltage, the energy filter becomes not only an advantage, but a requirement. The interest of working at low voltage is to reduce the irradiation damage. This will also be a major motivation for performing tilting experiments in a SEM (see sub-section 4.2.2).

We have had the opportunity to perform an EFTEM experiment at 80 kV on a C_s-corrected TEM located at Tohoku University in Sendai, Japan (§ 2.2.2). This experiment was conducted on a FEI TITAN equipped with a C_s-corrector on the objective lens which permits good resolution even at lower accelerating voltages. The aim is to try to avoid the shrinkage problem of the matrix with a beam of lower energy. In addition, a short pre-irradiation of several minutes was done to first stabilize the matrix. Our results have shown that despite these procedures, a residual shrinkage was unfortunately measured during the first half of the projection series. Apart from this effect, we have shown that high defocus and energy filtering proved to be really efficient to enhance the contrast in the projections, in particular at high tilt angles. Reasonable reconstructions could then be obtained, and some refinement to correct the residual defect (i.e. small shrinkage and focus variation, see details in sub-section 2.2.2.1) was also performed. They have shown a slight improvement, but essentially all results remain acceptable, which demonstrates the interest of C_s-corrected EFTEM at 80 kV.

The last parameter that we aimed to test was the temperature of the observations. It is well known that TEM observations at low temperature improve the resistance to irradiation by decreasing the efficiency of all diffusion processes within the sample (§ 1.3.1). A cryo-EFTEM tomography was thus also carried out on the P(BuA-*stat*-S)/MWNTs, but only at 200 kV owing to the alignments available on the microscope: the JEOL 2200FS installed at the Curie Institute in Orsay. This instrument is equipped with a cooling sample stage allowing the specimen to be observed in-situ at the temperature of liquid nitrogen. Without any specific pre-irradiation or dedicated procedure during the experiment, we obtained probably the best 3D reconstructions on both Evaporated and Freeze-dried Pressed samples (see for example Figure 2.40, Figure 2.41 and Figure 2.43), owing to the synergic effect of energy filtering and cryo-observations.

Basically and as expected, TEM tomography gives the best results in terms of spatial resolution. We will however see that there is a great advantage to complete this approach with SEM (and FIB-SEM) tomography for 2 main reasons: the lower voltage which helps preserving the integrity of the sample, and the larger field of view (however at a slightly lower resolution). Whereas the first point is partly solved with “cryo-tomography” in the TEM, the second one remains very important in order to get more quantitative and statistical results.

4.2.2 SEM tomography

According to the above, SEM tomography might present several complementary advantages compared to TEM tomography: firstly it is easier to handle, secondly it offers in principle better conditions regarding the possible irradiation of the sample, thirdly it may provide more easily large field of view, i.e. larger tomograms.

The irradiation-induced shrinkage of the sample during TEM observations was the main drawback of TEM tomography performed at room temperature. Even if a stabilization of this deformation is possible after a given pre-irradiation sequence, this ‘solution’ is not acceptable for certain situations. This is the case of the P(BuA-*stat*-S)/MWNTs system: it was studied in order to clarify the electrical properties measured in two types of materials elaborated according to two different routes (see sub-sections 2.1.2 and 2.1.3). Since the property of interest has to do with the density of contacts between nanotubes, it was obvious that any shrinkage of the matrix will affect the actual microstructure by possibly creating artificial contacts. According to the fact that it was difficult to perfectly control the shrinkage in the TEM (at least at room temperature, whatever the accelerating voltage), SEM results might be a good alternative to undertake a more correct quantification of the contacts density.

Two different microscopes have been used in this work to study the **P(BuA-*stat*-S)/MWNTs**. The first one is an ESEM (FEI XL30 at CLYM), in which a tilting tomography can be performed in transmission mode with a home-made dedicated ‘tomo-STEM®’ stage (see § 1.2.2.1 and [Jornsanoh2011]). The interest of the STEM mode in the SEM is to perform HAADF-like tomography with a much lower accelerating voltage (typically, 30 kV) by preserving the capacity of environment mode. It is extremely advantageous for polymer-based materials which are sensible to the high energy of electrons. Another interest of the ESEM, as any modern ‘low vacuum’ microscope, is to permit an easy observation of non-conductive materials without any drastic charge effect (due to charge compensation at the sample surface).
We have thus used TEM grids on which ultramicrotomic sections were mounted. The large field of view, as expected, helped to obtain images containing more fillers with only a little sacrifice of resolution. Indeed In order to estimate contacts between nanotubes, it was even better to ‘lose’ some resolution in order to binarize more easily the envelop of the tubes, treated as cylinders, without any strong internal contrast variations due to the walls and ‘empty’ core of the CNTs. Furthermore, no evident shrinkage of the matrix was measured during the tomographic acquisition with or without a short pre-irradiation. Unfortunately we still faced some problems with the contamination which degraded the contrast (see Figure 2.46) during the long exposure time (total manual operation of about 2 hours for a series between ± 70°). The same experiment was also tried on the **P(BuA-*stat*-MMA)/SiO$_2$** system, considering the small size of the objects to be reconstructed and the resolution insufficient, we did not obtain the best quality in the reconstructed tomograms, and thus no result was reported from these observations in the present document.

The other microscope used for the **P(BuA-*stat*-S)/MWNTs** was a Hitachi model equipped with a cold-FEG that permits a relatively higher resolution (S5500 SEM). This instrument accepts a commercial TEM grid on a TEM-type holder and also allows STEM-HAADF-type imaging. The acquisition time was slightly shorter than in the case of the ESEM tomography because the tilt range was limited to ± 40° in the standard configuration (and holder) that we could use. This limitation was largely compensated by the attainable resolution, owing to the cold-Field Emission, and despite some occasional charging effects since this instrument is a conventional high vacuum machine. No specific irradiation effect could be detected. The relatively small tilt angular range is ‘a priori’ not optimal for a first-rank reconstruction, but the results turned to be good enough (see Figure 2.52, Figure 2.53, Figure 2.55 and Figure 2.56), and better than those obtained from the ESEM.

As already mentioned, the tomography carried out in both SEMs has shown no significant shrinkage of the polymer matrix, and they have fulfilled our expectations in getting larger tomograms at slightly lower resolution, which in the present case was a relative advantage to segment and binarize the reconstructed volumes (identification of the nanotubes without resolving their walls, see sub-sections 2.5.1 and 4.2.4).

4.2.3 FIB-SEM tomography

The ‘slice-and-view’ tomography as it can be performed within a FIB-SEM microscope is increasingly applied to material sciences. Unlike the tilting tomography which collects projections of the material, the FIB-SEM allows to cut and image fresh cross-section slices successively [Holzer2004]. As for conventional SEM, no complicated sample preparation is required. The reconstructed volume can be very large since the number of slices is only limited by time but not the size of the sample since it does not need to be thin.

The main issues in 3D FIB remain the stability of the sample during the acquisition, and the resolution which is limited by the slice thickness (a few nanometres in the best case). These were the main problems encountered in the case of the **P(BuA-*stat*-S)/MWNTs** system. Indeed the tomographic experiments failed essentially because of the weak contrast of CNTs and the ‘curtaining’ effect (see § 2.4). The shrinkage also appeared to be a strong limitation (Figure 2.60); the polymer matrix has a T_g of only - 7° which makes it too soft even at room temperature. Working at low temperature (cooling stage) and using staining techniques may be useful to enhance the stability and contrast of such a nanocomposite.

For the **P(BuA-*stat*-MMA)/SiO$_2$**, the shrinkage was again the major problem encountered in FIB; it affected all samples, no matter their fraction of silica particles and elaboration conditions (pH value) (see § 3.2.1.3). But in this case the contrast between the fillers and the matrix was good enough to allow reasonable tomograms to be reconstructed. After correction from the shrinkage effect, we obtained volume fractions of the second phase which were not in agreement with the expectations for 2 of the 4 studied samples (see Table 3.3). A consistent analysis could be done according to the identification of a significant amount of ‘hidden’ matrix within agglomerates of particles which form in the samples elaborated under acidic condition (pH 5) (see § 3.3.3). The joined use of FIB and TEM tomography was fruitful: FIB allowed great statistics on large populations of objects, TEM allowed individual objects to be examined but at a resolution high enough to reveal the ‘hidden’ matrix within aggregates. Quantitative results could thus be obtained owing to this combined approach, which allowed pertinent corrections to be applied concerning the volume fraction of SiO_2 particles. In addition, we were also able to propose a new excavation geometry machined with the FIB in order to eliminate, or at least reduce the shrinkage effect (§ 3.4).

Despite of the failure of performing FIB-SEM tomography for the P(BuA-*stat*-S)/MWNTs system, the results obtained for the P(BuA-*stat*-MMA)/SiO$_2$ system indicate that it is indeed a powerful tool for obtaining significant results if the SEM/FIB resolution is sufficiently adapted to the studied microstructure. We have also demonstrated the interest of coupling complementary 3D techniques on the same material, such as FIB-SEM and TEM.

4.2.4 3D quantification

The experimental problems mentioned above had to be solved in order to obtain reconstructed volumes on which the real job begins: perform quantitative measurements. We had two different situations to treat in the different PNCs systems studied in this work, and thus different strategies were applied.

In the **P(BuA-*stat*-S)/MWNTs** system, we wanted to focus on the interactions between CNTs, more precisely on the density of contacts between them in order to understand previous electrical conductivity results (see § 2.1.3). A home-made program was developed in this perspective (§ 2.5). We made the choice to apply this approach on segmented 2D slices of tomograms, although it would certainly be better to treat the problem directly in 3D. In fact we essentially intend to compare two different microstructures obtained with an 'Evaporated' or a 'Freeze-dried and Pressed' elaboration route (see § 2.1.2); although imperfect, we believe that our approach can be sufficient to achieve this goal. The quantitative difference obtained, although quite small in absolute but nearly 50% in relative (see Table 2.1), has allowed us to conclude that more contacts were measured in the FP material than in the E material. This indicates a higher electrical efficiency of contacts in the E material, which in itself is an important result.

In the other system **P(BuA-*stat*-MMA)/SiO_2**, the quantification involved an a priori easier analysis, since it was question to measure the volume fraction of a second phase (silica particles) distributed in a matrix in what we can qualify of dilute concentrations (a few 5%). We have shown that several levels of corrections were required in order to obtain reasonable results, according to the fact that the correct values were known in advance (§ 3.2.2). Furthermore, the consistency of our treatments was discussed:

- We firstly focused on the resolution of the FIB/SEM approach (§ 3.1.3.1).
- We examined secondly the impact of the erosion/dilation steps during image treatment in order to determine sufficiently robust conditions (§ 3.1.3.2).
- We finally consider the statistical representativity of the reconstructed volumes and the homogeneity of the particles distribution (§ 3.1.3.3).

As already discussed in the previous section, the association with TEM tomography results provided the key to quantify properly the higher agglomeration level in the samples elaborated under acid conditions (§ 3.3.3).

This study was then very instructive, showing that for an unknown similar problem, several settings and conditions can be adjusted, which may end up with very large variations of results, even in the simple case of measuring a volume fraction of almost ideal spherical objects dispersed in a matrix.

4.3 Perspectives

Concerning TEM tomography:

As discussed in § 4.2.1, for PNC materials like those studied in this work, **working at low accelerating voltages**, **using cooling sample stages** and **filtering the images** (elastic imaging with an energy filter) appeared to be 3 ideal conditions for tomographic acquisitions on such materials. On this topic, CLYM has recently received a TEM of FEI TITAN with a column aligned at 80 kV, and equipped with a C_s-corrector; this important accessory is a further advantage since it allows conserving a good resolution with a large pole pieces gap permitting high tilts, as required in tilting tomography. The availability of an energy filter would be a further important advantage in this approach, certainly also applicable to various other kind of samples (for example, hybrid nano-systems). A cooling holder would also be a valuable investment.

From a methodological point of view, we have shown that the shrinkage, more generally the deformation of the sample during the rather long tilting acquisition, remains a severe limitation for polymer-based materials. A 3D shrinkage correction seems to be possible from the series in projections, as was very basically introduced with a procedure described in § 2.2.1.3. A more advanced image analysis by Digital Image Correlation should certainly be useful to detect properly the local strains and correct them in the projection series prior to reconstruction.

Concerning SEM tomography:

A second generation of the ‘tomo-STEM®’ stage developed at MATEIS (see Figure 4.1) was designed and fabricated in MATEIS, which provides certain advantages compared to the first one:

- A piezoelectric motor allows movements in three dimensions of the sample holder rapidly with a better precision, especially the highness which concerns the distance between the sample and the detector. The tilting range is reached to be 360° at an accuracy of mili-degree.
- It possesses the ability of adjusting in-situ the eucentric position of the sample with a dedicated controlling program, while it had to be adjusted ex-situ and visually under an optic microscope for the first generation stage.
- A Peltier cooling and heating part could be introduced to adjust the temperature, depending on the studied materials and objectives.
- A rod-shaped sample can be applied to obtain ± 90° tilting series which will be free of the ‘missing wedge’ in the tomograms, with the capacity of changing the sample holder (see Figure 4.2).

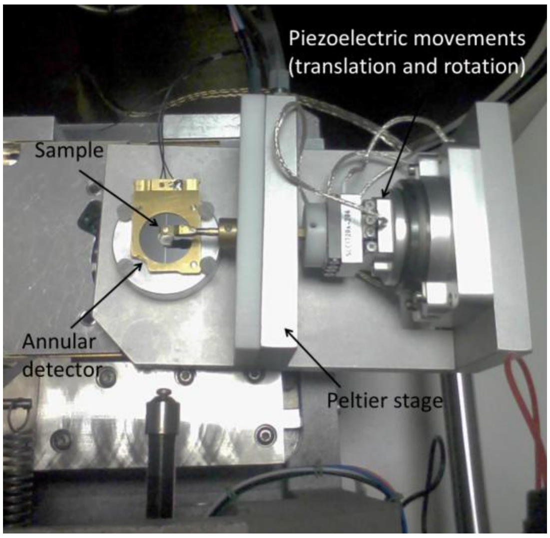

Figure 4.1: Newly developed ‘tomo-STEM®’ stage (second generation) as mounted in the ESEM. [Masenelli-Varlot2012, EMC]

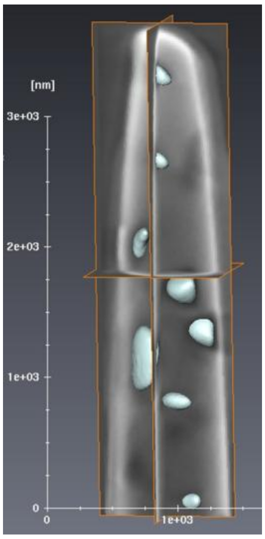

Figure 4.2: A reconstructed FIB-machined 700 nm thick rod of an alumina/zirconia composite (0-180°, tilt increment of 1°, low vacuum). [Masenelli-Varlot2012, EMC]

For **tilting tomography techniques**, tilting series at larger angular range will always be appreciated. And dual-axis or conical experiment could be useful to improve the quality of reconstructions, if low dose imaging is possible for the observations of light sensible materials.

Concerning FIB-SEM tomography:

As discussed throughout the study of PNC systems, the deformation issue of the polymer matrix is one of the most serious which also limits the FIB-SEM approach. Thus having the ability of cooling the samples in-situ to reduce or avoid the irradiation problems will be of great interest.

The resolution is also a limiting factor, which cannot be easily handled since sample and 'problematic'-dependent. In addition to the intrinsic resolution as permitted by (i) SEM imaging and (ii) the ion machining of small slices (at a nanometric level), one has to consider the numerical resolution defined by the magnification and the size of images.

Despite these difficulties, tomography in FIB-SEM is more and more becoming a routine technique to obtain 3D information on several kinds of materials and systems. In the course of this thesis, we had the opportunity to collaborate to different studies on different systems [Fiorido2013] [Destouches2013].

Concerning the quantification procedure:

We had to apply several quantification approaches in the present work. Some of them would certainly merit more developments:

- As discussed in § 4.2.4, the quantifications of the contacts between cylinder-shaped elongated particles (as nanotubes or nanowires) was done in 2D; adapting this routine to perform measurements directly in 3D, and improving the identification of the cylinder envelopes would certainly be interesting to obtain more accurate and reliable results.
- As already mentioned above, developing a numerical procedure to correct the projections obtained in tilting tomography from any local deformation could also be an exciting challenge for a future work.

References of chapter 4

[Dalmas2005] Dalmas F., Chazeau L., Gauthier C., Masenelli-Varlot K., Dendievel R., Cavaillé J.Y., and Forró L. *Multiwalled carbon nanotube/polymer nanocomposites: Processing and properties.* Journal of Polymer Science Part B: Polymer Physics (2005), vol.43, pp: 1186–1197.

[Dalmas2007] Dalmas F., Cavaillé J.-Y., Gauthier C., Chazeau L., and Dendievel R. *Viscoelastic behavior and electrical properties of flexible nanofiber filled polymer nanocomposites. Influence of processing conditions.* Composites Science and Technology (2007), vol.67, pp: 829–839.

[Destouches2013] Destouches N., Crespo-Monteiro N., Vitrant G., Lefkir Y., Reynaud S., Liu Y., Epicier T., Vocanson F., Pigeon F. *When light plays with metal nanoparticles in thin films and creates spontaneously active color filters*. Submitted to Nature Communications (NCOMMS-13-03011-T).

[Fiorido2013] Fiorido T., Galineau J., Salles V., Seveyrat L., Belhora F., Cottinet P.-J., Hu L., Liu Y., Guiffard B., Brioude A., Epicier T., and Guyomar D. *Innovative organic/inorganic nanocomposites for actuators and magnetic sensors applications.* Submitted to Advanced Functional Materials.

[Holzer2004] Holzer L., Indutnyi F., Gasser P.H., Münch B., and Wegmann M. *Three-dimensional analysis of porous BaTiO3 ceramics using FIB nanotomography.* J Microsc (2004), vol.216, pp: 84–95.

[Jornsanoh2011] Jornsanoh P., Thollet G., Ferreira J., Masenelli-Varlot K., Gauthier C., and Bogner A. *Electron tomography combining ESEM and STEM: A new 3D imaging technique.* Ultramicroscopy (2011), vol.111, pp: 1247–1254.

[Luther2006] Luther P.K. *Sample Shrinkage and Radiation Damage of Plastic Sections.* In Electron Tomography, J. Frank, ed. (Springer New York, 2006), pp. 17–48.

[Masenelli-Varlot2012, EMC] Masenelli-Varlot K., Bogner-Van de Moortèle A., Malchère A., Ferreira J. *Low-voltage STEM tomography in ESEM: 3D characterization in function of relative humidity with a nanometer resolution.* EMC 2012, Manchester (September 17-21, 2012), Vol. 2, PS 2.4, pp: 308-309.

[Midgley2003] Midgley P.A., and Weyland M. *3D electron microscopy in the physical sciences: the development of Z-contrast and EFTEM tomography.* Ultramicroscopy (2003), vol.96, pp: 413–431.

[Tatou2011] Tatou M., Genix A.-C., Imaz A., Forcada J., Banc A., Schweins R., Grillo I., and Oberdisse J. *Reinforcement and Polymer Mobility in Silica–Latex Nanocomposites with Controlled Aggregation.* Macromolecules (2011), vol.44, pp: 9029–9039.

FOLIO ADMINISTRATIF

THESE SOUTENUE DEVANT L'INSTITUT NATIONAL DES SCIENCES APPLIQUEES DE LYON

NOM : LIU DATE de SOUTENANCE : 25/07/2013

Prénoms : Yang

TITRE : 'Tri-3D' electron microscopy tomography by FIB, SEM and TEM: Application to polymer nanocomposites

NATURE : Doctorat Numéro d'ordre : 2013-ISAL- 0076

Ecole doctorale : Matériaux de Lyon (ED 34)

Spécialité : Génie des Matériaux

RESUME :

Ce travail a porté sur la caractérisation et la quantification en 3D de la répartition de charges de différents types (nanoparticules, nanotubes, etc.) dans des matrices polymères. Nous nous focalisons sur les techniques de tomographie en microscopie électronique. Une approche multiple en **tomographie électronique** a été réalisée : la tomographie en FIB/MEB (faisceau d'ions focalisé/microscope électronique à balayage), la tomographie en MEB et la tomographie en MET (microscope électronique en transmission).

Les nanocomposites polymère sont généralement élaborés aux fins d'améliorer les propriétés physiques (mécanique, électrique, etc.) du matériau polymère constituant la matrice, grâce à une addition contrôlée de charges nanométriques. La caractérisation de tels matériaux, et l'établissement de corrélations précises entre la microstructure et les propriétés d'usage, requièrent une approche tri-dimensionnelle. En raison de la taille nanométrique des charges, la microscopie électronique est incontournable.

Deux systèmes de nanocomposite polymère ont été étudiés par une approche multiple de tomographie électronique : **P(BuA-*stat*-S)/MWNTs** (copolymère statistique poly (styrène-*co*-acrylate de butyl) renforcé par des nanotubes de carbone multi-parois), et **P(BuA-*stat*-MMA)/SiO_2** (copolymère statistique poly(butyl acrylate-*co*-methyl methacrylate) renforcé par des nanoparticules de silice). Par combinaison de divers techniques, la caractérisation et la quantification des nanocharges ont été possibles. En particulier, la taille, la fraction volumique et la distribution des charges ont été mesurées. Cette étude a ainsi fourni des informations en 3D qui contribuent à mieux comprendre les propriétés des nanocomposites. Une attention particulière a été portée aux artefacts et causes d'erreur possibles durant l'étape de traitement 3D. Nous avons également essayé de comparer les différentes techniques utilisées du point de vue de leurs avantages et inconvénients respectifs, en dégageant des possibilités d'amélioration future.

MOTS-CLES : tomographie électronique, 3D, FIB/MEB, MEB, MET, nanocomposite polymère, nanotubes de carbone, nanoparticules de silice

Laboratoire (s) de recherche : MATEIS (UMR 5510)

Directeur de thèse: Thierry EPICIER
Agnès BOGNER-VAN DE MOORTELE†

Président de jury : Jean-François GERARD

Composition du jury : Julian OBERDISSE, Marco CANTONI, Jean-François GERARD, Maud GIOT, Laurent CHAZEAU, Bertrand VAN DE MOORTELE (invité), Thierry EPICIER